

AN ABSTRACT OF THE DISSERTATION OF

Patricio A. Catalán Mondaca for the degree of Doctor of Philosophy in
Civil Engineering presented on November 26, 2008.

Title: Microwave Scattering from Surf Zone Waves

Abstract approved:

Merrick C. Haller

Wave breaking in the surf zone is an important forcing mechanism on the generation of nearshore currents and in the driving of sediment transport. At the same time, wave breaking can have significant spatial and temporal variability that needs to be accounted for in the description of nearshore processes. Remote sensors are best suited to collect wave breaking measurements due to their large footprint and synoptic capabilities, but in order to extract quantitative wave parameters a proper understanding of the imaging mechanisms is essential. Microwave sensors have been shown to be able to measure wave parameters in deep water, but in the surf zone many of the assumptions the algorithms are based upon do not hold. Additionally, the dynamics of breaking waves are different and may affect in a yet determined way the signal.

This dissertation first intends to address an observational gap regarding surf zone microwave measurements. A novel combination of synchronous, large coverage marine radar, calibrated pulsed Doppler radar and video observations from a field site enable the analysis of the evolution and characteristics of the wave signature. The combined data sets yield superior discrimination rates between breaking and non-breaking waves. Discrimination also allows the study of the microwave scattering by source, where active

breaking is separated from remnant foam and steepening waves. Results show that the backscattered power from breaking waves, specifically from the wave roller, is a several dB larger than that of foam and steepening waves and independent of the environmental conditions and polarization state. While similar results have been obtained for deep water waves and variety of scattering models have been proposed, it is found that none of the models can describe all the data. Additionally, most of the models neglect the roller morphology. Therefore, in the last section a scattering model is introduced, in which the roller is treated as a volume where a collection of water droplets embedded in air can scatter incoherently. Multiple interactions of the scattered fields between particles and the boundaries are also accounted for. Though the model formulation is complex, it depends on a few physical parameters (diameter, volume fraction, medium permittivity) and no calibration constants. Comparison against data shows that the model does a reasonable job in predicting the observed scattering levels, polarization response and grazing angle dependencies, although is not capable to reproduce the maximum scattered levels observed and predicts polarization ratios always less than unity.

©Copyright by Patricio A. Catalán Mondaca

November 26, 2008

All Rights Reserved

Microwave Scattering from Surf Zone Waves

by

Patricio A. Catalán Mondaca

A DISSERTATION

submitted to

Oregon State University

in partial fulfillment of
the requirements for the
degree of

Doctor of Philosophy

Presented November 26, 2008

Commencement June 2009

Doctor of Philosophy dissertation of Patricio A. Catalán Mondaca
presented on November 26, 2008

APPROVED:

Major Professor, representing Civil Engineering

Head of the School of Civil and Construction Engineering

Dean of the Graduate School

I understand that my dissertation will become part of the permanent collection of the Oregon State University libraries. My signature below authorizes release of my dissertation to any reader upon request

Patricio A. Catalán Mondaca, Author

ACKNOWLEDGEMENTS

I would like to thank Mick Haller for his continuous support, help and guidance throughout these five years, when he was always ready to help me on seeing things from the brighter side. This was truly a learning experience and I hope that he enjoyed at least as much as I did.

Special thanks to my Rob Holman and John Stanley for their continuous support and help when I did not understand the intricacies of the Argus system and other things. Bill Plant was always available for me despite the distance and provided a collaboration that turned out to be essential for our success. Additionally I would like to thank Harry Yeh and Roger Graham for being part of my committee; Dennis Trizna for development and support of the marine radar and the staff at the Field Research Facility.

And last, but certainly not least I would like to thank Ximena, Beatriz and Maximiliano, for their love and support, for being there and being essential in my life.

TABLE OF CONTENTS

	<u>Page</u>
1. Introduction	1
2. Literature review	5
2.1 Introduction	5
2.2 Prior nearshore and surf zone observations	6
2.3 Scattering Mechanisms	9
2.3.1 Bragg scattering and Composite Surface Theory	9
2.3.2 Multipath models	12
2.3.3 Specular Scattering	16
2.3.4 Enhanced Surface Roughness	19
2.3.5 Plume and bore models	23
2.3.6 Roller related features	26
2.3.7 Ocean spray and foam	29
2.3.8 Volumetric scattering	31
2.4 The problem of detecting breaking waves	33
2.4.1 Radar Cross Sections	33
2.4.2 Backscatter distributions	37
2.5 Summary	40
3. Experiments and Data Processing	42
3.1 Introduction	42
3.2 Instrumentation	42
3.2.1 Marine Radar	42

TABLE OF CONTENTS (Continued)

	<u>Page</u>
3.2.2 River Rad	44
3.2.3 ARGUS III	46
3.3 Environmental Conditions	47
3.4 Preliminary data processing	50
3.4.1 Alignment	50
3.4.2 Microwave calibration	50
4. Optical and microwave backscatter statistics from breaking waves	57
4.1 Introduction	57
4.2 Theory	58
4.2.1 Optical sensors	59
4.2.2 Microwave sensors	63
4.3 Experimental Data and Preliminary Processing	65
4.4 Results	68
4.4.1 Probability density functions	68
4.4.2 Joint Probability Density Functions	75
4.5 Discussion	78
4.5.1 Validation	78
4.5.2 Sources of error	87
4.6 Summary	90
5. Backscattering from waves in the surf zone	92
5.1 Introduction	92
5.2 Experimental Data and Preliminary Processing	93

TABLE OF CONTENTS (Continued)

	<u>Page</u>
5.3 Results and Analysis	95
5.3.1 Breaking detection	96
5.3.2 Backscattered power	97
5.3.3 Evolution of individual events	114
5.3.4 Polarization ratios	123
5.3.5 Doppler spectrum	129
5.4 Summary	138
6. A model for microwave scattering from breaking waves	141
6.1 Introduction	141
6.2 Conceptual scattering model for the wave roller	141
6.3 EM model formulation	146
6.3.1 Basic scattering concepts	146
6.3.2 Dense Media Radiative Transfer Theory	148
6.3.3 Multiple scattering by discrete scatterers	154
6.3.4 QCA in dense media scattering	156
6.3.5 Extinction, absorption and phase matrices	161
6.3.6 Backscattering coefficient	165
6.4 Model parameters	166
6.5 Results and discussion	168
6.6 Summary	182
7. Summary and Conclusions	184

TABLE OF CONTENTS (Continued)

	<u>Page</u>
Bibliography	203
Appendix	204
A. Video and Radar Synchronization	205
A.1 Motivation	205
A.2 Experimental Setup	205
A.3 Data Analysis	207
A.3.1 Feature Tracking	207
A.3.2 Time lag Estimation	209
A.4 Results	211

LIST OF FIGURES

<u>Figure</u>	<u>Page</u>
2.1 Multipath scattering paths	13
2.2 Sketch of the slosh geometry	24
3.1 Geo-referencing of the microwave sensors	45
3.2 Field of view of the sensors	47
3.3 Wave height time series	48
3.4 Environmental conditions during May12th-16th	49
3.5 Looking angles of the microwave sensors	51
3.6 Marine radar calibration	54
3.7 Saturation of the marine radar	55
3.8 Saturation fraction time series	56
4.1 Zonification of the field of view	66
4.2 Wave conditions	68
4.3 Video snapshots	68
4.4 Video PDFs and CPDFs	70
4.5 Comparison of single-point and ensemble PDFs	71
4.6 Comparison of the intensity time series for Run 9 and Run 13	72
4.7 Marine Radar PDFs and CPDFs	73
4.8 JPDF for Camera 1 and Marine Radar	76
4.9 Characteristic regions of the JPDF	79
4.10 Combined breaking detection for Run 9	83
4.11 Combined breaking detection for Run 13	84

LIST OF FIGURES (Continued)

<u>Figure</u>	<u>Page</u>
4.12 Combined breaking detection for Run 18	85
4.13 Sensitivity tests for breaking detection	86
4.14 Sensitivity tests for breaking detection	86
4.15 JPDF for Camera 3 and Marine Radar	89
4.16 Percentage of saturated events	90
5.1 Fine tuning of the time record for RiverRad	94
5.2 Breaking detection results	97
5.3 Timestacks for Run 9-1	98
5.4 Timestacks for Run 13-1	99
5.5 Timestacks for Run 18-1	100
5.6 Timestacks for Run 9-28	101
5.7 Timestacks for Run 13-28	102
5.8 Timestacks for Run 18-28	103
5.9 Estimate of the difference between time series	105
5.10 Histograms of the NRCS of breaking waves	106
5.11 Grazing angle dependency of the NRCS from breaking waves	108
5.12 Histograms of the NRCS of steep waves	109
5.13 Grazing angle dependency of the NRCS from steep waves.	110
5.14 Histograms of the NRCS of foam	111
5.15 Grazing angle dependency of the NRCS from foam	112
5.16 Grazing angle dependency of the NRCS. Ensemble of events by source. . .	114
5.17 Number of breaking events by classified by backscattered power.	114

LIST OF FIGURES (Continued)

<u>Figure</u>	<u>Page</u>
5.18 Grazing angle dependency of the NRCS at each time step.	115
5.19 Least-squares fit to the breaking NRCS.	115
5.20 Selected events for study of the evolution of the signals.	116
5.21 Evolution of a wave. Energetic case at oblique azimuth.	117
5.22 Evolution of a wave. Foamy case at normal incidence.	119
5.23 Evolution of a wave. Steepening case at oblique azimuth.	120
5.24 Evolution of a wave. Steepening case at normal azimuth.	121
5.25 Histograms of the polarization ratio.	123
5.26 Grazing angle dependency of the polarization ratio.	124
5.27 Polarization ratio evolution. Energetic conditions, oblique look.	125
5.28 Polarization ratio evolution. Steep case, oblique look.	126
5.29 Polarization ratio evolution. Energetic conditions, upwave look.	127
5.30 Polarization ratio evolution. Steep case, upwave look.	127
5.31 Doppler Spectra for Run 9-28.	130
5.32 Doppler Spectra for Run 18-28.	131
5.33 Observed radial velocities, Run 9-28.	133
5.34 Observed radial velocities, Run 18-28.	133
5.35 Radial velocity profiles, Run 9-28.	134
5.36 Radial velocity profiles, Run 18-28.	135
5.37 Radial velocity profiles, Run 9-1.	136
5.38 Mean cross-shore bathymetric profile, Sept. 21, 2005	138
6.1 Droplets generated by a surf zone wave	143

LIST OF FIGURES (Continued)

<u>Figure</u>	<u>Page</u>
6.2 Conceptual roller model	145
6.3 Schematic of a layer	149
6.4 First order scattering modes	153
6.5 Absorption and scattering for non sticky particles	169
6.6 Absorption and scattering for sticky particles	170
6.7 Absorption and scattering for sticky and non sticky particles	172
6.8 Modeled backscattering coefficient	173
6.9 Modeled polarization ratio	175
6.10 Measured NRCS from an airship	176
6.11 Model-data comparison.	178
6.12 Model-data comparison including roller slope.	180
6.13 Model-data comparison of the polarization ratio R	181
A.1 ATV and corner reflectors.	206
A.2 Track positions of the ATV	208
A.3 Selection of an event for lag estimation.	209
A.4 Lag estimation.	210

LIST OF TABLES

<u>Table</u>	<u>Page</u>
4.1 Zone definition	67
4.2 Summary of the wave conditions	67
4.3 Threshold values for breaking detection	81
5.1 Summary of the RiverRad runs	95
6.1 Summary of the beach measurements from an airship	176
A.1 Results of the lag analysis.	210

MICROWAVE SCATTERING FROM SURF ZONE WAVES

1. INTRODUCTION

Coastal regions attract people and scientists for a wide range of reasons. Protection, development and management of these areas is important for economic, environmental and societal perspectives. The understanding of the processes involved in the coastal environment is therefore relevant not only for the scientific community, but also for the society as a whole.

The coastal region has a high level of complexity, with temporal and spatial scales ranging from [10^{-1} s, cm], as in turbulence and sediment suspension processes; to [decades, $O(100)$ km] for sea level rise, and large scale coastal change. The long-term goal of nearshore research is to obtain a predictive understanding of the processes at work during shoreline changes, and to understand their dependence on offshore and local conditions. Chief among the process taking place is wave breaking, which is fundamental in energy transfer and dissipation; and also the main forcing mechanism for the generation of nearshore currents and in the driving of sediment suspension and transport. Wave breaking can have significant spatial and temporal variability that needs to be accounted for in the description of nearshore processes. For instance, wave breaking in the surf zone drives the development of the wave roller, which is the turbulent body of air and water propagating with the broken wave. The presence of the roller can be a dominant factor in the mean balances of mass and momentum and in the generation of cross-shore currents. Most of the models for the hydrodynamics of the surf zone rely on the appropriate description of wave breaking (onset, frequency of occurrence) and of the roller (length scales and lifespan), therefore measurement of these quantities is highly desirable.

However, the appropriate measurement of these quantities is a difficult task. Traditional in-situ measurement techniques can provide high sampling rates and a direct

estimation of wave parameters such as the free surface displacement, orbital velocities and sediment concentration, but the occurrence of breaking is more difficult to identify. In addition, in-situ measurements can only provide a local (point) measurement, with the consequent coarse spatial resolution that is often too sparse to fully describe the complex physical processes taking place. A logical alternative is the deployment of large arrays of instruments, but this approach is inherently more expensive and still could cover only relatively small areas with limited spatial resolution. Additionally, instruments have to be deployed in a very energetic and sometimes hazardous environment, affecting the duty cycle and endangering not only the instruments, but also the personnel involved.

As an alternative, remote sensing techniques can provide large spatial coverage with a wide range of temporal and spatial resolutions. For nearshore applications they are typically shore-based, and are inherently more movable than in-situ measurements. Their main limitation is that the measured quantity is usually only a proxy of the imaged wave field. Estimation of the wave parameters requires the understanding of the imaging mechanism in order to obtain the transfer function between the measured quantity and the target (wave) quantity. This *modulation transfer function* (MTF) is often complex and depends on many aspects such as the nature of the scatterers, viewing geometry, and illumination conditions to name a few. Nevertheless, remote sensing techniques are very promising. For instance, video remote sensing has been extensively applied to nearshore monitoring over the past two decades (see *Holman and Stanley, 2007*, for a review). The video MTF is related with the variations in brightness recorded by the camera due to reflection from the incident sunlight on the free surface (specular reflection) or from the aerated and turbulent region present during active breaking and foam. Ambient conditions such as fog or rain can affect the technique and data can be obtained only during daylight hours. Even though it is a very important tool, optical monitoring alone can not provide the full picture required by our monitoring necessities, and needs to be complemented.

Although originally designed as a navigational aid where the ocean surface had to be

suppressed to correctly identify obstacles, marine radar systems can be modified to allow the recording of the sea signal. Radars are less affected by ambient conditions and can record data during night time. Although their spatial resolution is slightly coarse, $O(10)$ m, it does not degrade in range and it can cover large areas $O(10)$ km² synoptically. This spatial resolution may be enough to resolve nearshore wave phenomena, where characteristic wavelengths can be as short as 20 m. Temporal resolution is determined by the rotation rate of the antenna, for the case of marine radars, where 0.7 Hz is not uncommon. However, the MTF of radar systems is significantly more complex than that of video, as several backscattering mechanisms can be acting simultaneously with different weighing on their contributions depending on viewing geometry and the surface characteristics. Wave breaking has been correlated with several particularities in the sensed signal, thus prompting the notion that microwave sensors could be effective as breaking wave discriminators. Though wave breaking in deep water has been studied extensively due to their implication in air-sea exchange processes, the nearshore case is still poorly understood and the presence of depth-limited wave breaking contributes in an unknown way to the MTF. Furthermore, the dynamics of breaking between deep water and shallow water are different and can have a yet to be understood effect on the scattered signals and may affect the applicability of deep water models to the surf zone.

The necessary first step in developing the methodologies designed for the retrieval of wave parameters is to understand the nature of the imaging mechanisms taking place. This dissertation addresses this situation by means of data analysis and modeling efforts for waves in the surf zone. In Chapter 2 a comprehensive review of the state of the art regarding microwave scattering from the ocean surface and the problem of breaking detection is presented. In Chapter 3 the details of the field experiments performed are presented. Chapter 4 describes the analysis of microwave and optical signals, and the development of a technique to discriminate breaking from non-breaking waves. Results of this technique are applied in Chapter 5 to retrieve a suite of detailed scattering measurements from the surf zone classified by source. Its analysis allows a better characterization

of the backscatter from breaking waves which can be contrasted with prior results and models. In response to the observed results, in Chapter 6 a new model for the backscattering from breaking waves is introduced and evaluated. Finally Chapter 7 presents a brief summary of the results and overall conclusions.

2. LITERATURE REVIEW: BACKSCATTER ANOMALIES AND THE PROBLEM OF BREAKING IDENTIFICATION.

2.1 Introduction

Wave breaking is one of the most important forcing mechanisms in the nearshore environment, and as such its appropriate measurement and/or quantification is of significant interest. However, the proper identification of the occurrence of breaking from measured data is a difficult task, partly due to the fact that breaking loosely refers to the dissipation of organized wave energy into other energy states (turbulence, heat, sound) and thus is not readily quantifiable. In consequence, the occurrence of wave breaking has been traditionally identified in the nearshore by analyzing the evolution and transformation of the wave height profile, although other methods have been attempted in other environments, for example measuring the surface slope and associating breaking with large jumps of this parameter (*Longuett-Higgins and Smith, 1983*), or on the statistical quantification of breaking based on the wind-wave spectrum (*Phillips, 1985*). On the other hand, wave breaking is distinguishable by optical methods where the incident light is randomly scattered by bubbles and droplets present in the wave roller, a turbulent mass of air and water that is generated during the breaking process. The resulting optical signal is thus typically brighter than that of non-breaking waves, and it has been regarded as an isotropic scatterer (*Haller and Catalán, submitted manuscript Haller and Catalán*), allowing its identification. However, relict foam generated during the breaking process but not corresponding to active breaking can induce false detection or overestimation of the geometrical characteristics of the breaking wave.

Optical methods have been used extensively in the surf zone with emphasis on the analysis of time averaged images where zones of preferential breaking are highlighted (see *Holman and Stanley, 2007*, for a review). While being a powerful remote sensing tool,

video imagery can be affected by ambient conditions such as fog or rain, and can only work during daylight time. In addition, to date single camera video is not capable of providing estimates of wave height which is another relevant nearshore observable. It is apparent then, that at least a complementary tool is needed.

Radar-based remote sensing has been widely used in the open ocean to obtain a wide number of measurements, including significant wave heights (e.g. *Nieto-Borge et al.*, 2006; *Hessner et al.*, 2006) and sea surface elevation time series (e.g. *Dankert and Rosenthal*, 2004). However, the application of such methods to the nearshore has been limited, mainly due to the different nature of the mechanisms responsible for radar backscatter that may sometimes violate the assumptions on which these methods are constructed upon. Among these, the presence of "anomalous" radar backscatter events typically present at low grazing angles has been usually correlated, although not uniquely, with the presence of wave breaking. It seems reasonable that a proper identification and understanding of these "anomalous" events could lead to better observations of wave breaking in the surf zone using microwave sensors. This in turn could lead to the adaptation of existing methods or the development of new methods to extract wave related parameters in this environment.

2.2 Prior nearshore and surf zone observations

Despite microwave sensing of the ocean being a field of active research for more than 40 years, it might be surprising at first to find that relatively little attention has been put to the understanding of the radar scattering mechanisms in the surf zone. A possible explanation to this is the implicit assumption that the scattering mechanisms and their relative contributions would be the same for both deep water (steepness-limited) and shallow water (depth-limited) breaking waves. However, this assumption neglects the differences between the hydrodynamics of the two environments, which have implications on the scales (both temporal and spatial) and in the frequency and spatial coverage of the events.

Nevertheless, there are many situations where this understanding appears to be not essential in providing some sort of nearshore parameter of interest. For instance, in many cases it is the phase of the signal, rather than the power returned, that is relevant; for example in the estimation of nearshore bathymetry or wave celerities (*Bell, 1999; Wolff et al., 1999; Seemann et al., 2000; Trizna, 2001; Puleo et al., 2003; Ahmed and Taketawa, 2005; van Dongeren et al., 2008*). In other cases, measurements of returned power and signal-to-noise ratios are needed to obtain significant wave heights (*Wolf and Bell, 2001; Hessner et al., 2006*), but it is noteworthy that these studies have focused outside the surf zone, that is, away from depth-limited breaking waves. In some other cases the correlation between locations of preferential breaking and large returned power has been used in a time-averaged sense to estimate the location of sand bars (*Ruessink et al., 2002; McNinch, 2007*), akin to the methods typically used for optical imagery. Thus it seems that the contribution of wave breaking to the scattered signal has been either totally neglected or implicitly assumed to be perfectly correlated to large power.

Only a few authors have attempted quantifying and/or characterizing the scattering from surf zone waves. *Lewis and Olin (1980)* conducted low grazing experiments in shallow water, and found that sea spikes were well correlated with surface roughness associated to the whitecaps observed on optical records. Sea spikes is the term describing large amplitude events lasting for relatively large periods, and more strongly at horizontal polarization (*Trizna, 1997*). Although the data also showed the existence of events of similar characteristics in the absence of whitecaps, the amplitudes (power) were at least one order of magnitude less, suggesting a power differentiation between breaking and non-breaking events. *Haller and Lyzenga (2003)* conducted X-band, vertical transmit, vertical receive (VV), measurements at mid incidence (59° and 44°) in shallow water. They found that the backscattered power was well correlated with the proportional area coverage of turbulent breaking but less so with relict foam, which suggests that the dominant source is the turbulent region of a breaking wave. *Puleo et al. (2003)* used co-located video imagery and a Focused Phased Array Imaging Radar (*McIntosh et al., 1995*)

dual polarization at X-band in the surf zone. While their focus was on the extraction of velocity fields, they observed that large power features in the radar signal could be typically associated to surf zone breaking waves, although unbroken and steep waves could also yield high (but a few dB less) backscattered returns. Using the same data set, *Farquharson et al.* (2005) found the normalized radar cross sections of breaking waves to be typically in excess of -10 dB and exhibit a cross-shore decay consistent with the wave height evolution of the bore modeled as a scattering cylinder, although without taking into account the proportional size between the bore and the radar footprint. More recently, *Morris and Anderson* (2005) conducted polarimetric studies at X-band to study the physics of the scattering mechanisms in the surf zone at two locations. The method takes advantage of the polarimetric decomposition of the coherency matrix of the polarimetric data (*Cloude and Pottier*, 1996), which has been extended to extract entropy \hat{H} (*Cloude and Pottier*, 1997), alpha angle $\bar{\alpha}$ and anisotropy A information. These parameters can be derived from the coherent backscattering matrix, where the entropy \hat{H} is a measure of the statistical disorder within each target. A allows characterization of the relative contribution of scattering mechanisms. $A=0$ means a single dominant mechanism, or random scattering. α is a measure of the relative contribution of different scattering mechanisms, therefore the mean $\bar{\alpha}$ is indicative of whether surface, volume or multiple scattering take place (*Pottier and Lee*, 1999). *Cloude and Corr* (2002) generated the coherent backscatter matrix in terms of an extended Bragg scattering model, which *Morris et al.* (2003) used to study nearshore breaking waves. The combination of the parameters allows characterization of 9 zones in the parameter space $\hat{H} - \bar{\alpha} - A$ which can be used as a descriptor of the kind of the backscattering mechanisms present, for instance separating surface and volumetric scattering; dipole and multiple (bounce) scatterers; or to discriminate random scatterers against anisotropic individual particles (*Cloude and Pottier*, 1997). Although the method is not capable of identifying the source or the kind of scattering mechanism, it can shed light on the processes taking place at different stages of breaking. Based solely on this polarimetric decomposition (they did not compare

their radar data to other data sets to validate their observations) *Morris and Anderson* (2005) suggested that as the waves shoaled and began to break scattering was due to two competing mechanisms. As the waves further evolved and broke, scattering appeared to be of a random nature and the surface acted as a depolarizer. In some cases, the decomposition suggests a single dominant scattering mechanism near the wave front prior to breaking, which appears consistent with strong scattering from steep waves, that they associate with specular effects. They also analyzed the effect of look angle (azimuth), and found that the major differences were found in the decomposition zone of specular/steep scattering, which they attributed to the change in azimuthal look angle. However, the region with multiple scattering processes appeared to be insensitive to azimuthal angle. It was apparent also, that volumetric scattering was relevant for all look angles and wave conditions.

As can be seen, only a handful of studies have been conducted regarding the scattering from surf zone breaking waves, and while it seems characteristic that the surf zone is the source of high backscattered power, the proper identification of the mechanisms responsible of this scattering is still pending and it is usually necessary to resort to scattering models that have been proposed for deep water waves. In the following sections we offer a comprehensive review of these mechanisms.

2.3 Scattering Mechanisms

2.3.1 Bragg scattering and Composite Surface Theory

At moderate incidence angles, $\theta = 20 - 70^\circ$, radar backscatter from the ocean surface is generally well described by the Bragg scattering mechanism, in which the backscattered signal is derived from the resonant interaction between the incident radiation of wavelength λ and a slightly rough surface. The model assumptions are that the surface displacement and slopes are small when compared to the electromagnetic wavelength λ , where fulfillment of the latter is particularly difficult in real ocean situations. However, this apparent limitation can be overcome by using the composite surface theory (CST)

developed simultaneously by *Wright* (1968) and *Bass et al.* (1968), in which case the surface is modeled as a continuum of locally plane facets, each one of them being a (locally) flat and tilted surface where short Bragg resonant waves are responsible of the backscatter. The resulting backscatter signal is thus modulated by the tilting of the mean surface due to the presence of long waves, where the concept of *long wave* is applied to waves longer than 5λ (*Plant*, 1990). The normalized radar cross section (NRCS) of the Bragg model can be expressed as (*Valenzuela*, 1978; *Plant*, 1990)

$$\sigma_0 = 16\pi\kappa^4 |g_{PP}|^2 \psi(2\kappa \sin \theta) \quad (2.1)$$

where ψ is the power spectral density of the surface; $\kappa = 2\pi/\lambda$ is the incident electromagnetic wavenumber, and P denotes the polarization state (either horizontal or vertical). To first order, $2\kappa \sin \theta$ is the wave number of the resonant ocean wave, corresponding to nearly one half the wavelength of the incident radiation at grazing incidence, and larger at smaller incidence. g_{PP} are the scattering coefficients defined as (e.g. *Valenzuela*, 1978)

$$g_{VV} = \frac{(\epsilon - 1)[\epsilon(1 + \sin^2 \theta) - \sin^2 \theta] \cos^2 \theta}{(\epsilon \cos \theta + \sqrt{\epsilon - \sin^2 \theta})^2}, \quad (2.2a)$$

$$g_{HH} = \frac{(\epsilon - 1) \cos^2 \theta}{(\cos \theta + \sqrt{\epsilon - \sin^2 \theta})^2}, \quad (2.2b)$$

where ϵ is the relative dielectric constant of the ocean. It can be noted that for Bragg scattering, the polarization ratio is only dependent on the ratio g_{HH}/g_{VV} which is always less than unity, with the exception of $\theta = 90^\circ$.

In the composite model in turn, the radar cross section is obtained by averaging the Bragg cross section over all wave slopes within the radar footprint (e.g. *Wright*, 1968; *Valenzuela*, 1978; *Plant*, 1990)

$$\sigma_0^c = 16\pi\kappa^4 \int |G_{PP}(\theta, \xi, \zeta)|^2 \psi(2\kappa \sin \theta', 0) p(\theta', \zeta) d\xi d\zeta, \quad (2.3a)$$

$$G_{VV}(\theta, \xi, \zeta) \approx g_{VV}(\theta'), \quad (2.3b)$$

$$G_{HH}(\theta, \xi, \zeta) \approx g_{HH}(\theta') + \left(\frac{\zeta}{\sin \theta}\right)^2 g_{VV}(\theta), \quad (2.3c)$$

where $\theta' = \theta - \xi$ is the local incidence angle of each facet, ξ, ζ are the long wave tilt angles in and out of the vertical incidence plane, and $p(\xi, \zeta)$ is the probability distribution of these angles. In Eq. 2.3 it has been assumed ζ to be small. Note that shadowing can be included in this model by means of $p(\xi, \zeta)$.

However, while generally providing a good agreement with observed data, this model is not capable of reproducing all the features observed in the data. *Wright* (1968) noted that at low grazing angles (LGA), conversely high incidence angles, Bragg scattering and CST at horizontal (HH) polarization yields values that are too low when compared with the observed data. Similar results have been obtained by multiple studies both in deep water and in the nearshore (e.g. *Lewis and Olin*, 1980; *Frasier et al.*, 1998; *Liu et al.*, 1998). As suggested by *Lee et al.* (1995), and supported by the results of *Morris and Anderson* (2005), this does not mean that Bragg scattering is not valid at LGA, but that other mechanisms can be taking place simultaneously.

Three types of situations have been noticed at the LGA regime that suggest the Bragg scattering is not the only mechanism present. The first one is the occurrence of high ratios between the polarized signals, with values HH/VV exceeding unity if measured in power or conversely 0 dB. As mentioned previously, at all incidence angles, Bragg backscattering from a slightly rough surface predicts VV returns several dB larger than HH, which should yield HH/VV values always less than unity. The occurrence of these high polarization ratio events has been related, although not unequivocally, to the presence of whitecaps or wave breaking, both in the field (e.g. *Lewis and Olin*, 1980; *Jessup et al.*, 1990; *Trizna*, 1991; *Hwang et al.*, 2008a) and in laboratory experiments (e.g. *Kwoh and Lake*, 1984;

Trizna et al., 1991; *Lee et al.*, 1995). Recently *Hwang et al.* (2008a) suggest they can be used as the sole discriminator between breaking and non-breaking according to their deep water data.

If Doppler spectra are available, another feature has been noticed: HH spectra are shifted to higher frequencies than VV spectra, and have a broader spectral bandwidth (e.g. *Lee et al.*, 1995; *Plant*, 1997; *Ja et al.*, 2001; *Forget et al.*, 2006, and many others). While the presence of both peaks can be observed at mid-grazing angles for both HH and VV, separation is typically complete at LGA (e.g. *Lee et al.*, 1995, and references therein). This is in contradiction with CST and Bragg theory, because the Bragg-resonant scatterers are free waves traveling at their intrinsic speed and consequently, their Doppler shift should be identical at both polarizations and correspond to the speed of the Bragg waves plus advection by currents or the long wave orbital velocities. The presence of "fast" scatterers is more prominent in HH than in VV, which in some cases has been found to be the result of decreased sensitivity to the "slow" peak in HH (*Lee et al.*, 1995). This phenomena has also being linked to the occurrence of wave breaking events, although not uniquely. Finally, another anomalous characteristic of the sea spikes is the large decorrelation time for the spikes (of the order of seconds) when compared to that of typical radar scatter (a few milliseconds) (e.g. *Lewis and Olin*, 1980; *Trizna et al.*, 1991).

To date, several different models have been proposed to explain these anomalies, including wedge diffraction (*Kalmykov and Pustovoytenko*, 1976; *Lyzenga et al.*, 1983), plumes and bores (*Wetzel*, 1986), bound waves (e.g. *Plant*, 1997, 2003a), specular reflection (e.g. *Kwoh and Lake*, 1984; *Jessup et al.*, 1991; *Liu et al.*, 1998) and multipath models (e.g. *Sletten et al.*, 1996; *Trizna*, 1997; *West et al.*, 1998, and others). In the following we analyze with greater detail some of these models.

2.3.2 Multipath models

Multiple reflections (multipath) is a well known phenomenon affecting radar backscatter, when the direct-path backscattered signal from a target combines coherently or incoher-

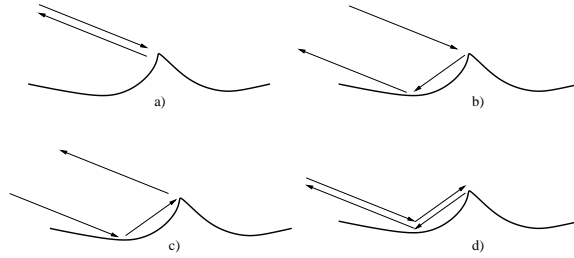


Fig. 2.1: Four-path model: (a) standard monostatic backscattering, (b)-(c)bistatic backscattering with a single bounce from the sea surface, (d)bistatic scattering with a double bounce from the sea surface)

ently with the signal arriving to the same target by a different path. This mechanism typically involves multiple reflections from the sea surface (*Sletten et al.*, 1996), and in general, it is possible to identify single-bounce mechanisms and double-bounce mechanisms, leading to a "four-path" model as shown in Fig. 2.1 (*Kim and Johnson*, 2002).

The resulting interference signals can be enhanced, if the path-length difference is a multiple of the radar wavelength; or attenuated, if the difference is an odd multiple of half the wavelength (*Sletten et al.*, 1996). This path length dependency makes the multipath behavior both frequency and grazing angle dependent. In addition, as the wave surface changes both in elevation and slope alternating interference ensues producing lobe patterns where maxima in HH correspond to minima in VV and viceversa. This effect is typically attributed to the phase difference between the reflection coefficients of the two polarizations (*Sletten et al.*, 2003), although *Rino and Ngo* (1998) attribute the phase reversal to the high curvature present near the crest of a breaking wave, but further research might be necessary. Furthermore, the VV polarized signal is affected by Brewster angle damping for grazing angles between 0-30° as shown by *Trizna* (1997), which can also lead to reflection coefficients that can be significantly lower (10 dB) for VV than HH (*Sletten and Wu*, 1996). The combination of HH-VV phase difference and VV damping can explain the occurrence of events where the value of HH/VV exceeds unity.

Lee et al. (1998) carried out experiments to study the backscattering mechanisms of

deep water breaking waves in the absence of wind, and suggested that multipath was able to reproduce the experimental results. However, they found that multipath had to be mainly out-of-plane, arguing that the strong cross-polarization observed could not be explained by in-plane multipath. This suggests that 3-D effects are relevant. *Fuchs et al.* (1999) studied the correlation between hydrodynamic features and radar backscatter following the time history of a chirping wave packet. They found that strong ray focusing leading to multipath occurred at the early stages of strong breaking (plunging) events, which was related with the parabolic shape of the surface during the jet falling phase. *Sletten and Wu* (1996) used a physical model of a wave with a 8-mm cylinder on its crest to resemble a developing plume, and compared the results with other experimental data, showing a good qualitative agreement, particularly regarding the frequency and grazing angle dependency. Thus small features could also lead to multipath effects.

On the other hand, a significant amount of research has used numerical simulations to calculate the scattered fields. For instance, *Trizna and Carlson* (1996) and *Trizna* (1997) further developed the original bore model of *Wetzel* (1986), in which a small-scale bore ($O(\text{cm})$) sliding down the front face of the wave can provide a surface from which incident radiation is reflected back to the preceding, smoother wave trough, leading to single bounce reflection. *Trizna* (1997) expanded this bore-like model and numerically studied the effects of having features of sizes 0.25-5 cm in any section of a 2-D sinusoidal wave at several frequency bands and reproduced several of the characteristics of sea spikes. Similar conclusions were obtained by *West et al.* (1998), but using a deep water breaking wave profile obtained from laboratory experiments instead. They suggest that single bounce contributions appear to be more important than those of double bounce origin, and also concluded that rather than a single incident-reflected path pair, a single incident ray can lead to multiple reflections that are likely to be the result of diffuse reflection across the wave face. It is of note that *West et al.* (1998) also suggest that the backscattering power can be correlated to the size of the breaking wave. This is in contrast with the results of *Holliday et al.* (1998a), who suggest that the magnitude of

the spike does not appear to be related with the wave height of a steepening wave, when scattering from either perfect (*Holliday et al.*, 1996) or imperfectly conducting near-breaking waves (*Holliday et al.*, 1998b). It must be noted that these studies were aimed at the development of more efficient algorithms for electromagnetic calculations rather than to study the spikes themselves. Further studies on multipath effects of jets or steep features have been conducted by *West* (2002), *Kim and Johnson* (2002) and *Sletten et al.* (2004). *Kim and Johnson* (2002) also focused on the time response of the backscatter for a static wave-like surface, showing that it would be possible to separate the contributions between different paths of the four-path model. However, the timescale for their result is typically of the order of 1 ns which is significantly shorter than the temporal resolution typically used in radar applications. For instance, for the marine radar used in this work, each target in the surface is illuminated for 80 ns.

In summary, it seems that multipath scattering is capable of reproducing many of the characteristics of sea spikes, most notably the large polarization ratios. This situation is further enhanced at LGA, because the resolution cell footprint is larger, thus encompassing a larger area from which reflections can take place, but also because the surface geometries are more prone to allow multiple reflection paths. In this regard, it is of note that different surface geometries can lead to multipath scattering, suggesting that this mechanism can occur not only for active breaking waves (where a bore-like feature can be present), but also for incipient breaking (when a jet is being formed) and also by steep features not necessarily leading to breaking as shown by *Holliday et al.* (1998a). It appears that this effect is more prone to show up at HH polarization, where its dynamic range is also less affected by Brewster angle damping (*Trizna*, 1997).

However, little analysis has been done regarding the distances required for occurrence of the reflection point(s), and whether these are physically plausible in the nearshore. Furthermore, in the majority of the numerical studies, waves have been deep water wave forms treated in isolation from other waves thus preventing the occurrence of shadowing, which could be important in the nearshore where the grazing angle is often very small,

wave heights are large, and the waves are skewed. Another factor is the duration of the events. As explained, multipath depends on the instantaneous slopes and heights of the features, and changes in the geometry can lead to interference patterns. With this in mind, *Farquharson et al.* (2005) for instance neglected multipath effects in the nearshore under the assumption that the timescales typical of nearshore monitoring are long enough for the interference patterns to average out, but no quantitative research is available on this matter.

2.3.3 Specular Scattering

If the surface has a radius of curvature ρ large compared to the incident radiation wavelength, it could be approximated by a tangent plane at each point in the surface. The solution method to the scattering equations under this approximation is the so called physical optics or Kirchhoff Approximation (KA) method. In the limit where $\lambda/\rho \rightarrow 0$ and infinite surface, the solution becomes exact (the geometrical optics (GO) limit). In the physical optics, the scattering cross section at normal incidence ($\theta = 0^\circ$) of an isotropic rough surface of Gaussian statistics and finite conductivity can be written as (*Valenzuela, 1978*)

$$\sigma_{sp} = \frac{|R(0)|^2 \sec^4 \theta}{s^2} \exp(-\tan^2 \theta/s^2) \quad (2.4)$$

where $R(0)$ is the Fresnel reflection coefficient at normal incidence, and s^2 is the total variance of the surface slope of wavelengths longer than the incident radiation, usually taken in the range 3 to 10 times longer (*Kudryavtsev et al., 2003a*). Away from normal incidence, the reflection coefficient needs to be modified by an factor that is also dependent on wind speed. In general, this specular reflection mechanism dominates at small incidence and becomes negligible in comparison with CST for $\theta > 20^\circ$.

Specular scattering has some important characteristics. First we can mention its implicit frequency dependency, which implies that a given surface with a given radius of curvature could yield a specular-like scattering if a) the frequency is large enough;

b) there is a facet that is oriented almost normally to the incident radiation (*Ja et al.*, 2001). Additionally, *Lee et al.* (1995) suggest that the power contribution of specular effects is significantly larger (they report a value of $O(10^5)$ times larger) than that of Bragg scattering. Hence, even a small fraction of specular facets in the radar footprint can yield large backscattered power, and again, this is frequency dependent. Finally, at normal incidence both the electric and magnetic fields are parallel to the surface, and consequently the scattered radiation becomes independent of polarization yielding values for the polarization ratio equal to unity.

Despite the fact of being strictly applicable to a narrow range of incidence angles, the model has been considered as a descriptor of the backscattered power from steep surface features present prior to wave breaking. In such conditions, the effective incidence angle (that is, the sum of the nominal incidence angle and the local sea surface slope, θ' in Eq. 2.3) can potentially reach low values. This combined effect between observation angle and the local surface means that specular scattering could be more likely to occur at mid incidence angles than at grazing, and this needs to be taken in account when studying backscattering. For instance *Trizna* (1991) emphasizes that no wave facet was capable of producing specular scattering for his LGA experiments. Nevertheless, it seems that this differentiation is more relevant for deep water waves, which in general exhibit small surface slopes and are steepness limited. Surf zone waves are depth limited and can typically reach large surface slopes, making the occurrence of specular effects plausible. However, an appropriate quantification of the wave surface slopes and its correlation with radar backscatter is not yet available for this environment.

On the other hand, multiple studies have been carried for deep water waves. For instance, *Kwoh and Lake* (1984) conducted their experiments at X band at mid-incidence (40° - 67.7°), and found that fractions larger than more than one sixth of the spiking events were specular events, and in general they had two to three times the power of the non-specular ones. The specular source was associated with steep capillary waves or discrete reflective surfaces in the turbulent wake of a breaking wave (henceforth the turbulent

scar). *Melville et al.* (1988) and *Loewen and Melville* (1991) made X band measurements at 65° incidence, and observed a large increase in backscatter just prior to breaking and also attributed it to specular effects. *Jessup et al.* (1991), working with Ku band at 40° , found that if the effective incidence angle was less than 25° , a large jump in the radar cross section could be expected, consistent with specular effects. On the other hand, *Ericson et al.* (1999) analyzed X band measurements at 45° for deep water breaking waves in the laboratory, and they found that although long wave tilting modified the backscattering signal, it did not appear to induce quasi-specular backscatter. *Jessup et al.* (1991) and *Walker et al.* (1996) found that the maxima in backscatter occurred downstream of the point of maximum slope, which appears to be inconsistent with specular scattering, although *Walker et al.* (1996) suggest the apparent contradiction could be due to the different hydrodynamics between transient and stationary breakers.

With regards to LGA, *Liu et al.* (1998) carried out field experiments at X band and 3° grazing and compared the radar returns with video observations. They found that only 30% percent of the spikes were active breaking waves, whereas a larger portion were steep features. However, a definition of what was considered steep was not provided and the backscattering mechanism was not identified. *Fuchs et al.* (1999) carried C band laboratory experiments at grazing (6°), where they found that specular reflection occurred during the steepening of the wave face for plunging breakers. Although the HH/VV ratio was close to unity, the backscattered power during this specular phase was several dB less than those observed during the active breaking phase. A different result was obtained by *Dano et al.* (2001a), in which the maximum backscatter was associated with specular effects on the steepening wave face, for X and K bands at mid-incidence (30° , 45° and 60°). This apparent contradiction seems to confirm the dependency on incidence angle and frequency of the power and relative contribution of specular effects. Finally, in their surf zone study *Puleo et al.* (2003) mention that prior to the onset of breaking, steep wave faces can yield large backscattered power that is just a few dB less than that of the active breaking waves.

Additionally, numerical methods have also been able to shed more light on the specular contribution. *Ja et al.* (2001) studied the backscatter from gently spilling breakers, finding that the maxima in HH backscatter occurred just before the onset of breaking, where a small bulge had formed on the wave surface. This feature yields ratios HH/VV of -4 dB (X band) and 0 dB (K band), and was considered to be of specular origin, despite the polarization ratio not reaching unity. The notion that the polarization ratio alone is not a good discriminator of the scattering mechanism is further reinforced by *West and Ja* (2002) who suggest that low HH/VV (less than unity, even as low as -10 dB) ratios are not enough to characterize an event as Bragg. They suggest that at low wind speeds or low energy conditions, even small polarization ratios could be correlated to non-Bragg features such as steep waves, whose size and relative footprint is electromagnetically too small to yield enough power to raise the polarization ratio to unity. *Lee et al.* (1999) suggests that these steep non-Bragg mechanisms can also occur even under slight breaking.

In summary, it seems that specular effects are more important for mid incidence regime, although some occurrences can be expected at low grazing angles, with a possible dependency on the breaker strength and local features. While most of the analysis has been performed for near-breaking waves, at least conceptually it is not difficult to imagine the wave roller as a collection of (electromagnetically) large curvature surfaces that could lead to specular scattering. However, *Lee et al.* (1999) argue that specular reflection must preserve polarization, which is inconsistent with their LGA data (*Lee et al.*, 1998). The vast majority of the studies to date do not include cross-polarized data, and therefore it is not possible to characterize spikes unequivocally as being of specular origin.

2.3.4 Enhanced Surface Roughness

Another possible source of large backscatter has been attributed to the presence of enhanced surface roughness present during a breaking event. The source for this roughness can be linked to several features present during the different stages of the breaking pro-

cess. For instance, *Kwoh and Lake* (1984) analyzed the case of parasitic capillary waves being superimposed over a background wave, and found that the former were the source of backscattering consistent with small perturbation theory or Bragg (in what constitutes a two scale model ,TSM). *Banner and Fooks* (1985) conducted laboratory experiments of small scale breaking waves at X band at mid incidence, and found that enhanced backscatter arose from bound Bragg scatterers near the crest front, typically leeward from it and this mechanism was suggested to be the source of sea spikes. Similar results were observed in the field by *Smith et al.* (1996), who compared Doppler spectra at both polarizations at different look angles, concluding that HH could be related to scatterers "trapped" in the front face of the waves. It is noteworthy that these observations depart from the traditional Bragg scattering model in the sense that the Bragg resonant waves should be traveling at their intrinsic wave speed plus advection from the orbital velocities from long waves and currents, but data shows the presence of scatterers traveling at larger velocities, in many cases close to the phase speed of the underlying waves. This apparent contradiction has led to the identification of "slow" and "fast" scatterers by some researchers, the latter also being termed "non-Bragg" events (e.g. *Lee et al.*, 1998), despite being the result of resonant Bragg-like interaction. Furthermore, HH is more sensitive to the presence of scatterers associated with the fast peak. It has been suggested that this is the result of each polarization scattering from two different populations of scatterers within the resolution cell, for instance VV being more sensitive to Bragg-like scatterers on the gently-sloping back of the wave (*Ja et al.*, 2001). HH in turn appears to be more sensitive to the wave crest, where multipath interference further suppress the VV returns (*Rino and Ngo*, 1998). Thus the main difference could lie not in the scattering mechanism, but in the scatterers. *Walker et al.* (1996) applied the Bragg model and CST to the surface profiles obtained from stationary breaking waves, and found good overall agreement with the measured data, but the model failed to explain the large polarization ratios. They argue that this could be due to the surface height variance exceeding the region of applicability of the Bragg model. *Plant* (1997) in turn

suggests that steep long waves can generate short, bound waves with nonzero mean tilt corresponding to the slope of the long wave. This mean tilt raises the Bragg backscatter of these short waves above the background Bragg scattering level of freely propagating waves, an effect that is more prominent at HH than VV due to the incident angle dependency of the Bragg scattering model (cf. Eq. 2.1). Although the Doppler shifts and overall scattering patterns were well described, the model could not explain high polarization ratios and it was suggested that other mechanisms acting simultaneously could account for that behavior. Similar results were obtained by *Voronovich and Zavorotny* (2000), by superimposing small scale steep features over a larger scale sea-like surface. They also argue that HH polarization is more sensitive than VV to these steep features and can lead to larger polarization ratios than a two-scale model, but without reaching unity. As mentioned previously, *Ja et al.* (2001) and *West and Ja* (2002) suggest that even though Bragg-like returns of bounded roughness are present in the front of wave, their overall contribution to the scattered power is smaller than that of steep features (hence specular effects), something in apparent contradiction with the results of *Plant* (1997). Bragg-like scattering from surface roughness was identified also by *Fuchs et al.* (1999) during the steepening/cresting phase of the wave, which is later overcome by a non-Bragg event just prior to breaking.

Another possible source of enhanced roughness affecting backscatter is the presence of turbulence perturbing the surface in the wake of the wave, especially for strong breaking events or in the presence of wind (*Lee et al.*, 1998; *Fuchs et al.*, 1999). *Ericson et al.* (1999) and *Dano et al.* (2001a) found that small scale roughness in the wake of the breaking wave could be modeled reasonably well by the small perturbation model at both polarizations, but the polarization ratios were significantly underpredicted near the breaking crest. *Ericson et al.* (1999) also performed numerical modeling based on the Kirchhoff Approximation that yielded somewhat opposite behavior, that is, better agreement near the breaking crest than in the wake. Therefore, a unified model combining both approaches (KA near the whitecap, Bragg elsewhere) could exist, for instance, the

Integral Equation Model (e.g. *Chen et al.*, 1992). The experiments of *Fuchs et al.* (1999) showed that at low grazing angles (6°), the turbulent wake and splashing of a breaking event could be an additional source of enhanced backscatter, with polarization ratios that appear to be close to unity at C-band, although *Lee et al.* (1998) obtained ratios significantly smaller at X-band for similar wave conditions. A common feature of these studies is that VV returns showed a somewhat longer lifespan with high return levels than HH, which may suggest that HH could be less sensitive to this persistent roughness. Numerical analysis in the LGA regime by *Ja et al.* (2001) also support the presence of Bragg-like scattering in the turbulent wake. Overall, it seems that the this turbulent scar can yield relatively large values of HH backscatter, but with shorter life spans than VV.

It is interesting to mention that the presence of this scar and its corresponding radar returns, may initially suggest that trailing turbulence from breaking waves can be a source of backscatter in the nearshore, especially at VV polarization. This is a result that is in apparent contradiction with the suggestion that radar is less sensitive to relict foam than optical sensors (*Haller and Lyzenga*, 2003), especially considering that their field data is at mid incidence (31°) and VV polarization, which has been found to be more sensitive to Bragg scattering. However, the look direction was 34° , a regime in which *Dano et al.* (2001b) found that the RCS could be 10-15 dB lower than the upwave value for low energy breaking waves, which may explain the part of the apparent contradiction. An alternative possibility is that there may be a distinction between the electromagnetic behavior of foam versus the trailing turbulence.

In summary, it is clear that Bragg like scattering from bound waves and surface turbulence is present during the different stages of the breaking wave process, although it is not capable of explaining the occurrence of large polarization ratios and large backscattered power.

2.3.5 Plume and bore models

Up to this point, the models reviewed have been general enough to be applicable to a wide range of incidence angles, albeit showing some angular dependency. On the other hand, a number of other models specifically aimed at low grazing angle backscatter have been proposed and enjoyed different levels of success. Among these, perhaps the best known is the "wedge" model (e.g. *Kalmykov and Pustovoytenko, 1976; Lyzenga et al., 1983*), but it seems that is more likely to be applied to deep water waves, which can exhibit a wedge-like form as described by Stokes wave theory. Furthermore, the effect of wedge diffraction can be effective at low frequencies only, hence it can be discarded for K, X and C bands (*Lyzenga and Ericson, 1998; Kudryavtsev et al., 2003a*). For these reasons, we will not dwell into the details of this model here.

There are some other models that have been explicitly designed or can be adapted easily to breaking waves, although their application has been relatively limited. Among these we can mention the slosh model and plume models (*Wetzel, 1990a*). The slosh model was developed having in mind the presence of micro-breakers induced by the formation of capillary waves on the wave crest during the onset of breaking. The geometry resembles the cross-section of annular waves formed by a droplet impinging in the free surface, with a steepening crest followed by a trough or dimple. The scattering behavior of this disturbance will depend on the dimensions a , R and L , corresponding to radii of the slosh, dimple, and the orthogonal extent of the feature, respectively (see Fig. 2.2). It is of note that the model focuses on the slosh and not on the mechanisms that could lead to its formation. This matter has been reviewed for instance by *Pierson (1990)*, who describes briefly the scattering from the vertical stalks and crown produced by impinging drops.

Wetzel (1990a) recognized that this was a purely speculative model, and no field data supported the choice of the appropriate length scales for these parameters. In consequence, he devised a scattering model based on the size of the slosh, basically a half cylinder of radius a , relative to the incident wave length λ . Of special interest is the case

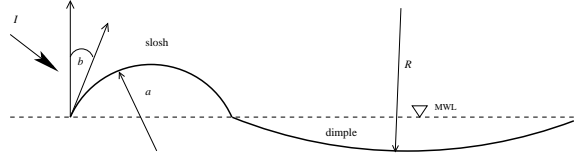


Fig. 2.2: Sketch of the slosh geometry. I is the incident radiation, b is the entry angle of the slosh and a the slosh radius.

of short-wavelength approximation ($\kappa a \gg 1$), in which a scattering model can be obtained based on the physical optics approximation. In this case, the cross section of a conducting smooth cylinder of radius a and length L has a known analytical solution (*Kerr*, 1951). However, *Wetzel* (1990a) noted that such a feature allows multipath reflections on the undisturbed free surface downwave of the slosh, and included a specular-point factor F_{PP} which depends on several parameters including the polarization state, frequency, slosh geometry, local grazing angle and the reflection coefficient at the boundary. The cross-section is then

$$\sigma = 0.5\kappa a L^2 F_{PP}^2 \quad (2.5)$$

where PP can be HH or VV . This model was subsequently extended into a *plume* model, in which plumes (or bores) were considered to be generated by the breaking process and to slide down the face of the wave. In this extended model, the bore had a thickness that was assumed to be of the same order of magnitude of the radius of the bore front (a in Fig. 2.2) and could be approximated as a cylinder (*Wetzel*, 1986). By doing this, bores were usually constrained to small thicknesses ($\approx 3\text{cm}$) thus limiting the applicability of the model to a very narrow range of incident frequencies which is dependent on the plume geometrical characteristics, outside of which Rayleigh scattering and pure physical optics would be the dominant mechanisms. For instance, for bores 3 cm thick he suggests that the applicable range of frequencies is roughly 2-10 GHz. In addition, the model allowed the contribution of several plumes with different lifetimes being present simultaneously over the radar footprint and was found to provide reasonable agreement with measured

radar cross sections. Of significant interest was the grazing angle dependency of F_{PP} at each polarization (Wetzel, 1986, Fig. 7), which showed sharp decays in HH but not as marked in VV. These were correlated with the temporal evolution of the backscattered signal under the assumption that the local grazing angle changed with time, but the other parameters remained constant and showed good qualitative agreement with the observed temporal behavior of sea spikes. One potential disadvantage however is that the values of F_{HH}^2 are typically less than 0.5 for grazing angles less than 12° (thus low backscattered power) and $F_{HH} < F_{VV}$ thus yielding polarization ratios always less than unity (Wetzel, 1986). Additionally, it is of note that the model is only devised for zero azimuthal angle.

Nevertheless, an interesting result has been obtained by Farquharson *et al.* (2005), which used Eq. 2.5 and neglected the contribution of F_{PP} to model the backscatter of surf zone bores under the assumption that these multipath effects average out during the observation times used. They used a depth limited criterion to estimate the wave height, and assumed the bore resembled a cylinder of radius $a = H = \gamma h$ and L was set to the radar pixel azimuthal extent, which might be a good approximation for waves propagating normally to the radar, but less so for oblique azimuthal angles. The modeled radar cross sections recovered the observed trends present in the field data, although they exhibited a relatively constant bias. The bias was nearly reduced to zero if $a = H/2$. This result seems to suggest that such a model could be used to obtain bore heights if properly calibrated. It is of note as well that the assumption of $F_{PP}=1$ removes the polarization dependency and yields ratios equal to 1. However, Trizna (1991) also used $F_{PP} = 1$ and data assimilation to find the (a, L) pairs that best matched his measurements. Although results were found reasonable, the model was not capable of reproducing an observed polarization dependency, which was thus linked to F_{PP} . Trizna (1991) further suggested that the required L values of $O(10)$ m are unrealistic for deep water waves, and suggested that the alternative of using a collection of independent bores of shorter lengths as proposed by Wetzel (1986) would decrease the average NRCS in the

radar footprint. It seems, however, that in the surf zone those $L = O(10)$ m values are perfectly feasible. Furthermore, the assumption $\kappa a \gg 1$ would be fulfilled rather easily.

It is important to notice as well that polarization effects are included in this model solely by the inclusion of the proximity factor F_{PP} , which in turns depends on the reflection coefficient. Thus the model dismisses additional polarization dependency induced by objects showing preferential orientations, as in the case of cylinders (*Tsang et al.*, 2000b). According to *Lee et al.* (1995), these horizontal scattering objects (assuming the cylinder axis is horizontal) are capable of explaining large polarization ratios, but the geometrical ratios required are physically not plausible.

Finally, although the geometry is very similar, this model is different from the bore model of *Trizna and Carlson* (1996) and *Trizna* (1997) in the sense that the latter is purely multipath, whereas the former is a physical optics model that is enhanced by multipath effects. In either case, the effect of surface roughness present in the bore itself is usually neglected, as the bore and the slosh are modeled as smooth cylinders. *Wetzel* (1990a) mentions that the scattering amplitude needs to be augmented by a factor $-2(\kappa h_p)^2$, where h_p is the root-mean-square roughness of the bore surface.

2.3.6 Roller related features

The fact that bore roughness has been traditionally neglected is somewhat unexpected, although part of the reason could be attributed to the inherent difficulties in obtaining the appropriate statistics for the surface. One conceptual model would be to assume the surface of the broken wave which is advected with the underlying water wave to be electromagnetically very rough, as suggested by *Lewis and Olin* (1980). Their analysis focused on the decorrelation times that such a very rough surface would have, and the effect of these times on the overall backscatter, rather than on an accurate description of the surface. Nevertheless, the analysis supported the idea of scattering from very rough surface or droplets, which could be treated as isotropic reflectors whose NRCS should be about 3 dB.

The results of *Ericson et al.* (1999) seem to support this formulation as well, in the sense that scattering from a roughened surface near the breaking crest was well reproduced by using the Kirchhoff Approximation at mid-incidence, and it was not necessary to invoke other mechanisms to explain the backscattering behavior. This result was used in turn by *Kudryavtsev et al.* (2003a), who accounted for the surface roughness associated with deep water breaking. Their model aimed to characterize the backscatter in the mid-incidence regime under a wide range of incident frequencies, wind speeds and azimuthal angles. The model expands the notion of *Phillips* (1988) that the total backscatter from the ocean surface can be modeled as the sum of Bragg scattering and a non Bragg contributions, where the latter is determined somewhat empirically from observations and could eventually include different scattering mechanisms. In order to reduce the number of unknowns and provide a physical meaning to the non-Bragg contribution, *Kudryavtsev et al.* (2003a) modeled the breaking surfaces as a sum of breaking plumes. However, unlike *Wetzel* (1986) who modeled the multiple scattering from a smooth cylinder-like water surface, they focus on the rough surface of the plumes instead, and assumed that it constitutes an isotropic scatterer whose roughness is inversely proportional to the wavenumber of the breaking waves and independent of polarization. In consequence, the scattering from a fundamental plume is modeled as a simple quasi-specular scatterer, which represents the asymptotic solution to the Kirchhoff Approximation, whose use was validated by *Ericson et al.* (1999). The specular contribution in turn is a function of tilting, which was assumed constant for all broken waves based on their self-similarity. They also included the effect of the fractional area of breaking waves and the effect of the interface between the plume sides and the underlying wave as an empirical term, which becomes dominant at grazing. Since the non Bragg contribution is polarization independent, the simple addition of this component raises the polarization ratio above that predicted by Bragg scattering alone. Although devised for mid incidence angles, the model showed that the non-Bragg contribution dominated the NRCS at large incidence (grazing), consistent with LGA observations *Kudryavtsev et al.* (2003b). Overall, to date

this is the only effort that actually includes the notion of enhanced roughness on the breaker front and the results are encouraging.

However, if this approach were to be expanded, a proper description of the whitecap or roller surface is required, and to date this appears to be lacking. To the author's knowledge, only *Coakley et al.* (2001) attempted to study the presence of turbulent disturbances on the roller surface of a stationary breaking wave and their relation with radar backscatter. Unlike previous laboratory studies, they generated relatively large waves (30-40 cm in height) in conjunction with a high resolution (15 cm) X-band radar and video imaging of the surface. They also measured the water fraction distribution in the roller on a vertical plane along the wave. They found that the turbulent region can be described as a two phase flow of increasing density with depth, and that the contour representing 50% water fraction yield a good description of the free surface as defined by optical methods. This contour could be on average as deep as 60 cm below the 1% contour, suggesting the presence of a relatively large spatial volume of low fractional water volumes. It was also found that coherent surface disturbances had multiple length scales and a rather chaotic motion, propagating back and forth relative to the bore itself, and relatively short lifespans. Additionally, for the case of stronger breakers, they found that droplets and elongated tendrils were often ejected. Analysis of the median NRCS showed that the peak values presented a cosine dependency similar to what would be expected from a Lambertian scatterer, attributed to a very rough surface, while analysis of the Doppler spectrum hinted that the small scale disturbances were the main scatterers.

Coakley et al. (2001) finally suggest that the relatively large cross-sectional area above the 50% water fraction contour prevents the applicability of traditional scattering models, based on the size and discontinuous nature of the perturbations on this region. They suggest that previous experiments, for instance those of *Ericson et al.* (1999), were in general for relatively small scale waves, with low levels of air entrainment that enabled the use of more traditional scattering models. In this regard, to the naked eye it seems plausible that this scaling and the difference in breaking strength between deep water

waves and surf zone waves could make this distinction even more important and cause nearshore waves to exhibit a different scattering regime. Although a proper model was not brought forward, they suggest that volume scattering could be possible, akin to that of leaves and branches for vegetation models; or to use the idea of a model with Lambertian behavior (e.g. *Wetzel, 1990b*), based on the fact that scattering seems to become rather independent of electromagnetic parameters (frequency, incidence angle).

In summary, scattering from the wave roller considered as a very rough surface or a multi-phase body where volumetric scattering is taking place are models that have not been considered in the literature. It is of interest to consider these situations and to attempt to model the roller in such way.

2.3.7 Ocean spray and foam

Ocean spray and foam are also present during the breaking process. Ocean spray has been accounted for in active remote sensing (*Kalmykov et al., 1976; Huang and Jin, 1995; Gutnik et al., 2001; Plant, 2003a*) whereas foam has been traditionally a subject of passive sensing owing to the high absorption losses leading to thermal emission (e.g. *Chen et al., 2003b; Padmanabhan et al., 2006; Sharkov, 2007; Raizer, 2007; Anguelova, 2008*).

Kalmykov et al. (1976) measured the cross sections of waves breaking over a submerged breakwater, in an attempt to separate the effect of spray and foam from the steepening of the wave. The grazing angle was 1° . The maximum cross sections coincided with the onset of breaking, showing a high degree of repeatability in magnitude for different waves. The signal of foam was weaker (5-10 dB at X band), but both were significantly larger than the background, unbroken waves. Polarization ratios were close to unity. They used a precipitation model, where small water droplets scattered independently in the Rayleigh regime, thus no volumetric effects were included. They needed a very large precipitation rate ($i = 1000$ mm/hr) to account for the observed NRCS. *Lewis and Olin (1980)* briefly speculate that the source of large backscatter from whitecaps

could be also a result of scattering from droplets and spray. The idea appears to have been largely forgotten, and it was not reconsidered until the last few years. *Gutnik et al.* (2001) analyzed the statistical properties of sea spikes and concluded that one mechanism for explaining the observations is the formation of sea spray under strong breakers. However, the reasons supporting this hypothesis are not clearly presented. More substantial is the work of *Plant* (2003a), who expanded the model originally proposed in *Plant* (1997). By adding an empirical Gaussian distributed field to the scattering, the simulated results were found to be in good agreement with the data at large incidence. One possible physical source for this field was the presence of sea spray, which accounted for many of the observed patterns. For instance, if the droplets were spherical, no polarization dependency should be present. Additionally, if the droplet concentration was small, attenuation would be small and the scattering would be independent of incidence angle. Furthermore, if the backscattered power of this non-Bragg mechanism was small, its contribution would be negligible unless the mean Bragg fields dropped to values too small, as occurs with HH at high incidence. *Plant* (2003a) therefore considered droplets as independent Rayleigh scatterers with concentrations as low as $1.6 \cdot 10^{-5}$ in water volume although an enhancement factor associated to multipath effects was included. The results were considered satisfactory, although caution was suggested especially with regards to the droplet distribution above the sea surface, a relevant parameter in the model for which appropriate measurements are almost non-existent. Moreover, it is of note that unlike *Lewis and Olin* (1980) or *Gutnik et al.* (2001), in this case the scattering by droplets is considered a mechanism secondary to Bragg scattering from rough surfaces. A similar assumption was made by *Huang and Jin* (1995), who included a layer of droplets affecting the rough surface scattering from the ocean at mid incidence angles. They modeled the interactions in the frame of Dense Media Radiative theory with the foam droplets being modeled in the Rayleigh regime.

One may speculate that the reason why active sensing of these ocean features has not been considered in detail is due to its expected small contribution when compared with

surface scattering. Alternatively, the high permittivity contrast of the water appears to ensure that surface scattering is the only viable approach. However, this might not be true if the water concentration is low, something that has been shown to occur in breaking waves by *Coakley et al.* (2001).

On the other hand, passive sensing from foam has been an area of active research over the last few decades. One of the key differences with active sensing is that, in general, passive emission from the ocean is relatively small, therefore the contribution to the emission by bubbles and surface foam becomes relevant (*Padmanabhan et al.*, 2006). State of the art models account for volumetric scattering from bubbly structures in which the size and age of the foam are included, thus resulting in dielectric permittivities that are depth dependent (e.g. *Raizer*, 2007; *Anguelova*, 2008), or in models based on the solution of Dense Media Radiative Transfer formulation (*Chen et al.*, 2003b). The latter method has also been successfully applied to both active and passive sensing of aqueous particles (snow) (e.g. *Liang et al.*, 2007; *Tsang et al.*, 2007; *Tse et al.*, 2007), although in general the permittivity contrast has been considered to be small ($\epsilon_r \approx 3$). It seems appropriate to explore to what extent these volumetric models could be applied to the ocean surface.

2.3.8 Volumetric scattering

Volumetric scattering models are used in several remote sensing applications, for instance for the remote sensing of vegetation, where the interaction among leaves, branches and stalks is included and also allows interaction with the soil (*Ulaby et al.*, 1986). Another field is the active and passive sensing from snow or ice. Individual scatterers were originally treated as independent scatterers, that is the total scattering is the simple sum of their individual contributions. However, it has been found that when the particles are closer together, there is a net interaction between them inducing both coherent and non-coherent interactions which may prove relevant depending on the scatterer's volume fraction. To account for these interactions, several models have been brought forward

including the Quasi-Crystalline Approximation (QCA) (*Lax, 1952; Tsang et al., 2000b*). In the case of snow, it has been found that clustering (e.g. *Zurk et al., 1995*) and packing (e.g. *Zurk et al., 1996*) can have a significant effect on the backscattering behavior, which has prompted the use of layered models (*Liang et al., 2007*).

It seems that these ideas could be useful in describing the morphological structure of the roller, in the sense of a spatial volume partially filled with scatterers whose concentration increases with depth. Furthermore, random positioning and clustering of those scatterers could represent a first approximation for the very rough surface.

However, modeling the scattering goes beyond the simple morphology of the roller. Also of interest is the polarization dependency of the scattered fields. Recent results by *Tsang et al. (2007)* have shown that for snow, the backscattered polarization ratio is slightly less than unity for a wide range of incident angles, and perhaps more importantly, cross-polarized backscattering is generated as well. In addition, if spherical particles are used, the scattering becomes independent of azimuthal look, something that has also been observed in the data.

The question then becomes what are the appropriate particles to be used, especially considering that the upper layers of the roller are the ones that would be more illuminated. These are characterized by very low water volume fractions (e.g. *Coakley et al., 2001; Blenkinsopp and Chaplin, 2007*). One alternative is to consider bubbles immersed in water. The potential benefit of such approach is that several measurements are available with regards to bubble size and populations resulting from wave breaking, both in the open ocean (e.g. *Vagle and Farmer, 1998; Terrill and Melville, 2000*) and in the nearshore (*Mori et al., 2007*). However, bubbles and foam induce large absorption and weak scattering (*Chen et al., 2003b; Anguelova, 2008*). The alternative approach would be to model this volume as a collection of droplets, which could cluster to form larger aggregated volumes which may resemble the surface disturbances observed. However, statistics and field data for the size of such droplets is not available.

2.4 The problem of detecting breaking waves

Up to this point, we have considered the scattering anomalies, and models explaining them, that have been associated with the presence of breaking waves. Considering that in general the anomalies have been well identified, it seems natural to explore to what extent this knowledge has been used in the context of breaking identification. Yet there are surprisingly few studies that have focused on the problem of wave breaking identification from radar data. On one side of the problem is the definition of what constitutes wave breaking. For instance, in the open ocean breaking takes place over a wide range of scales, from micro and small scale events that do not produce an optical signature (turbulent white water or foam), to large scale events that produce whitecaps and spray. In the nearshore, wave breaking is of large scale and its optical signature is usually considered as a good discriminator, although relict foam may affect the detection rates. At the same time, we have seen that many of the anomalies seem to have complex dependencies on microwave frequency, incident angle and polarization state. Furthermore, many of the anomalies have signatures that can only be detected by dual-polarization data or by using the Doppler spectrum.

2.4.1 Radar Cross Sections

It is tempting to think that the first step in a discrimination procedure is to consider backscattered power in conjunction with threshold (false alarm) methods. This alternative is useful from a marine radar perspective, because these systems are typically designed to retrieve only backscattered power at a single polarization, therefore other quantities such as polarization ratios and Doppler spectra are not available for discrimination.

As shown previously in this review, sea spikes and other backscatter phenomena associated with breaking waves are typically characterized by their polarization ratio and relatively large returned power when compared with Bragg scattering, especially at HH polarization. However, if a threshold method is used, it means that a discrimination be-

tween the background levels and those of the signal of interest is needed. In this regard, environmental parameters such as the wind conditions could play an important role, as the frequency and intensity of the spiking events increases with wind. Nevertheless, *Jessup et al.* (1990) assumed that the scale of the breaking event is more relevant and neglected the dependency on the friction velocity, thus selecting a fixed threshold (-6 dB) to identify "large spikes". Posterior analysis of the resulting spikes suggested that there is indeed a cubic-like dependency between the NRCS and the wind friction velocity, consistent with *Phillips* (1988). *Frasier et al.* (1998) focused on sea spike detection (not necessarily wave breaking) using different thresholds on the polarization ratio and found that sea spike coverage (the average fractional area occupied by sea spikes over the radar swath) showed a dependency on wind speed that was rather independent of the threshold value used. Moreover, the mean sea spike power (that is the spike cross-section divided by its fractional area) was fairly insensitive to wind speed, suggesting that the increase in power returned by the spikes was due more to changes in surface coverage rather than on the intrinsic power of the spikes. This could also suggest that the backscattering mechanism of the spikes could be independent of wind, and could be related to wave geometry (steep, multipath, specular) or non wind related roughness (micro breakers, breaking induced turbulence, bubbles, spray). For instance, *Wetzel* (1990b) suggests that for high wind speeds, the sea surface reflectivity appears to reach a constant value independent of polarization, grazing angle and frequency. In fact, this apparent independency motivated *Coakley et al.* (2001) to suggest the presence of Lambertian scattering from breaking waves. A quantification of the scattered power from breaking waves is thus needed.

In an attempt to quantify the cross section of breaking waves, *Lee et al.* (1998) compared their experimental data to targets of known cross section. They found a nominal value of RCS for HH of $\sigma_{\text{HH}} \approx 0.09 \text{ m}^2$, which yield a NRCS of about $\sigma_{\text{HH}}^0 \approx 0.7 \text{ dB}$ (it is interesting to note that they argue this is equivalent to 100 1-in diameter metal spheres within the radar footprint); although maximum values of up to $\sigma_{\text{HH}} \approx 0.5 \text{ m}^2$

were measured from individual events. The nominal value is significantly larger than a reported deep water value of $\sigma_{\text{HH}}^0 \approx 0.05$ dB (peak value in this case), although smaller than the values reported by *Wetzel* (1990a), who suggests that RCS for sea spikes are generally above 1 m^2 , and could exceed 100 m^2 . *Lewis and Olin* (1980) briefly report values up to 9 m^2 . *Lee et al.* (1998) attributed this difference between experimental and field values to the amount of visible whitecap coverage in the radar footprint, where they determined a beam filling factor of about 7%. While this value is larger than the normal estimate for deep water coverage mentioned ($O(1 - 2\%)$), it is significantly less than that determined by *Haller and Lyzenga* (2003) for the surf zone, where peak beam filling values near 30% were obtained by comparing with video records. The peak NRCS in this case was $\sigma_{\text{VV}}^0 \approx 0.20$ dB, and it can be argued that this value would be even larger for HH if the polarization ratio exceeds unity. This may indicate that parameters obtained for deep water waves, for instance absolute power thresholds, might not be directly transferable to the nearshore environment, where the dynamics and scales of breaking are different. On the other hand, this dependency on beam filling adds a further complication in using power thresholds because an estimate of the beam filling factor is needed, especially for low resolution radars. For instance, *Melief et al.* (2006) suggest that sea spikes smaller than a resolution cell can bring the polarization ratio to values too high to be Bragg, although not reaching unity. This in turn will be correlated with the relative power of the different scattering mechanisms, as pointed out by *Lee et al.* (1995). For example, a 20% fraction of specular events could yield a different result than that of 20% coverage of purely multipath effects.

It is not surprising then, that few studies have focused on using radar signatures as breaking wave discriminators directly. *Jessup et al.* (1991) compared video records with radar returns at both polarizations for *Ku* band and mid-incidence angles (45°) of deep water waves. In this case, they used as ground truth video records, where they defined as "breaking" a wave that developed a whitecap within 5 m downwave of the center of the radar footprint. By doing this, they allowed inclusion of events whose

whitecap signature was outside the -3 dB radar footprint hence delayed from the spike itself (typical delay of 0.25-0.5 s), thus they implicitly counted steep features as breaking waves. They compared the performance of four different procedures for wave breaking detection; first they used a cross-section (i.e. power) threshold which was determined as the minimum power value for which the polarization ratio exceeded unity. It is of note then that although power was the explicit variable used, a measure of the polarization ratio was needed. This method was capable of detecting no more than 28% (19% on average) of the breaking events. Later they used a wave-by-wave selection procedure which showed that power thresholds were capable of identifying true breaking events, but not necessarily identify true non-breaking events, i.e., events that showed spiky nature but did not have the optical signature of breaking waves. Furthermore, some spiky events showed polarization ratios that did not exceed unity even for breaking waves. In light of these results, they discourage the use of polarization ratio as a discriminator. As a consequence, they focused the analysis on the Doppler spectra and peak frequencies, but this method did not enhance discrimination success rate. They observed that the Doppler bandwidth (the square root of the second moment of the power spectrum) exhibited a jump in magnitude that was well correlated with the occurrence of sea spikes, arguably due to the increased velocities near the wave crest. A threshold method based on the bandwidth was found to yield significantly higher detection rates than the other methods. Finally, a combination of this method with a power threshold (this time not based on the polarization ratio) enhanced the detection rate, with false detection of $O(10\%)$. A combination method based on power and velocity was also used by *Smith et al.* (1996), although they did not perform any validation of the results.

More recently, *Melief et al.* (2006) attempted to separate spikes from the background clutter by using a pixel by pixel, two-standard deviation above the mean threshold for power, polarization ratio and Doppler velocity. Pixels exceeding threshold values for all variables were considered to be sea spikes. It is of note though that this spike was not necessarily considered a breaking wave. This in contrast with *Hwang et al.* (2008a) and

Hwang et al. (2008b), who attribute as breaking waves events whose polarization ratio exceeds unity for their X-band data at very low grazing angles (0.5° to 6.3°). They did not, however, validate their measurements against other breaking detection methods, but rather validate against other indirect measurements such as phase speeds and whitecap coverage. In this regard, and perhaps not surprisingly, they found that sea spike coverage was larger than field measurements and model predictions. This, coupled with the notion that whitecap coverage is also affected by relict foam, suggests that their data included non breaking waves as well. They attributed the difference to spikes being caused by wave events leading to the formation of bound waves but without inducing white water, such as micro breakers and incipient breaking. According to *Plant* (2003b), the probability of finding such events is larger than that of whitecaps. It is clear, however, that such a result does not apply to the surf zone.

It is important to notice also, that using the polarization ratio as a discriminator implicitly assumes that both polarizations are responding to the same scatterers or illumination patch. It is known that VV is more affected by diffraction and thus could be affected by features located on the back side of the wave, therefore HH and VV could be obtaining returns from different locations within the illuminated area (*Lee et al.*, 1995).

Finally, a different method was used by *Haller and Lyzenga* (2003) which was loosely based on power. They defined as spikes all the events whose temporal excursion above the mean NRCS was longer than 0.2 s. The results were in general good agreement with the observed video signal, where 92% of the detected events could be associated with some degree of visual breaking. They showed that the spikes were well correlated with scattering from the front of the breaking wave, where active breaking accounted for about 50% of the radar cross section.

2.4.2 Backscatter distributions

For the goal of extracting information from the backscattered signal, a good understanding of the probability density function (pdf) of the backscattered field can be useful. If

the resolution cell or radar footprint is large enough, or the integration time is long, the resulting backscatter can be considered the arithmetic sum of a large number of uncorrelated backscattering centers and therefore the field would be normally distributed based on the central limit theorem. Consequently, the scattering amplitudes will become Rayleigh distributed (*Gotwols and Thompson, 1994; Toporkov and Sletten, 2007*), although this implicitly assumes that the nature of the scatterers is uniform within the resolution cell. In particular, *Gotwols and Thompson (1994)* used relatively small footprints, $O(1 - 3) \text{ m}^2$, to get Rayleigh distributions. However, when the footprint is small (several decorrelation lengths *Gotwols and Thompson (1994)*) or when multiple mechanisms occur over the radar footprint (although not necessarily simultaneously), other distributions have been considered in the literature, for instance Gaussian (*Trizna et al., 1991*), log-normal (*Trizna and Carlson, 1996*), Weibull (*Trizna, 1991; Toporkov and Sletten, 2007*), K-distributions (*Gotwols and Thompson, 1994; Toporkov and Sletten, 2007*) and translation models (*Lamont-Smith, 2000*). We must recall at this point that the Rayleigh distribution is a special case of a Weibull distribution with a slope parameter $b = 2$.

Again, significant differences can be observed depending on grazing angle. For instance, *Toporkov and Sletten (2007)* used numerical simulations of backscatter in the absence of breaking and compared the results with different distributions. They found that incidence angle, cell resolution and polarization were the most relevant variables. For instance, a Weibull distribution based on either the median cross section or the second moment of the cross section (n_2) fitted the HH data rather well at LGA, whereas K- and n_2 - based distributions worked well for VV.

In the mid-incidence regime, compound distributions can be used as well, in which case the PDF is defined in terms of the conditional probability at different surface wavelengths based on Bayes' theorem. Results have been shown to fit the field data rather well (*Gotwols and Thompson, 1994; Barrowes and Long, 2002*) as opposed to single Weibull distributions, although the former explicitly makes the distinction that the model is not

related to the PDF of breaking waves.

The presence of spikes affects the upper tail of the distribution changing the slope, which has led some authors to use multiple distributions to fit the data. *Trizna* (1991) and *Trizna et al.* (1991) used two Weibull distributions for HH data and a Gaussian distribution for VV data in the LGA regime, although later *Trizna and Carlson* (1996) found the VV data to be log-normally distributed. However, in both cases the HH data showed the existence of two distinct trends in the distribution that according to the authors, is evidence of two separate scattering mechanisms. Similar results were obtained for LGA of steepness-limited breaking waves by *Sletten* (1998), although a second linear fit to the upper tail was not evident for VV but clear for HH. He also found that the upper 1% of the HH data had mean polarization ratios that increased with incidence angle, although individual polarization ratios ranged from -10 dB to 30 dB, that is, including events that could be classified as Bragg if based on polarization ratio alone. A different approach was followed by *Lamont-Smith* (2000), who noted that the log-normal distribution is the simplest case of translation methods, and used cumulative distributions to model the different slopes present in the data PDF at grazing angle instead. In particular, he tried the convolution of Rayleigh+Weibull (which is essentially a two component Weibull as in *Trizna* (1991)), Rayleigh+K-distribution and a translation model based on the logarithm of the amplitude plus a sinusoidal bound. While he found that the latter fitted the single-point statistics (no integration time) rather well, it lacked a physics-related background which may affect its use as target detector.

Another important aspect to be considered is the variable under study. In many cases, the variable under study has been the NRCS (*Trizna*, 1991; *Trizna and Carlson*, 1996), but *Thompson and Gotwols* (1994) mention that the scattering amplitude is a better estimator than the scattered power, basically because for small amplitude the PDF of the former goes to zero, but for power the PDF is a maximum. This behavior can obscure the details of the distribution at low amplitude, and according to *Gotwols and Thompson* (1994) induced ,for instance, *Gotwols and Keller* (1990) to erroneously

find good agreement with a K-distribution. Consequently, this amplitude-based approach has been followed, for instance, by *Toporkov and Sletten* (2005, 2007).

On the other hand, there is an implicit power dependency on radar range that needs to be addressed in order to compare results at different locations. *Sletten* (1998) found that results correlated well with a r^3 (for clutter) correction for VV polarization but followed a r^4 fall-off (as if it were a point scatterer) for HH. Signal-to-noise levels and saturation seem to play an important role as well.

In summary, it seems that the use of probability density functions as wave breaking discriminators is still not possible and requires a significant amount of gymnastics to determine the proper distribution(s), and their parameters. Nevertheless, they could lead to some insight to the identification of locations where breaking is likely to occur in an average sense akin to the use of time exposure in video data.

2.5 Summary

We have presented here a comprehensive review of observations and models for the backscattering from the ocean surface, with emphasis on the low grazing angle regime and/or breaking waves. While the observations typically agree that active breaking can be correlated to large scattered power, large polarization ratios and broad and "fast" Doppler spectra, these characteristics appear not to be unique to breaking waves therefore an adequate discrimination procedure remains elusive. At the same time, the fact that these characteristics could also be correlated to other stages of the wave evolution (most notably the steepening phase of waves of any size), has prompted its modeling to focus on surface features. While some of the existing models have been capable of explaining successfully some of these characteristics, it appears that a unified model capable of explaining them all does not exist at the moment. However, one aspect missing from the modeling efforts is the contribution of the active breaking region, also termed the wave roller, which is an aerated volume with a very rough surface. The roller contribution to the signal becomes particularly important in shallow water, where depth limited breaking

makes its presence ubiquitous, with larger lengthscales and longer lifespans than those of deep water. Unfortunately, there is an observational gap in the quantification of the contribution of the wave roller to the radar cross section in the surf zone.

3. EXPERIMENTS AND DATA PROCESSING

3.1 Introduction

A nearshore field experiment was conducted over a six week period at the Field Research Facility, US Army Corp of Engineers, in Duck, NC, between April 10 and May 22,2008. Data were collected using three remote sensing instruments, namely a single polarization X-band marine radar; a calibrated coherent dual polarization X-band radar (RiverRad) and a video imaging system, ARGUS III. The data thus collected are unique in the sense that they combine both calibrated and non calibrated microwave data with high resolution, geo-referenced optical data. Therefore, the spatial and temporal evolution of the signal for each sensor can be compared and correlated, allowing a better characterization of the scattering sources and potentially could lead to an improved understanding of the scattering mechanisms.

Of special interest is the characterization of the signal from breaking events. In this regard, we consider the optical signature of breaking and non-breaking waves to be fairly well understood. However, quantification of breaking events requires special care due to the presence of optically bright areas not arising from active breaking but from remnant foam, for which a robust discrimination rule is not available. With these considerations in mind, we will use the optical signal as our initial best proxy for breaking detection and the signal of the other sensors will be compared against it.

3.2 Instrumentation

3.2.1 Marine Radar

This instrument is an X-band (9.45 GHz), single polarization (horizontal-horizontal transmit-receive) radar mounted atop a 10 m tower at the north end of the FRF fa-

cility, at $x=17.37$ m, $y=971.38$ m, $z=13.83$ m in FRF reference system. The reference system is a right-handed cartesian grid, where x is the cross-shore axis, positive pointing offshore, and y is the along shore axis, positive northward and deviating about 18° from True North. The marine radar is an active sensor with a nominal power of 25 kW that utilizes a 9 ft open array antenna rotating at 44 rpm, meaning that a given point on the surface is sampled roughly every 1.36 s (0.73 Hz). A Pulse Repetition Frequency (PRF) of 2000 Hz was used along with pulse width of 80 ns resulting in an intrinsic range resolution of 12 m. Nevertheless, the system internally oversamples yielding a working range resolution of 3 m which remains constant in range. The horizontal antenna beamwidth is 0.8° and the vertical beamwidth is about 25° .

Data acquisition was designed to average 7 received waveforms (a dwell time of about 0.0035 s) thus reducing noise but decreasing the azimuthal resolution to roughly 2° . Special care was taken to avoid saturation of the incoming signal, by introducing the maximum offset possible (-500 mV) to the received signal before it is processed by the internal logarithmic amplifier. This in turn results in a decrease in the sensitivity at long range, and consequently a potential loss of the non-breaking wave signal but is not considered relevant because our focus is on detection of breaking events. The internal logarithmic amplifier is designed to improve the dynamic range and consequently data is delivered in terms of an uncalibrated grayscale intensity (0-255). The acquisition system was designed to record the relative azimuth and time (accurate to 10 ms using the clock of the operating system) of each sample, which enables geo-location and synchronization with the other sensors. To ensure synchronization, the computer clock of the acquisition system was initialized daily using a GPS to minimize the possible drift of the computer clock.

The data acquisition scheme for this sensor was to collect 420 range bins (roughly 1200 m in ground range), and 288 azimuths, which under nominal rotation speeds covers a circular sector of about 270° . The system was setup to record 1266 rotations beginning at the top of each hour, which under nominal rotation speeds corresponds to 30 minute

collections. The antenna zero angle was offset 5° CCW from the FRF y-axis (along shore). The data can thus be geo-referenced in FRF cartesian coordinate system.

3.2.2 River Rad

This is a X-band (9.36 GHz), dual polarization (HH and VV) coherent radar developed by the Applied Physics Lab, University of Washington (APL-UW). It was deployed over the crest of the dune at the north end of the FRF property, at $x = 54.40$, $y = 936.22$ and $z = 10.24$ m in the FRF reference system.

This is an active sensor with a nominal transmitted power of 6W that utilizes two parabolic antennas (one for each polarization) with a pencil beam whose two way half-power beamwidth is 2.6° . The system was operated with a PRF of 39.0625 KHz. 20 of these instantaneous triggers are averaged to form a single frame, 512 of which are then processed to deliver Doppler spectra which once frequency integrated yield received power, in what constitutes a *record* delivered for each range bin. Therefore, the effective dwell time is about 0.262 s for each polarization. The system then alternates between polarization states, resulting in a sampling rate between two consecutive records of the same polarization of about 1.4 s (0.7 Hz). The pulse width of 50 ns yields a range resolution of 7.5 m.

Data are delivered in terms of received power which can be then converted into normalized radar cross sections σ_0 (NRCS). The timing of each sample is recorded accurate to 1 s by querying a GPS receiver and the computer clock. Considering that the actual sampling rate is a fraction of a second and that higher precision is required, for the purpose of this work the delivered GPS time is linearly interpolated using the nominal sampling rate during post processing. The azimuthal location is recorded by measuring the displacement of the mechanic arm used to rotate the antenna. The zero heading of the system was offset 37° CW from the FRF x-axis.

In order to maximize the overlapping area coverage with the other two sensors, the acquisition scheme was set to record 128 range bins (roughly 960 m in range) for two

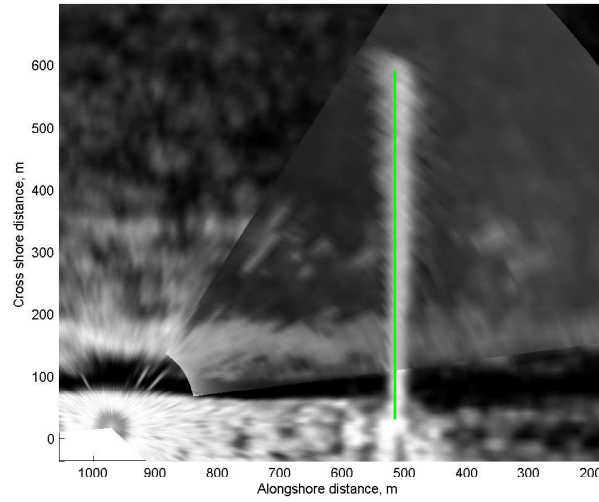


Fig. 3.1: Overlay of the RiverRad and Marine Radar runs used for geo-referencing. The vertical line represents the location of the north end of the FRF pier.

minutes at a fixed azimuthal location, after which the antennas were rotated. A total of 9 azimuthal locations separated roughly 10° were used, resulting in the partial coverage of a circular sector of about 80° , spanning from a directly offshore look direction to a nearly alongshore look direction at the shoreline. This area was scanned both in CW and CCW directions. The time required for the rotation between azimuthal looks was not predefined, and it was dependent on the mechanical rotation speed of the antennas. Although it could have been possible to collect at a higher azimuthal resolution, it would have come at the expense of a) a longer time to cover the defined 80° swath; or b) shorter recording times at each azimuthal location. The former was considered inadequate to ensure stationarity of the wave conditions between both ends of the sector scan, and the latter would have reduced the number of waves present on each data set. Nevertheless, a unique set of runs at higher azimuthal resolution was performed to geo-reference the system by means of identifying the location of the FRF pier, as shown in Fig. 3.1.

3.2.3 ARGUS III

For this experiment we used three of the ARGUS III cameras permanently deployed at the FRF by the Coastal Imaging Lab, College of Oceanic and Atmospheric Sciences, OSU. These are high resolution (passive sensing, optical) RGB cameras mounted at the top of a 45 m tower which can be merged to form a synoptic, plan view map of the nearshore.

Data are delivered as time series of video pixel intensity (grayscale) at locations predefined by means of their FRF coordinates. The pixel footprint ranges from $O(100)$ cm^2 close to the base of the tower to $O(10)$ m^2 in the far field of the field of view used for this experiment. Pixel locations in the image space can be converted to world coordinates by means of a transformation as described for instance in *Holland et al.* (1997). The system records the time of each frame, accurate to the millisecond. More details of the system can be found in *Holman and Stanley* (2007).

For the purpose of this experiment, two distinct pixel sets were used. The first involved large area coverage at a relatively coarse resolution (henceforth semi-full frame, SF array) aimed to provide the maximum overlap with the microwave sensors. In particular, a rectangular array was designed spanning $x=60\text{-}600$ m and $y=500\text{-}1000$ m with spatial resolution of $\Delta x = 2$ m and $\Delta y=5$ m using cameras 0, 3 and 1. The second array (high resolution, HF array) involved a smaller area at higher resolution, aimed at a better capture of the onset of breaking. This record had a resolution of $\Delta x = \Delta y= 0.5$ m and covered $x=60\text{-}600$ m and $y=565\text{-}595$ m using only Camera 1. While both sets were collected during daylight hours at a sampling rate of 2 Hz, the duration of each record was different; the SF array was intended to maximize the temporal overlap with the microwave sensors, therefore it recorded for 3720 samples (31 minutes) beginning at the top of each hour. The HR array recorded only for two minutes (240 samples), beginning 6 minutes after the hour.

Fig. 3.2 shows the footprint of the different sensors along with the resolution of a single trigger for both active sensors. While both active sensors cover a significantly

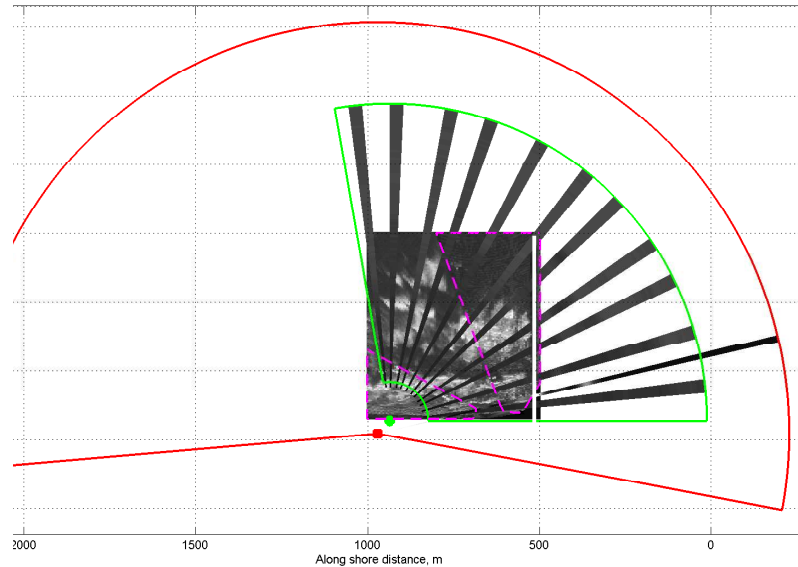


Fig. 3.2: Field of view of the sensors and sensor location. Circular lines denote the swath covered by the marine radar and RiverRad, respectively. Ten sectors of the RiverRad scan are shown, and also a single sector of a marine radar trigger. As background, a merged image from the ARGUS III cameras is presented, with magenta dashed lines denoting boundaries between cameras. The vertical white line denotes the location of the FRF pier.

larger area than that of the video system, we will focus on the overlapping region. It is of note that the inner surf zone close to the RiverRad falls within its self-listening region. Similarly, the shoreline is shadowed by the dune for the marine radar. Therefore, no microwave data are available in these areas.

3.3 Environmental Conditions

An extensive set of environmental parameters are monitored regularly at the FRF. Of special interest for the purpose of this study are wave parameters recorded at the 8-m array, most notably wave heights and wave periods. Additionally, due to the dependency of certain backscattering mechanisms such as Bragg scattering on wind speeds and direction, wind data are also relevant. Fig. 3.3 shows an overview of the significant wave height. It can be seen that during most of the experiment, wave height conditions

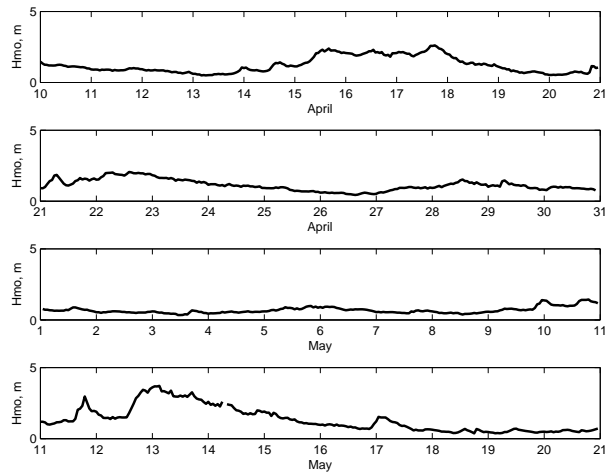


Fig. 3.3: Significant wave height time series throughout the field experiment

remained relatively calm, which induced a relatively weak breaking signal that fell just within the field of view of the active sensors. However, two storms took place during the field campaign. Of special interest is the second storm (whose detailed environmental data are shown in Fig. 3.4), which started on May 12, when the wind showed a steady increase peaking at midnight, then showing a gentle decay followed by a strong decrease during the night on May 14th. Wave heights increased sharply on the afternoon of May 12, increasing from $H_{mo}=1$ m to nearly 4 m. After that, wave heights gently decayed over the next three days, whilst wave periods remained relatively constant throughout. This combination of wide range of wave heights and wind speeds provides an excellent opportunity to compare the response of the sensors under a different conditions. Fig. 3.4 also displays the tide signal and the wave steepness calculated at the 8-m array, the latter calculated using as input the significant wave height and the linear wavelength corresponding to the peak wave period. It can be seen that wave steepnesses showed a gentle decay correlated with the decay in wave height.

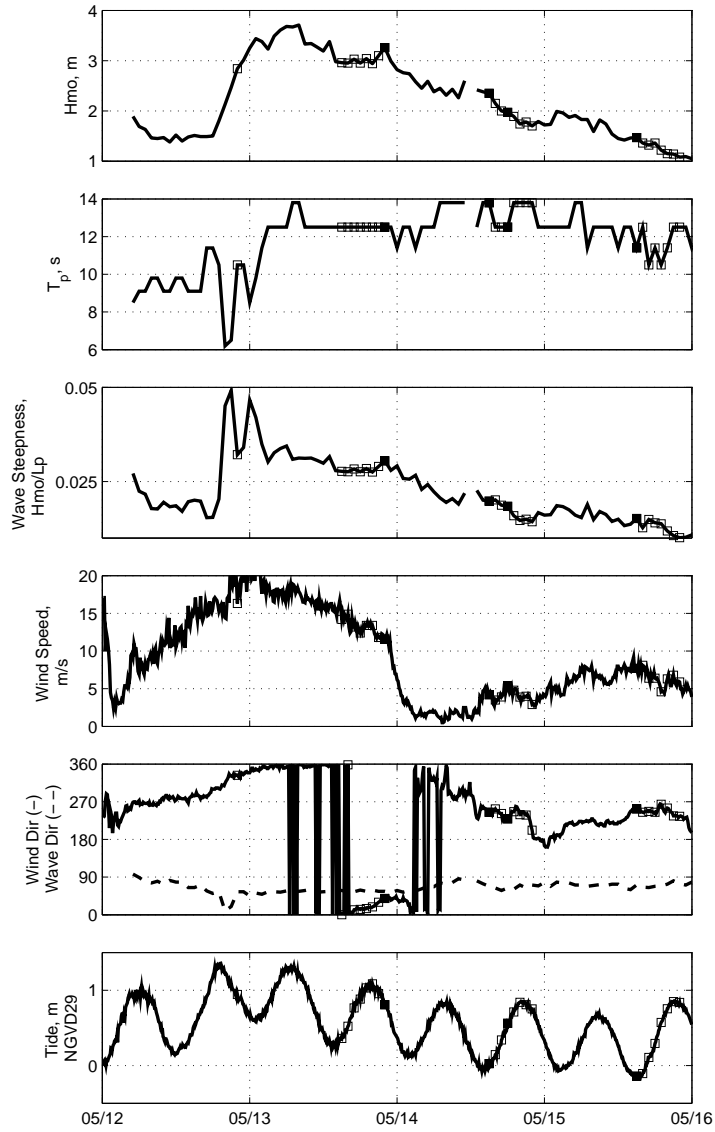


Fig. 3.4: Environmental conditions during the storm between May12th -May16th. (a) Significant wave height (m) at the 8-m array; (b) Peak wave period (s) at the 8-m array; (c) Wave steepness (H_{mo}/L_p); (d) wind speed (5 min steady) m/s; (e) wind direction (solid) and peak wave direction (dashed) in degrees from the true north; (f) tide, in m. from NVGD 88 datum. Blue squares denote the times were both video and radar data is available.

3.4 Preliminary data processing

3.4.1 Alignment

The different spatial location between microwave sensors induces slight differences in the vertical (grazing) and horizontal (azimuthal) angles of a given point in space. It could be possible that these differences may induce differences in the backscattered power received by each sensor owing to its dependency on incidence and azimuthal angles; and frequency. The angles are quantified in Fig. 3.5, where it can be seen that differences in grazing angle are typically less than a degree outside the surf zone, where the Bragg mechanism and the Composite Surface Theory are expected to dominate. Nevertheless, the regime is of very low grazing angles, where Bragg scattering exhibits a very marked dependency on grazing angle. In turn, azimuthal angles show a monotonic variation of the difference between sensors, with an absolute minimum at $\phi = 43.51^\circ$, where the rays coming from both sensors are aligned.

3.4.2 Microwave calibration

RiverRad measurements are calibrated following the procedure outlined in *Plant et al.* (1994). Relevant parameters for the calibration are the nominal incidence angle, range, the antenna gain pattern and the backscattered power of at least one known target. The latter was provided as backscattered cross section of a trihedral measured at APL-UW shortly before the present experiment. The gain pattern of the parabolic antennas is also known.

On the other hand, the marine radar system is equipped with a logarithmic amplifier designed to increase detectability at far ranges while reducing the probability of saturation at short ranges. The resulting signal is delivered in terms of an uncalibrated intensity scale, typically in the range 0-255. However, this parameter is ill suited for the purpose of understanding the nature of the backscattered signal because a) it implicitly includes system dependent parameters such as losses and amplification characteristics; b) it does not provide a normalized quantity that could be compared between data recorded with

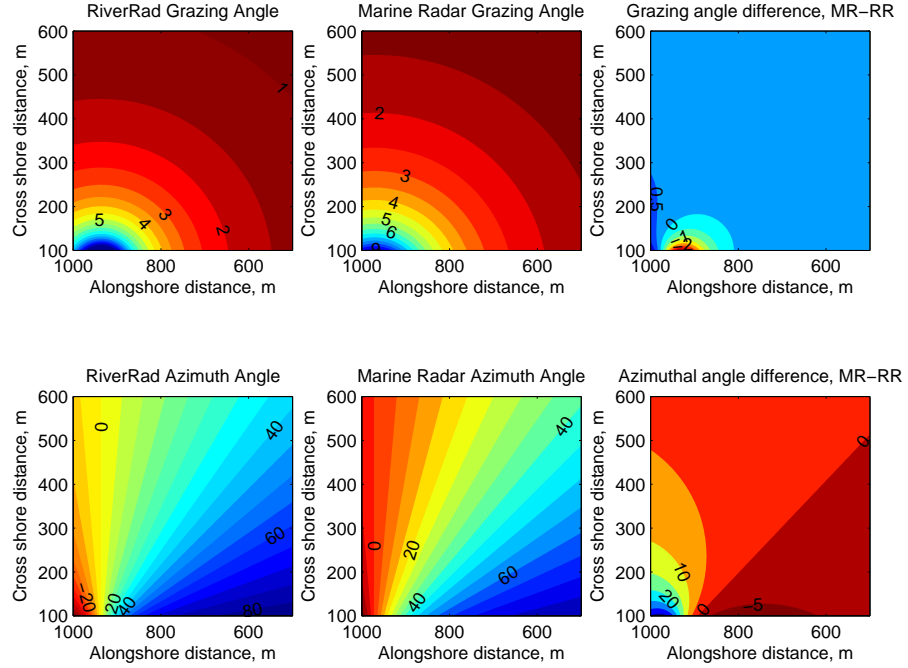


Fig. 3.5: Looking angles for the microwave sensors. Upper row, nominal grazing angle θ_g (degrees); Lower row, CW Azimuthal angle ϕ relative to $y = 0$; Left column, River Rad; center column, Marine Radar; right column, differences between sensors (Marine-RiverRad)

different settings. Therefore, it is essential to perform a calibration of the transfer function between this intensity index and the actual received power at the antenna, which in turn could be later related to the normalized radar cross section. While a proper calibration process such as that described by *Gommenginger et al.* (2000) requires the use of targets of known cross-section and also knowledge of all the parameters of the acquisition system, for the present experiment we follow an alternative approach and attempt a cross-calibration using the RiverRad data as reference.

As a first approximation, the index intensity recorded in the marine radar can be assumed to be a linear function of the logarithm of the received power

$$I = C_1 \log_{10} P_r + C_2, \quad (3.1)$$

where I is the grayscale intensity, P_r is the received power and $C_{1,2}$ are constants that

depend on the system characteristics and could be determined by the calibration. At the same time, the radar equation relating the received power to system parameters is well known (e.g. *Valenzuela, 1978*)

$$P_r = \frac{P_t G A_r \hat{\sigma}_0 A_e}{(4\pi)^2 R^4}, \quad (3.2)$$

where P_t is the transmitted power (W); G is an approximation for the antenna gain pattern, in this case taken as the maximum antenna gain (dB); R is the slant range (m) and A_r is the physical area of the target in m^2 . A_e is the effective aperture of the antenna which can be related to the maximum antenna gain as $A_e = G\lambda^2/(4\pi)$ (*Gommenginger et al., 2000*). It can be seen that $\hat{\sigma}_0$ corresponds to the NRCS of the target. Converting to a decibel scale (by taking $10 * \log_{10}$) and grouping all system constants into a single constant K_1 , Eq. 3.2 reads

$$\sigma_0 = 10 * \log_{10} P_r + 10 * \log_{10} R^4 - 10 * \log_{10} A_r - 10 * \log_{10} K_1, \quad (3.3)$$

where we have removed the hat in $\hat{\sigma}_0$ to indicate a dB scale. Eq. 3.3 is essentially valid for a single, non distributed target of area A_r . For the case of clutter it is possible to assume that the entire radar footprint is covered by a uniform distribution of scatterers, therefore the physical area of the target is equivalent to the radar footprint. This is defined by the antenna horizontal beamwidth (ω) and the range resolution, ΔR , where the latter is directly proportional to the pulse length τ as $\Delta R = c\tau/2$, where c is the speed of light. At grazing ($\theta_g \ll$) angles and small antenna apertures, the clutter cell area can be approximated as (*Gommenginger et al., 2000*)

$$A_r = \frac{R\omega\tau c}{2 \cos \theta_g}. \quad (3.4)$$

Combining Eqs. 3.1, 3.3 and 3.4 we obtain

$$\sigma_0 = \frac{I - C_2}{C_1} + 10 * \log_{10} R^3 - 10 * \log_{10} K_2 - 10 * \log_{10}(\cos \psi), \quad (3.5a)$$

$$\sigma_0 = I * D_1 + 10 * \log_{10} R^3 - D_2 - 10 * \log_{10}(\cos \psi), \quad (3.5b)$$

where the R^3 decay is typical of distributed targets.

In order to calibrate the system, backscattered power from targets of known cross-section need to be measured at different ranges to solve for the new unknown constants $D_{1,2}$. For the present case, a cross-calibration was performed in which the NRCS values of the ocean surface as measured at HH by RiverRad were linked to their synchronous intensity values as obtained by the marine system. Care was taken to remove from the calibration instances where the marine radar record showed zero intensity. Those points result from either received power below the noise floor of the system, or shadowed regions. In either case, those points would be uncorrelated with the RiverRad signal and would bias the calibration results. A set of 5 consecutive RiverRad runs (1815 to 1819, with aggregate length of 10 minutes) at azimuthal angles $\phi = 18.0^\circ, 28.5^\circ, 36.5^\circ, 46.2^\circ, 55.0^\circ$ were used as reference and compared against a single marine radar run (number 1001400). Constants $D_{1,2}$ were determined using a linear least squares fit. A sample of the result is shown in Fig. 3.6.

As can be seen, the overall trend is well recovered, showing good agreement in terms of dynamic range and overall response. However, there are some noticeable point-to-point differences between the calibrated signals. These could be due to differences between the systems such as antenna patterns and size of the resolution cell. The effect of resolution cell can also be related to the implicit assumption that the whole radar footprint would be covered by distributed scatterers, and that both systems will be reacting in the same way to those scatterers. It is known that some scattering mechanisms are sensitive to incidence and azimuthal angles, thus the slight differences in alignment, grazing angle, reported could explain part of the difference in NRCS values outside of the surf zone. The difference in elevation could also mean that waves shadowed for RiverRad might

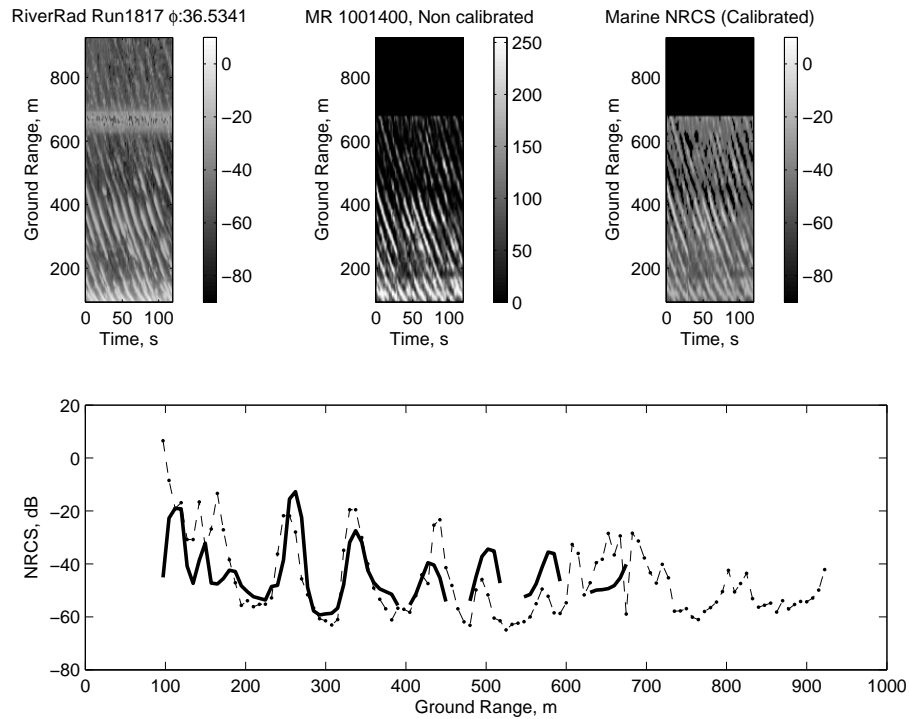


Fig. 3.6: Example of the marine radar calibration. Upper row shows (left) HH NRCS (dB) timestack of RiverRad Run 1817; (center) the corresponding grayscale intensity from marine radar; (right) the resulting NRCS values of the marine radar run. Lower panel shows a time transect of the calibrated NRCS (thick line) compared against the synchronous RiverRad measurement (thin dotted line).

not be shadowed for the marine radar. As waves progress onshore and begin to break, the contribution of other scattering mechanisms could depend on their fractional area coverage of the radar footprint and therefore the difference in radar footprints could be also a factor.

Additionally, there were some events that saturated the marine receiver. Application of Eq. 3.5b would mean that the first term reaches an upper limit, but the range and grazing angle terms can still vary. Moreover, closer to the antenna the range term decreases but the (negative) grazing term increases in magnitude. Therefore, a wave moving towards the antenna while saturating will exhibit a decay of the calibrated signal. This effect is exemplified in Fig. 3.7 a)-b). The left panel displays a spatial map of the

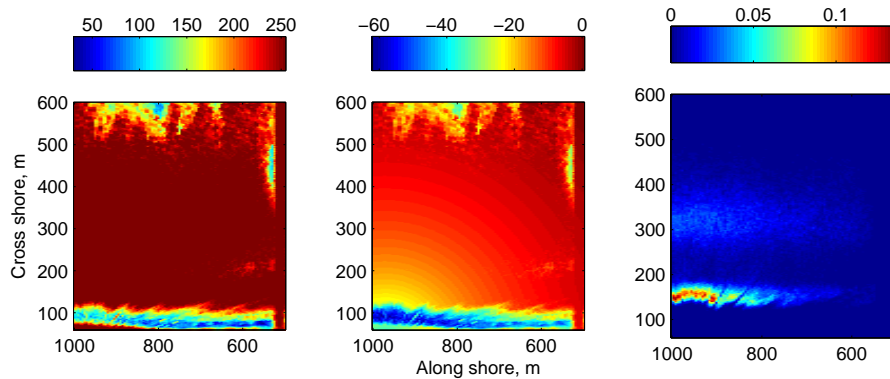


Fig. 3.7: Example of the marine radar saturation and its effect on the NRCS (Run 1351100). (a) Spatial map of the maxima in grayscale intensity recorded over the marine radar footprint; (b) Spatial map of the maxima in the calibrated NRCS; (c) Spatial map of the saturation fraction.

maxima of grayscale intensity time series, where it can be seen that saturation was reached at least once during the recording time for virtually all the pixels in the image. Therefore the corresponding maximum NRCS (middle panel) shows a decay pattern that is uncorrelated with the maximum intensity. Although there is no appropriate way to overcome this effect, it was determined that it affected only a small fraction of the recorded events. For example, for the 25 marine radar runs recorded during the storm of May 12-16th, the maximum saturation fraction of the time series at a single point was 13.7%, while the average saturation over the entire footprint did not exceed 0.6% (see Fig. 3.7 c) and Fig. 3.8). Assuming for instance a peak period of $T_p = 10$ s, there would be approximately 160 waves over the run, and only 22 of those would saturate at the same spot. It is expected however, that these will correspond to breaking waves and consequently the effect of saturation needs to be considered.

In summary, rather than to obtain an absolute calibration, the intention of this exercise is to remove the system characteristics and range dependencies implicit on a intensity scale. Saturation of the original signal plays an important factor and can affect the effectiveness of the calibration, although affecting fewer events. Therefore, in the following the marine radar measurements will be treated as calibrated. The resulting

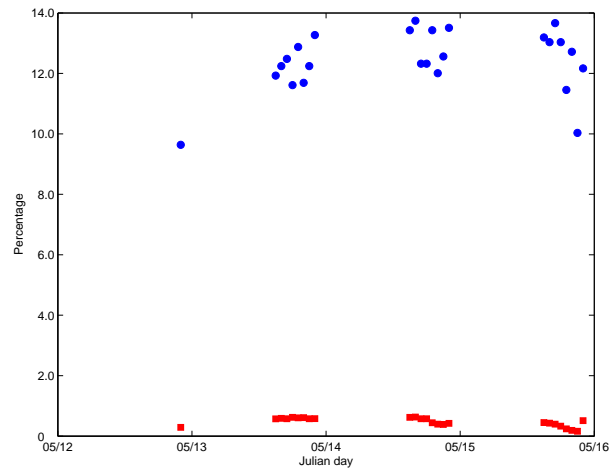


Fig. 3.8: Saturation fraction time series of the marine radar during the storm of May 12-16th. Maxima (circles) and average (squares) of the saturation fraction over the whole radar footprint.

constants for calibration are $D_1 = 0.1973$ and $D_2 = 135.75$.

4. OPTICAL AND MICROWAVE BACKSCATTER STATISTICS FROM BREAKING WAVES

4.1 Introduction

As shown in Chapter 2, while microwave backscatter from steep and breaking waves can produce some distinct characteristics in the returned power and Doppler spectrum, accurate discrimination of individual breaking events has remained an elusive task, with relatively high false detection rates (*Jessup et al.*, 1991; *Liu et al.*, 1998). Despite some evidence to the contrary, *Hwang et al.* (2008a) have recently claimed that using the polarization ratio alone is a good measure to define the occurrence of breaking for deep water waves.

However, commercial marine radars operate at a single polarization, therefore polarization ratios estimates are not measured. Furthermore, the dynamics of waves in deep water are different from those in shallow water and the polarization ratios are likely to be as well. Therefore, an alternate discrimination method is necessary. Typically, surveillance and target detection methods rely on the statistical description of the signal, which can be used to estimate detection probabilities if the appropriate statistical characterization of the signal is used (e.g. *Ward et al.*, 1990). This approach typically involves the study of the probability density function (PDF) and cumulative PDF (CPDF) of the signal.

At the same time, the data presented in Chapter 3 represents a unique set in the sense that for the first time, high resolution synchronous and synoptic optical and microwave measurements in the field can be used for the characterization of the surf zone scattering. The point-to-point comparisons make it possible to obtain not only the PDF and CPDF, but also the joint probability density function (JPDF), thus encapsulating a higher degree of information. For instance, it could provide useful information aimed

at the characterization of the scattering sources based on their optical signature. Additionally, it could shed more light in the possibility of developing improved detection rules and algorithms for the detection of breaking waves.

In the following sections these ideas are pursued. As a first step, the current state of the art of the statistical characterization of both optical and microwave signals is presented. The focus is to identify the global characteristics of the PDFs and CPDFs rather than to obtain a defined statistical distribution. Once this task is accomplished, the results for the present data set are reviewed and compared. Finally, a breaking detection method is presented and validated.

4.2 Theory

In pursuing the use of remote sensors as target detectors, for instance for wave breaking detection, algorithms must rely on the knowledge of the signature of both the target and the underlying background. Typically, this knowledge has been pursued by the study of the statistical properties of the signal, which at a basic level is characterized by lower order moments such as the mean and the standard deviation. A prime example of this approach is the use of optical time exposures (a temporal mean of the intensity series) to correlate the optical signal with zones of preferential breaking in the surf zone (e.g. *Lippmann and Holman, 1989*). A similar approach has been used for microwave sensors by *Ruessink et al. (2002)* and *McNinch (2007)*. However, the level of useful information to be extracted can be enhanced if the PDF of the fluctuating signal is known.

While the use of PDFs has been a subject of ample research in the field of microwave sensing, it seems that this has not been the case for optical imagery. Therefore, as a first step we review some of the scattering models of incident radiation (either in the visible or microwave range), and their corresponding PDFs.

4.2.1 Optical sensors

Optical sensing systems typically measure the radiance reaching the sensor. This can be described in terms of the amount of irradiance being reflected by a surface in the direction of the sensor, under the assumption that both the upwelling radiance contribution and direct radiance from the light source are negligible. In the case of optical cameras, the source of the surface irradiance is the sun, whose visible radiation is absorbed and diffused by the atmosphere. Thus the radiance reaching the sensor can be considered to be emanating from the sky and it depends on the atmospheric conditions (at its simplest level, on whether the sky is sunny, fully or partially overcast). The sky radiance is then reflected by the ocean surface and the radiance reaching the sensor can be described as (e.g. *Stilwell*, 1969)

$$I = L(\theta_S, \phi_S) * R(\alpha), \quad (4.1)$$

where $L(\theta_S, \phi_S)$ is the sky radiance dependent on the sun's elevation (θ_S) and azimuthal (ϕ_S) angles; R is the Fresnel reflection coefficient of unpolarized light. Treating the sun location as fixed, $L(\theta_S, \phi_S)$ can be considered isotropic and homogeneous for sunny and fully overcast skies. Therefore, the irradiance reaching the sensor is dependent solely on the reflection coefficient, which can be taken as the average of the reflection coefficients for horizontal (ρ_{\parallel}) and vertical (ρ_{\perp}) polarizations (e.g. *Jähne et al.*, 1994)

$$\rho_{\parallel} = \frac{\tan^2(\alpha - \beta)}{\tan^2(\alpha + \beta)}, \quad \rho_{\perp} = \frac{\sin^2(\alpha - \beta)}{\sin^2(\alpha + \beta)}, \quad (4.2)$$

where α is the angle of the incident ray relative to the surface normal, and β is the angle of the refracted ray related to α by Snell's law of refraction. Therefore, the radiance measured at the sensor depends on α , which can be related to the wave slope as $\tan \alpha = s$. Here

$$s = |\vec{s}|, \quad \vec{s} = (s_1, s_2, 1) = \nabla\eta,$$

and η is the surface displacement. The dependency of α on $s_{1,2}$ can be found, for instance, in *Jähne et al.* (1994).

However, a simpler model for I was proposed by *Stilwell* (1969), who used a first order Taylor expansion on the wave slope

$$I \approx I_0 + s \cos(\phi_w - \phi_c) * K, \quad (4.3)$$

where K is a constant and I_0 is the radiance of a flat surface, which is modulated by the wave slope and also depends on the angle between wave (ϕ_w) and camera look (ϕ_c) directions. This emphasizes that waves are best imaged when viewed along their direction of propagation and that negative slopes (steep faces if the wave propagates toward the camera) will be darker. The model presented assumes small wave slopes ($s < 20^\circ$).

This result is also relevant for the estimation of the probability density function of the radiance because the dependency between I and s is linear (to first order). Although this further supposes several assumptions and simplifications, a statistical description of the surface slope will suffice to characterize statistically the observed radiance (*Walker*, 1994). Regarding slope distributions, the results of *Cox and Munk* (1954) are usually called upon. They showed that in deep water the sea surface slope is best described as a Gaussian process whose PDF is described as the product of two Gaussian distributions, dependent on the co-wind and cross-wind slopes respectively (*Walker*, 1994). Therefore, it can be expected that the PDF of the radiance I would be also Gaussian distributed to first order. It must be noted that this true only for relatively smooth surfaces (thus small slopes), due to the nonlinear relation between radiance and slopes. The nonlinearity causes positive slopes to be related to a narrow range of reflectivity indices (thus irradiance), while for negative slopes it becomes very steep (*Jähne et al.*, 1994). The PDF would show a steep increase at low intensities followed by a exponential-like decay (*Walker*, 1994). Additionally, even under the simplifying assumption of a linear relation, the distribution could depart from Gaussian, for instance for nonlinear waves; or asymmetric or skewed waves. *Shaw and Churnside* (1997) found that for wind driven

asymmetric waves, the PDF visually resembles a Gaussian distribution, but differences are noticeable at higher order moments such as skewness and kurtosis. Furthermore, *Longuet-Higgins* (1963) suggests that the skewness of surface slopes is larger than the skewness of the surface elevation, which might suggest that the slope distribution would depart further from Gaussian statistics for skewed waves. In the shoaling region, waves can exhibit all these characteristics simultaneously.

It must be noted though, that it has been assumed that the observational mechanisms is reflection of light. This assumption is not valid for the case of breaking waves or whitecap coverage, in which case the radiance model departs completely from that predicted by Eq. 4.1 and can be written as (*Walker*, 1994)

$$I = E_0 \frac{R}{\pi}, \quad (4.4)$$

where E_0 is the downwelling irradiance and R is a diffuse reflectance of the whitecap. The resulting reflectance is attributed to be that of an unbroken surface that is further scattered by a layer of aerosols or scattered directly by a foam layer. Whitecap reflectance measurements in the surf zone show that foam-covered areas reflect about one order of magnitude more than foam-free areas, and the passage of actively breaking waves showed sharp increases in reflectance followed by an exponential decay (*Frouin et al.*, 1996). A more detailed discussion of this falls outside the scope of the present work, at the moment it suffices to acknowledge that wave breaking and foam are a sources of bright optical signals.

The PDF of a broken wave will depend on the duration and spatial extent of the breaker and foam coverage. *Walker* (1994) also suggests that deep water whitecap duration exhibits a probability distribution that is almost exponential. In the case of the surf zone, it is possible to use a simple model for the optical intensity as measured by an uncalibrated camera to estimate the PDF characteristics. The model of the time series of intensity is of the form (*Aarninkhof and Ruessink*, 2004)

$$I = \Delta I_b \exp\left(-\frac{\lambda t}{T}\right) + I_0, \quad (4.5)$$

where I represents an intensity index instead of radiance. ΔI_b is the maximum intensity of the breaking event above some background level I_0 , T is the wave period, t is the time and λ is a nondimensional parameter that determines the decay rate of the signal, and could be related to the persistence of relict foam. It can be noted that the model does not assume that the background level will be reached at $t = T$, thus allowing for fast decays or stubborn persistence through a suitable choice of λ . The model can be inverted to identify the time at which a given intensity value I_* above the background is reached

$$t_* = -\frac{T}{\lambda} \ln\left(\frac{I_*}{\Delta I_b}\right). \quad (4.6)$$

Due to the prescribed monotonic decay, the ratio t_*/T represents the fraction of the time that the intensity would exceed a certain value. In other words, it resembles the cumulative probability density function of the intensity signal

$$P(I \leq I_*) = 1 - \frac{t_*}{T} = 1 + \frac{1}{\lambda} \ln\left(\frac{I_*}{\Delta I_b}\right), \quad (4.7)$$

from which the PDF could be obtained by differentiating with respect to I_*

$$p(I) = \frac{1}{\lambda I}, \quad (4.8)$$

where I is defined in the interval $(I_0, I_0 + \Delta I_b]$, since foam can persist for periods longer than a wave period before reaching the background level. It can be seen that the resulting PDF also resembles an exponential decay which is governed by foam persistence.

However, in the surf zone the signal will usually be from a mixture of breaking and non-breaking waves. Therefore, the resulting radiance will be the sum of the area-weighted contributions arising from breaking and non-breaking areas (e.g. *Koepke*, 1984). The PDFs are expected to be a combination of a two exponential like processes at different

intensity ranges. Considering that the system is not calibrated and some of the settings vary from camera to camera and run to run the absolute definition of bright and dark remains ambiguous. The tail of the distribution will be governed by the persistence of foam and the frequency of breaking events, and the characteristics of this upper section of the PDF could be related to a characteristic λ value. However, to date the dependency of the intensity signal on the strength of breaking and whether it could be distinguished from foam is not known. The model presented assumes that this is true and that active breaking can be associated with the brightest events.

4.2.2 Microwave sensors

On the other hand, the statistical distribution of radar backscatter has been a subject of a significant amount of research due to their implications for target detection algorithms (e.g. *Ward et al.*, 1990; *Trizna*, 1991; *Gotwols and Thompson*, 1994; *Toporkov and Sletten*, 2007, and many others).

For microwave sensing, several factors need to be taken into account when determining the appropriate statistical description. For large footprints and uniform scatterers, the scattered complex electric field will be Gaussian distributed owing to the Central Limit Theorem. Consequently the amplitudes will be Rayleigh distributed while the power (or radar cross section) will be exponentially distributed (*Gotwols and Thompson*, 1994). This notion has been used in conjunction with the assumption of Gaussian sea slopes to solve the inverse problem, that is to determine mean sea slope statistics from backscatter data at low incidence angles (*Vandemark et al.*, 2004; *Schuler et al.*, 2004).

However, the presence of spikes from non-uniform scatterers (similar to the case of high resolution cells where the Central Limit Theorem can not be applied) will cause departures from Gaussian distributions. Attempts to include the contribution of spikes have prompted the use of compound models, combinations of Weibull distributions and the K-distribution with varying levels of success (e.g. *Gotwols and Keller*, 1990; *Trizna*, 1991; *Thompson and Gotwols*, 1994; *Gotwols and Thompson*, 1994; *Trizna and Carlson*,

1996; *Toporkov and Sletten, 2007*).

In the present case, the variable of interest is the NRCS, σ_0 . Assuming for a moment that σ_0 is well described by Bragg scattering and CST, it can be seen that σ_0 will depend mainly on the local wave slope in the incidence plane, s_x . Therefore, the probability density function of the NRCS is given by (*Gotwols and Thompson, 1994*)

$$p(\sigma_0) = \frac{p(s_x)}{|d\sigma_0/ds_x|}, \quad (4.9)$$

where the relationship between σ_0 and s_x is given by Eqs. 2.1 to 2.2 and $\tan \xi = -s_x$. *Gotwols and Thompson (1994)* showed that using some simple assumptions at mid incidence ($\theta = 45^\circ$), the relationship could be reduced to an exponential function of the slope. Furthermore, if the surface slope is normally distributed, the PDF for horizontal polarization takes the form of a log-normal distribution. On the other hand, at grazing incidence where the scattered field departs from Gaussian due to the more frequent spiky events, the K-distribution has usually been considered a good descriptor (*Gotwols and Keller, 1990; Ward et al., 1990*)

$$p(\sigma_0) = \frac{b}{\sqrt{\sigma_0} \Gamma(M)} \left(\frac{b\sqrt{\sigma_0}}{2} \right)^M K_{M-1}(b\sqrt{\sigma_0}), \quad (4.10)$$

where

$$M = \frac{2}{n-1}, \quad (4.11a)$$

$$b = 2\sqrt{\frac{M}{\langle \sigma_0 \rangle}}, \quad (4.11b)$$

$$n = \frac{\langle \sigma_0^2 \rangle}{\langle \sigma_0 \rangle^2} - 1. \quad (4.11c)$$

It can be seen that the K-distribution is defined by the mean and normalized variance (Eq. 4.11c) of the backscattered signal and the normalized variance determines how much the distribution deviates from an exponential distribution as measured by the parameter n . Consequently *Gotwols and Keller (1990)* suggest that for the study of the spikes, it

is only necessary to describe the normalized variance when comparing between runs.

However, at this time our interest is focused on the general shape of the PDFs rather than its accurate statistical description. In this context, based on these studies it suffices to say that the expected behavior of the PDF should be to exhibit a peak at low NRCS and an exponential-like decay as the NRCS increases.

4.3 Experimental Data and Preliminary Processing

In the following the focus is on the analysis of two of the three sensors, namely the marine radar and the video system. The reason for this choice is the large swath of the semi full frame array and the long dwell time of each of these data sets (30 min), which allows the use of a large number of points to ensure statistical significance. At the same time, the time series are short enough to ensure that the environmental conditions remained stable.

However, differences in sampling rates and spatial resolution between sensors require at least one of the sensors to be interpolated to a common domain. This is achieved in two steps. The first involves interpolation in the time domain of the video signal to match the time domain of the marine radar. It is of note that although the radar scans the field of view in a finite time, for the present purpose it can be considered as a snapshot of the surface. For example, the time required for the marine radar to scan through the area defined by the semi full frame is $t \approx 0.3$ s, which is less than the video sampling rate (0.5 s). Furthermore, using the time of the trigger that bisects the SF array as reference time for the interpolation, a difference of about ± 0.15 s with the corners of the array is obtained. During this time the waves would travel 1.5 m (at a phase speed of 10 m/s), which is less than a resolution cell. The temporal interpolation of the optical signal was performed on a pixel-by-pixel basis using simple linear interpolation.

The second step required is interpolation to a common spatial grid. Although the spatial coordinates of each pixel are known for both sensors, it was considered preferable to transform both data sets to the uniform grid defined by the semi full frame array.

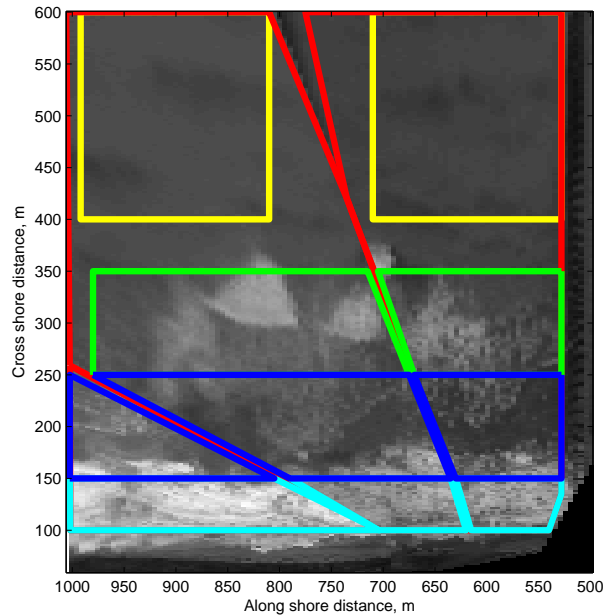


Fig. 4.1: Zonification of the field of view. (cyan) surf zone, $x = 100\text{-}150$ m; (blue) bar trough $x = 150\text{-}250$ m; (green) bar $x = 250\text{-}250$ m; (yellow) off shore $x = 400\text{-}600$ m. Red denotes camera boundaries, from left to right, Cameras 0, 3 and 1.

This induces some smearing of the signals, which is more evident in the case of the optical records at the boundaries between cameras, where differences in camera gain and integration time caused sharp gradients not related with the actual ocean surface. In order to minimize the effect of camera gradients, in the following the analysis is performed on a camera-by-camera basis and away from camera boundaries.

Analysis of the time exposures showed that during the storm of May 12-16th, active breaking took place near the shoreline and also over an outer bar. In order to differentiate the behavior of the signal between areas of persistent, intermittent and sporadic breaking, we further divide each camera field of view in 4 areas, as shown in Fig. 4.1 and defined in Table 4.1. Although the characteristics of the signal emanating from each zone will be strongly dependent on the environmental conditions (wave height, period, tide, and wind), these zones will remain constant throughout the analysis and will enable the study of the evolution of the signal as wave and environmental conditions changed.

The analysis focuses on three data sets, labeled Run 9, 13 and 18 respectively. As

shown in Fig. 4.2 and Table 4.2, the environmental conditions show significant variations in at least two of the parameters, most notably the significant wave height and wind speed. Wind direction also changed, from a situation of blowing onshore (upwind- relative to the antennas) to offshore directed (downwind) for the last two runs. In addition, the combined effect of wind and increased wave height result in varying degrees of foaminess (see Fig. 4.3), which will further allow evaluating the effect of remnant foam on the signals.

Each of the data sets is rectified including tidal variations, and processed on a zonal basis. The aggregate of the all pixels within each zone is processed as a joint histogram. Integration of the histogram along each coordinate axis yields the individual histogram for each data set. Special care is taken to remove the occurrence of points of zero marine radar signal and its corresponding record in the video series, as its presence would bias the distributions toward low backscattered power not necessarily correlated with their optical signature.

Table 4.1: Definition of zones. Values expressed in terms of the cross-shore coordinate in FRF reference system.

Identifier	Cross-shore Limits (m)	
	x_{\min}	x_{\max}
Surf	100	150
Trough	150	250
Outer Bar	250	350
Offshore	400	600

Table 4.2: Summary of the wave conditions measured at the 8-m array during the storm of May 12-15, 2008 for the three selected runs. Relative (rel) directions are measured CW with 0° pointing along the FRF x axis.

Id. No.	Marine Run	Date	Time GMT	H_{mo}	T_p	Tide	Wind	Wind	Wave
				m	s	<small>NAVD88</small> m	Speed m/s	Dir. $^\circ$ TN (rel)	Dir. $^\circ$ TN (rel)
9	1341700	May 13	22:00	3.26	12.5	0.51	11.6	56 (-16)	56 (-16)
13	1351300	May 14	18:00	1.97	12.5	0.26	5.4	229 (157)	64 (-8)
18	1361000	May 15	15:00	1.47	11.4	-0.44	7.7	253 (181)	71 (-1)

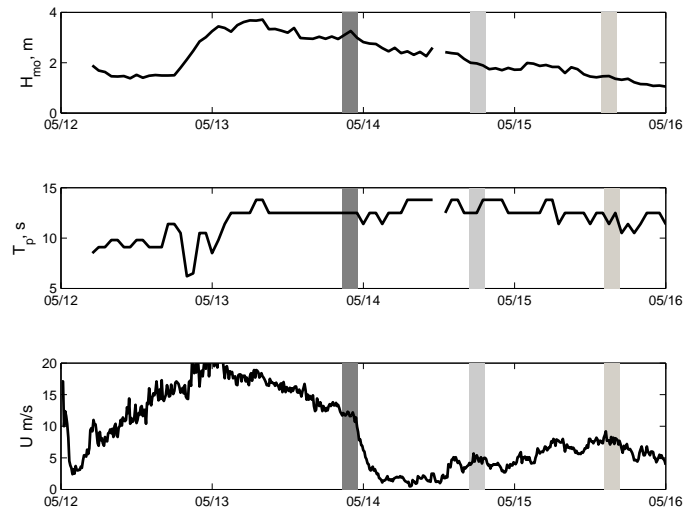


Fig. 4.2: Wave conditions measured at the 8-m array during the storm of May 12-15, 2008. (a) Significant wave height; (b) Peak wave period; (c) Wind speed. Bars denote the occurrence of the three selected runs 9, 13, and 18



Fig. 4.3: Video snapshots taken from Camera 1 for each of the three selected runs. Left to right, Runs 9, 13, and 18.

4.4 Results

4.4.1 Probability density functions

Joint histograms are estimated by counting the frequency of occurrence of a given intensity pair (I, σ_0) in the ensemble of samples collected on a given zone throughout the run. The minimum number of usable samples (after removal of marine radar data with zero intensity) thus counted was of the order of 535,000 (Camera 1, Surf zone, Run 18), whereas the minimum fraction of usable samples was 18% (857,656 usable samples, Camera 1,

Offshore zone, Run13), although values typically exceeded 60%. The joint and individual histograms were constructed using 25 predefined bins 11 intensity values wide for video and 3 dB wide for the case of marine radar. In the case of the latter, the variable of interest is the cross-calibrated NRCS in order to minimize possible range dependencies. For simplicity, results are presented in terms of the field of view corresponding to Camera 1 for both sensors. Results from the other cameras show similar behavior unless noted otherwise. In addition, in the following we treat the histograms as representative of the PDF and JPDF, noting that normalization by the bin width has not been included.

Video data

Fig. 4.4 shows the probability distributions obtained for the video data, the left column showing the PDFs and the right column showing the corresponding CPDFs. In general the PDFs have three different shapes. The first type is the expected peak at low intensity values accounting for a large fraction of the data, for instance, the offshore series for run 18 (dashed-dot series in Fig. 4.4a). This corresponds to non-breaking waves, which, as explained before, modulate the incident radiance on the sensor as a function of the wave slope. The resulting signal has a relatively narrow dynamic range which spans a few bins of the histogram thus explaining the peakiness of the PDF. It can be noticed as well that though the shape is preserved, the means are offset between runs owing to changes in the environmental conditions (wave height, period hence slope) and/or changes in camera settings such as shutter speed and aperture, which were allowed to be adjusted freely between runs depending on the illumination conditions. Additionally, the color of the sea surface will change depending on ambient conditions. However, we neglect these details and we focus on changes in the shape of the PDFs.

A second type of shape can be identified as a smaller magnitude peak at low intensities followed by an exponentially decaying tail. This kind of behavior would be expected of zones where breaking takes place with some degree of foam persistency. This can be seen for instance in the offshore zone (see Fig. 4.4a) where Run 9 differs from the other

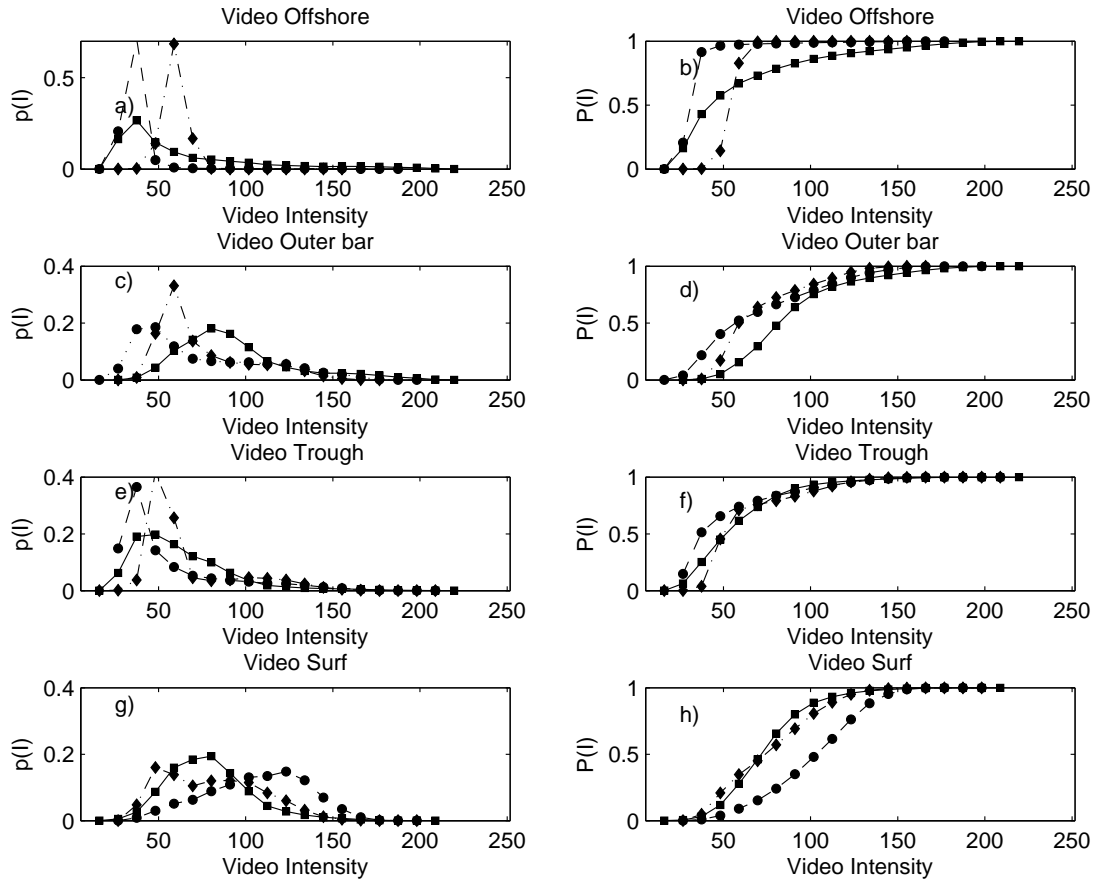


Fig. 4.4: Probability (left) and Cumulative (right) Density Functions for the video data taken from Camera 1. Top to bottom correspond to measurements taken in the Offshore, Outer Bar, Bar trough and Surf zone boxes, respectively. (\square) Run 09; (\circ) Run 13; (\diamond) Run 18

runs due to intermittent breaking (see Fig. 4.3). In some situations both the PDF the CPDF are characterized by step increases in value at low intensities (see Fig. 4.4f), suggesting that a large fraction of the time the signal falls back to the level of non-breaking waves, thus either intermittent breaking or low foam persistence. As foam persistence becomes more pronounced, the frequency count increases at mid I values, while breaking contributes at higher I values. The low intensity portion of the CPDF curve becomes less steep due to simultaneous presence within the field of view of patches of remnant foam persisting between waves and patches of dark water. An extreme case of this behavior occurs for Run 18 in the surf zone, where the PDF exhibit a bimodal

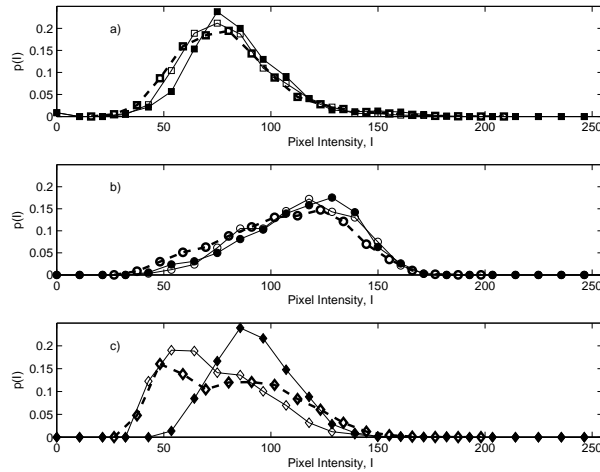


Fig. 4.5: Comparison of single-point and ensemble PDFs for the video data taken from Camera 1 in the surf zone. Top to bottom correspond to different runs (Run 9, 13 and 18, respectively). Solid lines are histograms obtained from the time series at two random (x, y) points within the field of view. Dashed lines correspond to the PDF of the ensemble of data within the field of view.

distribution, with a clear peak at low intensities and a secondary peak at somewhat larger intensities. This is further exemplified in Fig. 4.5 where it can be seen that the PDFs obtained from the time series of a fixed point in space do not deviate significantly from the ensemble PDF (all spatial points) for Run 9 and Run 13. Run 18 seems to indicate that the ensemble PDF could be the result of averaging time series showing a larger variability.

Up to this point, a good correlation between the observed shapes and the hypotheses based on the observational mechanisms is apparent. There are, however, some situations where the shape departs significantly from the expected patterns. An example is given by the signal in the surf zone for Run 13 (Fig. 4.4 g), circles and dashed curve). In this case the PDF shows a linear increase at low intensities with a maxima at a relatively large intensity value, followed by a sharp decay. Fig. 4.6 shows the time series of random points in the surf zone for Run 9 and Run 13. It can be seen that Run 9 shows spiky events well correlated with the peak wave period, followed by periods of decreased intensity. In Run 13 the intensity shows persistent bright values at time scales shorter than the

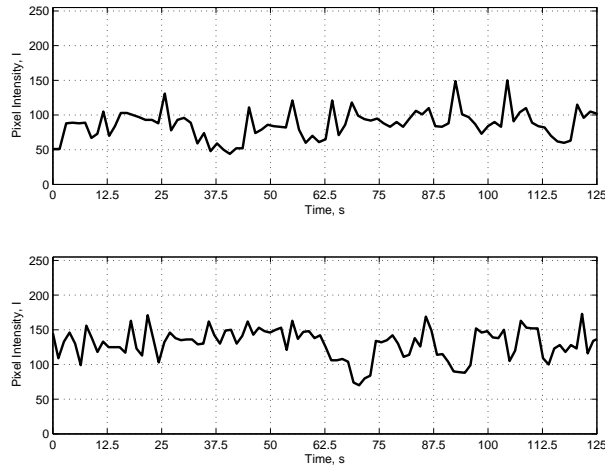


Fig. 4.6: Comparison of the intensity time series for Run 9 (top) and Run 13 (bottom). Horizontal grid is defined in terms of the peak wave period.

wave period. This is suggestive of foam patches scattering as brightly as the wave roller biasing the histogram toward large intensity values.

Marine Radar

Fig. 4.7 shows the resulting PDFs and CPDFs for the marine radar data. Unlike the video data, the majority of the curves show a relatively constant shape characterized by sharp peak at low backscattered power, usually about -55 to -50 dB, followed by an exponential-like decay at higher power.

Consistent with the idea of scattering according to the CST model, the magnitude of the peak and the relative contribution of the tail show dependency on ambient parameters. It is of note that the curves follow a clear transition from low peaks and high tail values for Run 9 to high peaks and low tails for Run 18 without changing significantly the overall curve shape. Possible reasons for this could be related to changes in the surface roughness due wind effects, foam or breaking. For instance, the transition of Run 9 from Fig. 4.7c to Fig. 4.7g) (increasing foam) is similar to the change between runs in the trough (Fig. 4.7e). At the same time, tidal elevation changes for these selected runs were monotonically decreasing. This causes the nominal grazing angle to increase fractions of

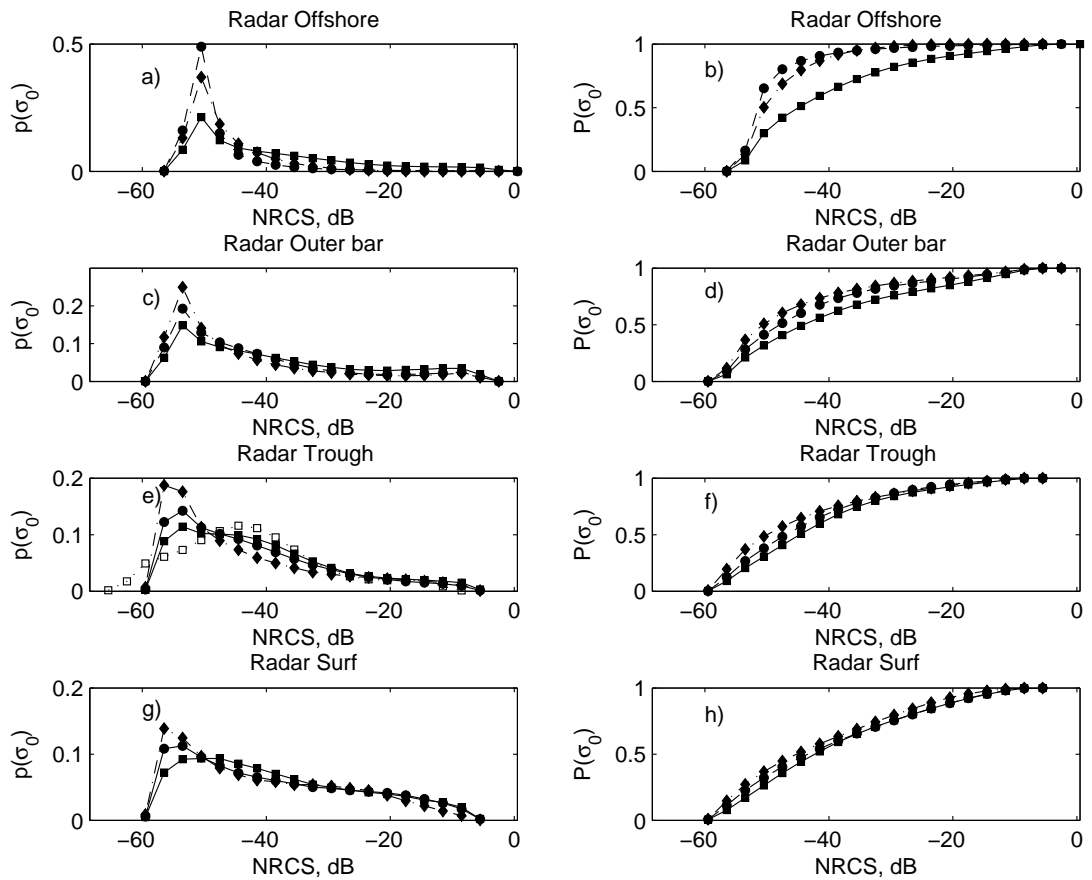


Fig. 4.7: Probability (left) and Cumulative (right) Density Functions for the Marine Radar data. Key is the same as in Fig. 4.4. Open symbols in (e) correspond to the PDF as measured in the field of view of camera 3.

a degree. Though this would seem small, the experimental setup is at extreme grazing and changes of a few degrees can induce significant changes in the predicted behavior of Bragg scattering. Additionally, the overall foaminess in the surf zone is reduced between runs.

Of particular interest is the effect of intermittent breaking, for instance at the outer bar. It can be seen that in this zone, the PDF curves are very similar in shape varying only in magnitude as the wave conditions evolved. One significant aspect is the presence of clear departure from the monotonic decay near -25 dB, where the PDF stabilizes and then increases its magnitude reaching a maxima around -7 dB, after which it shows a

linear decay. Similar results have been obtained for all runs in the outer bar, trough and surf for the field of view of Cameras 3 and 0 (not shown), and for the offshore zone in Camera 1 (squares in Fig. 4.7a). The linear trend seems to be correlated to the effect of waves saturating the signal and whose calibration to NRCS is linearly dependent on range and grazing angle on the dB scale (cf. Eq. 3.5b). Therefore, we consider that this high NRCS section of the PDF can not be analyzed properly. On the other hand, it is apparent that the increased probability values at NRCS greater than -20 dB can not be explained by the traditional scattering models, which as we have seen previously would predict an exponential or exponential-like decay. It seems reasonable at this point to presume that this is related with another scattering mechanism that could be associated to either active breaking or to the presence of foam. However, at this point the study of the PDF alone is not capable to provide further insight in this matter.

Additionally, it was observed that both the PDF and CPDF shapes are fairly consistent between runs and zones. However, a few selected cases exhibited a strong departure from those general shapes. One of those cases can be seen in the bar trough zone for Run 9 and camera 3 and included in Fig. 4.7 e) as open symbols. In this case the PDF resembles a Gaussian curve, with a gradual increase in the PDF as power increases. Visual observation of the marine radar time series shows that the signal rarely reached low values, and that it exhibits a significant amount of speckle not necessarily associated with the passage of waves but with relict foam instead. The effect of increasing foam can be seen as well in the PDFs of the surf zone, although this is associated with a gentle decaying tail that retains the steep increase at low backscattered power. It is of note that the PDFs collapse to a single curve for NRCS values larger than -35 dB. In this NRCS range, the PDFs values are larger than those of other zones and do not show the same evolution between runs observed in the other zones. This suggests scattering from scatterers with relatively high persistence and not correlated with the environmental conditions. One obvious possibility is the case of foam or persistent breaking.

4.4.2 Joint Probability Density Functions

Up to this point the analysis of the scattering sources has relied on prior understanding of the video PDF, which enabled us to characterize the presence of foam but not necessarily distinguish it from active breaking. The same analysis is less conclusive for the radar PDF although there are some strong indications that the presence of breaking and/or foam have a clearly defined signature in the PDF, namely an inflexion point followed by secondary peak at NRCS values larger than -30 dB. In order to overcome the apparent limitations of using both sensors independently, it is possible to combine the information in the joint probability density function. This procedure enables the characterization of the scattering sources as seen by the radar sensor based on their optical signature, under the assumption that the brightest optical signals are associated with active breaking.

Fig. 4.8 shows the JPDFs for all the zones and runs considered. It can be seen that for almost all cases the peak of the JPDF occurs at relatively low video intensities and low backscattered power. This is consistent with the notion of scattering from unbroken waves over a large fraction of the wave phase. When only non-breaking waves are present (thus darker video intensities), it is found that the JPDF is concentrated over a ridge spanning a relatively narrow range of video intensity bins but spread over a wide range of radar NRCS bins (e.g. Fig. 4.8b and Fig. 4.8c). This can be explained in terms of a modulation of the signal by the wave slope, which induces a relatively large dynamic range for the NRCS in accordance with the CST but a narrow dynamic range in video. One interesting detail present in for instance in Fig. 4.8c is the presence of events that are very dark (in a video intensity sense) but associated with relatively large scattered power (larger than -30 dB). This means that strong scattering occurs for dark video corresponding to the front face of unbroken waves, another indication of scattering in accordance with CST. A similar behavior can be seen in the trough for decaying wave heights (Fig. 4.8h and Fig. 4.8i), but the signal shows a somewhat broader video range making the conclusion less obvious. A secondary ridge is also apparent in other cases (e.g. Fig. 4.8a, e, and f). This vertical ridge spans a wide range of video intensity bins

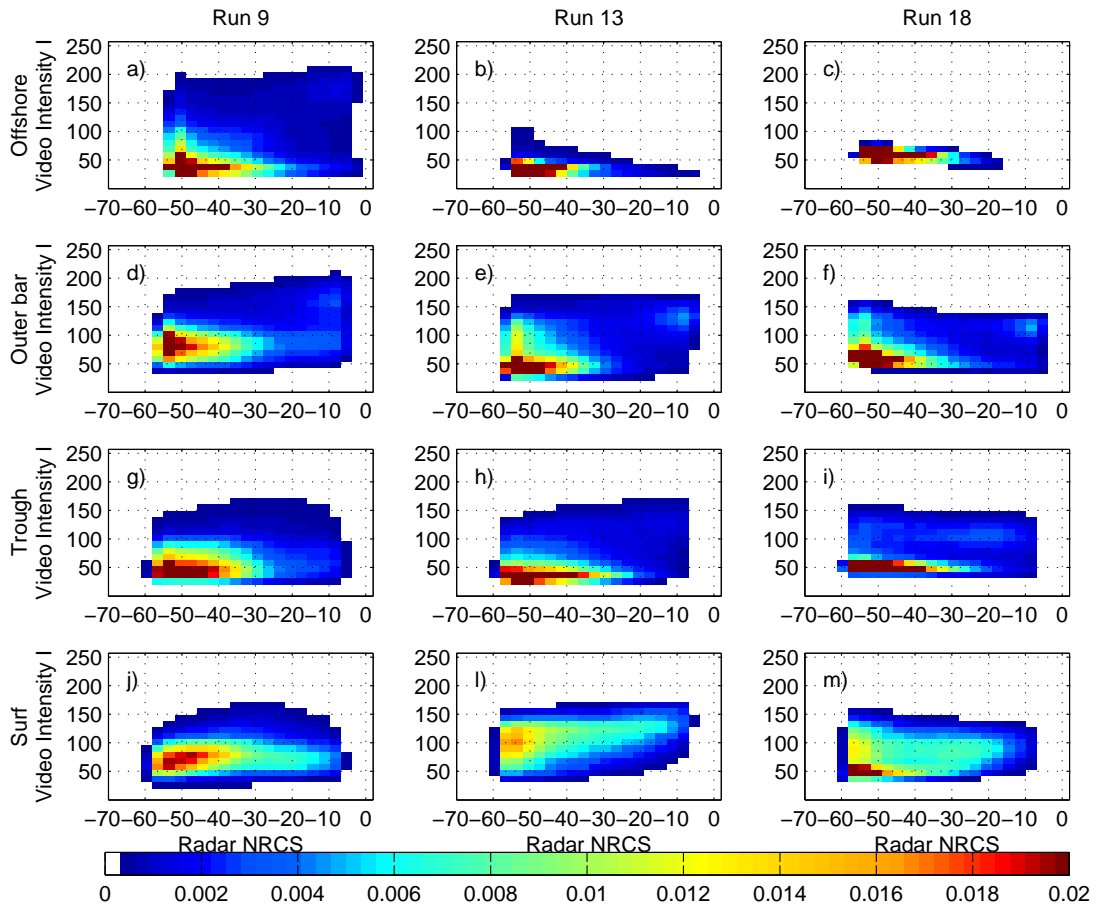


Fig. 4.8: Joint Probability Density function for video (Camera 1) and Marine radar. Columns correspond to Runs 9, 13 and 18, respectively. Rows correspond to zones according to Fig. 4.1.

but a relatively narrow range of backscattered power. This pattern could be explained as remnant foam (which induces a wide video intensity dynamic range) not scattering strongly from microwaves.

These two ridges in the JPDF can be explained by the presence of unbroken waves, very steep waves and to some degree, foam. The presence of active breaking in turn could be associated with large video intensity indices and large radar backscattering. Accordingly we can see that many of the zones exhibit a local peak in the upper right quadrant of the JPDF (e.g. Fig. 4.8 a, d, e, f, h i). The presence of this peak suggests a clear separation between foam and active breaking for both sensors, foam being the

source of less intense optical returns than active breaking. Consequently, the results are consistent with intermittent breaking taking place in the offshore zone and outer bar for Run 9, when wave height was largest; or in the outer bar for the other two environmental conditions. For these cases the ridges are also well defined.

However, in the inner surf zone where wave breaking is more frequent, the JPDFs are not consistent with the results from the other zones. For instance, Fig. 4.8j (large wave height, strong onshore wind, large amounts of foam) do not exhibit a clear peak associated with wave breaking, and in turn at high video intensities the peak is shifted toward mid power NRCS. On the other hand, the bulk of the signal for this case appears to be concentrated at mid video intensities (consistent with decaying foam in our model) but with radar scattering somewhat strongly from it. A similar behavior is observed for the case of low wave heights and mild wind (Fig. 4.8m), although in this case a peak is present at low intensities suggestive of foam-free water scattering weakly. Nevertheless, the peak at large video intensities, suggestive of breaking, is absent and a uniform distribution across the microwave range is apparent instead. The remaining surf zone case, mid wave heights and weak wind speeds, shows yet another pattern. Unlike the other two cases, there is defined trend toward the upper right quadrant, although the presence of the peak itself is not so readily apparent. Part of the reason could be associated with the anomalous behavior of the video signal, which showed bright intensities associated with remnant foam instead of active breaking. This could explain the almost uniform distribution of NRCS at high video intensity values. However, there is a clear trend toward stronger scattering associated to brighter intensity patches, but the distinction between active breaking and foam is not clear. Additionally, saturation of the marine radar signal induced an apparent decay of the NRCS, which could explain a wider NRCS range at large video intensities.

4.5 Discussion

4.5.1 Validation

Single and joint probability density functions obtained from data gathered with two remote sensors have been presented. Results show that qualitatively the PDFs resemble the expected behavior. Additionally, the presence of relict foam seems to affect the behavior of the video signal more than that of the microwave sensor. The PDFs of the latter showed a relatively constant shape despite the variability of ambient parameters, and showed some strong indications of a change in the frequency of occurrence above the NRCS range -30 to -20 dB that could be indicative of active breaking. However, the analysis of both sensors independently was considered not sufficient for the appropriate characterization of the signal origin nor for breaking detection.

In contrast, the use of the joint probability density function showed that when both sensors are used simultaneously, discrimination between the different stages of the breaking process is feasible. In particular, it was possible to identify four distinct regions on the JPDF that could be associated to different stages of wave breaking conditions in the surf zone. These are presented in Fig. 4.9. Region 1 corresponds to low pixel intensities and low backscattered power, thus non-breaking waves. Region 2 in turn corresponds to large pixel intensities and large backscattered power due to active breaking waves. Region 3 may correspond to large pixel intensities at relatively low backscattered power, that have been associated to relict foam. The fourth region corresponds to not-so-bright to dark pixel intensities and large returned power. This region could be divided further in two subzones, the first one (4a) corresponding to relatively bright optical intensities, which could be related to foam being the source of strong scattering, which was shown to occur for instance in the surf zone. Subzone (4b) is perhaps more interesting, because it can be defined in terms of low pixel intensities and large backscattered power. Given a suitable definition of what is considered a low intensity value, this could be associated with the presence of steepening waves scattering strongly from the front face of the wave, something that has been reported numerous times in the literature (for instance by *Puleo*

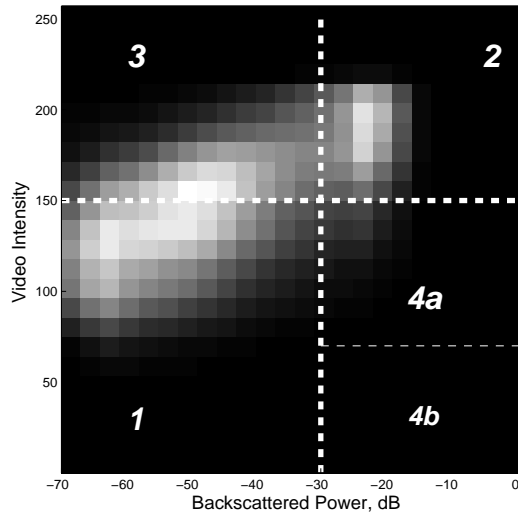


Fig. 4.9: Characterization of the JPDF in four regions. White lines denote arbitrarily thresholds defined for illustration purposes only.

et al. (2003) in the surf zone). Therefore a good working definition of this "low" threshold could be relevant for instance to differentiate the returned power levels between breaking and steepening waves. Based on the analysis of the JPDF, it seems that typically the backscattered power associated with breaking events is slightly larger than that associated to steepening waves, as suggested in Fig. 4.8d, e, and h) for instance. However, there are other situations where this differentiation it is not so readily apparent (Fig. 4.8a and Fig. 4.8f).

Perhaps the most contradictory results are those attributed to the presence of foam. While the secondary ridge identified (low backscattered power, wide dynamic range of pixel intensities) is consistent with previous findings by *Haller and Lyzenga* (2003) in the sense that active microwave scattering is less sensitive to foam, it appears to be contradicted by the results in the inner surf zone, where foam has been associated with a wide range of radar returns.

This situation highlights the fact that up to this point, the characterization of the scattering sources has been based solely on the information as provided by the PDFs and JPDF, under the assumption that the brightest optical signal could be associated to active

breaking and foam could be associated to less bright events. In order to substantiate these claims, it is possible to use the knowledge gained by the present analysis and use the results to discriminate breaking from non-breaking waves. The procedure is conceptually simple, in the sense that given a suitable selection of the threshold lines presented in Fig. 4.9 it would be straightforward to differentiate between regions. However, the caveat is that at this stage the selection of the appropriate thresholds is not a straightforward process because it is apparent that no universal values exist, most notably in the case of the optical signal. A clear example of this would be the comparison of Fig. 4.8d, Fig. 4.8e, and Fig. 4.8f, which all exhibit the peak in region 2 but the optical threshold value appears to decrease as the environmental conditions evolved.

In consequence, the problem is approached in an *ad-hoc* manner by using visual inspection to select the threshold values that appear to provide the best detection rate on a run-by-run basis. It should be noted as well that presently a proper measure of the success or skill of the method is lacking because there are no other methods capable of providing robust estimates of the occurrence of breaking. Therefore, although the assessment of the detection rates will be qualitative it is considered sufficient to qualify the success of the breaking detection procedure.

The following discrimination rules are used

$$\text{Breaking: } I(x, y, t) \geq I^t \quad \& \quad \sigma_0(x, y, t) \geq \sigma_0^t, \quad (4.12a)$$

$$\text{Foam: } I(x, y, t) \geq I^t \quad \& \quad \sigma_0(x, y, t) < \sigma_0^t, \quad (4.12b)$$

$$\text{Dark Zones: } I(x, y, t) < I^{td}, \quad (4.12c)$$

$$\text{Steep waves: } I(x, y, t) < I^{td} \quad \& \quad \sigma_0(x, y, t) \geq \sigma_0^t, \quad (4.12d)$$

where I^t , I^{td} denote the bright and dark pixel intensity thresholds for the video record, and σ_0^t is the power threshold for the marine radar record, in dB. These rules correspond to regions 2 (Breaking) and 3 (Foam) as defined in Fig. 4.9. The occurrence of optically dark wave faces corresponds to steep waves, where a further differentiation is made by

separating regular steep faces (Eq. 4.12c) and those scattering as strongly as breaking waves (Eq. 4.12d), corresponding to region 4b of the JPDF.

Table 4.3 presents the thresholds selected, along with some other statistics from each run obtained from the field of view associated with Camera 1. The procedure used was trial and error, by which different (I^t, σ_0^t) pairs were tested to verify the accuracy of breaking detection by applying them to multiple snapshots of the wave field. It can be seen that the selected thresholds are relatively constant between runs, with the exception of the dark threshold for Run 13, which had to be brought to very low values to allow discrimination of the steep fronts. Typically thresholds will depend on the illumination conditions, sun position and wave characteristics such as the steepness. For instance, in the case of Run 9 it was nearly impossible to discriminate the fronts from the rest of the wave due to the presence of foam and lack of contrast at low intensities due to overcast skies. Therefore the dark threshold was set to a default value of 50. One interesting result is that the selected optical thresholds were found to be $I^t = 2/3 * \bar{I}(x, y)_{\max}$ where $\bar{I}(x, y)$ is the mean of each pixel time series. Although this suggests that a rule could be established, the idea is not followed up at this point.

Regarding the microwave sensor, it can be seen that the thresholds and statistics showed almost zero variability again suggesting the possibility of the existence of universal values and that those values would be independent of environmental conditions. Furthermore, the threshold value suggested falls within the range of backscattered power associated with the departure of the microwave PDF from the exponentially decaying

Table 4.3: Summary of threshold values for the combined breaking detection method. Absolute maxima and maxima of the time exposure are provided for reference. Video values given in grayscale intensity, radar values in dB.

Id	Video I^t	Video $\text{Max}(I)$	Video $\text{Max}(\bar{I})$	Video $I^t/\text{Max}(\bar{I})$	Video I^{td}	Radar σ_0^t	Radar $\text{Max}(\sigma_0)$	Radar $\text{Max}(\bar{\sigma}_0)$
9	70	219	105	66%	50	-28	0	-17
13	77	205	128	60%	32	-28	-1	-18
18	75	207	119	63%	51	-28	-3	-18

tail, which could be indicative of different scattering mechanisms for breaking and non-breaking waves. It should be noted that the use of global values for the case of the marine radar requires the range dependencies to be removed.

Fig. 4.10 to Fig. 4.12 show the performance of the joint method of detection, where random snapshots (taken from the 30-min long series) of each sensor are overlaid with spatial contours associated to each of the discrimination rules defined. As can be seen, active breaking is well detected when compared with the visual signature, especially under conditions when the roller fronts are not so easily discernible, for example the event at $x = 280\text{m}$, $y = 670\text{m}$ in Fig. 4.12. Foam patches and steepening waves in turn are also clearly identified. The method struggles in properly detecting steepening wave fronts throughout the image, partly due to the very narrow intensity dynamic range of unbroken waves and especially front faces. A I_t^d value too low only detects the largest waves, whereas a value too high will include all wave phases. This effect can be seen for instance in Fig. 4.12, where a large area of unbroken waves is identified as steep wave fronts near $x = 200\text{ m}$, but true fronts were not identified at farther ranges ($x = 500\text{ m}$ and beyond). However, it is considered that large steep waves scattering strongly are the most interesting feature, due to their implications for understanding radar scattering mechanisms. The method was successful in detecting these events and therefore fine tuning of the dark values was not pursued.

Typically the spatial extent and location of the breaking events are well recovered, although some events are falsely detected as breaking, most notably in Run 9 and in the inner surf zone of Run18, where a big patch of foam appears to be modulated by a steepening wave yielding a false detection ($x = 150\text{ m}$, $y = 500\text{ to }625\text{ m}$). It is possible, though not tested, that using more stringent thresholds would remove these false alarms.

An obvious question is to qualify the skill of a threshold method on each sensor independently, most notably for the case of the video sensor considering that it is implicitly being used as a benchmark for detection. Therefore, the sensitivity of the detection skill to the thresholds I^t and σ_0^t is tested for each sensor independently. For the case of the

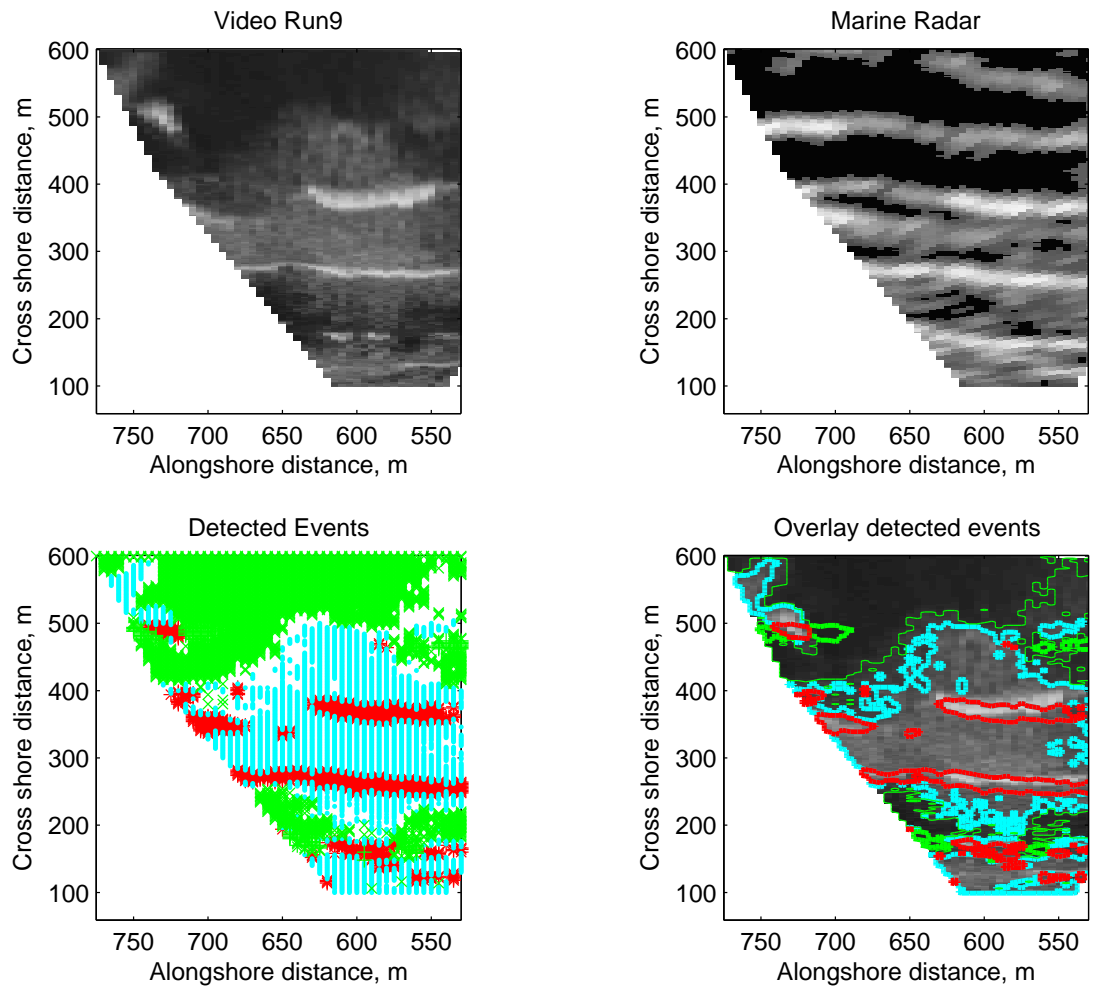


Fig. 4.10: Combined breaking detection (Run 9). (a) Video snapshot; (b) Marine radar snapshot; (c) Discrimination results. Red markers denote breaking; cyan denote remnant foam; green markers denote steep waves. (d) Video snapshots and contours demarcating the discrimination shown in (c). Thin green lines denote dark video patches and thick green lines denote steep waves. See text for further details.

optical record, thresholds are defined based on selected ratios relative to the maximum of the time exposure due to the apparent rule found from the trial and error procedure. In the case of marine radar, a range of power thresholds centered at the baseline threshold used in the joint detection is defined on a dB (thus nonlinear) scale. Fig. 4.13 shows the result for Run 9. As can be expected, increasing the threshold values yields a better agreement with the optical signature of breaking, most notably for the video record,

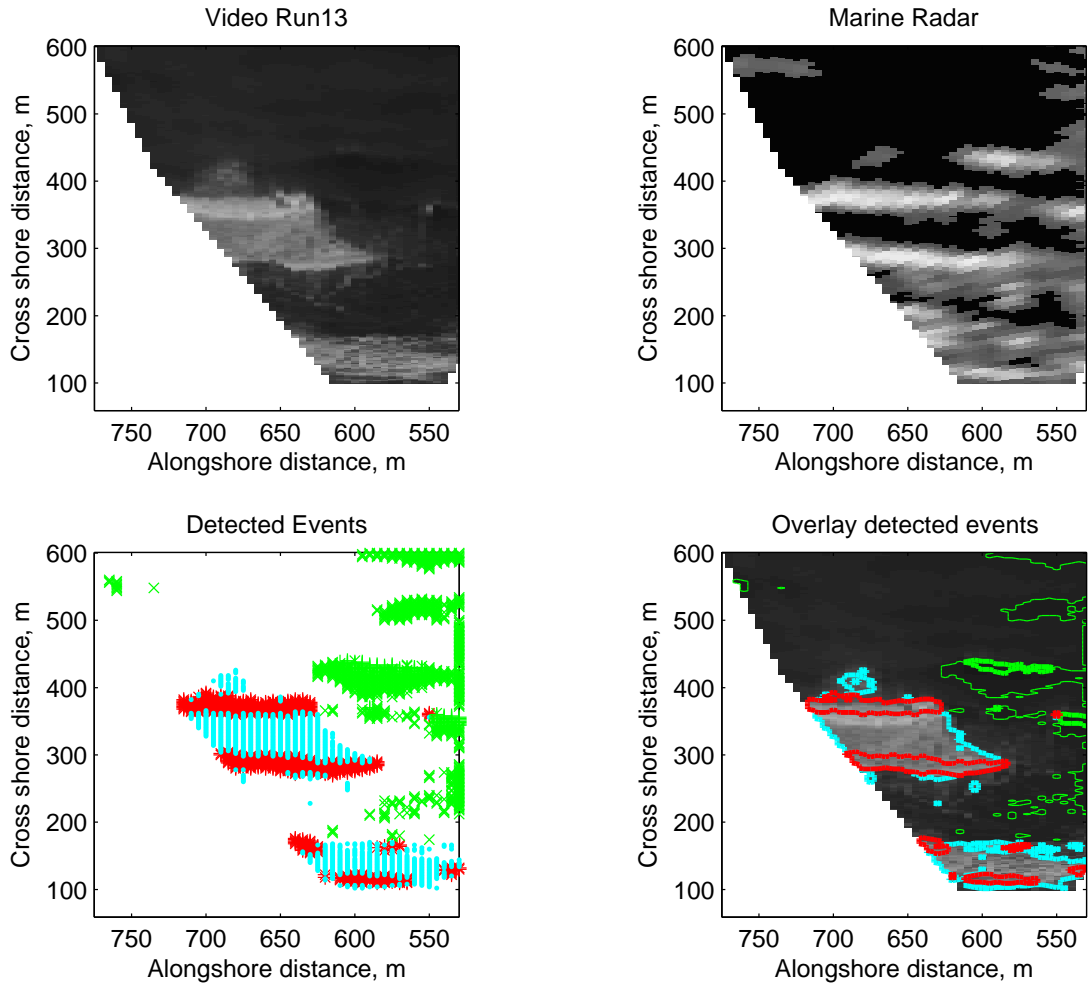


Fig. 4.11: Combined breaking detection (Run 13). Same key as Fig. 4.10.

where a good agreement is obtained for $I^t = 1.5\bar{I}(x, y)_{\max}$. The maximum power threshold for the radar in this case also yields a relatively good agreement, but overpredicts the spatial extent of the breaking events, most notably close to shore, suggesting that a higher value could have been used instead. At the same time, it can be seen that conservative thresholds tend to include remnant foam in the case of video and steepening waves in the case of radar. However, the conditions for Run 9 were near optimal in terms of the assumption that the brightest optical signal could be associated with the wave roller. The skill in detecting breaking changes drastically for Run13, which as can be recalled exhibited foam being as bright as the wave roller. As can be seen in Fig. 4.14, the use of

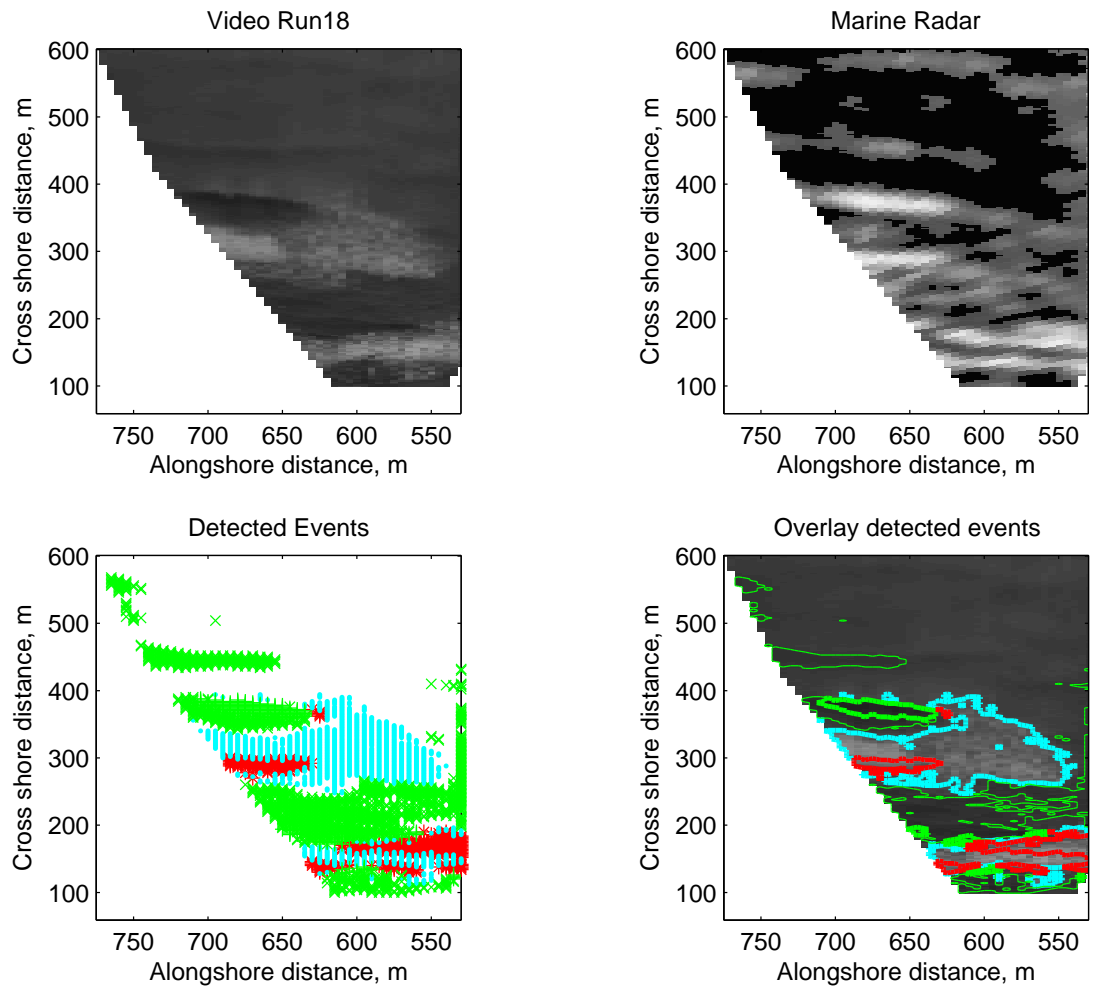


Fig. 4.12: Combined breaking detection (Run 18). Same key as Fig. 4.10

the largest ratio for the video case provides zero detection, and while the second largest ratio improves the detection rate, it does so at the expense of including foam patches. The situation is worse for the marine radar, where non-breaking waves are included even for the largest threshold used, again suggesting that either a more stringent value should be used or that it is not possible to separate steep waves from breaking waves. Similar results were obtained for Run 18 (not shown). It is apparent then, that either sensor acting independently can not provide reliable detection with predefined thresholds in an automated way. On the other hand, the thresholds used successfully in the joint method correspond to the minimum (optical) and mid value (marine radar) tested in Fig. 4.13

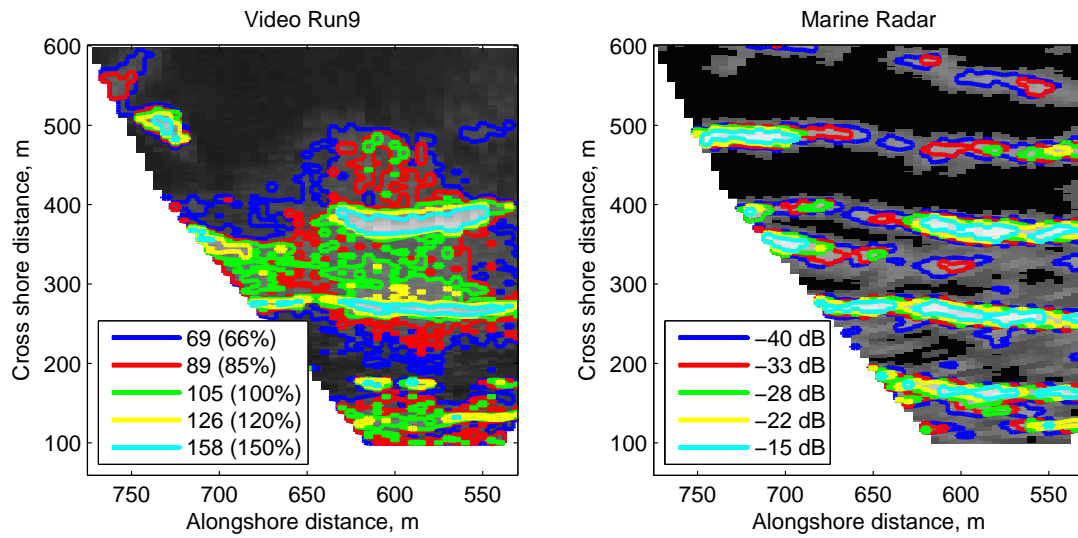


Fig. 4.13: Sensitivity tests for independent breaking detection. Run 9

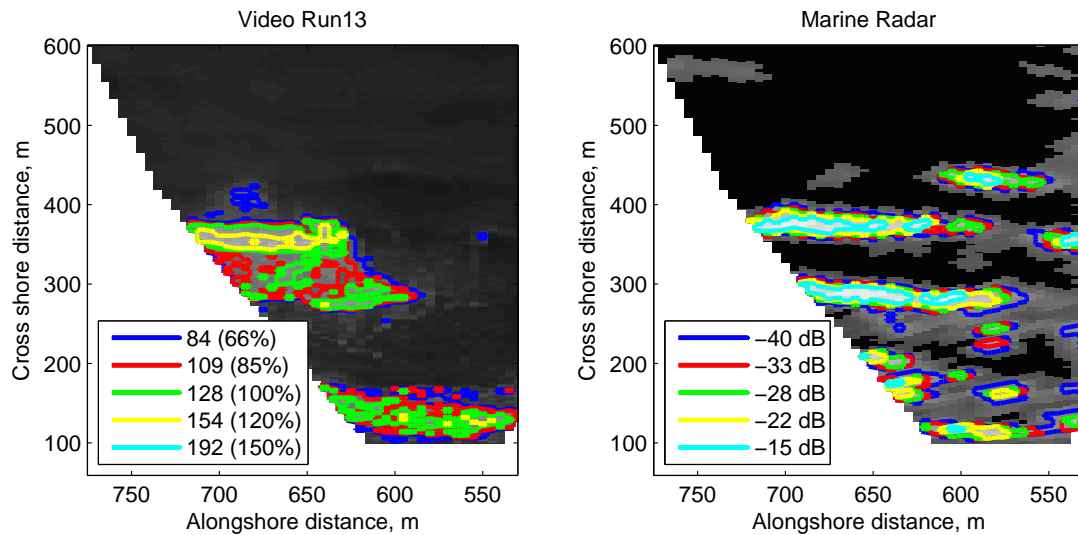


Fig. 4.14: Sensitivity tests for independent breaking detection. Run 13

and Fig. 4.14 which yield poor detection when used independently. Therefore even conservative thresholds appear to work well when both sensors are used together.

The success in the breaking detection by the joint method not only validates the new method, but also validates the hypotheses concerning the qualitative interpretation of the PDFs and JPDF regarding the scattering sources. There are however, some

outstanding issues that have not been cleared up yet, most notably the effects of foam for microwave scattering and the possibility of discriminating steep waves from breaking waves unequivocally. However, it is considered that the marine radar and its uncalibrated and single polarized nature may not be the appropriate tool to address these questions and the answer is deferred to the following Chapter.

4.5.2 Sources of error

During the analysis, it has been implicitly assumed that the records were accurately synchronized and geo-located, which allows a point to point comparison. However, there are several factors that can affect this one-to-one relation and may affect the results. For instance, Fig. 4.10 to Fig. 4.12 show that the spatial location of the identified breaking events is not always well retrieved. One possible factor explaining this is misregistration of the signal in either sensor due to finite wave amplitude effects. This appears to be more important in the case of video imagery, due to line-of-view registration (as opposed to time-of-flight for the microwave sensor) which implies that a point at a higher vertical level than that of the predefined reference (usually the mean water level) will be imaged as being further away from the camera. This effect might be relevant for the onset of breaking, in which case the roller and spray are generated at the wave crest and slide down the face of the wave. During this stage, the optical signature would be shifted backwards relative to that of an event in the front (assumed at the mean water level), an effect that would depend on wave height. This effect is apparent in Run 9 (Fig. 4.10) for the strong breaker at $x = 400$ m (cross shore) which is spreading sideways. However, in most of the situations the error in the spatial location shows the opposite situation, that is the radar signal being offset to the back of the wave roller (alternatively, video leading the radar signal; e.g. Fig. 4.11, Run 13, breaker at $x=380$). This could be attributed a misregistration of the radar sensor or errors in the time synchronization between sensors. However, it is not possible to validate these claims at this point because it would require another data set such as free surface displacements.

Another possible source of error is the difference in the size and orientation of the intrinsic resolution cells. For the cases under study (Camera 1), the difference becomes more noticeable in the inner surf zone, where optical resolution is at its best but the radar azimuthal resolution is not (the surf zone in Camera 1 is at large ground ranges). Moreover, the relative location of the sensors means that azimuthal angles of about 60° or more are used, making the radar cell oblique to the incident wave field with a size of 12 m (range) x 13 m (cross-range), thus potentially encompassing both active breaking and non-breaking scatterers whose relative contribution to the signal is unknown, an effect known as beam filling. It is obvious, however, that partial beam filling would have cross sections that would be different from those scattering from pure breaking or non-breaking centers. Assuming for a moment that both foam and a breaking wave roller are within the resolution cell, and that the roller scatters more powerfully, the effect of this combined cell on the JPDF would be to make the video observed foam appear to be scattering more power, thus populating Region 3 and toward region 2, and the video observed roller to be scattering less powerfully, thus leaving region 2 toward region 3 on the JPDF. This effect is less pronounced outside the surf zone because although the azimuthal resolution decreases (for instance to 21 m at 700 m in range), the look angle decreases as well and the resolution cell becomes more aligned with the oncoming waves, increasing the chance of uniformity of scatterers. This hypothesis seems to be confirmed by the analysis of the JPDF for camera 3, in which case the incoming waves direction was almost aligned with the radar look direction. Therefore, wave crests were aligned with the radar cell, minimizing the beam filling effect. Fig. 4.15 shows a clearer differentiation between active breaking and foam even in the inner surf zone.

Another aspect is related to the magnitude of the radar intrinsic resolution (12 m), which induces an apparent smearing of targets smaller than the resolution cell. Therefore, and considering that a single radar cell can overlap a few video pixels, the point to point comparison will show a significant disagreement if there is non-uniformity of their optical signature. This will typically mean more scattered power being associated with non-

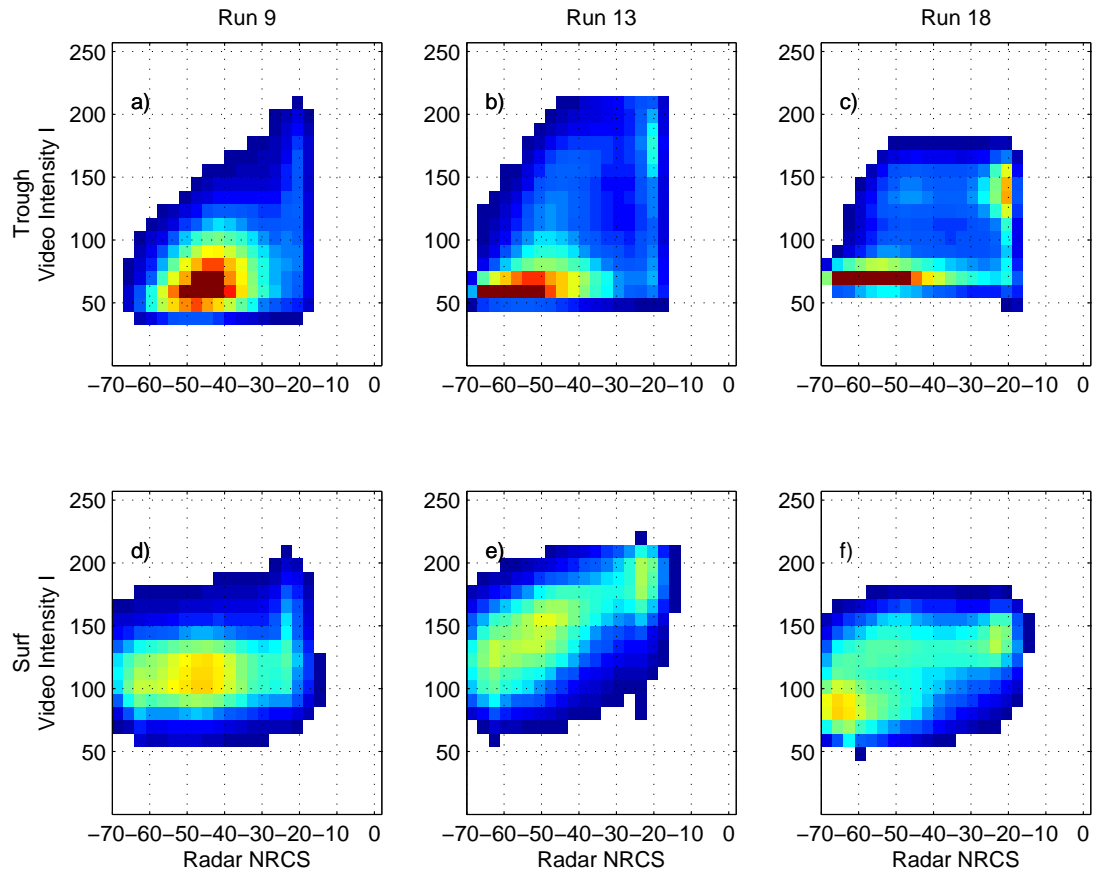


Fig. 4.15: Joint Probability Density function for video (Camera 3) and Marine radar. Columns correspond to Runs 9, 13 and 18, respectively. Rows correspond to zones according to Fig. 4.1.

breaking centers (due to beam filling), therefore populating the JPDF in zone 4a for instance. This situation also affects the spatial extent of active breaking events, that tend to show larger sizes on a radar image than in video. It is of note however, that the use of the joint detection method tends to preserve the sizes despite the apparent misplacement or misregistration.

On the other hand, the effect of saturation of the radar signal can also play a role in the JPDF. Saturation implies underprediction of the NRCS estimate, and if we further assume that breaking events would be more likely to saturate the signal, this would induce a shift in the joint distribution toward mid NRCS values at large video intensity values,

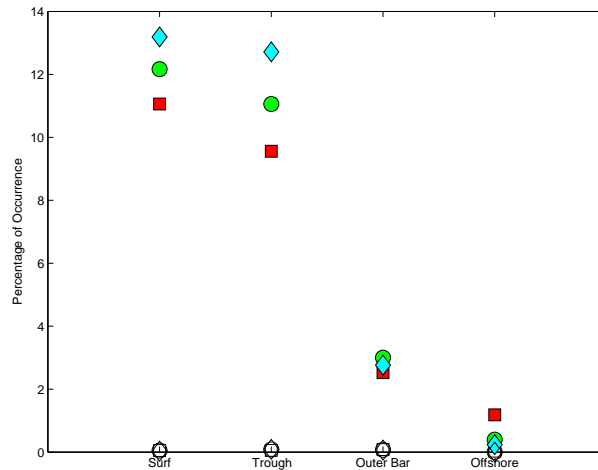


Fig. 4.16: Percentage of saturated events per run and per zone. Filled symbols denote the maximum saturation rate within the zone. Empty symbols correspond to the average saturation rate within the zone. (\square) Run 09; (\circ) Run 13; (\diamond) Run 18

causing a smearing of the breaking signal with foam (when looking at large azimuthal angles such as for Camera 1) or a shift of the breaking peak to lower intensity values (when looking upwave). Both effects are visible in the inner surf zone and bar trough JPDFs where, as can be seen in Fig. 4.16, certain locations saturated as much as 14% of the time.

4.6 Summary

The objective of the present work was to quantify the contribution of the wave breaking roller to the total microwave backscatter and optical intensity signals by using a statistical analysis. Consistent with the findings of previous research (e.g. *Jessup et al.*, 1991; *Liu et al.*, 1998; *Puleo et al.*, 2003) it was found that the strongest backscattered power can be related to both steepening and breaking waves. However, unlike *Liu et al.* (1998) who dealt with steepness limited waves affected by wind, it is apparent from the present results that in the surf zone, depth limited breaking waves are the dominant mechanism. Steep waves appear to scatter as strongly as breaking waves in some situations, although the statistical approach followed here and the uncalibrated nature of the microwave sensor

used are ill suited for to further validate these observations.

On the other hand, the synoptic nature of the present data set allowed a more robust qualification of the scattering origin and at the same time enabled introduction of a joint discrimination method that proved highly successful in identifying breaking events on a wave by wave basis. It was found that rather conservative values for the joint thresholds could be used and in fact recommended, as opposed to the more restrictive thresholds required if a single sensor is used. For instance, a optical threshold value representing 2/3 of the maximum intensity value of the intensity time average allowed inclusion of foam events that could be later discriminated by using the marine radar information. Regarding the latter, our results show the presence of an inflexion point in its PDF, suggesting a change in the scattering mechanism. This inflexion point was located in the range -30 to -20 dB and as such a universal value of -28 dB was used in the detection algorithm, irrespective of ambient conditions.

An extension of the method also allowed the identification of strong backscatter events associated with steepening waves. The successful detection of these events could be used in conjunction with the calibrated sensor for the purpose of characterizing the scattering mechanisms.

Moreover, if a nearshore observatory is equipped with both sensors, our results suggest this could be advantageous, since it enables quantification of other relevant parameters for the nearshore region, such as the fraction of breaking waves and its spatial variability, opens the possibility of evaluating roller length-scales, assessing the effect of using time exposures (including foam) against the contribution due to active breaking alone for both sensors, among other relevant research.

5. BACKSCATTERING FROM WAVES IN THE SURF ZONE

5.1 Introduction

Microwave scattering from breaking waves has been a subject of ample research both in laboratory and field. The former has the advantage of repeatability and control over the wave conditions, which coupled with the use of high resolution instruments, allows the study of backscattering during different stages of the wave breaking process (e.g. *Fuchs et al.*, 1999; *Coakley et al.*, 2001; *Dano et al.*, 2001a; *Sletten et al.*, 2003). However, most of the focus in these experiments has been on backscattering from deep water waves. As mentioned by *Coakley et al.* (2001), the relative scales between scatterers and the underlying wave field has not been accounted for and may prevent extrapolation of the results to larger wave conditions. Field experiments, on the other hand, do not exhibit this scaling problem but might be hampered by the difficulties in discriminating the different stages of the breaking process. While video data has been available in many of these studies to aid in the discrimination, in just a handful of cases has the data showed the level of collocation needed for a proper one-to-one comparison, such as rectification to an horizontal plane. For instance, *Haller and Lyzenga* (2003) used collocated video and microwave radar data to discriminate between active breaking and relict foam while collecting NRCS data at a single polarization (VV). *Puleo et al.* (2003) and *Farquharson et al.* (2005) collected single polarization (VV) Doppler data in the nearshore but, while acknowledging the complex mixture of broken and unbroken waves in the surf zone, did not pursue the characterization by scattering source in detail.

Therefore it seems that a proper characterization of the scattering characteristics of both breaking and non-breaking waves in the surf zone is currently lacking. For the present study, we intend to address this problem by taking advantage of an improved breaking detection method (presented in Chapter 4) whose results can be coupled with

the suite of microwave data retrieved by a dual polarization Doppler microwave system (RiverRad). In this way, it is possible to shed more light on the backscattered power, polarization ratio, and Doppler characteristics of nearshore waves during their different evolution stages.

5.2 Experimental Data and Preliminary Processing

Although data were collected regularly throughout the experiment, we will focus on the RiverRad data sets that overlapped the video and marine data used in cf. § 4.3. The RiverRad collection scheme was designed to gather data in at least 10 azimuthal directions during the course of a 30 min marine radar and video run, the aggregate number of the matching RiverRad runs was 38.

RiverRad collected data in a staring mode, meaning that during the run the antenna look direction did not change. For the analysis, it was assumed that the look direction was that of the mean value of the recorded azimuthal position of both antennas. The marine radar in turn collected in a rotating mode, and video collected data at prescribed cartesian coordinates. Any vibrations in the sensors are not accounted for. It was therefore necessary to consolidate all the measurements to a uniform coordinate system. In order to minimize degradation through the interpolation of the RiverRad data, the data of the other sensors was transformed to the space-time grid defined for each RiverRad run. Gathering of data in space was done based on the range distance of each RiverRad sample, which coupled to the spatial location of the sensor and the look direction could be transformed to cartesian FRF coordinates for each range bin. The collocated data from the other sensors was thus retrieved by table look up procedures. It is of note that this procedure involved retrieval of video data as collected by different cameras, thus different camera settings and consequently image intensity gradients are expected at camera boundaries.

Unfortunately, synchronization between RiverRad and the other sensors was not optimal and not achieved for all the 38 RiverRad runs. A run-by-run analysis was performed

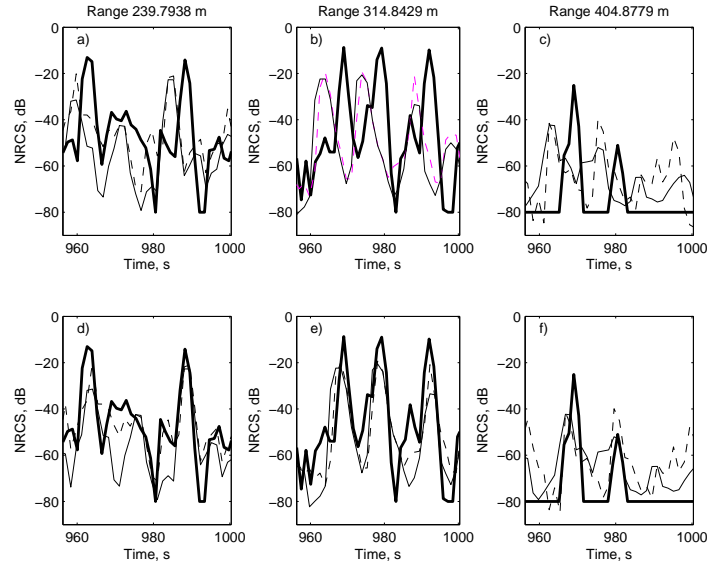


Fig. 5.1: Fine tuning of the time record for RiverRad Run 24263 at three different ground ranges. Left to right $r = 240, 315$ and 405 m. Upper row is raw data, bottom row shows corrected RiverRad data. (Thick lines) Calibrated marine radar, Run 1351300; (thin line) RiverRad HH; (dashed line) RiverRad VV. Offset was found to be 3 frames.

in an attempt to improve synchronization by manually shifting the timing of the beginning of each of the RiverRad records. The shift was introduced as an integer multiple of the sample rate on a trial-and-error basis. Alignment of the HH signals from the marine radar and RiverRad was evaluated at three different radial locations by simply looking at the peaks of the signals, but a constant shift was applied to all ranges. The maximum delay was found to be of order 3 times the sampling, roughly 4.3 s. An example of the procedure is shown for RiverRad run 24263 (May 14, 2008, 18:15:41 GMT) in Fig. 5.1.

Additionally, the time series of the video and marine radar were reduced and interpolated to the time domain of the RiverRad VV record. Furthermore, the time series of HH from RiverRad lags with respect to that of VV by instrument design. Therefore, the time series of HH is interpolated to that of VV assuming a constant offset between these records of half the sampling time. With this step, spatial and temporal point to point comparisons are feasible, and calculations of the polarization ratio are more accurate.

5.3 Results and Analysis

The procedure outlined above was applied to the 38 runs, of which 6 showed a distinguishable visual correlation and are used in the remainder of the section. These runs are listed in Table 5.1. To facilitate comparison with our previous results, the identifier is a combination of the identifier used previously for the marine radar-video comparisons followed by the look angle from the RiverRad runs. Runs 9-28, 13-28 and 18-28 correspond to roughly the same look direction ($\phi \approx 28^\circ$), enabling the comparison of results as wave conditions evolve. Runs 9-1, 13-1 and 18-1 are also included to illustrate the effect of look angle, as these conditions were collected with RiverRad looking almost upwave.

Wave breaking, remnant foam and steep waves scattering strongly are identified following the joint method described in Chapter 4 with the threshold values as given in Table 5.1. We will focus our attention in backscattered power at both polarizations σ_{0HH} and σ_{0VV} , the polarization ratio, $\sigma_{0HH}/\sigma_{0VV}$ and the Doppler spectrum at each polarization. Unlike the previous analysis where snapshots in the FRF cartesian coordinate system were used, in the following time-space maps or timestacks are used. Time is given in seconds relative to the beginning of the corresponding video run, and the space coordinate corresponds to the ground distance to RiverRad along the look direction, thus radial distances and denoted r , in m.

Table 5.1: Summary of the RiverRad runs used. Threshold values used in the joint detection algorithm are included. Identifier is a combination of the identifier used previously for the marine radar-video comparisons followed by the look angle from the RiverRad runs. Marine radar and RiverRad numbering is sequential. See Chapter 3.

Id.	Marine Run	RiverRad Run	ϕ degrees	Video I_t	Video I_t^d	Radar σ_0^t dB
9-1	1341700	23688	0.60	70	50	-28
9-28	1341700	23691	27.91	70	50	-28
13-28	1351300	24263	28.97	77	35	-28
13-1	1351300	24266	2.07	77	40	-33
18-1	1361000	24863	28.61	75	57	-28
18-28	1361000	24866	1.15	75	56	-28

5.3.1 Breaking detection

Fig. 5.2 shows the results of breaking detection for all the runs. It can be seen that good results are obtained, most notably for the cases at $\phi \approx 28^\circ$. However, there are a few situations that are worth taking into account. For instance, for run 9-1 (Fig. 5.2a) the detection of breaking shows some significant errors, most notably due to non detection of breaking events at long range and the misplacement of the detected events. Both effects are related to the marine radar signal leading the video signal, a result that could be attributed to misregistration. However, detection for the other cases and for the other look angle during the same video run show a high degree of successful detection, suggesting that the systems were well registered and synchronized. Although finite amplitude misregistration could be another factor with a similar signature, this can not be determined and can not be corrected for.

Another situation affecting the detection algorithm is the difference in camera settings, as seen for instance in Fig. 5.2 e), where differences in background video intensities are noticeable around $r = 425$ m. These differences affect primarily the detection of steep faces. Attempts to remove camera gradients, for instance by minimizing gradients in the mean and variance of the signal at the boundaries, were not successful and it was considered that they introduced imaging artifacts that could further affect the analysis, for instance, excessive darkening of the wave fronts or signal saturation. A post processing alternative would have been to increase the global intensity threshold I_t^d , but this comes at the expense of false detection for the darker camera. Camera gradients are more pronounced at the boundary between cameras 0 and 3 (at $r < 150$ m and $r < 175$ m for $\phi \approx 28^\circ$ and 1° , respectively). However, steep faces were less frequent within the field of view of Camera 0 thus independent thresholds I_t^d were not needed. On the other hand, it has been shown that the use of conservative values for the foam threshold I_t is not disadvantageous for the method and a global value can be used. Overall detection of steep waves at far ranges was successful.

It was therefore considered that a good discrimination between zones of active break-

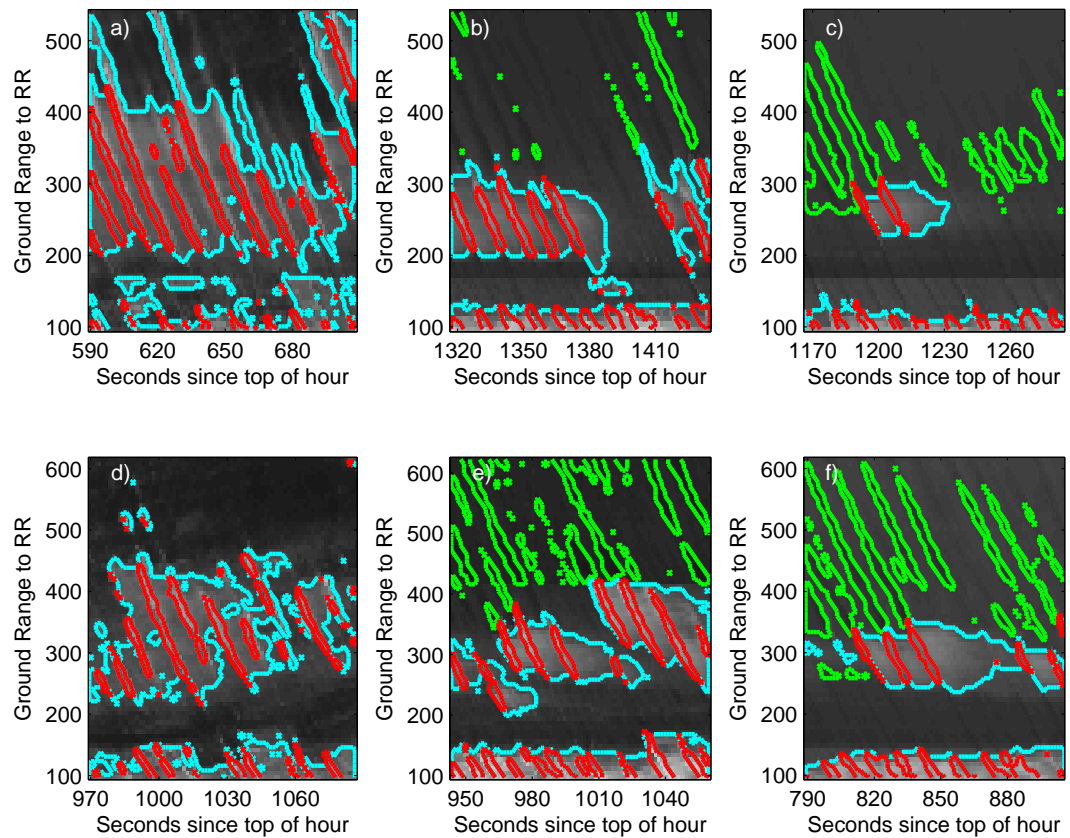


Fig. 5.2: Results of the breaking detection algorithm. Red contours denote breaking events, green contours denote steep events; cyan contours denote remnant foam. (a) Run 9-1; (b) Run 13-1; (c) Run 18-1; (d) Run 9-28; (e) Run 13-28; (f) Run 18-28

ing, steepening waves scattering strongly and foam was achieved using camera independent thresholds. The time-space coordinates of these events are then passed to the RiverRad records to retrieve the suite of calibrated microwave data.

5.3.2 Backscattered power

Fig. 5.3 to Fig. 5.8 show the time-space maps for the video intensity signal, the calibrated marine radar NRCS, the backscattered HH and VV NRCS along with the breaking identification results. It can be seen that the microwave signal of non-breaking events seems to follow a good correlation with wind speed, both parameters following a trend

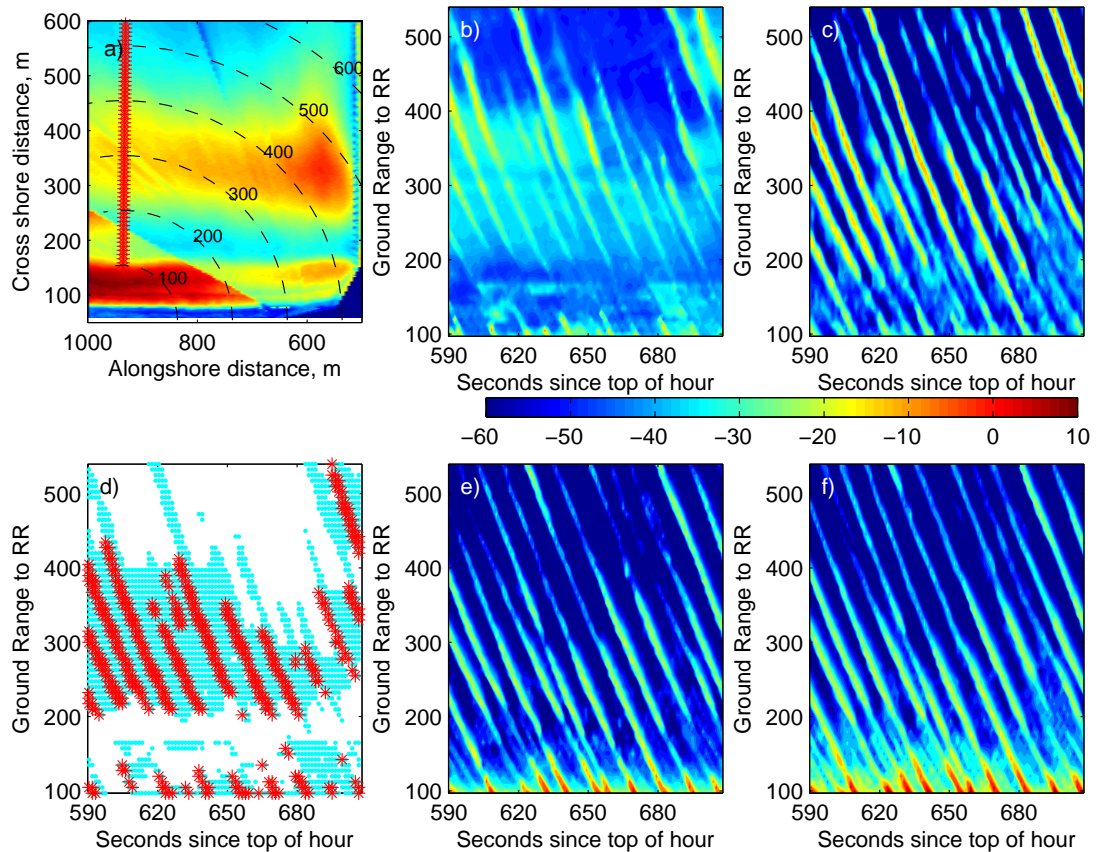


Fig. 5.3: Timestacks for Run 9-1. (a) Video time exposure showing the RiverRad look direction. Arcs correspond to radial distances to RiverRad; (b) Video time stack; (c) Marine radar calibrated NRCS timestack; (d) Breaking detection showing breaking (red *), foam (cyan ·) and steep waves (green +); (e) RiverRad HH NRCS; (f) RiverRad VV NRCS. Color scale corresponds to the microwave NRCS (dB).

from high to low to mid backscattered power and speed, respectively (cf. Table 4.2 and Fig. 4.2). On the other hand, the backscatter from breaking showed less variability.

In comparing HH to VV, the signals show a clear tendency for VV values to be slightly larger than HH, especially for unbroken waves. This is to be expected within the frame of CST, where VV is always larger than HH. However, the timestacks suggest that in some cases the VV NRCS resembles the marine radar signature more than that of HH (e.g. Run 18-28, see Fig. 5.8c and Fig. 5.8f). It must be remembered that the marine radar is also horizontally polarized. In order to evaluate this claim, we measure

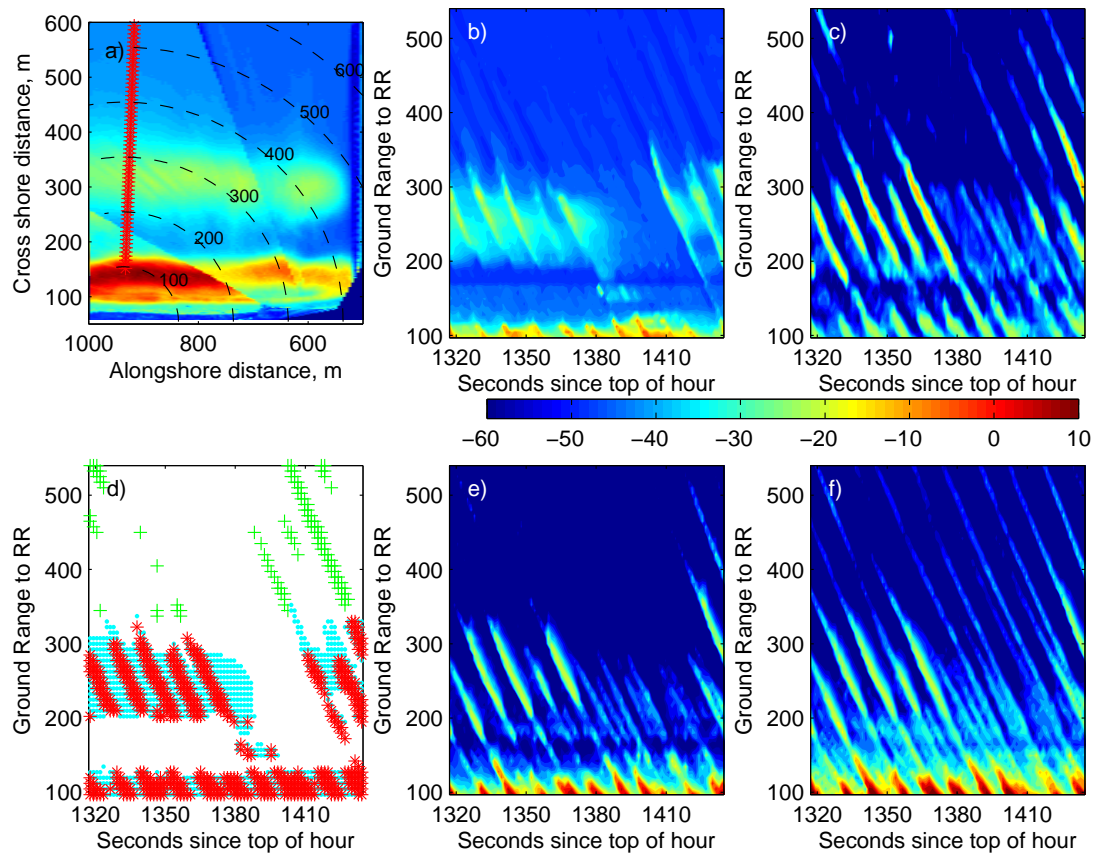


Fig. 5.4: Timestacks for Run 13-1. Same key as Fig. 5.3.

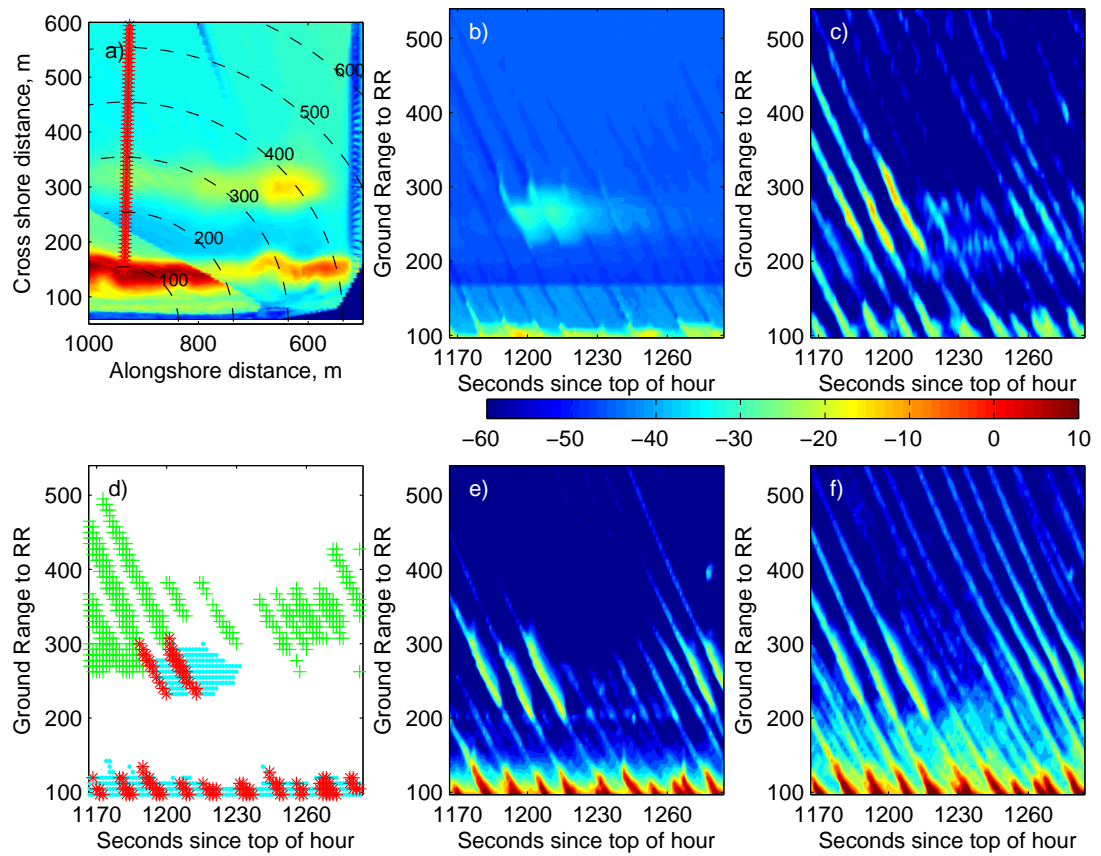


Fig. 5.5: Timestacks for Run 18-1. Same key as Fig. 5.3.

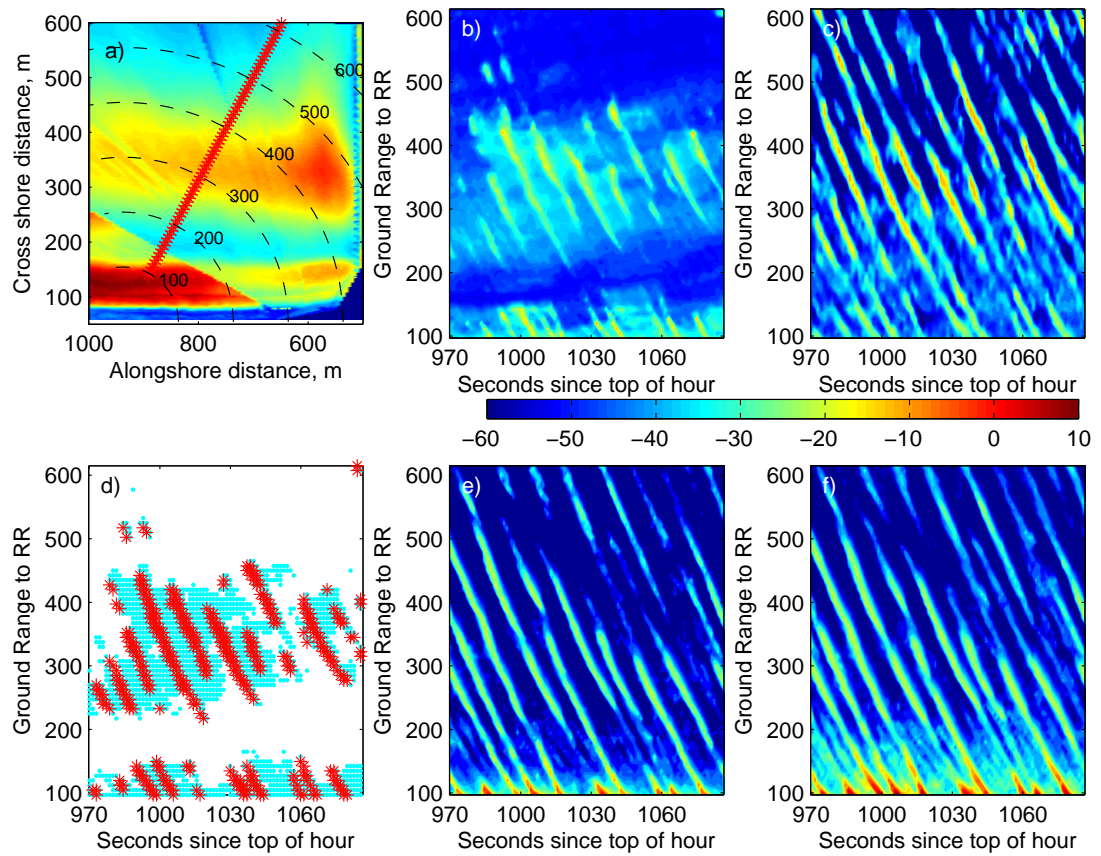


Fig. 5.6: Timestacks for Run 9-28. Same key as Fig. 5.3.

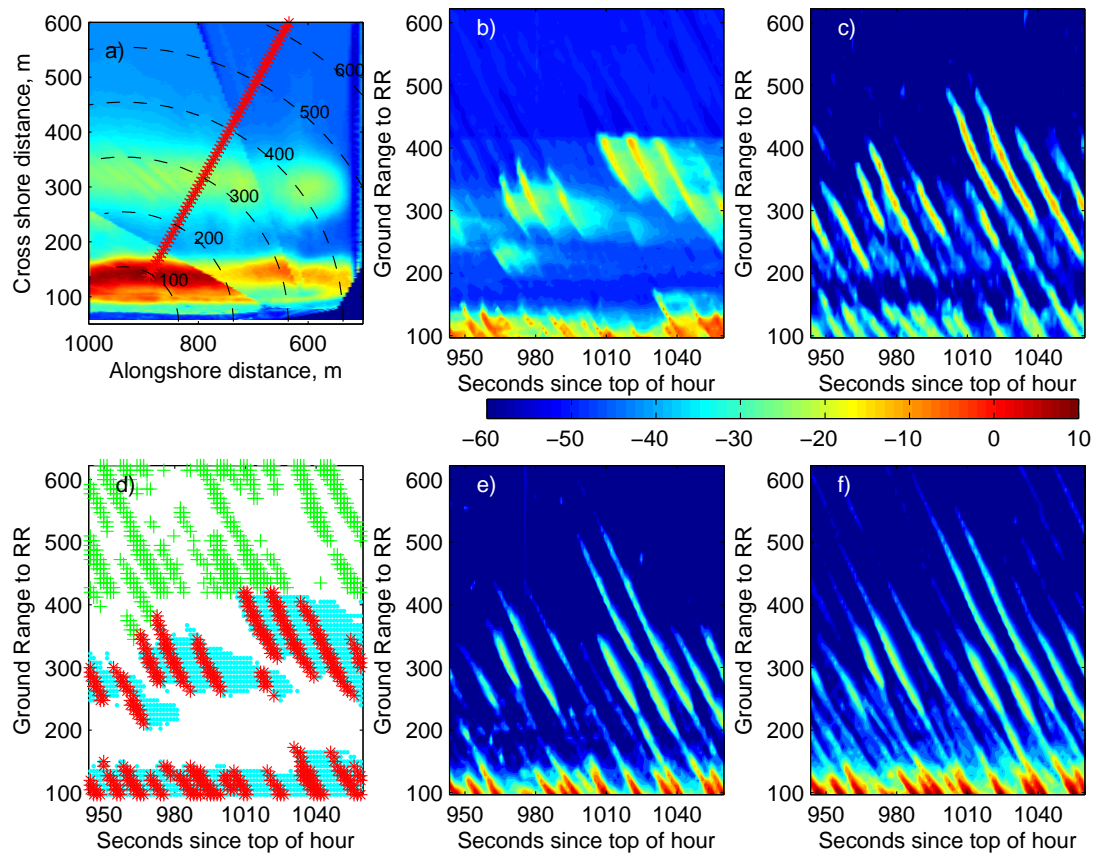


Fig. 5.7: Timestacks for Run 13-28. Same key as Fig. 5.3.

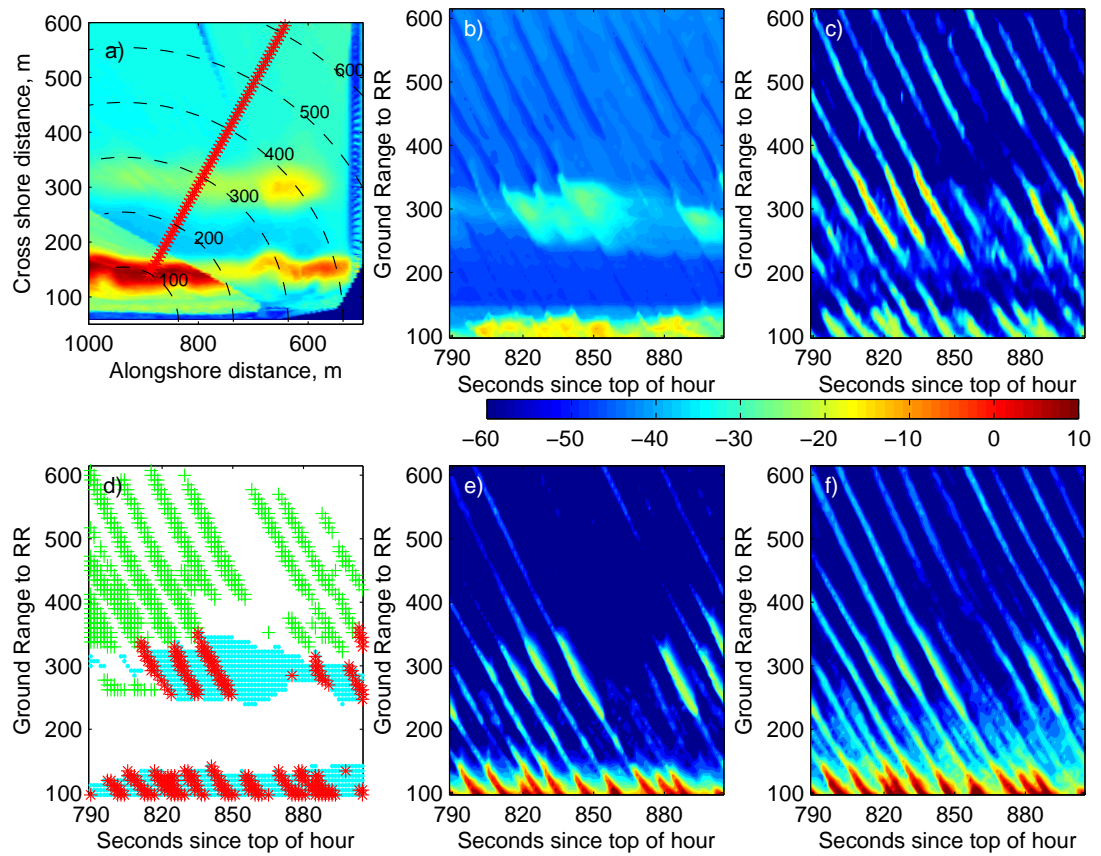


Fig. 5.8: Timestacks for Run 18-28. Same key as Fig. 5.3.

the difference between the time series following *Puleo et al.* (2003)

$$E_{\alpha,\beta} = \frac{\langle |\beta - \alpha| \rangle}{|\langle \beta \rangle|} \pm \frac{\sigma_{\beta-\alpha}}{|\langle \beta \rangle|}, \quad (5.1)$$

where α, β are the time series at each range. Here α is either HH or VV, and β is the marine radar series. $\langle \rangle$ denote ensemble averages and $\sigma_{\beta-\alpha}$ is the standard deviation of the series. $||$ denotes absolute values, which have been included to minimize cancelation of values of opposite sign. Range dependent plots of the first term of the error estimate are presented in Fig. 5.9 where it can be seen at short ranges HH shows a better agreement with the marine radar. However, in some cases (most notably those corresponding to Run 9) it seems that VV could be better correlated, although the difference between the $E_{\alpha,\beta}$ of each series is minimal. As the environmental conditions decayed, HH tends to have the upper hand although $E_{\alpha,\beta}$ error values tend to be very similar in magnitude with the sole exception of Run 18-1, where clearly VV seems to be more sensitive to the presence of steepening waves thus deviating from the marine radar signal. As before, instances when the marine radar fell to the base level have been removed from the comparison, although calculations made including all events led to similar results. The apparent similitude between the marine radar and VV while keeping a good agreement with HH seem to suggest the existence of scattering sources that do not discriminate between polarization states, and that they dominate the signal for most of the cases selected. When the scattering mechanism is polarization dependent, for instance according to CST for steepening waves, VV exhibits stronger signals and deviate from the marine radar.

Therefore, it is interesting to focus on the scattering characteristics depending on the source. To do so, histograms of the NRCS from breaking, foam, steep waves and the remainder of the pixels not included in the other three categories are computed using bins 5 dB-wide. Fig. 5.10 shows the histogram of backscattered power from breaking waves. Results for the marine radar are trivial, in the sense that the clear cut off at $\sigma_0 \approx -30$ dB is due to the threshold value used as input for breaking detection. Above this value, the

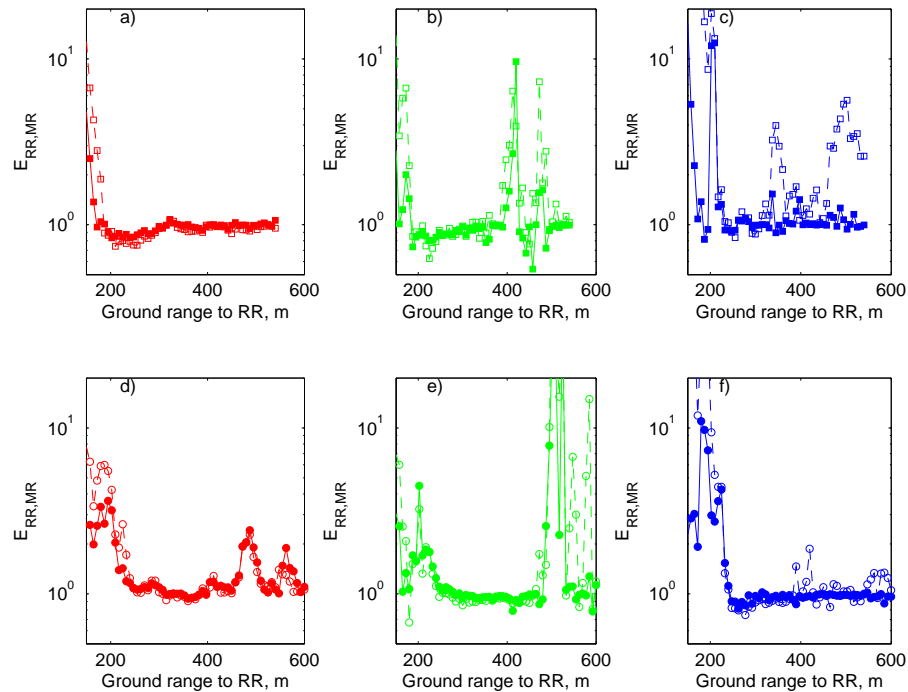


Fig. 5.9: Estimate of the difference between the NRCS time series for HH (solid) and VV (dashed-open symbols) respect to marine radar. a) Run 9-1; b) Run 13-1; c) Run 18-1; d) Run 9-28; e) Run 13-28; f) Run 18-28

signal shows a narrow distribution of power whose dynamic range and NRCS at the peak of the histogram appear to be independent of the wave conditions. Maximum frequency counts showed little variability with the exception of Run 13-1. Saturation of the signal was negligible for these runs, therefore the histogram represents actual pseudo calibrated NRCS.

Fig. 5.10b and Fig. 5.10c show the histograms of the HH and VV signal from breaking events, where it must be noted that for these histograms signals below the noise level of the sensor have been included. Unlike the marine radar results, the signals do not show a clear cut off and span the whole NRCS scale, although typically the frequency of events at low backscattered power ($\sigma_0 \leq -30\text{dB}$) is small. The exception appears to be Run 9-28, in which case there were some noticeable differences between the signals from the different sensors (cf. Fig. 5.6). For instance, the event at $t = 1040$ s, $r = 450$ m was detected as a breaking wave but it does not show strong scattering from RiverRad. This

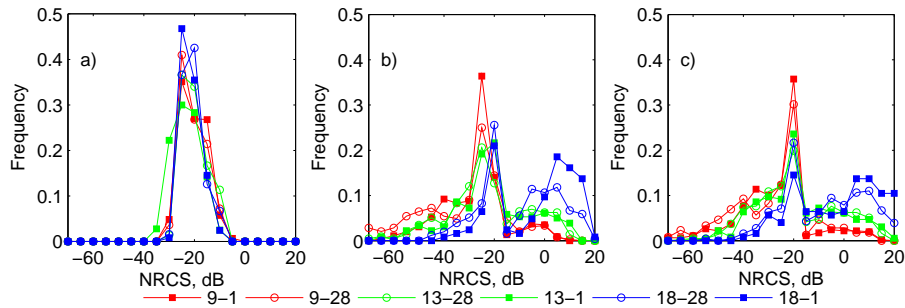


Fig. 5.10: Histograms of the NRCS of breaking waves. (a) Marine radar; (b) RiverRad HH; (c) River Rad VV.

result could be explained in terms of partial shadowing of the roller by the simultaneous presence of wave breaking further onshore (at closer range). Slight differences in vantage height between the microwave sensors (the marine radar is 3.5 m higher) could explain RiverRad being more prone to shadowing than the marine radar therefore showing less backscattered power, thus higher frequency count in the histogram. Runs corresponding to May-14 (Runs 13-1 and Run 13-28) also show returns at low NRCS values, but they tend to be less uniform and concentrate near -40 to -30 dB. In comparing VV and HH within these NRCS bins, it can be seen that VV results tend to be more bunched toward larger power, which could be related to VV being less sensitive to shadowing due to diffraction, therefore being capable of observing more of the partially shadowed roller (e.g. *Wetzel, 1990a*). This could also explain the favorable comparison between VV and the marine radar for energetic wave conditions (cf. Fig. 5.9).

The histograms show a clear peak within a narrow set of backscattered power (≈ -25 dB), which is relatively insensitive to the wave conditions. In fact, of the 12 sets (6 at each polarization), 8 show the peak at the same dB bin and the remainder 4 are shifted to the next bin down power. Although it is tempting to interpret this as wave breaking being independent of the conditions and look geometry (most notably grazing angle), the result could be biased due to the size of the breaking event and the number of pixels included in the analysis. As can be seen from the detection results, waves breaking at the offshore bar tend to have a larger footprint and therefore encompass a larger

number of pixels scattering at similar NRCS levels, thus increasing the frequency count. As the wave conditions decay, fewer events break at the offshore bar and the relative importance of the breaking events in the inner bar is exacerbated. The outstanding case is Run 18-1, where few breaking events were detected on the outer bar and the bulk of the detected events are located in the inner surf zone (at short ranges). The presence of a bimodal distribution suggests that even these few offshore events aggregate enough pixels to balance a larger number of smaller events in the inner surf zone.

Therefore, the analysis is shifted towards determination of characteristic values for an event, rather than for the ensemble of pixels scattering individually. An event is thus defined as the ensemble of connected pixels with a common discrimination tag (breaker, foam, steep). With this approach, statistics of the event are computed as well as the location of its centroid, and the results are delivered as a function of the grazing angle evaluated at the centroid. This definition is well suited for breaking waves and steep waves, since they are typically single-connected regions. Foam patches in turn can be multiply connected and span large areas and its results could be smeared, both in the centroid location as in NRCS values. Backscattered power falling below the noise level has been removed from the analysis. The median is the preferred statistic for the analysis under the consideration that is less prone to be affected by the presence of outliers.

Fig. 5.11 shows the median backscattered power of each of the 153 breaking events detected. Results show similar trends as those indicated by the analysis of the histogram, in the sense that most of the data appears to cap off at -20 dB for angles smaller than $\theta_g \approx 3.5^\circ$. At larger grazing, there is a change in the trend with a steeper dependency on grazing angle and significantly larger NRCS. Analysis of the calibration procedure showed that for $\theta_g > 3.5^\circ$, the gain pattern G of the antenna fell more than 15 dB from its peak value. These very low values tend to amplify the NRCS due to the G^{-2} dependency of the calibration equation. In consequence, we focused the analysis in the region $\theta_g < 3.5^\circ$ ($r > 200$ m), although values at higher grazing will be retained because other quantities such as the polarization ratio and Doppler offset are not affected by this

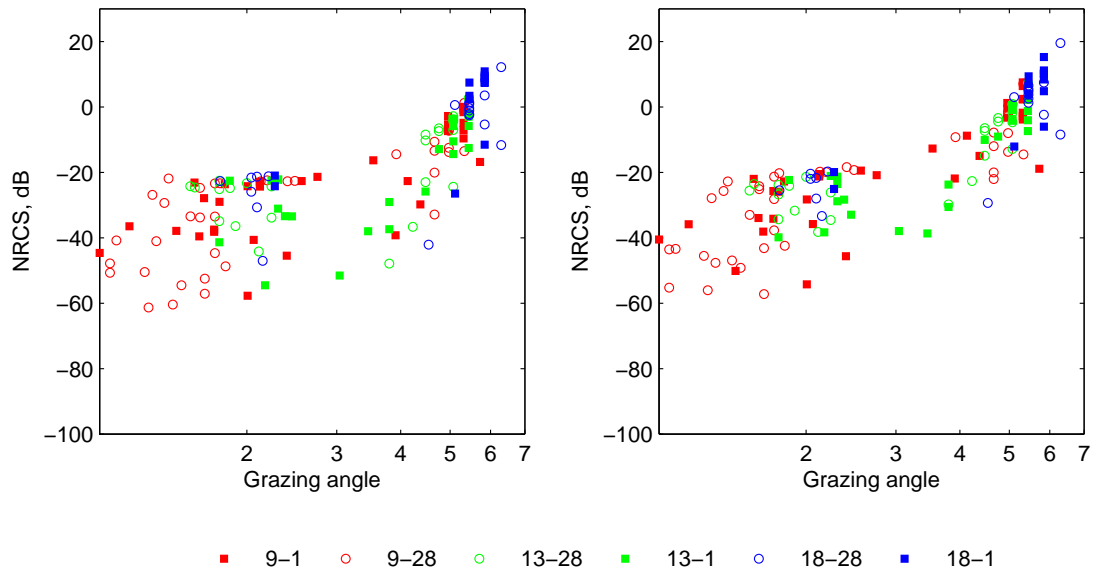


Fig. 5.11: Grazing angle dependency of the median of the backscattered power of individual breaking events. Color code correspond to different runs. HH (left) VV (right).

correction.

It can be seen that using this approach reduces the effect of pixel count. For example, for Run 18-1 when only two events are present offshore. However, those events had a larger footprint (thus a large number of pixels) and therefore biased the histogram estimates causing the apparent bimodal distribution. At the same time, it can be seen that Run 9-28 exhibits a large dynamic range of the NRCS, consistent with the existence of large values of its histogram at low backscattered power which have been correlated to partial shadowing.

Results seem to confirm insensitivity of the backscattering from breaking waves to the environmental conditions with the exception of the effect of shadowing which is dependent on wave height. Although results for Run 13 at both look directions show some events scattering weakly, analysis of the location of breaking events showed that they correspond to events of small footprint (in the video image) that scattered weakly to RiverRad (cf. the three events at $r = 150$ m and $t = 1400$ s in Fig. 5.2b), suggesting that

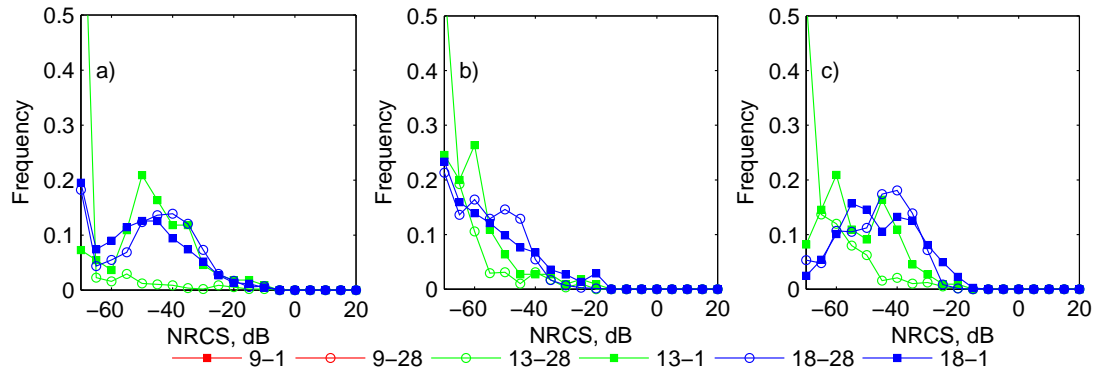


Fig. 5.12: Histograms of the NRCS of steep waves. (a) Marine radar; (b) RiverRad HH; (c) River Rad VV.

the radar resolution cell was not uniformly covered by breaking, thus fractional beam filling could explain the decrease in NRCS.

At the same time, it is possible to observe the presence of two clusters in Fig. 5.11, which correspond to preferential breaking in the inner surf zone (for large grazing angles) and the outer bar (low grazing angles). The dependency of the cluster angular spread on the wave conditions is obvious. Runs 9-1 and 9-28 show a large spread due to breaking taking place over long distances, which is reduced in extent as wave height decays and the surf zone width becomes narrower.

Acknowledging the caveat with pixel count biasing the histograms, we can proceed to analyze the backscattering from steep waves, whose histograms and median per event are presented in Fig. 5.12 and Fig. 5.13 respectively. These have been identified only in May-14 (Run 13) and May-15 (Run 18). The histogram of the marine radar spans all the NRCS scale because these waves have been selected based on their video signature alone (that is, using the rule given by Eq. 4.12c). As a result the marine radar histogram shows the presence of events scattering at levels larger than $\sigma_0^t \approx -28\text{dB}$, that is events that could have been considered breaking. However, this occurs for a small fraction of the events. In fact, Fig. 5.13 suggest that at most two events reach or exceed this level. Thus it can be said that steepening waves scatter less strongly than active breaking

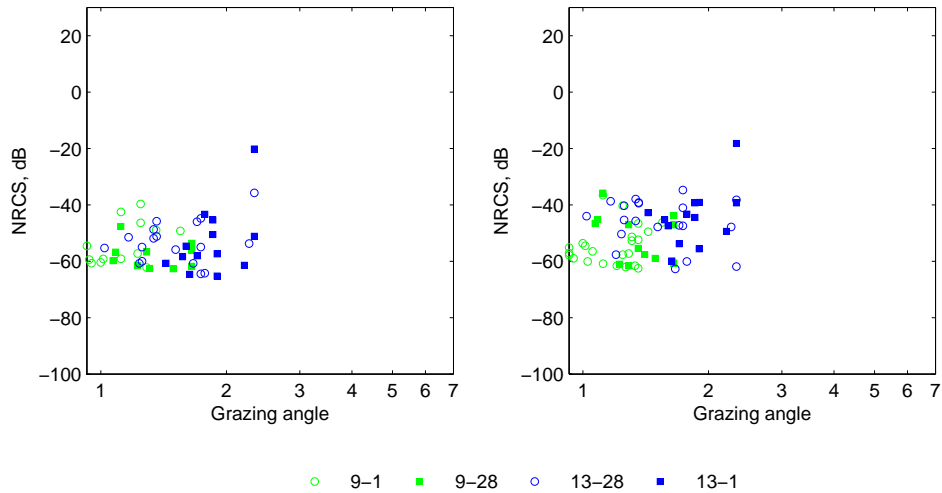


Fig. 5.13: Grazing angle dependency of the median of the backscattered power from steep waves. Color code correspond to different runs. HH (left) VV (right).

waves. Although the quantification of a definite limit is less obvious, the NRCS appears not to exceed -30 dB.

Additionally, there is a clear dependency of the scattered power on ambient conditions. Both the histogram and the grazing angle dependency plots show a transition from low backscattered power for Run 13 (green markers) to slightly larger power returns for Run 18 (blue markers). Furthermore, the difference in scattering levels is more pronounced for the VV data, where differences of order -10 to -15 dB are noticeable between sets at the same look direction. Slight differences are also noticeable between look directions for the same environmental conditions, with the upwave looking data set showing a slightly larger concentration of events at larger return power. These situations are in accordance with the enhancement of surface roughness with increasing wind speed, which is then modulated by the long waves and modeled by CST.

Fig. 5.14 and Fig. 5.15 show the results for events classified as foam. As in the case of breaking events, the marine radar histogram shows a clear cut-off due to the definition of the threshold. It is of note, however, that for all three sensors both the histograms and the grazing angle dependency tend to collapse and that the values are dominated by low

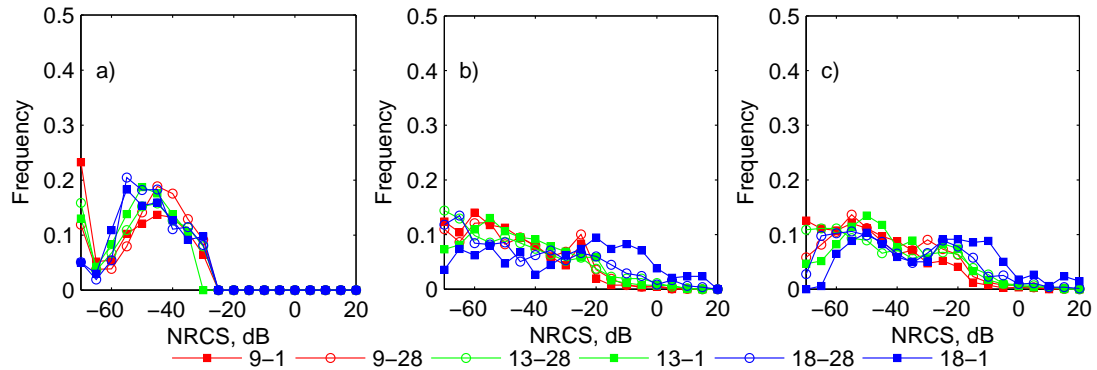


Fig. 5.14: Histograms of the NRCS from remnant foam. (a) Marine radar; (b) RiverRad HH; (c) River Rad VV.

backscattered power on the histogram. However, removal of the instances falling below the noise level shows that some event characteristics compare well with those of active breaking (see Fig. 5.15) especially for the more energetic conditions, but the bulk of the foam events scatters rather weakly. For strong breaking events, remnant foam can persist over several waves, thus being present during the receding phase of a wave and is usually associated with weak backscattering, although whether this is the result of foam being a weak scattering source or due to partial shadowing can not be distinguished at this point. On the other hand, when foam is modulated near the front of the wave, it appears to be the source of scatter as powerful as that of an active breaking event. However, it can not be ruled out at this point the possibility that those large power events could correspond to active breaking being not properly identified by the detection algorithm. When a clear separation exists (e.g. for Run 18-1 and 18-28), the water surface is clearly the source of weak scattering.

Just like scattering from active breaking, scattering from foam appears to be independent of the environmental conditions except for its angular spread and dynamic range. The latter could be influenced by errors in the detection algorithm (undetected breaking events) which could bias the median toward larger NRCS values. Therefore, at this point, a clear characterization of the scattering from foam is not possible.

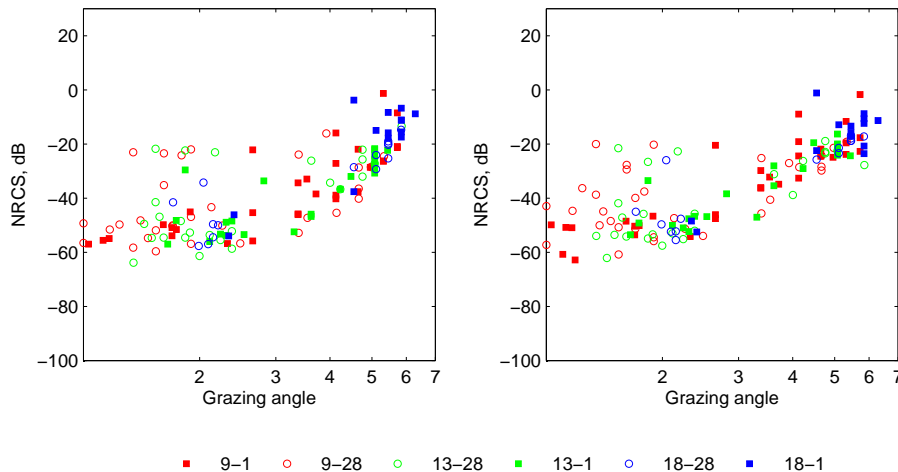


Fig. 5.15: Grazing angle dependency of the median of the backscattered power from foam. Color code correspond to different runs. HH (left) VV (right).

Nevertheless, it can be said that the results presented so far suggest that the backscattered power does depend on the wave stage. To further evaluate this, the ensemble of the data sets is presented in Fig. 5.16. It is readily noticeable that breaking events tend to concentrate at large backscattered power, with the presence of an upper limit around -20 dB that shows a weak dependency on grazing angle for events at $\theta_g < 3.5^\circ$. This limit appears to be independent of the polarization state. In contrast, a lower limit for the breakers is not readily discernible and the data shows a large dynamic range at both polarizations. However, most of the data showing $\sigma_0 < -30$ dB corresponds to a single data set, (Run 9-28, cf. Fig. 5.17), for which case partial shadowing can be called upon to explain these results. In all the remainder data sets, the bulk of the events is concentrated in the range -30 dB $< \sigma_0 \leq -20$ dB. Typically, more than 70% of the breaking events scatter at $\sigma_0 \geq -20$ dB.

At the same time, steep events seem to be confined over a narrower dynamic range (spanning about 30 dB) and do not exceed -30 dB. Their signature shows a weak dependency on grazing angle for the case of HH. VV polarization shows slightly more spread in terms of NRCS, reaching relatively large values ($O(-30)$ dB) occasionally. From these results, it appears that for discrimination purposes it is more plausible to misidentify a

breaking event as steep than viceversa. In Fig. 5.16 the θ_g^4 dependency of the Bragg scatterers (cf. Eq. 2.1) at low grazing angles has been included. According to *Trizna and Carlson* (1996), the existence of this trend could be attributed to Bragg scatterers in the front face of long (in a EM sense) waves satisfying $kh \ll 1$, k being the Bragg wavenumber and h the Bragg wave height. It can be seen that steep waves seem to follow well this trend, further suggesting Bragg scattering according to CST or bound Bragg waves.

On the other hand, foam seems to be the source of backscattering at all NRCS levels, although it shows a tendency to cluster at either high backscattered power ($O(-20)$ dB) or at the lowest power for a given range at grazing angles smaller than $\theta_g \leq 3.5^\circ$. This clustering suggests that rather than foam being capable of scattering strongly, there is a problem with the discrimination of some events as breakers or foam. On the other hand, for steeper grazing angles ($\theta_g > 3.5^\circ$), the separation between the scattering arising from breaking waves and foam is more obvious, although it is not possible to draw clear conclusions regarding the actual scattering levels of each source due to the effect of the antenna gain pattern.

Fig. 5.18 shows the median of the NRCS at each time step and classified by scattering source. This approach reduces the spatial smearing that could be introduced by using the event as whole. Despite the apparent scatter, the results confirm that scattering from breaking waves is a few dB larger than that of non-breaking events. This is further emphasized by fitting a nonlinear polynomial of the form

$$\sigma_0^{\text{LSQ}} = 10 * \log_{10}(C_1 + \theta_g^{C_2}), \quad (5.2)$$

to the NRCS of breaking waves at angles $\theta_g > 3.5^\circ$. Figfig:LSQ shows that despite the presence of events scattering rather weakly, the bulk of the events does it at large values and consequently the least-squares fit shows a slight bias toward lower values.

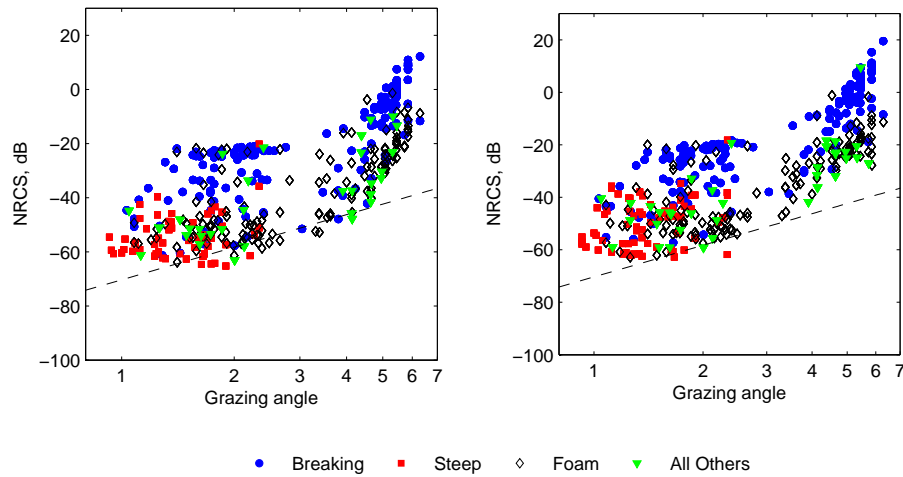


Fig. 5.16: Grazing angle dependency of the median of the backscattered power for the ensemble of all detected events and classified by source. Color code correspond to different sources. Dashed line corresponds to θ_g^4 trend. HH (left) VV (right).

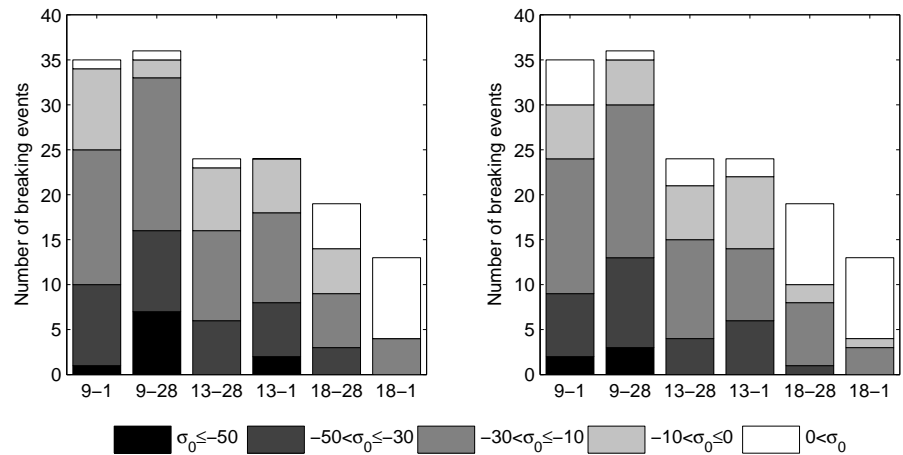


Fig. 5.17: Number of breaking events per run classified by backscattered power. HH (left) VV (right).

5.3.3 Evolution of individual events

The analysis presented thus far, reduces the information of each event to its median and the location of its center of mass. A complementary analysis using the evolution of individual events can lead to improved understanding of the previous results.

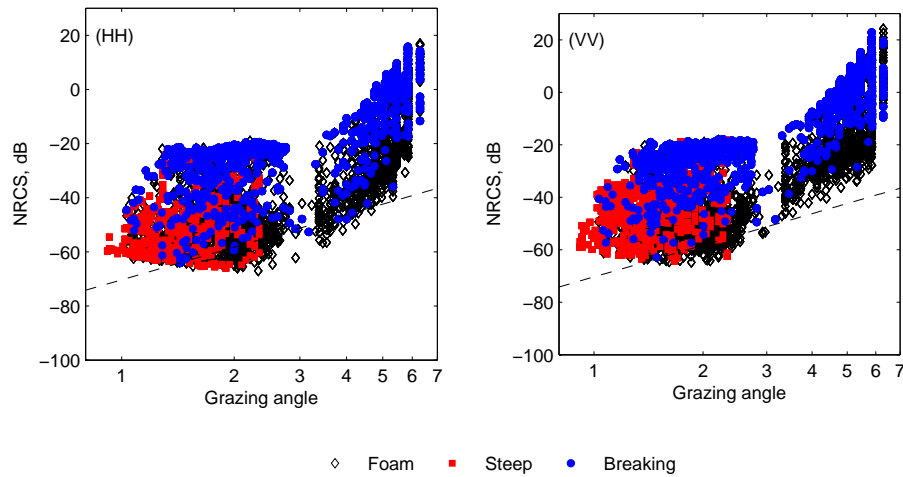


Fig. 5.18: Grazing angle dependency of the median of the backscattered power at each time step and classified by source. Color code correspond to different sources. Dashed line corresponds to θ_g^4 trend. HH (left) VV (right).

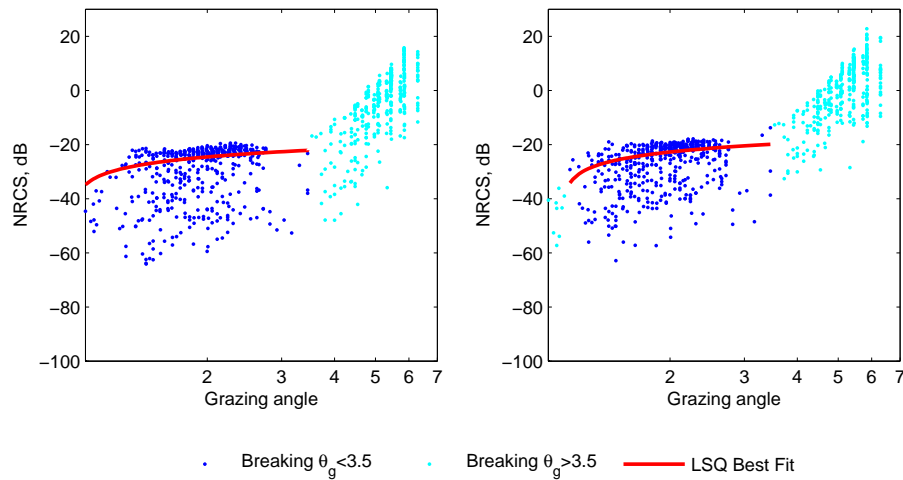


Fig. 5.19: Least-squares fit to the breaking NRCS. HH (left) VV (right).

To this effect, one event per run has been selected. Selection is based on the video data, by following the space-time evolution of the wave front, trying to include active breaking and, if available, a clear signature of the dark fronts. This enables the study of the signal as the wave steepens and breaks. In the following analysis, we focus on two conditions. The first is the high energy wave climate of May-13 (Run 9) which also

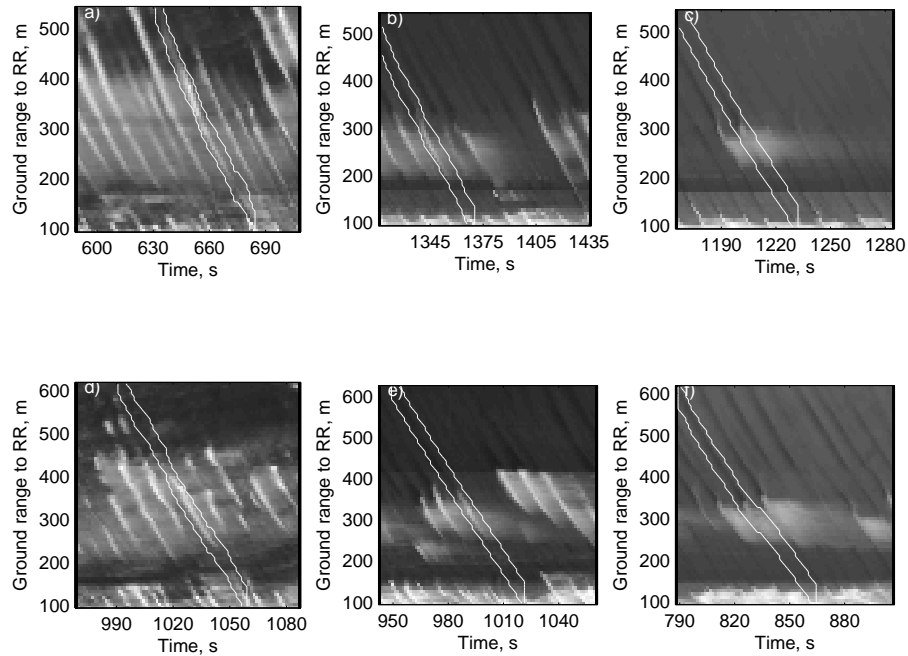


Fig. 5.20: Selected events for study of the evolution of the signals. (a) Run 9-1; (b) Run 13-1; (c) Run 18-1; (d) Run 9-28; (e) Run 13-28; (f) Run 18-28.

exhibit a large amount of remnant foam. The second is the run of May-15, which although showing less contrast between active breaking and relict foam, it has clearer signatures of the (dark) fronts during the unbroken phase of the wave. In order to highlight the effects of looking direction, results at $\phi \approx 1^\circ$ and 28° are presented. Fig. 5.20 shows the selected events overlaid the video signal, where it can be seen that the whole evolution of the wave has been considered. For each case, a range section 52.5 m long (7 RiverRad resolution cells) centered on the wave front has been manually selected at each time step. Thus the signal of remnant foam on the trough of the previous wave is generally not included in the analysis. The exception is Run 9-1, when the breaking detection showed a lag between the video signal and the microwave sensors, in which case the selection ranges were shifted forward relative to the video signal peak. In the following the data including instances below the noise level are presented and the noise levels are included for reference.

Fig. 5.21 shows the spatial profiles of the signals at selected times for the more

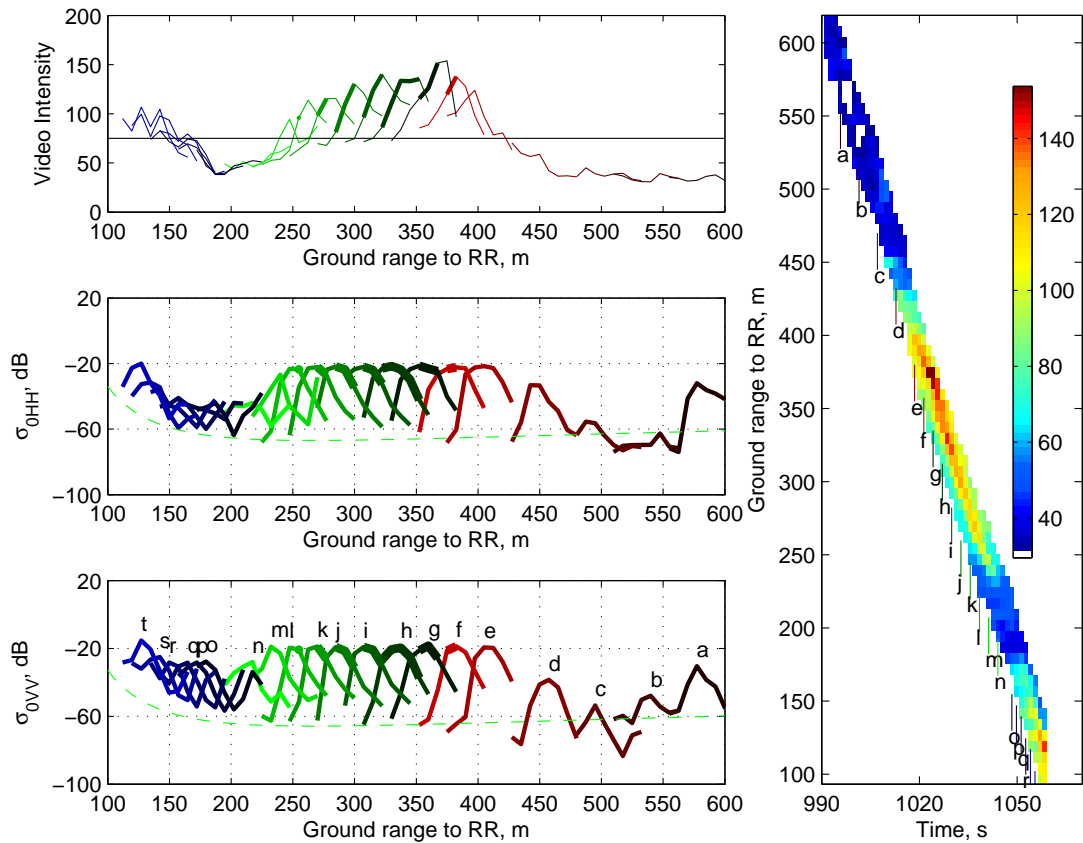


Fig. 5.21: Space-time evolution of a wave under energetic conditions at $\phi \approx 28^\circ$, Run 9-28. (a) Video intensity space profiles at selected time steps; (b) Corresponding HH NRCS (dB); (c) Corresponding VV NRCS (dB); (d) Video timestack of the event, showing occurrence of the profiles. In (a) the horizontal line is the video threshold, I^t . Thicker lines denote sections of the profiles identified as wave breaking. In (b) and (c) Green lines correspond to the noise level (dB). Color scale in the vertical panel corresponds to video pixel intensity.

energetic wave conditions. The profile marked as *a* shows a dark signature in the video data, but strong scattering at both polarizations and also on the marine radar (cf. Fig. 5.6b), suggesting the presence of localized roughness modulated by a steepening wave. However, profiles *b* and *c*, show a sudden drop in the backscattered signal below the noise level at HH, which can be attributed to shadowing caused by the previous breaker. VV shows a slightly larger response possibly due to diffraction effects. The wave continues to evolve and resumes scattering at similar levels (-30 dB) in *d*, confirming that this

correspond to the steepening phase of a wave that was partially shadowed. At e the wave enters the zone of remanent foam from the previous breaker and begins to break, although this particular instance has been identified as foam by the detection algorithm. It can be seen that both polarizations scatter at similar levels (peaking around -20 dB) and the range-dependent shape is similar, although HH shows a broader peak which spans about 30 m at f and decays to 15 m at l . At the same time, the video pixel intensity decays gradually but all these profiles have been classified as breaking events. The last profile above the foam threshold, n , shows a decay of the backscattered power, with VV scattering more strongly. VV keeps scattering stronger than HH for the remainder profiles, which though exceeding the video intensity threshold, have not been classified as breaking events. It must be noted that the effect of antenna gain pattern becomes more pronounced at ranges shorter than $r = 200$ m.

Fig. 5.22 shows the evolution profiles of a wave observed upwave for the same conditions. It can be noticed that, unlike the previous case where the detected breaking signal is forward of the peak of the video intensity on each profile, in this case is shifted backwards. Similarly, the NRCS profiles show breaking being detected at farther ranges than the peak NRCS. This suggests some level of misregistration between sensors, possibly due to finite amplitude misregistration of the video signal. Despite this, the NRCS profiles show similar patterns as those observed at the oblique incidence case, with both polarizations reaching a similar NRCS level throughout the breaking zone (profiles e to k). As before, HH shows broader peaks than VV, although in this case the range extent is reduced in both to about $O(20)$ m, possibly due to the influence of azimuthal angle. For instance, assuming alongshore uniformity of the roller geometry, an oblique look would see the roller as being $1/\cos(\phi)$ times larger at the oblique look than at the upwave look. At the offshore profiles (a through d) both signals scatter less strongly than the breaking events (peaking around -30 dB), but HH has larger returns at the offshore profiles, possibly due to local multipath. This will be discussed in detail below.

Fig. 5.23 shows a similar set of profiles for mid energy conditions and increasing wind

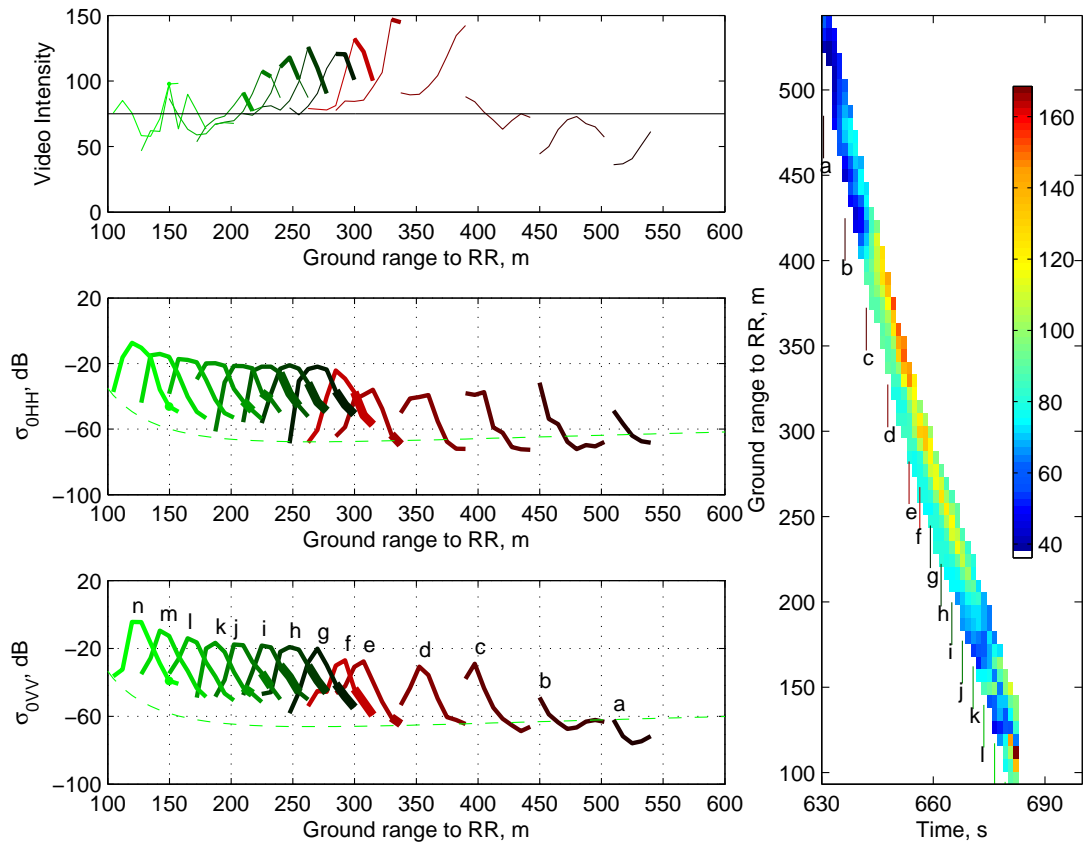


Fig. 5.22: Space-time evolution of a wave under foamy conditions at $\phi \approx 1^\circ$, Run 9-1. Same key as Fig. 5.21.

at $\phi \approx 28^\circ$. Unlike the foamy (high energy) waves, in this case the optical signal shows a clear structure with darker fronts and brighter crests until the onset of breaking, thus steepening waves. It can be seen that during the steepening phase (profiles a through i), VV shows larger returns than HH (typically around 20 dB larger) and the peaks of both align well with the minima in the video signal, thus the steepest section of the wave front. It is noticeable as well that as the nominal grazing angle increases (r decreases) and the wave shoals there is a gradual increase in the maxima of the NRCS which is consistent with scattering in accordance to CST. However, the maxima for these steep waves is at least -10 dB less than the maximum values observed for breaking waves (profile k). The exceptions are profile j (near the onset of breaking) and profile l, which scatter rather

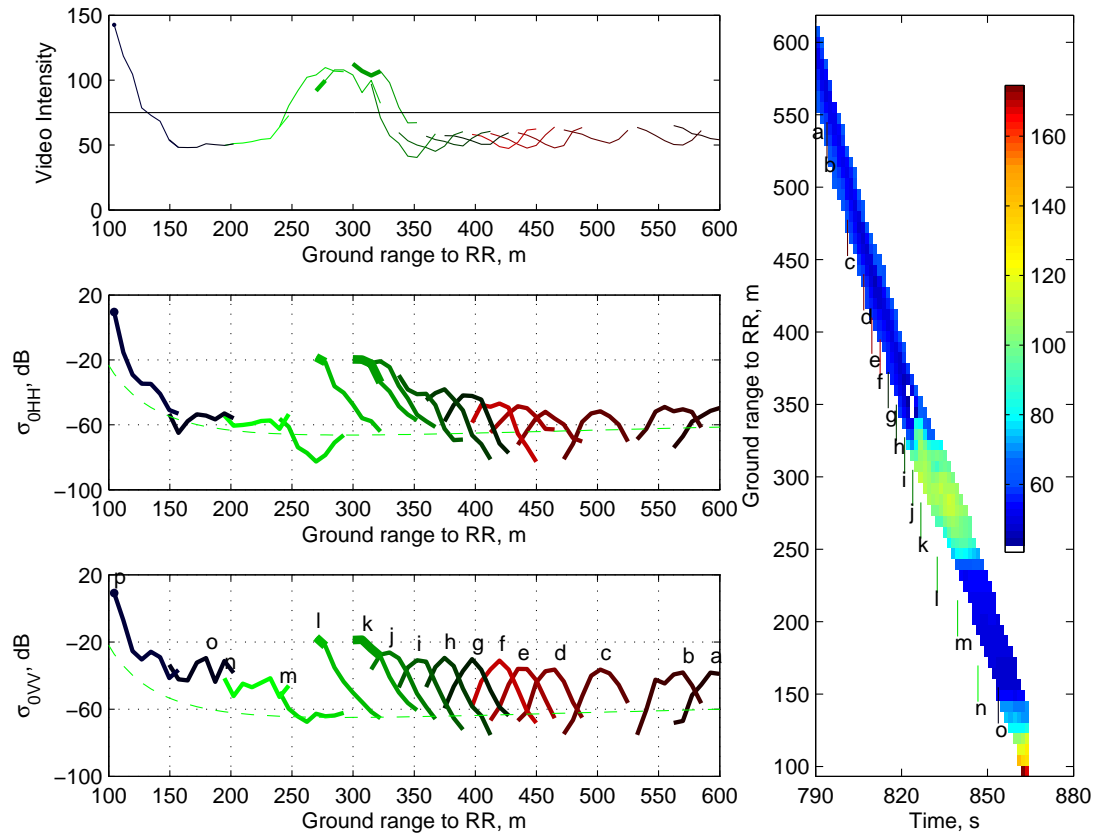


Fig. 5.23: Space-time evolution of a steepening wave at $\phi \approx 28^\circ$, Run 18-28. Same key as Fig. 5.21.

strongly despite not being classified as a breaking event. It is of note that the location of breaking appears to be shifted forward in the intensity signal (e.g. profile *l*) and slightly backwards in the RiverRad data, probably a result of misregistration between the marine radar and the optical signal.

Finally, Fig. 5.24 shows an upwave look for the low energy conditions. Although the evolution is similar to the oblique incidence case, the HH NRCS is significantly less during the steepening phase, barely exceeding the noise level of the sensor. VV in turn show returns that correspond well to the trend observed for the oblique case. Azimuthal dependencies within the frame of Bragg scattering and CST have a clear dependency on look angle, with the signal decreasing in magnitude as the angle increases toward $\phi = 90^\circ$ (*Trizna and Carlson, 1996*, report differences of about 10 dB at X-band, VV).

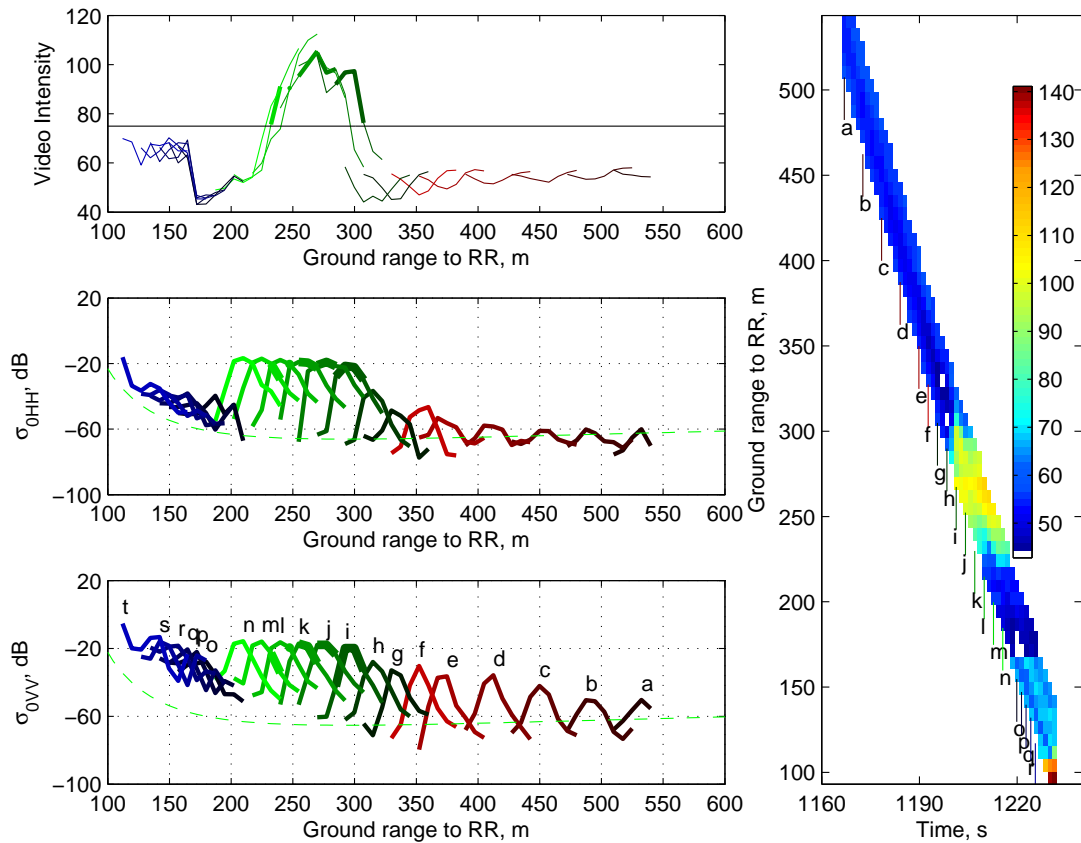


Fig. 5.24: Space-time evolution of a steepening wave at $\phi \approx 1^\circ$, Run 18-1. Same key as Fig. 5.21.

Thus the behavior at both polarizations shown here exhibits the opposite trend; both decrease when looking upwave relative the oblique look. We discuss this in detail in the following section.

On the other hand, these results seem to confirm the hypothesis that the high returns of foam are a result of errors in the detection algorithm, in which case breaking events are misclassified as foam. These events have large video intensities, therefore they must have backscattered returns below the threshold level set for marine radar signal, yet they scatter at high levels in the RiverRad data. This may suggest differences between the observational mechanisms of both microwave sensors. One possibility is the different range resolution between the sensors which would imply slight differences in beam fill-

ing during the stages of breaking, most notably at instances where the radar footprint might not be uniformly covered by scatterers of the same nature. For instance near the wave breaking front or during the onset of breaking. Alternatively, the scattering mechanism, whatever it might be, could show dependencies on electromagnetic frequency, and observation angles (both grazing and azimuthal angle) resulting in slight differences in the NRCS and consequently affecting discrimination. Although both scenarios suggest that these differences should be omnipresent in the data sets, they would be noticeable only when the marine radar is slightly less than the threshold value, thus affecting the discrimination.

Despite the possible inaccuracies in the detection, the results also suggest that active breaking shows a weak inverse dependency on grazing angle, that is, the NRCS weakly increases as the grazing angle decreases. This result is in contradiction with the results of *Farquharson et al.* (2005), who showed excellent correlation between the decay in wave height and the *maximum* bore NRCS as the waves progressed onshore, therefore, increasing grazing angles. Although our results have been presented in terms of the median NRCS, analysis of the maxima of the event shows a similar grazing angle dependency as the median but shifted slightly toward higher NRCS (not shown). Wave conditions in *Farquharson et al.* (2005) were similar to this study, $H_s = 1.22\text{m}$, $T_p=5.22$, but a secondary spectral peak (swell) was present at $T=11.6$ s. System differences between both studies are not significant, with FOPAIR having a higher ground (3 m) and azimuthal resolution (0.5°). These differences would indicate that beam filling could be relevant, although the effect would be the opposite to the one observed, with RiverRad NRCSs being decreased by partial filling due to its larger footprint, thus increasing the dependency on grazing angle. Additionally, the results presented here suggested sustained levels of NRCS for 3 or 4 resolution cells, suggesting that those cells have an uniform distribution of scatterers. A clear explanation of these differences remains elusive.

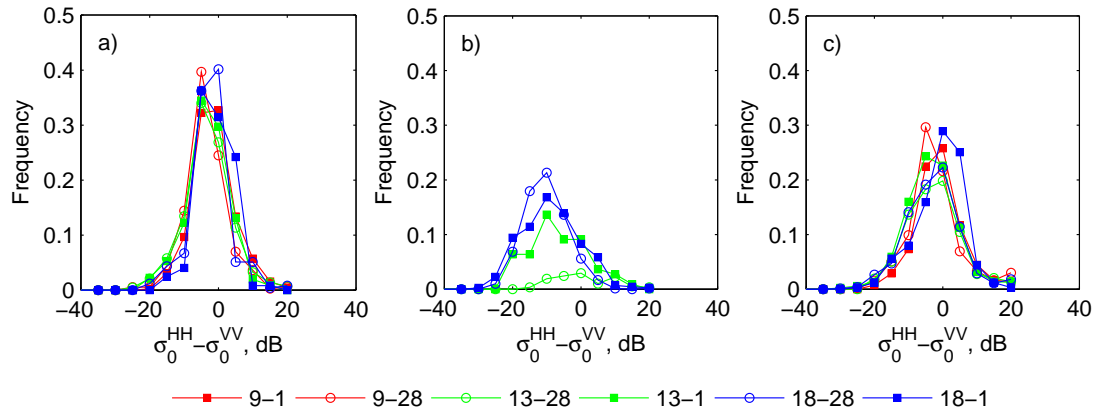


Fig. 5.25: Histograms of the polarization ratio $R = \sigma_{0HH}(\text{dB}) - \sigma_{0VV}(\text{dB})$, classified by scattering source. (a) Breaking waves; (b) Steepening waves; (c) Foam.

5.3.4 Polarization ratios

Polarization ratios are another variable of interest for the analysis of scattering mechanisms and breaking detection. For many of the scattering models, a defined range of values for the polarization ratio $\sigma_{0HH}/\sigma_{0VV}$ can be expected. For instance, values always less than unity (or 0 dB) for CST, and close to unity for specular scattering. Previous research has suggested that scattering from breaking waves yields large polarization ratios (even exceeding unity) (e.g. *Lewis and Olin, 1980; Kwok and Lake, 1984; Trizna et al., 1991; Lee et al., 1995*), and therefore values in this range have been considered as an indication of wave breaking. However, in some cases large polarization ratios have been associated with steep waves as well (*Liu et al., 1998; West and Ja, 2002*). Despite this variability in the observations, some researchers have suggested that polarization ratios can be used as the sole discriminator for breaking waves (*Hwang et al., 2008a*).

In studying the polarization ratio, we follow the same approach as for the backscattered power. First, we analyze the data as classified by source on a pixel by pixel basis to generate histograms of the ratio estimated as $R(\text{dB}) = \sigma_{0HH}(\text{dB}) - \sigma_{0VV}(\text{dB})$. Instances of backscattered power below the noise level were marked as not-a-number but their pixels were counted, thus integration of the histograms does not yield unity. As shown in Fig. 5.25b, steepening waves exhibit a clear increase in the number of events above the

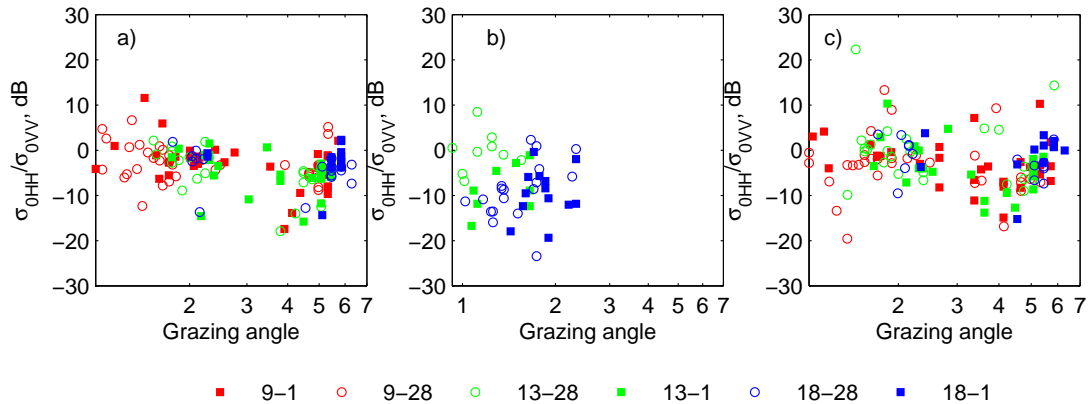


Fig. 5.26: Grazing angle dependency of the polarization ratio R , classified by scattering source. (a) Breaking waves; (b) Steepening waves; (c) Foam.

noise level and a gradual shift of the peak toward smaller ratios as the wave conditions evolved. This reinforces the idea of steepening waves scattering according to CST. There are, however, instances where R exceeds 0 dB.

On the other hand, breaking waves and foam show polarization ratios that are independent of the ambient conditions, as expected due to the negligible dependency shown by the respective backscattered power. The histograms peak around -5 dB whilst still showing a few events at smaller ratios. For all scattering sources, the ratios show bias toward negative values and cover a wide range of NRCS values (spanning about -50 dB).

Fig. 5.26 shows the grazing angle distribution of the median polarization ratio, classified by event and scattering source. It can be seen that for breakers and foam, the ratio shows a significant amount of scatter, with a small bias toward negative values. Despite the scatter there is a weak trend showing an inverse proportionality between median R and grazing angle for all sources. Additionally, steepening waves also show the dependency on environmental parameters with a decrease in R as wind speed increased. For steep waves only events recorded at $\phi \approx 28^\circ$ exceed 0 dB, suggesting some dependency on look angle which may enhance the HH returns, consistent with our previous analysis of the NRCS dependency on looking angle. While the scattering coefficients g_{pp} are modified differently by out of plane tilting (cf. Eq. 2.3), simple Bragg scattering can not

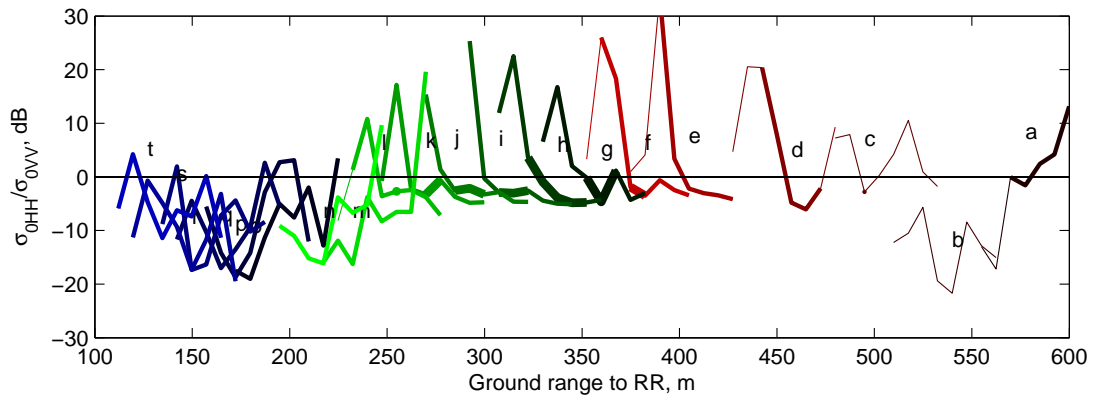


Fig. 5.27: Space-time evolution of the polarization ratio under foamy conditions (Run 9) at $\phi \approx 28^\circ$. Profiles correspond to those defined in Fig. 5.21. Thin, thick and thicker lines are polarization ratios computed with NRCS below and above the noise level; and breaking events, respectively.

account for this increase. Numerical studies of 3D surfaces by *Li and West* (2006) have shown that the polarization ratios can show a complex behavior dependent on both incidence and azimuthal angles. Changes in the illumination pattern and relative positioning of reflection points can induce multipath reflections which can lead to a wide range of polarization ratios if the conditions are appropriate to develop interference patterns. Additionally, for the cases compared, a given range corresponds to a wave closer to shore for $\phi \approx 28^\circ$ than for $\phi \approx 1^\circ$. If the wave has been breaking, a smaller wave height can be thus expected and the relative distance between crests is augmented due to the oblique look. These conditions can lead to a reduction in shadowing at $\phi \approx 28^\circ$ and a potential increase of multipath from small scale steep waves, which could explain the increase in the polarization ratios observed between look directions.

Finally, Fig. 5.27 and Fig. 5.28 show the evolution of the polarization ratio for the profiles shown in Fig. 5.21 and Fig. 5.23, respectively. It can be seen that the polarization ratio of breaking waves tends to show a distinct spatial profile, where it peaks near the front of the wave at large values ($R > 20$ dB) to be followed by a sharp decay to 0 dB, after which it levels off at negative values. The self similarity of the profiles is notable and all the foamy/breaking profiles level off around $R \approx -5$ dB. Furthermore, the sections

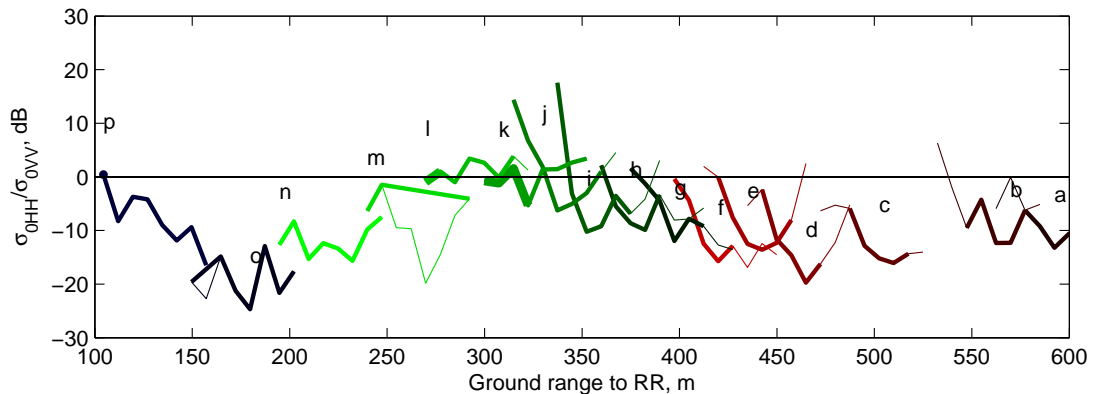


Fig. 5.28: Space-time evolution of the polarization ratio for a steepening wave (Run 18) at $\phi \approx 28^\circ$. Profiles correspond to those defined in Fig. 5.23. Same key as Fig. 5.27.

identified as breaking show polarization ratios close or below 0 dB, during this plateau. A similar situation is shown by the breaking profiles in the steep wave (Fig. 5.28 profile *k* and *l*), which, although they do not exhibit the initial region of large R , do scatter around $R \approx \pm 5$ dB when breaking has been identified.

Non-breaking instances also show this pattern of large polarization ratios decaying over short distances (20-30 m) followed by a steady level. While in many cases the polarization ratio remains below 0 dB (e.g. profiles *d* to *g* in Fig. 5.28), there are some instances that show this pattern offset toward positive R values (e.g. profiles *d* to *f* in Fig. 5.27; *i* and *k* in Fig. 5.28). Most of these correspond to the presence of foam, therefore allowing the possibility of breaking not being properly identified by the algorithm. However, there are other instances that clearly correspond to steepening waves (e.g. Fig. 5.27 profile *a*). Furthermore, a few profiles shoreward of the main event in Fig. 5.27 also show R larger than 0 dB, apparently during the second steepening phase as the wave reforms and reshools after cessation of breaking in the bar trough.

Profiles for the polarization ratio for the cases looking upwave are presented in Fig. 5.29 and Fig. 5.30. Although the presence of the plateau is not as clear as in the oblique cases, the overall structure of the profile of R during breaking is maintained, that is, a sudden increase in R to large values consistent with the profile HH being more broad in

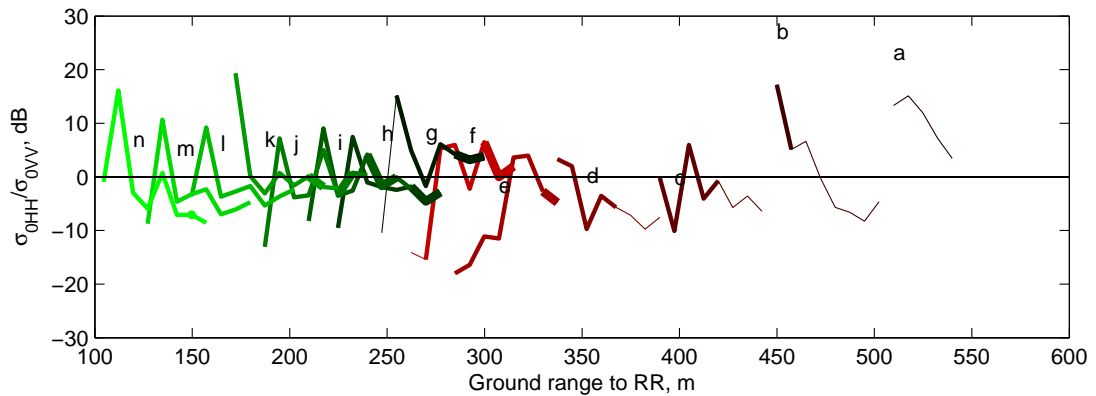


Fig. 5.29: Space-time evolution of the polarization ratio under energetic conditions (Run 9) at $\phi \approx 1^\circ$. Profiles correspond to those defined in Fig. 5.22. Same key as Fig. 5.27.

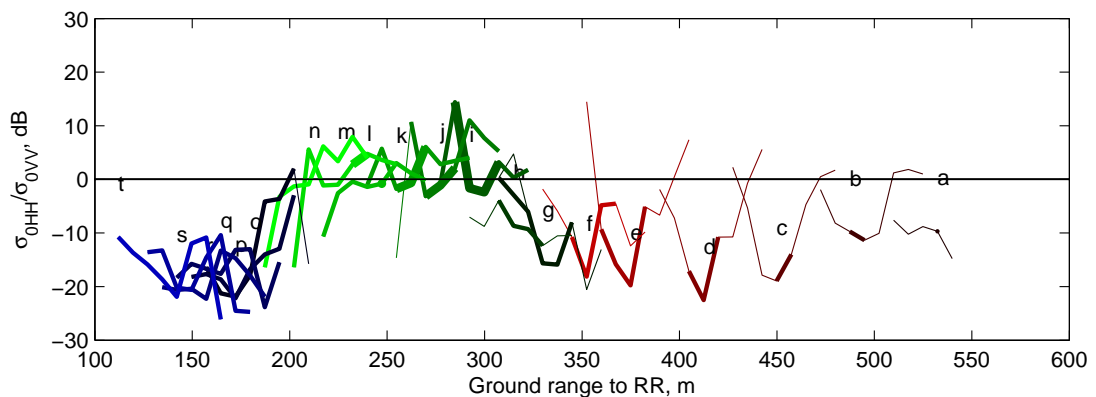


Fig. 5.30: Space-time evolution of the polarization ratio for a steepening wave (run 18) at $\phi \approx 1^\circ$. Profiles correspond to those defined in Fig. 5.24. Same key as Fig. 5.27

range, followed by a section of nearly constant values. Unlike the oblique look, R can exceed 0 dB for breaking waves, but it typically fluctuates near 0 dB. It can be seen as well that the increase in R is always very abrupt, typically changing from very low negative values to large positive ones. This suggests that the increase in the ratio are mostly due to local changes in HH not accompanied by a corresponding increase in VV. A possible situation is the multipath scattering from the bore front, akin to the plume model of *Wetzel* (1986).

Finally, in Fig. 5.29 it can be seen that R has similar profiles throughout the wave evolution, consistent with a wave that breaks almost continuously. Although the video record does not show indications of breaking, analysis of the video full frame showed that these events corresponded to a wave that showed alongshore breaking intermittency. Furthermore, the RiverRad targets were located close to the spreading edge of the broken wave, suggesting a very steep wave, thus potentially leading to multipath returns.

In summary, the polarization ratio is strongly dependent on the phase of the long wave. For the case of breaking waves, it seems that at the toe of the breaker the polarization ratio can reach large positive values. This situation could be explained in terms of multipath scattering from the front of the bore, where HH shows more sensitivity than VV. However, the interference pattern expected between HH and VV is not present, possibly due to VV being affected by damping near the Brewster angle (*Trizna, 1997*). Passage of the bore itself results in both polarizations scattering at similar levels, with VV being slightly larger at oblique incidence and competing magnitudes at normal incidence. These results are consistent with the findings of *Ja et al. (2001)* who found HH scattering more strongly near the front of gently spilling waves due to the presence of a bulge, whereas VV took the upper hand in the back of the wave where persistent roughness and the scar are present (see also *Ericson et al., 1999*).

Steepening waves in turn, generally scatter in accordance with CST, although occasional occurrences of large R do exist possibly due to small scale multipath, both in plane or 3D. In deep water, steep waves have been correlated with the occurrence of sea spikes due to multipath scattering as well. For instance, the results of *Liu et al. (1998)* using a high resolution FOPAIR ($\Delta r = 1.5$ m), showed mean values of $R \approx 5$ dB at various stages of wind seas. In that case it was found that short scale steepening waves were the main source of sea spikes. For the present case, the vertical and horizontal scale of the events (shoaling long gravity waves in the nearshore) and shadowing may suggest that multipath from the front face of the wave and the previous trough is not the main mechanism, in fact it is expected to be rather infrequent. However, shorter waves riding

on top of the long (unbroken) wave could do it locally, thus explaining the occurrence of instances where $R > 0$ dB (*Plant, 1997*).

5.3.5 Doppler spectrum

In addition to the backscattered power at each polarization, the mean Doppler spectra (averaged over the time series), the time series of the Doppler offset and the Doppler bandwidth at each range bin were also recorded. These are relevant quantities in the sense that they could provide a more clear picture with regards to the scattering mechanisms taking place. For instance, if Bragg scattering were to be the only mechanism, the mean Doppler spectra would show a peak at a frequency given by the Bragg resonant condition

$$f_B = \frac{c_B}{\lambda_B} = \frac{2 \sin \theta c_B}{\lambda_0}, \quad (5.3)$$

where f_B , λ_B , c_B are the frequency, wavelength and phase speed of the Bragg waves. The latter is derived from the dispersion relation for water waves in deep water. λ_0 is the wavelength of the EM wave and θ is the incidence angle. Doppler spectra yield a good indication of the modulation of Bragg waves by longer waves, in which case the peak frequency differs from f_B due to the shift in velocity of the Bragg scatterers caused by the long wave surface velocity and/or by surface mean currents. However, in some cases the Doppler spectrum is shifted toward even higher frequencies (thus larger velocities) that correlate well with the phase speed of the underlying long wave (e.g. *Lee et al., 1995; Plant, 1997; Farquharson et al., 2005*), which can not be modeled by traditional CST and has suggested the presence of other scattering mechanisms.

Fig. 5.31 and Fig. 5.32 show the range distribution of the mean Doppler spectrum at each polarization for runs 9-28 and 18-28, respectively. It can be seen that the spectra shows a distinct behavior between ranges where at least one breaking event has been identified (denoted by the vertical white lines) and those where no breaking occurs. For the latter, the spectra are typically concentrated within a narrow range of frequencies around the origin, with a clear bias toward positive frequencies, thus scatterers traveling

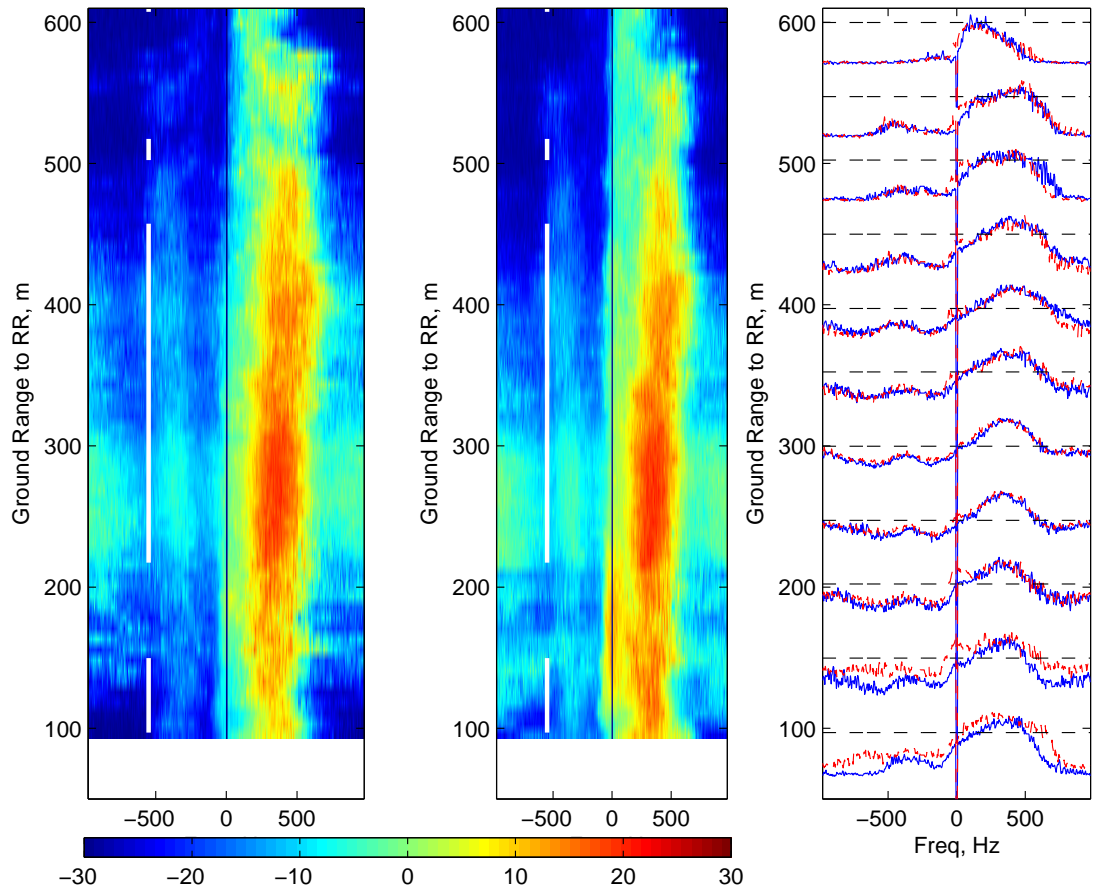


Fig. 5.31: Mean Doppler spectra (dB) of Run 9-28. (a)HH ; (b) VV; (c) Comparison between HH (blue solid) and VV(red dashed) at selected cross-shore locations. White line in (a) denotes radial locations where at least one breaking event was detected.

towards the radar. For non-breaking locations, VV spectra tend to show larger magnitudes although both polarizations peak near the vicinity of the Bragg frequency but without exceeding 0 dB (e.g. Fig. 5.32, $r = 600$ to 400 m). As the waves begin to break, the spectra at both polarizations broaden even in the absence of active breaking, but without increasing significantly their peak frequency and magnitude. As observed by *Lee et al.* (1995), VV appears to retain a local peak at low frequencies, which is significantly weaker in magnitude at HH. (e.g. Fig. 5.31 c) at $r=600$ m and Fig. 5.32 at $r = 350$ m) suggesting that the two polarizations are scattering from different populations of scatterers. Once the wave breaks, the distinction between polarizations becomes

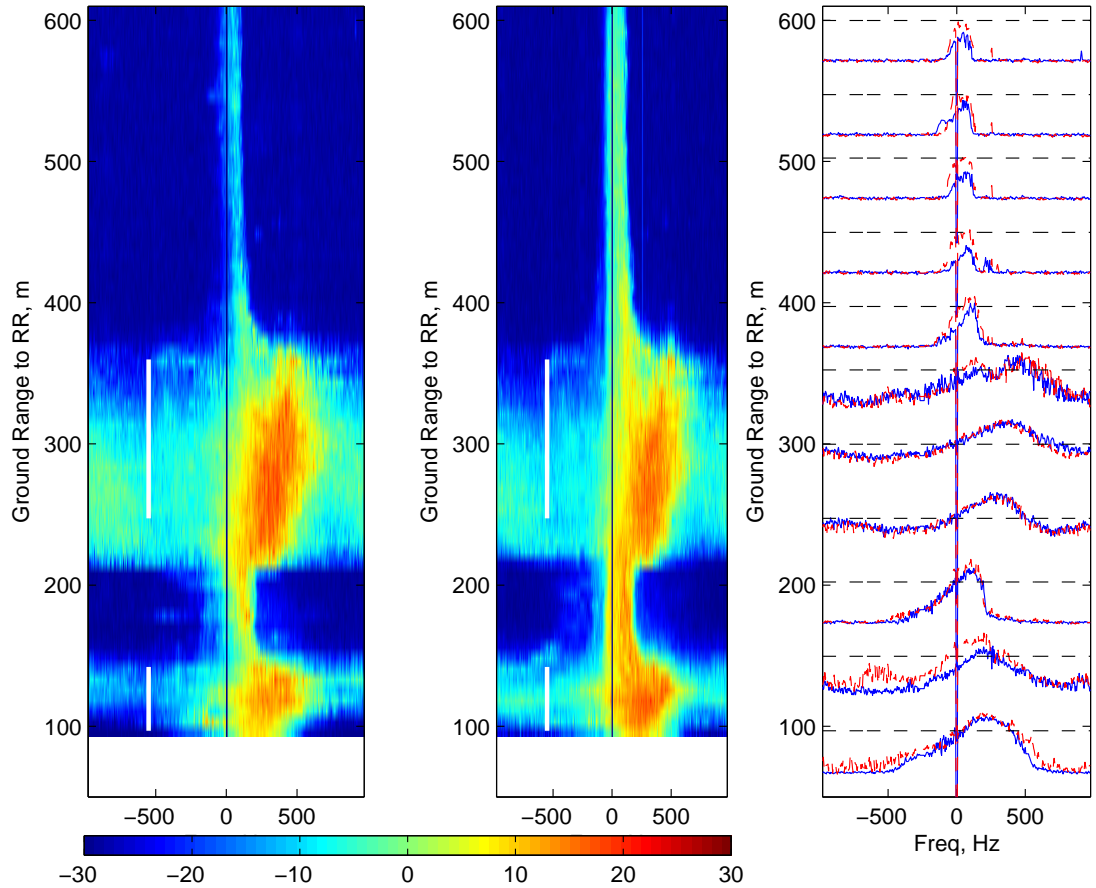


Fig. 5.32: Mean Doppler spectra (dB) of Run 18-28. Same key as Fig. 5.31.

negligible, both spectra become broader peaking at high frequencies, with values exceeding 0 dB. The broadening of the spectrum in conjunction with large NRCS was shown to be a good discriminator of breaking by *Jessup et al.* (1991). A physical explanation is provided by *Coakley et al.* (2001), who found that disturbances on the water surface of the roller can have different lifespans and travel both up and down relative to the carrier wave, with velocity deviations as large as ± 1 m/s. These disturbances were found to scatter energetically, thus resulting in a broad spectrum.

After cessation of breaking at mid ranges, the spectra become narrower again and resume peaking around the Bragg frequency (Fig. 5.32 at $r = 200$ m). Further onshore, the spectral profiles have a more complex structure, where broad peaks at high frequencies

are present but more power is scattered at negative frequencies. When breaking takes place, HH and VV spectra around the "fast" peak are similar in magnitude, but outside this frequency range VV scatters more powerfully, most notably at negative frequencies. It can be noted that this effect is not necessarily related to the presence of remnant foam, which is known to be advected by longshore currents with a surface signature (*Chickadel et al.*, 2003). For instance Fig. 5.32 at $r = 150$ m shows this increase in power at negative frequencies without foam being present. Since the wave is closer to the antenna, the steeper grazing angle means that the back of the waves are more visible and therefore orbital motions can account for the increase response at negative frequencies. However, advection of the Bragg scatterers by the longshore current in a bar-trough system or by wind could also have a similar signature (*Braun et al.*, 2008), or both effects can be taking place simultaneously.

The mean Doppler spectrum, however, is subject to bias in the frequency response by infrequent, but large power, scattering events. A clear example is Fig. 5.32 where the mean spectra seem to be dominated by only three breaking events. An alternative approach is to analyze the space and time evolution of the spectral peak (Doppler offset f_D), although the information at frequencies other than the spectral peak is lost. For simplicity in the analysis, the Doppler offset has been converted to radial surface velocity by (*Plant et al.*, 2005)

$$V = \frac{f_D \lambda_0}{2 \sin \theta}. \quad (5.4)$$

The data are shown in Fig. 5.33 and Fig. 5.34, where active breaking tends to exhibit large velocities that decay as the waves progress onshore. However, not only active breaking waves exhibit this behavior, as shown by the unbroken wave at $r = 200$ m and $t = 1030$ s in Fig. 5.33, which also does not show foam. This particular wave also showed very large NRCS on RiverRad but not in the marine radar (cf. Fig. 5.6). As mentioned before, analysis of the video full frame data suggested that the wave was near its breaking point.

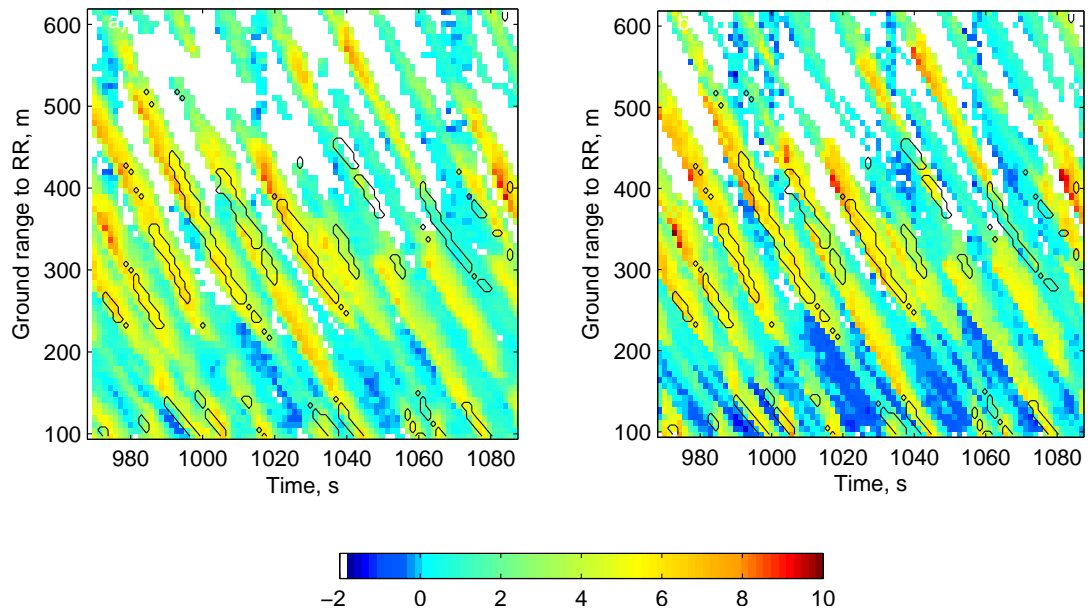


Fig. 5.33: Surface radial velocities (m/s) corresponding to the Doppler offset. Run 9-28. (a) HH ; (b) VV. Contours denote locations identified as breaking.

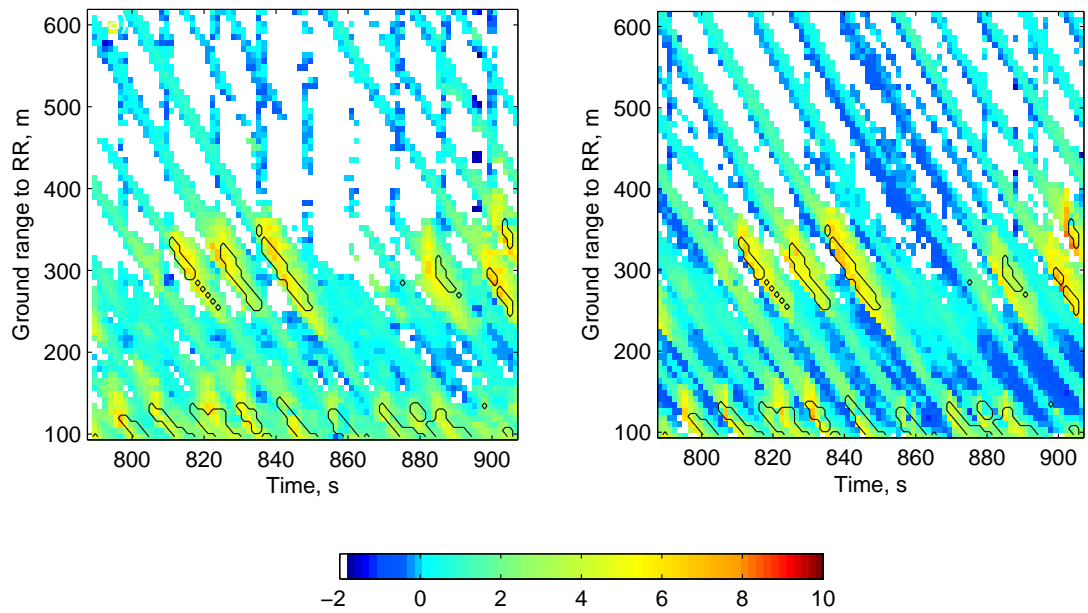


Fig. 5.34: Surface radial velocities (m/s) corresponding to the Doppler offset. Run 18-28. Same key as Fig. 5.33.

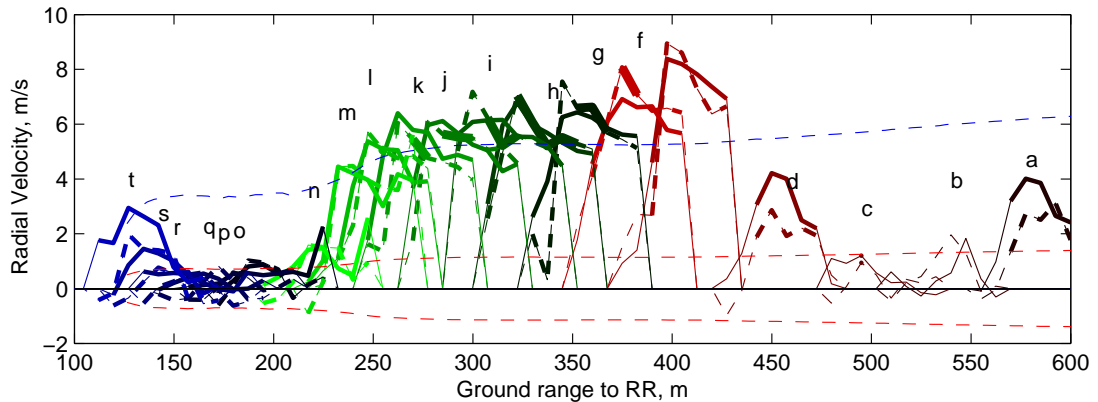


Fig. 5.35: Surface radial velocity profiles for a single wave (Run 9) at $\phi \approx 28^\circ$. HH (Solid lines), VV (dashed lines). Blue and red dashed lines correspond to the linear phase speed and orbital velocity, respectively.

One interesting feature is that the velocity extrema are concentrated near the leading edge of the waves. Behind it the speeds remain large, but less so, suggesting that the scatterers tend to separate or that the roller is expanding.

If the grazing angle becomes steep or the wave height small enough to decrease shadowing, it is possible to observe the velocities at the wave trough. For instance, at ranges closer than $r = 200$ m (steep grazing) for all waves; or at farther range for the low energy waves. As before, VV shows more sensitivity than HH which can be explained according to Bragg scattering and CST and possibly diffraction effects (cf. Fig. 5.34).

Fig. 5.35 and Fig. 5.36 show the evolution profiles of the Doppler offset. It can be seen that for the energetic case (Fig. 5.35), most of the profiles exhibit a wave-like shape in the sense that they are characterized by small, but positive, speeds followed by a sudden increase after which they decay. The rate of decay is more pronounced for the offshore profiles, which also show faster speeds at HH than VV. Near the onset of breaking, the speeds obtained at each polarization are similar in magnitude and show similar profiles. Additionally, the speed has increased significantly to about 8 m/s at $r = 400$ m, a value that appears to be typical at that range for the oblique cases (cf. Fig. 5.33). Peak speeds decay gently during the breaking phase of the wave showing

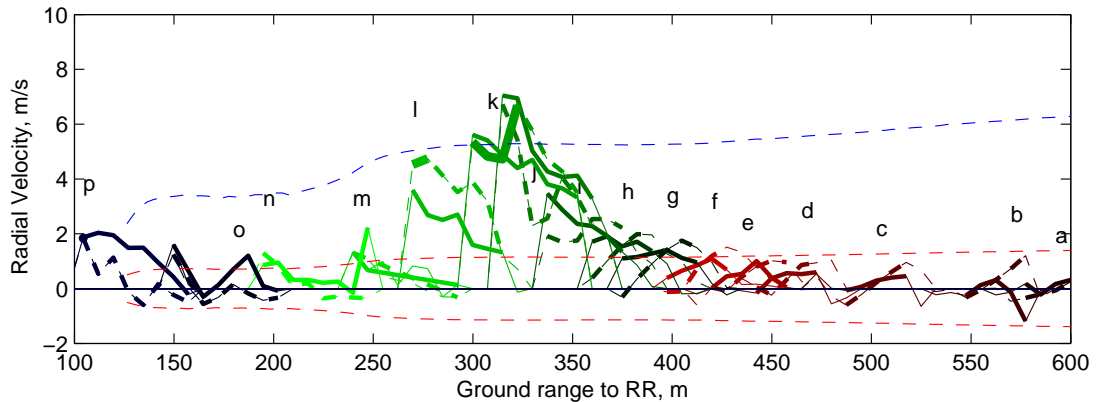


Fig. 5.36: Surface radial velocity profiles for a single wave, at $\phi \approx 28^\circ$, Run 18-28. Same key as Fig. 5.35.

similar profiles, characterized by a sudden increase in speeds followed by a gently fall off, as observed from the timestacks. Once breaking has ceased, peak speeds decay very abruptly at first, only to pick up speed again near the shore once they resume breaking. This suggest scattering from a different population of scatterers during the different phases of the wave.

The steep wave in turn (Fig. 5.36), shows a different pattern, with offshore speeds gradually increasing until the onset of breaking, but with significantly smaller speeds (not exceeding 2 m/s) than those of breaking phase. HH results tend to be more uniform in range than VV, the latter showing a relatively steep increase in magnitude from negative to positive values. Once the wave breaks, the profiles resemble those observed in the previous case and peak speeds are of the same order of magnitude than those of the foamy case.

Fig. 5.37 shows the corresponding velocity profiles for the energetic conditions at $\phi \approx 1^\circ$. As in the oblique looking case, the offshore speeds are relatively large, but slower than those during the breaking phase. However, even though the wave appears to cease breaking, the observed speeds remain high showing no signs of deceleration, although each local profile show similar pattern, with a large peak followed by a gradual decay. The profiles for Run 18-1 resemble those of the oblique cases and are not shown.

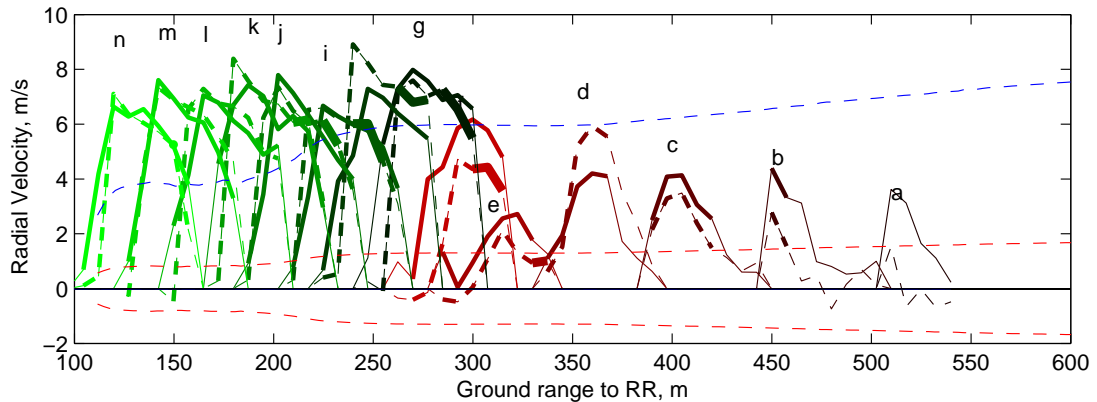


Fig. 5.37: Surface radial velocity profiles for a single wave, at $\phi \approx 1^\circ$, Run 9-1. Same key as Fig. 5.35.

The occurrence of large Doppler speeds have been observed in the field and in the lab, and has been attributed to scatterers being locked to the long wave thus traveling at its phase speed. The results presented here suggest that this might be true for breaking waves only. Although some large speeds were also observed offshore (non-breaking waves) for the more energetic wind conditions, the magnitude was less than that of the breaking waves. Breaking waves show a large peak followed by a gradual decay, suggesting spreading or separation of the scatterers. In the nearshore, *Farquharson et al.* (2005) speculated that these large front velocities are due to the overturning crest of plunging breakers that exceeds the phase speed of the wave. However, it is unlikely that all the breakers remained plunging throughout their breaking lifespan and this situation does not explain the sustained large velocities behind the (possible) plunger. *Fuchs et al.* (1999) in turn found that during the plunging phase, Doppler speeds were of order $0.8c_0$, where c_0 was the linear phase speed of deep water waves. However, during the splashing/ploughing phase, the speed maxima at both HH and VV were near the front of the wave, with values about $1.3c_0$ being typical, and also with large positive polarization ratios. This was correlated to the forward ejection of a body of water by plunging jets. Trailing these jets, the speed was found to decrease gradually to about $0.5c_0$ as the turbulent scar was left behind. Qualitatively, the present results resemble their observations.

In order to compare the obtained velocities with wave related speeds, at least bathymetric data and the wave period are needed. Thus the linear phase speed c and maximum orbital phase speed u_m can be calculated from linear wave theory

$$c = \sqrt{\frac{g}{k} \tanh(kh)} \quad (5.5)$$

$$u_m = \frac{H}{2} \frac{2\pi}{T} \frac{\cosh(kh)}{\sinh(kh)}, \quad (5.6)$$

where h is the local water depth, T is the wave period, k is the long wave wavenumber, H is the wave height which can be approximated by $H = \gamma h, \gamma = 0.42$ in the surf zone (Thornton and Guza (1982)). Although nonlinear effects are important in the surf zone (Catalán and Haller, 2008), we use the linear dispersion model as a first step in the comparison. Similarly, we use only the cross-shore orbital velocity under the assumption that the waves are propagating normal to the shore. Unfortunately, no collection of bathymetric data was performed during the experiment although bathymetry was collected regularly at the FRF in the past. Therefore, bathymetric data from September 21, 2005 is used to provide a best guess estimate of c and u_m . This bathymetry showed nearly alongshore uniform profiles, with an offshore bar near $x = 400$ m in the FRF system (see Fig. 5.38). Since the measurements are expressed in ground range relative to RiverRad, the velocity profiles are adjusted to the same origin and, for the case of oblique looking, the speeds are transformed to a radial component by multiplying them by $\cos \phi$. The results of this exercise are the blue (for c) and red dashed lines ($\pm u_m$) shown in Fig. 5.35 to Fig. 5.37. Despite the crudeness of the assumptions made, the phase speed profiles correlate fairly well with the observed Doppler speeds for breaking waves, with the exception of the onshore profiles for Run 9-1. On the other hand, close to the shoreline where shadowing has been reduced and waves are not breaking, the extrema of the observed velocities correlate very well with the orbital velocities (e.g. Fig. 5.35, $r < 250$ m). For offshore non-breaking waves, however, only the non foamy runs show good agreement

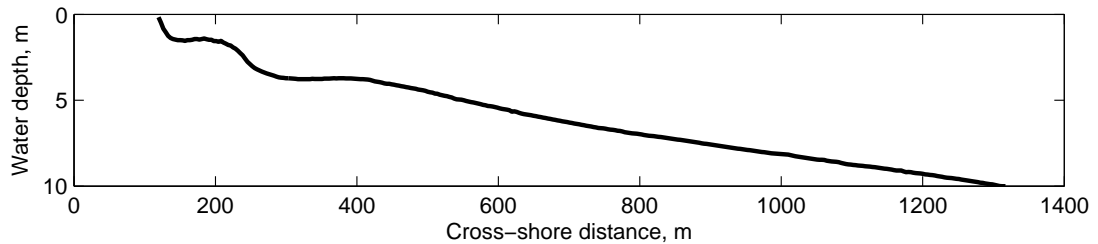


Fig. 5.38: Mean cross-shore bathymetric profile, Sept. 21, 2005.

(Fig. 5.36). Both the upwave and oblique looks for the foamy case show velocities that exceed the orbital speed yet do not reach the phase speed of the carrier wave. It must be noted that for this condition, strong wind velocities at oblique angles were recorded, which may induce surface currents that have not been accounted for in the analysis (e.g. *Braun et al.*, 2008).

5.4 Summary

In this chapter the backscatter associated to breaking, non-breaking and foam events in the surf zone has been presented and characterized, with a special emphasis on the signal arising from breaking waves. It was found that

- Active breaking events show similar scattering levels at both polarizations, typically scattering around -20 dB with a weak dependency on grazing angle.
- For these events, HH shows a broader response than VV, typically raising its backscattering levels near the front of the breaking waves. This has been explained in terms of multipath scattering near the roller front.
- Foam can be the source of relatively strong scattering, although not as strong as active breaking. Events showing strong scattering from foam in the statistical analysis could be related to breaking events that have not been identified as such by the detection algorithm used.
- Steepening waves scatter in accordance with the modulation of Bragg scatterers by

long waves, with peak VV values typically larger than HH. Peak values, however, are typically -20 dB or more smaller than those of active breaking waves.

- Polarization ratios show a weak differentiation between breaking and non-breaking waves. However, it was found that it is not possible to use the polarization ratio as a discriminator, as all the sources considered showed instances of $R \geq 0$ dB.
- Doppler spectra of breaking waves show a distinct broadening, most notably when breaking waves are present, consistent with a population of scatterers traveling at different speeds around the phase speed of the underlying long wave.
- Velocities derived from Doppler offsets show good correlation with the phase speed of breaking waves and the long wave orbital speed for non-breaking waves.
- The velocity distribution of a breaking wave shows to be non uniform, as it can be characterized in terms of ejection of scatterers near the wave front due to splashing/ploughing. Trailing this, velocities remain uniform to gently decay to lower values.

While most of these observations are consistent in one way or another with prior research at low grazing angles, perhaps the most outstanding result is that observed for the scattering of the active breaking portion of the wave, where both polarizations present sustained levels of large and nearly identical scattered power for distances exceeding 15 m in range. Furthermore, these levels appear to be independent of the ambient conditions, yet they show a weak dependency on grazing angle. These results are not consistent with Bragg scattering based on the large polarization ratio observed. Additionally, multipath effects behind the bore front are likely to be averaged out due to the random nature of the surface of the wave roller and the interference patterns typical of multipath scattering. Bound waves and increased surface roughness are typically well correlated with the broadening of the Doppler spectrum and the presence of scatterers traveling near the phase speed of the long wave, but are not capable to provide large polarization ratios. Plume models such as that of *Wetzel* (1990a) have been shown to

predict decaying NRCS which although well correlated with wave height decay, are not consistent with the present data set. The remaining possibility from traditional models is that of specular scattering, in which case surface roughness could present facets whose orientation induces nearly normal incidence for the incoming radiation. As shown by *Lee et al.* (1995), a collection of such facets covering a small fractional area could account for large NRCS at both polarizations. However, to sustain similar NRCS levels regardless of the wave conditions and yet showing a weak grazing angle dependency would require that the fractional facet coverage remains constant at similar ranges, independent of the wave conditions. Therefore, it seems that another scattering mechanism could be present to complement these.

6. A MODEL FOR MICROWAVE SCATTERING FROM BREAKING WAVES

6.1 Introduction

A significant amount of research has been devoted of explaining the so called anomalies present at low grazing angles, which have been usually attributed to the scattering from breaking waves. These include large backscattered power, large polarization ratios and a broad Doppler spectrum peaking at frequencies that match well those of the phase velocity of the carrier wave. The levels of success of the models vary and in most cases they can explain some, but not all, of these characteristics. As a result it can be said that the nature of the scattering mechanisms is still not fully understood. The problem might be exacerbated in the surf zone where the spatial scales of breaking waves are significantly larger and breaking is more frequent and persistent than for the case of deep water waves, for which most of these models have been devised. In addition, one interesting aspect from most of the formulations is the fact that the surface roughness of the roller and its multi-phase nature have been omitted. It is of interest to study to what extent inclusion of some of these characteristics would improve the modeling, and therefore our understanding, of the scattering from breaking waves.

6.2 Conceptual scattering model for the wave roller

Part of the problem in characterizing the scattering mechanisms lies in the complex morphological structure present during the wave breaking process, where the roller surface becomes highly irregular, with multiple length scales coexisting each with different lifespans. Furthermore, the roller cannot be treated as a monophasic medium, as air and water are mixed continuously. Air is trapped during the plunging phase of the wave, and the resulting cavity breaks up into multiple bubbles of varying size which can later evolve

into smaller scales due to degassing, diffusion and dissolution (*Deane, 1997*). Air entrainment due to deep water breaking waves creates bubbles that are typically less than $600 \mu\text{m}$ (0.06 cm) in diameter (*Vagle and Farmer, 1998; Terrill and Melville, 2000*). Studies conducted in the surf zone found that extreme bubble diameter values up to 2 cm could be present, but median values were typically of order 0.01 cm (*Deane and Stokes, 1999; Mori et al., 2007*). Most of these measurements are made below the trough level and it remains unclear whether these bubble values are also characteristic for the roller, although *Chanson (2004)* reports bubble sizes of up to 2.0 cm (median $0.3\text{-}0.6 \text{ cm}$) for small scale laboratory experiments of a dam break wave.

Spray is also generated due to several processes during wave breaking. For instance, *Raizer (2007)* reports that bubble bursting can generate droplets of size $d \approx O(10)\mu\text{m}$ due to thinning of the bubble film, or up to $d \approx O(3-20)\mu\text{m}$ if the generation mechanism is the rupture of the water column resulting from bubble bursting (*Andreas et al., 1995*). In contrast, mechanical tearing of the wave crest due to wind can generate spray of sizes up to $200 \mu\text{m}$ (*Raizer, 2007*). While relevant for sea spray generation in deep water and their implication on air-sea transfer of heat and moisture, these mechanisms can not explain the occurrence of large droplets resulting from large scale breaking typical of the nearshore. For instance, in Fig. 6.1 it can be seen that multiple droplets of relatively large diameter are ejected from a surf zone breaking wave due to splashing and turbulence. To the best of our knowledge, measurements of the size and distribution of these droplets in the surf zone are not available, although *Chanson (2004)* reports droplets sizes of up to 3.0 cm (median $0.3\text{-}0.6 \text{ cm}$), thus comparable to the bubble sizes, for their small scale experiments.

Additionally, bubble structures and foam can become independent of the roller, for instance being injected below the trough level and resurfacing at the back of the wave. Regarding the structure of the roller, only *Coakley et al. (2001)* have studied it for steady breakers with a focus on microwave sensing. Their data suggests that the breaking roller can be considered (on average) as a layered medium where the volume fraction of water

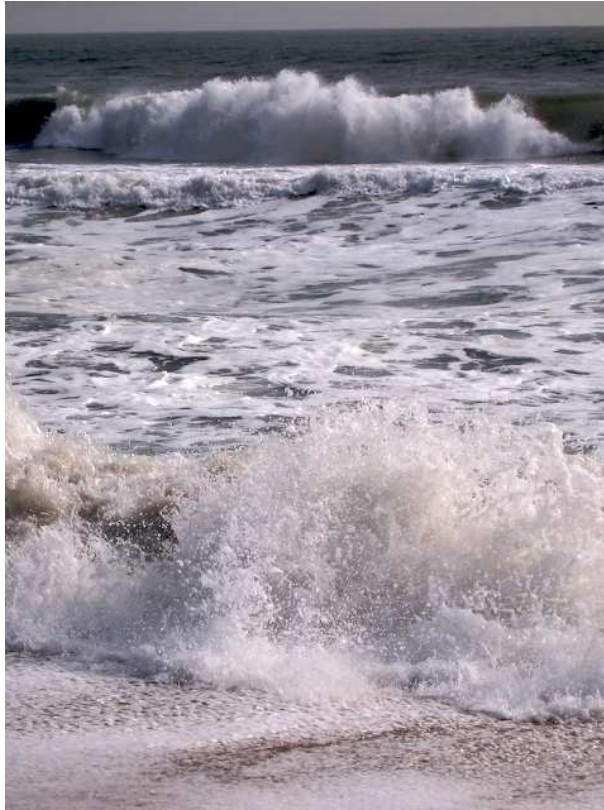


Fig. 6.1: Droplets generated by a surf zone breaking wave.

increases gradually with depth, where it was found that the 50% contour correlated well with the optical signature of the free surface. This suggests that a non negligible volume where the main medium is air can exist above the main surface. However, a detailed characterization of the morphology of the upper layers is not available because it was found that multiple length scales coexist without a clearly defined structure. At the same time, it was observed that droplets were ejected continuously from the roller. Similar stratification results were found by *Blenkinsopp and Chaplin (2007)* for plunging breakers, where the initial spray resulting from splashing of the initial jet can lead to a relative large volume above the 50% contour. Normalized results for spilling breakers showed similar results thus a weak dependency on the breaking regime. Individual droplets typically reached up to $1.2H_b$, H_b the breaking wave height, but occasionally were as high as $5H_b$.

These measurements suggest that the roller can be considered as a two phase flow

where bubbles and spray (droplets) coexist. Additionally, sea water is a lossy electromagnetic medium from which bubbles and foam induce high absorption therefore high thermal emissions. Previous studies suggest that, for foam and bubbles, absorption is the dominant process but scattering is relatively weak (*Chen et al.*, 2003b; *Anguelova*, 2008), thus explaining prior results in the surf zone such as those of *Haller and Lyzenga* (2003). For instance, *Chen et al.* (2003b) report that scattering contributes to at most 4% of the total extinction (hence small reflectivity) of foam for 0.1 cm particles at X-band, and decreases as d decreases. Therefore, microwave scattering from foam is usually measured passively and volumetric models are often called upon using effective permittivities to account for the vertical structure of foam (e.g. *Raizer*, 2007; *Sharkov*, 2007; *Anguelova*, 2008). On the other hand, water droplets can show both high absorption and high scattering, depending on the relative particle size (*Oguchi*, 1983). Furthermore, a handful of active sensing microwave studies have shown that droplets can have a relatively large impact on the measured cross sections. For instance, *Kalmykov et al.* (1976) used precipitation rates of 1000 mm/h to describe the measured cross sections of waves breaking over a submerged breakwater. It is possible that the assumption of independent scattering in the Rayleigh regime (to be defined later), with small particle sizes ($0.05 \leq d \leq 0.5$ cm, where absorption might be relevant), was not appropriate thus it needed to be compensated by such a large precipitation rate. As mentioned in Chapter 2, *Lewis and Olin* (1980) briefly commented that droplets could account for the measured cross sections, but without delving into the possible scattering mechanisms. *Plant* (2003a) used a correction term based on Rayleigh scattering from a low concentration of droplets to improve the agreement with data at low grazing angles. Volumetric scattering coupled with the radiative transfer theory was used by *Huang and Jin* (1995) to model the effect of discrete droplets over the rough scattering from the ocean surface. The scatterers were considered to be of millimeter size and scattering in the Rayleigh regime. The method was in relatively good agreement with observed data, when applied to unbroken surfaces.

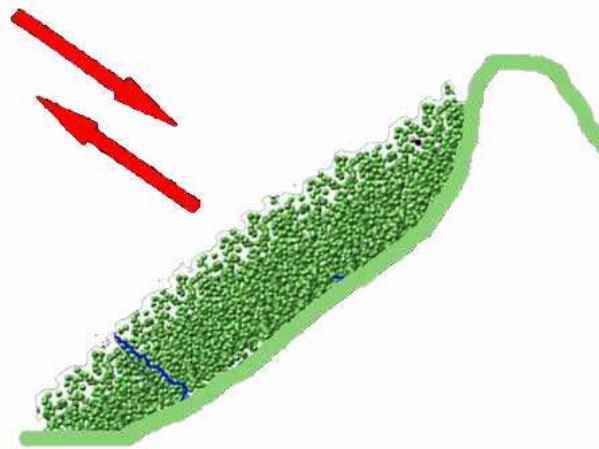


Fig. 6.2: Conceptual roller model, where the scatterers are water droplets traveling with the underlying wave.

Therefore, for the present study the contribution of bubbles to the cross section is discarded based on its absorptive nature. The roller is modeled as a single layer where the main scatterers are water droplets embedded in air, as shown in Fig. 6.2 and Fig. 6.3. The model is intended to describe the upper layers of the wave roller, which typically show low water volume fractions (*Coakley et al.*, 2001; *Blenkinsopp and Chaplin*, 2007). Although these studies show stratification of the roller, as a first step in the modeling a single layer is considered to highlight the capabilities of the approach. However, it is possible to include stratification through the use of additional layers (e.g. *Zuniga et al.*, 1979; *Liang et al.*, 2008). This single layer has a definite bottom boundary, corresponding to the underlying sea water surface. In addition, this boundary is considered to be devoid of roughness; although, it is possible to incorporate a measure of roughness as shown by *Huang and Jin* (1995) and *Liang et al.* (2008). The upper boundary separates the droplets layer from the air. The roller is assumed to travel with the underlying water wave, as originally proposed by *Svendsen* (1984), but the particles are considered to remain stationary relative to the roller.

This conceptual model for the roller morphology needs to be coupled to an appropriate scattering model. The latter follows largely the state-of-the-art models used for

microwave sensing of tenuous particles such as snow (*Tsang et al.*, 2007; *Tse et al.*, 2007; *Liang et al.*, 2008). The common characteristic is the assumption that the main scattering medium is a layer of densely packed scatterers, although layering can also be included. Electromagnetic interactions within the layer and with the layer boundaries account for scattering of the incident radiation in multiple directions.

While more detailed descriptions can be found in the literature, the basic ideas associated with electromagnetic scattering from individual and multiple particles are presented in the following sections for completeness. Introduction of the dense media radiative transfer (DMRT) theory provides the fundamental equations to be used in the model. Next, in order to make the equations more tractable, the concept of the quasi-crystalline approximation (QCA) is introduced, which completes the set of equations needed to calculate the scattered fields. Physical considerations regarding the nature of the scatterers in the wave roller are presented next, followed by the model results and comparison against field data.

6.3 EM model formulation

6.3.1 Basic scattering concepts

An electromagnetic wave traveling in direction \hat{k}_i has electric and electromagnetic fields given by

$$\vec{E} = E_o e^{-ik\hat{k}_i \cdot \vec{r}} \hat{e}_i, \quad (6.1a)$$

$$\vec{H} = \frac{1}{\eta} \hat{k}_i \times \vec{E}, \quad (6.1b)$$

where \vec{r} is the position in a suitable coordinate system, k is the electromagnetic wavenumber and \hat{e}_i is a direction orthogonal to \hat{k}_i . $\eta = \sqrt{\mu\epsilon^{-1}}$ is the medium impedance, where ϵ and μ are the medium electric permittivity and magnetic permeability. For non magnetic materials, μ can be considered equal to that of free space therefore the relevant quantity becomes ϵ , usually expressed as relative to the free space value $\epsilon_r = \epsilon\epsilon_0^{-1}$. In Eq. 6.1

the harmonic time variations have been suppressed for simplicity. If these fields impinge upon a particle, they will generate scattered fields

$$\vec{E}_s \propto f(\hat{k}_s, \hat{k}_i) E_o \hat{e}_s, \quad (6.2)$$

where f is the *scattering amplitude* from direction \hat{k}_i into direction \hat{k}_s , thus describing the redistribution of E_o due to scattering. It can be shown that the ratio between the scattered power per unit area dP_s and the incident power P_i is (*Tsang et al.*, 2000b)

$$\frac{dP_s}{P_i} = |f|^2 d\Omega_s, \quad (6.3)$$

where $d\Omega_s$ is a differential of solid angle. The total scattered power can be defined in terms of the *scattering cross section* σ_s as

$$P_s = \sigma_s P_i, \quad (6.4a)$$

$$\sigma_s = \int_{4\pi} |f|^2 d\Omega_s, \quad (6.4b)$$

where it can be noted that the transmitter and receiver characteristics such as gain patterns have not been included. Their inclusion leads to the traditional form of the radar equation (cf. Eq. 3.2). Therefore, the scattering problem consists of finding a suitable description for σ_s . For instance, if the field is polarized, the scattering amplitude needs to be expanded into a *scattering amplitude matrix* to account for cross polarization interactions. Additionally, rather than working with the EM fields, it is preferred to use the Stokes parameters, defined in terms of the magnitude of the power flow per unit area

$$I_v = \frac{|E_v|^2}{\eta}, \quad (6.5a)$$

$$I_h = \frac{|E_h|^2}{\eta}, \quad (6.5b)$$

$$U = \frac{2}{\eta} \text{Re}(E_v E_h^*), \quad (6.5c)$$

$$V = \frac{2}{\eta} \text{Im}(E_v E_h^*), \quad (6.5d)$$

$$\bar{I} = [I_v, I_h, U, V]^T. \quad (6.6)$$

where T indicates the transpose. Just as in the case of scattering of a wave by a particle for which the scattering amplitude was defined, we can define a new quantity describing the relation of the incident wave Stokes parameters with those of the scattered wave

$$\bar{I}_s = V_o \mathbf{P}(\hat{k}_s, \hat{k}_i) \bar{I}_i, \quad (6.7)$$

where \mathbf{P} is the *phase matrix* describing the polarimetric scattering cross section per unit volume, and V_o is the appropriate volume. The mathematical description of the phase matrix has been a subject of significant research, and its formulation depends upon some approximations which will be reviewed in detail in § 6.3.4.

6.3.2 Dense Media Radiative Transfer Theory

If the scattering volume consists of a large number of particles, several approaches can be followed to estimate the scattered fields. For instance, direct numerical simulations can be used to solve the Maxwell equations within the volume using finite difference time domain calculations (FDTD) (e.g. *Zurk et al.*, 2007). Monte Carlo based simulations in which the particle positioning is varied from run to run are also possible but simulations are typically limited to a few thousand particles (*Zurk et al.*, 1995; *Ding et al.*, 2001; *Chen et al.*, 2003a). Both methods are still computationally intensive. A less demanding approach is to use simplified formulations and approximations for some of the relevant parameters.

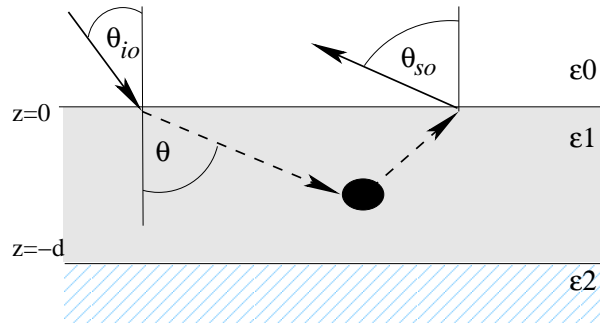


Fig. 6.3: Schematic of scattering from a layer. Azimuthal angles are measured in the plane perpendicular to the figure (not shown).

For instance, the radiative transfer (RT) theory is an integro-differential formulation that deals with the transport of energy through a medium consisting of random discrete scatterers without the mathematical rigor of a proper wave propagation theory. The model is conceptually simple, and allows inclusion of complex phenomena such as dense media involving multiple scatterer species, layered media, and rough boundaries. Within this medium, discrete particles scatter and absorb the incident energy, thus potentially affecting its propagation through the medium. The energy eventually reaches a boundary or interface from which it is reflected back and/or transmitted to the following layer, if any. Fields exiting the layered media can reach the receiver and scattered quantities can be estimated.

Fig. 6.3 depicts some of the angular coordinates relevant for this problem. θ_{0i} is the incident angle on air, which is refracted to θ_i inside the layer. A particle at a depth z will scatter energy in 4π directions defined by the angles θ_s (vertical) and ϕ_s (azimuthal). Exiting energy will be refracted back to the air in directions θ_{0s} , ϕ_{0s} . For the backscattering problem, the relevant directions are $\theta_{0s} = -\theta_{0i}$ and $\phi_{0s} = \pi - \phi_{0i}$, where $\phi_{0i} = 0$ is assumed for simplicity.

The quantity of interest is the transport of the intensity, which is a function of the position and propagation direction $I(\vec{r}, \hat{k}_i)$. The transport equation is

$$\frac{dI(z, \theta, \phi)}{d\tau} = -\kappa_e I(z, \theta, \phi) + \int_0^{\pi/2} \left(\sin \theta' \int_0^{2\pi} \mathbf{P}(\theta, \phi, \theta', \phi') I(z, \theta, \phi) d\phi' \right) d\theta' + \mathbf{S}, \quad (6.8)$$

which accounts for the variation of the intensity as it propagates through the medium in the direction defined by $\tau = z(\cos \theta)^{-1}$. The three main constituents in the formulation of the RT equation are present in Eq. 6.8. First, the extinction matrix κ_e , which accounts for the attenuation of the incident intensity I due to scattering and absorption. Second, the phase matrix \mathbf{P} , which accounts for the intensity redistribution between the two directions (θ, ϕ) and (θ', ϕ') due to scattering; and finally, a source vector \mathbf{S} (*Tsang et al.*, 2000b). The latter is relevant for passive sensing but it can be neglected for active sensing applications.

Let us consider a single horizontal layer of thickness d within which a number of scatterers (of relative permittivity ϵ_1) are positioned randomly (see Fig. 6.3). Above the layer the medium is air (permittivity ϵ_0) and below a medium of permittivity ϵ_2 . Therefore, the layer has two boundaries on which reflection and transmission of I can occur. In consequence, within the layer, both upward and downward traveling intensities can coexist and interact and Eq. 6.8 can be rewritten as (*Tsang et al.*, 2007)

$$\cos \theta \frac{dI_u}{dz} = -\kappa_e I_u + \int_0^{\pi/2} \int_0^{2\pi} \sin \theta' \mathbf{P}_{uu} I'_u d\phi' d\theta' + \int_0^{\pi/2} \int_0^{2\pi} \sin \theta' \mathbf{P}_{ud} I'_d d\phi' d\theta' \quad (6.9a)$$

$$-\cos \theta \frac{dI_d}{dz} = -\kappa_e I_d + \int_0^{\pi/2} \int_0^{2\pi} \sin \theta' \mathbf{P}_{dd} I'_d d\phi' d\theta' + \int_0^{\pi/2} \int_0^{2\pi} \sin \theta' \mathbf{P}_{du} I'_u d\phi' d\theta' \quad (6.9b)$$

where the subscripts u and d denote upward and downward traveling waves, respectively. It can be seen that the system is coupled in the sense that upward traveling intensities can scatter in the direction of downward traveling intensities and vice-versa. At the upper (air-medium) interface ($z = 0$) the incident intensity is refracted and transmitted into the domain, and the upward intensity is reflected back into the domain

$$I_d(z = 0) = R_{10} I_u(z = 0) + T_{01} I_0 \delta(\cos \theta_0 - \cos \theta_{0i}) \delta(\phi_0 - \phi_{0i}), \quad (6.10)$$

where the subscript 0 corresponds to quantities defined in the air region and the subscript i to incident quantities, which are defined in both the air and the medium. R and T are the corresponding components of the reflectivity and transmission matrices, as given in Eqs. A9 and A10 of *Wen et al.* (1990). The Dirac δ indicate that transmission of the incident intensity occurs only at angles aligned with the refracted angles. θ_0 is related to the angle in the medium by Snell's law

$$n_0 \sin \theta_{0i} = n_1 \sin \theta_i, \quad (6.11)$$

where n is the refractive index $n = \sqrt{\mu_r \epsilon_r}$.

At the bottom boundary, for the single layer case only the reflected intensity is of interest

$$I_d(z = 0) = R_{12} I_d(z = -d). \quad (6.12)$$

The solution for I_u and I_d remains implicit and coupled (cf. Eq. 6.9). One approach to solve the problem is to decompose each intensity into diffuse and reduced intensities (*Ishimaru, 1978; Tsang et al., 2000b*). The reduced intensities refer to intensities traveling in the incident direction (θ_i, ϕ_i) which are reduced due to absorption and scattering. The diffuse intensities in turn correspond to intensities scattered in all directions. While a rigorous treatment of the problem is presented in the cited references, it can be said that the procedure involves treating the integrals in Eq. 6.9 as unknown source terms. Integration of the equations between $z = -d$ and an arbitrary level $z = z$ and use of the boundary conditions yields a solution of the form

$$I_\alpha = I_\alpha^{(0)} + I_\alpha^{(D)}, \quad (6.13)$$

where α denotes upward or downward intensities, and $I_\alpha^{(0)}, I_\alpha^{(D)}$ are the reduced and diffuse intensity. It can be shown that the solution for the reduced intensity is (*Tsang et al., 2000b, 2007*)

$$I_u^{(0)} = R_{12} \left[\mathbf{I} - R_{10} R_{12} e^{-2\kappa_e \sec \theta d} \right]^{-1} \times T_{01} I_0 \delta(\cos \theta_0 - \cos \theta_{0i}) \delta(\phi - \phi_i) \times e^{-\kappa_e \sec \theta (z+2d)}, \quad (6.14a)$$

$$I_d^{(0)} = \left[\mathbf{I} - R_{10} R_{12} e^{-2\kappa_e \sec \theta d} \right]^{-1} \times T_{01} I_0 \delta(\cos \theta_0 - \cos \theta_{0i}) \delta(\phi - \phi_i) \times e^{\kappa_e \sec \theta z}. \quad (6.14b)$$

where \mathbf{I} is the identity matrix.

The solution procedure then becomes a perturbation method, using the phase matrix as a small parameter. In that sense, the perturbation affects mainly the diffuse intensities but requires evaluation of the solution of the reduced intensities at a lower order (Eq. 6.14) in the source terms. This yields a new system of equations which can be solved for the second order solution and so forth. *Tsang et al.* (2007) used numerical solutions to solve for the diffuse intensities, thus accounting for the full multiple particle interactions with the boundaries. However, analytical solutions exist for first order and second order interactions (e.g. *Tsang et al.*, 2000b, 2007). We note also that we have included multiple scattering between particles and the boundaries. Additionally, it is possible to account for multiple interactions *within* the medium, that is, interactions resulting from multiple scattering between particles not involving a boundary. A good measure of the degree of multiple interaction for this situation is the albedo $\tilde{\omega}$, defined as the ratio between scattering and the total extinction. Large albedo means that most of the extinction of the incoming wave is due to scattering, therefore the medium is reflective. *Tsang and Ishimaru* (1985) showed that for $\tilde{\omega} > 0.8$, second order scattering and multiple scattering can be 4 dB larger than the first order solution, but results were comparable to the first order solution for smaller albedo. It has been found that for classic Mie scattering, the n -th order solution will be proportional to $\tilde{\omega}^n$ (*Tsang et al.*, 2000b). For the case of dense media, multiple scattering can be accounted for by the Quasi-Crystalline Approximation, which will be presented in the following sections.

For the remainder of this work, the multiple scattering interaction with the boundaries

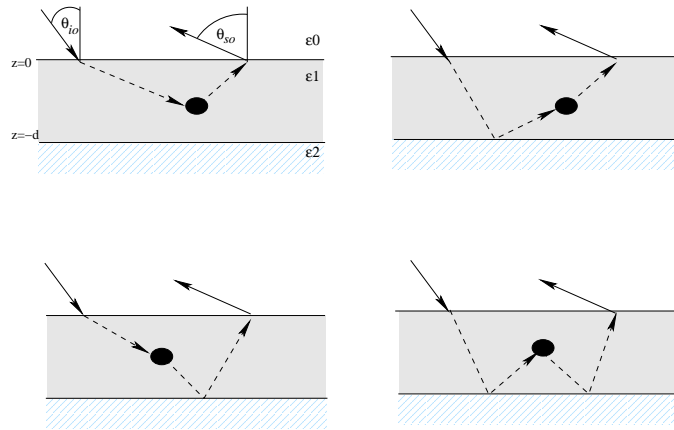


Fig. 6.4: First order scattering modes

will be modeled to first order with the intention of illustrating the capabilities of the model to explain the observed scattering characteristics from breaking waves. If needed, the model could be expanded to higher order in subsequent research. This first order solution involves four terms accounting for the different interactions between a single particle and the boundaries, as shown in Fig. 6.4. The first mode corresponds to simple scattering by a particle back into the air region. The second and third modes correspond to single bounces from the bottom boundary (reflection) before (after) scattering from the particle, respectively. The fourth mode is a double bounce from the bottom layer, before and after scattering from the particle. Reflections from the upper boundary are not included as these would be considered second order interactions. The second order solution includes these terms and the terms arising from the multiple interaction between two particles and the boundaries, sixteen terms in total.

It can be noted that the solution presented is generic enough to be applied to a wide variety of physical cases. However, the formulation of the most relevant parameters, the phase matrix \mathbf{P} and the extinction coefficient κ_e has not been provided because it depends on the scatterer characteristics and medium configuration. We address this in the following section.

6.3.3 Multiple scattering by discrete scatterers

First we focus on the multiple scattering within the medium, where we consider the case of N particles contained in a volume V . The incident field acting upon the volume is E_i . Each particle j within the volume will generate a scattered field which can be described as (*Tsang and Kong, 2001*)

$$E_j^s = GT_j E_j^E, \quad (6.15)$$

where the superscript s denotes a scattered field, G is a propagator function usually defined in terms of Green's functions; T is a transition operator denoting the response of the particle when in isolation and the superscript E denotes an exciting field acting on the particle. The latter quantity remains undefined and it will depend on the level of interaction between particles. For instance, if only two particles l and j were in the volume, the exciting fields could be written as

$$E_j^E = E_i + GT_l E_i + GT_l GT_j E_i + GT_l GT_j GT_l E_i + \dots \quad (6.16)$$

Thus the exciting field acting on particle j corresponds to the sum of the incident field E_i , plus the field directly scattered by particle l into particle j , $GT_l E_i$, plus the field being scattered from l after scattering from j , $GT_l GT_j E_i$ and so on. Note that a particle does not excite itself. Generalization to N particles yields

$$E_j^E = E_i + \sum_{\substack{l=1 \\ l \neq j}}^N GT_l E_l^E, \quad (6.17a)$$

which corresponds to the total field exciting the j -th particle. The total scattered field is

$$E_s = \sum_{j=1}^N GT_j E_j^E, \quad (6.17b)$$

and the total field is simply

$$E = E_i + E_s. \quad (6.17c)$$

Eq. 6.17 are exact relations involving no approximations, known as the Foldy-Lax multiple scattering equations. Note that these are implicit equations (through the cross-dependency of the exciting fields in Eq. 6.17a), therefore usually consisting of N equations with N unknowns (the fields E_j^E). Despite being exact, solving this system of equations requires some additional assumptions or approximations.

The simplest scenario is to assume zero interaction between particles, in which case the scattered field is simply

$$E_s = NGTE_i, \quad (6.18)$$

where it has been assumed for simplicity that all the particles are identical, but extension to a collection of different particles is straightforward and involves summation over families of particles. This approach, known as *independent scattering*, yields good results when the volume fraction f_v of scatterers is very small (less than $f_v < 5\%$), but leads to an overestimation of the scattering effects otherwise (e.g. *Tsang and Kong*, 1980; *Mandt et al.*, 1992; *West et al.*, 1994).

The next level involves interaction between particles in which case the scattered fields will depend on the relative position between particles. With the advent of increased computing power, Monte Carlo based techniques have been used to account for particle positioning (e.g. *Tse et al.*, 2007). However, the problem remains computationally costly, therefore existing approximations are widely used. One possibility is to use configurational averages, that is, the statistical average of the scattering resulting from all possible particle positions. The problem then depends on the probability density function of finding a particle at a given position \vec{r}_j , which in turn is conditioned by the probability of finding a second particle at \vec{r}_l and so on. To the lowest level, only interac-

tions and positions between two particles are accounted for, in an approach known as the Quasi-Crystalline Approximation (QCA, *Lax*, 1952). The key assumption in the QCA is that the configurational average of two particles is well approximated by the ensemble average of a single particle, thus providing closure to the system of equations. However, in deriving the equations for the original QCA procedure, the Green's function of the background medium is used which might not be valid when the particle concentration becomes large, since in that case the EM wave will be subject to propagation through an effective medium instead. Accounting for this effective propagation led to the concept of Coherent Potential (CP), which was applied to improve the approximations (e.g. *Tsang and Kong*, 1980, 1982). The QCA and QCA-CP approximations have been used extensively in the study of microwave scattering by tenuous particles (low permittivity contrast with the background medium), and in the case of dense media scattering.

6.3.4 QCA in dense media scattering

The closeness of the particles means that the far field assumption might not be valid, therefore it is convenient to rewrite the fields in terms of spherical waves, or more specifically, in terms of the spherical wave functions $Rg\bar{M}_{mn}$ and $Rg\bar{N}_{mn}$, which depend on the spatial phase kr and the angles θ and ϕ . With this approach, the incident and exciting fields for the j -th particle can be written as an infinite series (*Tsang and Kong*, 2001)

$$E_i = \sum_{m,n} a_{mn}^{(M)} Rg\bar{M}_{mn} + a_{mn}^{(N)} Rg\bar{N}_{mn}, \quad (6.19a)$$

$$E_j^E = \sum_{m,n} w_{mn}^{(M)} Rg\bar{M}_{mn} + w_{mn}^{(N)} Rg\bar{N}_{mn}, \quad (6.19b)$$

where the only unknowns are the coefficients $w_{mn}^{(M)}, w_{mn}^{(N)}$. The coefficients $a_{mn}^{(M)}, a_{mn}^{(N)}$ describe the known incident wave, and $Rg\bar{M}_{mn}$ and $Rg\bar{N}_{mn}$ have known mathematical representations. The unknowns can be grouped in a vector \vec{w} and Eq. 6.17a can be rewritten as

$$\vec{w}_j = \sum_{\substack{l=1 \\ l \neq j}} \Phi \mathbf{T}_M \vec{w}_l + \vec{a}_i e^{i\vec{k} \cdot \vec{r}_j}, \quad (6.20)$$

where Φ is a matrix accounting for particle positioning between particles j and l , and \mathbf{T}_M is the T-matrix of the particle. The latter is a formalism by which the scattering of particles of arbitrary shapes can be described by modifying the scattering of a spherical particle (*Tsang et al.*, 2000b).

So far we have only recast the Foldy-Lax equations in spherical form. To estimate the statistical average, the probability density function of the position of all the other particles given the position of particle l , $p(\vec{r}_i | \vec{r}_l, i \neq l)$ needs to be used. The expected configurational value is

$$\langle \vec{w}_j \rangle = \int \vec{w}_l p(\vec{r}_i | \vec{r}_l) d\vec{r}_i, \quad i \neq l, \quad (6.21)$$

which means that the expected solution for particle j will depend on other particles' solution weighted by the probability of finding the particles at those locations. Since the Φ matrix also depends on both particles' positions, incorporating Eq. 6.21 into Eq. 6.20 requires the use of Bayes' rule and the conditional average using two particles fixed. Here the QCA approximation is introduced to bring closure to the system. After these manipulations, Eq. 6.20 can be written as

$$\langle \vec{w}_j \rangle = \vec{a}_i e^{i\vec{k} \cdot \vec{r}_j} + \sum_{\substack{l=1 \\ l \neq j}} \Phi \mathbf{T}_M \vec{w}_l p(\vec{r}_l | \vec{r}_j) d\vec{r}_l, \quad (6.22)$$

where it can be seen that l becomes a dummy variable and the sum can be replaced by $(N - 1)$. One important aspect of this last step is that it allows the introduction of the pair distribution function $g(\vec{r}_l - \vec{r}_j)$ defined as (*Tsang et al.*, 2000b; *Tsang and Kong*, 2001)

$$n_o g(\vec{r}_l - \vec{r}_j) = (N - 1) p(\vec{r}_l | \vec{r}_j), \quad (6.23)$$

where n_o is the number of particles per unit volume, which depends on the particle diameter d and volume fraction f_v as

$$n_o = \frac{6f_v}{\pi d^3}. \quad (6.24)$$

The pair distribution function is a concept amply used in statistical mechanics, and allows a simple characterization of the geometrical structure of substances, gases, crystalline solids or liquids. It can be measured for instance by counting the frequency of occurrence of the separation distances between particle centers. For gases with a high degree of randomness, the pair distribution function is exactly 1 because all separations are equally probable, therefore particle positioning is independent of the other particles. For a crystalline solid composed of particles of diameter b , $g(\vec{r}_i - \vec{r}_j)$ will show peaks at integer multiples of b , and for a liquid or an amorphous solid it will be a mixture between the gas and solid descriptions. At large separations, the pair distribution of liquids approach unity, thus independency. Therefore, the pair distribution function is a measure of the total influence of a particle on another. Furthermore, it is possible to include the tendency for particles to form clusters by the inclusion of a parameter τ . In this case, the interaction between particles is of very short range, but if the particles are close enough they can bind to each other. τ , called the stickiness parameter, is a dimensionless parameter describing the system temperature, being zero at zero temperatures (*Baxter*, 1968) and inversely proportional to the attraction between particles (*Zurk et al.*, 1995). Typical values are in the range of 0.1 – 0.2 for sticky surfaces (*Seaton and Glandt*, 1987; *Zurk et al.*, 1995), and $\tau = \infty$ for non adhesive particles. Using the Percus-Yevick approximation, it is possible to show that the pair distribution function will depend only on particle diameter, the fractional volume occupied by the particles, and the stickiness parameter (*Zurk et al.*, 1997; *Tsang et al.*, 2001).

With this it is possible to solve Eq. 6.20. To do this, it is assumed that the wave coefficients can be approximated by (*Tsang and Kong*, 2001)

$$\vec{w}_j = \vec{a}^E e^{i\vec{K}_d \cdot \vec{r}_j}, \quad (6.25)$$

where \vec{K}_d is an effective, downward-propagating wavevector of magnitude K , the effective wavenumber. Thus the propagating wave has different dispersion characteristics than that of the incident wave due to the presence of the medium. Note as well that with this approximation, an additional unknown has been introduced (K). The next step in the solution involves integration over the domain where the scatterers are present, which leads to rather cumbersome algebra that is fully documented in the cited references. However, two important aspects are worth noting. The expressions for the unknown wave parameters \vec{a}^E contain two kinds of waves dependencies. The first is a group of waves that travel with the wavevector of the incident wave, and the second is a group traveling at the effective wavenumber. This can be interpreted physically as the medium generating waves which extinguish the incident wave. Balancing of the incident wave terms with those of the generated wave yields the Ewald-Ossen extinction theorem. Balancing of the terms associated with the effective wavenumber K yields the generalized Lorentz-Lorenz law (e.g. *Tsang et al.*, 2000b). The phase matching condition for the incident and effective wave vectors reads

$$K_x = k_{ix}, \quad (6.26a)$$

$$K_y = k_{iy}, \quad (6.26b)$$

$$K_z = \sqrt{K^2 - k^2 \sin^2 \theta_i}, \quad (6.26c)$$

$$K \sin \theta_t = k \sin \theta_i \quad (6.26d)$$

the last equation being Snell's law.

The resulting set of equations for the Lorentz-Lorenz law for the case of a single

family of particles are (*Tsang et al.*, 2000a)

$$X_\nu^{(M)} = -2\pi n_o \sum_{n=1}^{N_{\max}} \sum_{p=|n-\nu|}^{|n+\nu|} (2n+1) [L_p(k, K|d) + M_p(k, K|d)] \times \\ \left(T_n^{(M)} X_n^{(M)} a(1, n| - 1, \nu|p) A(n, \nu, p) + T_n^{(N)} X_n^{(N)} a(1, n| - 1, \nu|p-1) B(n, \nu, p) \right), \quad (6.27a)$$

$$X_\nu^{(N)} = -2\pi n_o \sum_{n=1}^{N_{\max}} \sum_{p=|n-\nu|}^{|n+\nu|} (2n+1) [L_p(k, K|d) + M_p(k, K|d)] \times \\ \left(T_n^{(M)} X_n^{(M)} a(1, n| - 1, \nu|p-1) B(n, \nu, p) + T_n^{(N)} X_n^{(N)} a(1, n| - 1, \nu|p) A(n, \nu, p) \right), \quad (6.27b)$$

where $\nu = 1 \dots N_{\max}$, N_{\max} being the maximum multipole expansion in the series (cf. Eq. 6.20) and chosen as $N_{\max} = \text{floor}(kd) + 1$ (*Tsang et al.*, 2007). M_p and L_p are given by (*Tsang and Kong*, 2001)

$$M_p(k, K|d) = \int_d^\infty r^2 (g(r) - 1) h_p(kr) j_p(Kr) dr, \quad (6.28a)$$

$$L_p(k, K|d) = -\frac{d^2}{K^2 - k^2} (k h'_p(kd) j_p(Kd) - K h_p(kd) j'_p(Kd)). \quad (6.28b)$$

Despite the apparent complexity, most of the coefficients are known. n_o is the particle number density; $A(n, \nu, p)$ and $B(n, \nu, p)$ have simple algebraic expressions given in Eq. 6.1.44 of *Tsang and Kong* (2001). Similarly for $a(1, n| - 1, \nu|p)$ and $a(1, n| - 1, \nu|p-1)$ (see Eq. 10.4.14 to 10.4.20, *Tsang et al.*, 2001). j_p and j'_p are the spherical Bessel function and its derivative, h_p and h'_p are the spherical Hankel function and its derivative. All these coefficients arise from the expressions for the vector spherical waves and their translation (implicit in Eq. 6.20 in Φ). The remaining terms are $T_n^{(M)}$, $T_n^{(N)}$, $X_n^{(M)}$ and $X_n^{(N)}$. The T terms correspond to the scattering characteristics of individual particles in the frame of the T-matrix formalism previously mentioned, whose definition is deferred to the

following section. The X_n terms are the amplitudes of the exciting fields and correspond to the unknowns, along with K .

Eq. 6.27 is a system of $2N_{\max}$ homogeneous equations, therefore its solution can be obtained by forcing the determinant to vanish. Numerical algorithms for the solution are provided by *Tsang et al.* (2001) and freely available. However, forcing the determinant to vanish yields a new equation for the effective propagation constant K , which is therefore determined but includes an unknown constant. To solve for this constant, the generalized Ewald-Ossen theorem is invoked. For the case of oblique incidence it reads (*Tsang et al.*, 2000a)

$$-\frac{(K_z - k_{iz})k_{iz}k}{2\pi} = in_o \sum_n \frac{2n+1}{n(n+1)} \times \left\{ X_n^{(M)} T_n^{(M)} \left(\frac{P_n^1(\cos \theta_d)}{|\sin \theta_d|} \cos \theta_d + n(n+1)P_n(\cos \theta_d) \right) - X_n^{(N)} T_n^{(N)} \frac{P_n^1(\cos \theta_d)}{|\sin \theta_d|} \right\}, \quad (6.29)$$

where P_n and P_n^1 are the Legendre polynomial and Legendre polynomial of degree 1, respectively. Its argument $\theta_d = \theta_i - \theta_t$ corresponds to the difference between the incident and transmitted directions. Subscripts z denote the vertical component of the incident and effective wavevectors. It must be noted that the Eq. 6.29 corresponds to the case of horizontal polarization. The expression for vertical polarization is similar and omitted here for brevity.

6.3.5 Extinction, absorption and phase matrices

With the scattering behavior inside the medium defined, it is possible to calculate the extinction matrix κ_e and the phase matrix \mathbf{P} , which are required for the solution of the DMRT. We follow the approach used by *Tsang et al.* (2007) who were able to derive simple expressions for the phase matrix based on some extra manipulations of the spherical wave vectors. They found that it is convenient to manipulate the expressions in a reference

frame that is aligned with the scattering direction inside the domain, \vec{k}_s and one of the remaining unit vectors is perpendicular to both \vec{k}_s and \vec{k}_i . In this frame, and assuming that the scatterers are spherical, the phase matrix has the form

$$\mathbf{P}^l = \begin{bmatrix} P_{11}^l & 0 & 0 & 0 \\ 0 & P_{22}^l & 0 & 0 \\ 0 & 0 & P_{33}^l & P_{34}^l \\ 0 & 0 & P_{43}^l & P_{44}^l \end{bmatrix} \quad (6.30)$$

where the cross-polarization components P_{12} and P_{21} are zero due to the sphericity of the scatterers. The remaining components are

$$P_{11}^l = |f_{11}(\Theta)|^2 q(\Theta), \quad (6.31a)$$

$$P_{22}^l = |f_{22}(\Theta)|^2 q(\Theta), \quad (6.31b)$$

$$P_{33}^l = \text{Re}(f_{11}(\Theta)f_{22}^*(\Theta))q(\Theta), \quad (6.31c)$$

$$P_{44}^l = P_{33}^l, \quad (6.31d)$$

$$P_{33}^l = -\text{Im}(f_{11}(\Theta)f_{22}^*(\Theta))q(\Theta), \quad (6.31e)$$

$$P_{43}^l = -P_{34}^l, \quad (6.31f)$$

where Θ is the angle between \vec{k}_s and \vec{k}_i ; $q(\Theta) = n_0(1 + n_0(2\pi)^3)H(\Theta)$, with $H(\Theta)$ being the structure factor, defined as the Fourier transform of the pair distribution function $g(\vec{r}) - 1$. The coefficients f are defined as

$$f_{11}(\Theta) = -\frac{i}{1-R} \sqrt{\frac{1}{kK_r}} \sum_{n=1}^{N_{\max}} \frac{2n+1}{n(n+1)} \times \left\{ T_n^{(M)} X_n^{(M)} \tau_n(\cos \Theta) + T_n^{(N)} X_n^{(N)} \pi_n(\cos \Theta) \right\}, \quad (6.32a)$$

$$f_{22}(\Theta) = -\frac{i}{1-R} \sqrt{\frac{1}{kK_r}} \sum_{n=1}^{N_{\max}} \frac{2n+1}{n(n+1)} \times \left\{ T_n^{(M)} X_n^{(M)} \pi_n(\cos \Theta) + T_n^{(N)} X_n^{(N)} \tau_n(\cos \Theta) \right\}, \quad (6.32b)$$

where the coefficients π_n and τ_n are dependent on the Legendre polynomials and given for instance in *Fowler (1983)*. R in turn corresponds to the coherent reflection coefficient (coherency to be defined below), which for oblique incidence and horizontal polarization is

$$R = \frac{i2\pi n_0}{kk_z(K_r + k_{iz})} \sum_{n=1}^{N_{\max}} (-1)^n \frac{2n+1}{n(n+1)} \times \left\{ X_n^{(M)} T_n^{(M)} (n(n+1)P_n(\cos\theta_a) + \cot\theta_a P_N^1(\cos\theta_a)) + X_n^{(N)} T_n^{(N)} \frac{P_n^1(\cos\theta_a)}{\sin\theta_a} \right\}, \quad (6.33)$$

where $\theta_a = \theta_i + \theta_t$ and $K_r = \text{Re}(K)$ following *Tsang et al. (2007)*. This also allows computation of the effective dielectric constant of the medium $\epsilon_{\text{eff}} = (K_r/k)^2$, to be used in the calculations of the transmitted angle (Eq. 6.11) and in the reflectivity and transmissivity matrix terms needed for Eqs. 6.10, 6.12 and 6.14.

Thus the phase matrix is defined in the local coordinate system, which needs to be rotated to the main coordinate system (aligned with the layer) for every scattering direction. To do so, two rotations need to be performed to account for the orientation of the incident direction and the scattered direction. Let α_i and α_s define those rotations, then the phase matrix in the main coordinate system is (*Ishimaru, 1978*)

$$\mathbf{P} = \begin{bmatrix} c_s^2 & s_s^2 & -c_s s_s & 0 \\ s_s^2 & c_s^2 & c_s s_s & 0 \\ 2c_s s_s & -2c_s s_s & c_s^2 - s_s^2 & 0 \\ 0 & 0 & 0 & 1 \end{bmatrix} \cdot \mathbf{P}^l \cdot \begin{bmatrix} c_i^2 & s_i^2 & c_i s_i & 0 \\ s_i^2 & c_i^2 & -c_i s_i & 0 \\ -2c_i s_i & 2c_i s_i & c_i^2 - s_i^2 & 0 \\ 0 & 0 & 0 & 1 \end{bmatrix}, \quad (6.34)$$

where $c_i = \cos\alpha_i$, $s_i = \sin\alpha_i$, $c_s = \cos\alpha_s$ and $s_s = \sin\alpha_s$. With this, the phase matrix has been fully determined. In the principal frame of reference it is possible to relate the components of the phase matrix to the polarization state as $P_{VV} = P_{11}$, $P_{VH} =$

$$P_{12}, P_{HV} = P_{12}, P_{HH} = P_{22}.$$

The next step is to determine the extinction coefficient, which is defined as $\kappa_e = \kappa_s + \kappa_a$. Therefore, the total extinction is the combination of scattering of the incident wave into other directions (κ_s) and the absorption (κ_a) by the particles. In order to evaluate these parameters, it is convenient to introduce the concepts of coherent and incoherent fields. These concepts arise from the notion that any field Υ can be treated as random function of position \vec{r} due to the randomness of the particles. Therefore, the field can be separated into an average field and a fluctuating field

$$\Upsilon(\vec{r}) = \langle \Upsilon(\vec{r}) \rangle + \hat{\Upsilon}(\vec{r}), \quad (6.35)$$

where $\langle \rangle$ denote ensemble averaging. The concept is akin to the separation of mean components and turbulence for fluid flows. The resulting average field $\langle \Upsilon(\vec{r}) \rangle$ is called the coherent field, and $\hat{\Upsilon}(\vec{r})$ is the incoherent field. By definition $\langle \hat{\Upsilon}(\vec{r}) \rangle = 0$. The physical implications of this separation on the scattering of the fields are best illustrated if we depart for a moment from volumetric scattering from particles and we focus on surface scattering. In this case, the randomness is provided by the surface and typically quantified in terms of the root-mean-square surface elevation. In the absence of surface roughness (a flat surface), the scattering will only occur in the specular direction (e.g. *Beckmann and Spizzichino, 1987*). For the case of a rough surface within the frame of the small perturbation model, the ensemble averaging of the scattered field yields that the coherent wave propagates only in the specular direction. However, the power of the coherent wave is less than the power of the incident wave. This means that in order to ensure energy conservation, the incoherent waves need to propagate energy into other directions as well, including $\theta_s = -\theta_i$ (backscattering.) It can be shown that the traditional model for the backscattering from the rough ocean surface (Bragg) arises from the incoherent waves (e.g. *Wu and Fung, 1972; Tsang et al., 2000b*).

Returning to the case of volumetric scattering, the situation is analogous in the sense that the coherent wave will propagate only in the incident and specular directions,

whereas the scattering in other directions will be due to the incoherent waves. Therefore, in order to calculate the absorption of the incident wave, it is only necessary to account for the coherent wave. The resulting absorption coefficient is (Tsang *et al.*, 2007)

$$\begin{aligned} \kappa_a = & \frac{k}{K_r} \frac{\pi n_0}{k^2 |1 - R|^2} \sum_{n=1}^{N_{\max}} (2n + 1) \\ & \times \left\{ |X_n^{(M)}|^2 \left(-\operatorname{Re}(T_n^{(M)}) - |T_n^{(M)}|^2 \right) + |X_n^{(N)}|^2 \left(-\operatorname{Re}(T_n^{(N)}) - |T_n^{(N)}|^2 \right) \right\}, \end{aligned} \quad (6.36)$$

which is polarization dependent.

The scattering coefficient is simply the integration of the scattering in all directions, usually assuming azimuthal symmetry (Tsang and Kong, 2001)

$$\begin{aligned} \kappa_s = & \int_0^\pi \sin \theta \left(\int_0^{2\pi} P_{HV} d\phi + \int_0^{2\pi} P_{VV} d\phi \right) d\theta, \\ = & \int_0^\pi \sin \theta \left(\int_0^{2\pi} P_{HH} d\phi + \int_0^{2\pi} P_{VH} d\phi \right) d\theta. \end{aligned} \quad (6.37)$$

It must be mentioned that the calculation of the incoherent fields has been based on the distorted Born Approximation, which assumes the total exciting field over the particles can be approximated by the mean (coherent) first order field. It is for this reason that the phase matrix terms f in Eq. 6.32 depend on the coherent reflection coefficient.

6.3.6 Backscattering coefficient

Once all the relevant terms have been defined, it is possible to estimate the intensity that is transmitted into the air region after the multiple scattering inside the medium. We have seen that the scattering in multiple directions is due to the diffuse intensities,

$$I_0^{(D)}(\theta_0, \phi) = T_{10} I^{(D)}(\theta, \phi, z = 0), \quad (6.38)$$

where $I^{(D)}$ is the first order, upward-going diffuse intensity, whose analytic solution is given in *Tsang et al.* (2007). Note that the scattered direction is θ_0 , which needs to be computed using Snell's law.

Finally, the quantity of interest is the backscattering coefficient which is defined as

$$\sigma_{\beta,\alpha} = 4\pi \frac{\cos \theta_0 I_{0,\beta}^{(D)}(\theta_0, \phi_i + \pi)}{I_{0,\alpha}}, \quad (6.39)$$

where $\alpha, \beta = H$ or V , thus accounting for all polarization combinations. For the present case, we are interested only in VV and HH combinations, because both measurements were taken independently. Additionally, Eq. 6.39 is considered to correspond to the normalized radar cross section under the assumption that the radar cell is uniformly covered by the scattering layer (i.e. the wave roller).

6.4 Model parameters

The model thus defined depends on a few physical parameters and requires no calibration constants. The parameters are the microwave frequency (or incident wavenumber k_i) and the medium properties. These include the medium permittivity ϵ_1 , the particle diameter d , and the volume fraction f_v . The final parameter is the stickiness τ .

For the present experiments, the microwave frequency corresponds to X-band, which for the RiverRad measurements was 9.36 GHz. While most of the following analysis is performed for this (fixed) frequency, the marine radar operated at a slightly higher frequency of 9.45 GHz and we will compare the difference in response for this frequency variation.

The obvious initial implication of the frequency is, in conjunction with the particle diameter, to define the scattering characteristics of the particles. If the relative particle size is small ($kd \ll 1$), the particle can be treated as if under the influence of electrostatic fields. In this case, known as the *Rayleigh* or *low frequency regime*, the backscattering efficiency, defined as the ratio between the radar and geometrical cross sections, follows a simple power law proportional to $(kd)^{-4}$ (e.g. *Wetzel*, 1990a; *Sharkov*, 2007).

However, the upper limit for this region is $d = 0.1\lambda$ (*Sharkov*, 2007) or $8d \sin \theta < \lambda$ (*Long*, 1983), where $\lambda = 2\pi/k$. For the present case, $\lambda \approx 3$ cm, and particles of diameter less than 3 mm are needed to satisfy this condition. While droplet measurements are scarce, at least the data from *Chanson* (2004) suggest that median values typically exceed this value.

The second case corresponds to the resonance (or Mie) region and spans a wide range of kd values, up to 25 (*Sharkov*, 2007), thus covering the diameter range expected for water droplets. Here the scattering is characterized by the resonant response of the particle to the excitation induced by the incident fields. For this case, the corresponding T-matrix terms can be written as (*Tsang et al.*, 2000b)

$$T_n^{(M)} = -\frac{j_n(k_s a)[ka j_n(ka)]' - j_n(ka)[k_s a j_n(k_s a)]'}{j_n(k_s a)[ka h_n(ka)]' - h_n(ka)[k_s a j_n(k_s a)]'}, \quad (6.40a)$$

$$T_n^{(N)} = -\frac{k^2 a^2 j_n(k_s a)[ka j_n(ka)]' - k^2 a^2 j_n(ka)[k_s a j_n(k_s a)]'}{k^2 a^2 j_n(k_s a)[ka h_n(ka)]' - k^2 a^2 h_n(ka)[k_s a j_n(k_s a)]'}, \quad (6.40b)$$

where $a = d/2$ is the particle radius, and j_n and h_n are the Bessel and Hankel functions as before. This approach allows a large range of particle diameters, including both the Rayleigh and Mie regimes.

The next relevant parameter is the volume fraction, f_v . As mentioned previously, the model is treated as a single layer of droplets, with special focus on the volume above the 50% volume fraction contour. Therefore, fractions no larger than 50% will be used, with typical values less than 20%, based on the measurements of *Blenkinsopp and Chaplin* (2007) who showed a relatively large spatial volume with very low water fractions. The volume fraction also has an implication for cluster formation, which is also defined by the stickiness parameter τ . For a fixed diameter, increasing the volume fraction reduces the space available for particles to relocate, thus increasing the possibility to form clusters. For the present case, stickiness parameters $\tau = 0.1$ (sticky case) and $\tau = \infty$ will be used.

The final parameter is the media permittivity. We treat the particles and the underlying medium as the same material, namely salt water, while the background medium

is air. The permittivity for salt water is given by a Debye -type equation (e.g. *Ellison et al.*, 1998)

$$\epsilon = \epsilon_{\infty} + \frac{\epsilon_s - \epsilon_{\infty}}{1 - i2\pi ft} + i\frac{\sigma}{2\pi f\epsilon_0}, \quad (6.41)$$

where ϵ_s and ϵ_{∞} are the static and high frequency dielectric constants (74 and 4.9), t is the relaxation time in seconds (12.2 ps), σ is the ionic conductivity of dissolved salts (31 S/m), f is the electromagnetic frequency in Hz, and ϵ_0 is the permittivity of free space (8.8419×10^{-12} F/m). While most of these parameters are a function of temperature and salinity, a weak dependency is assumed. Values given in parentheses are taken from *Trizna* (1997). Therefore, for the frequencies of interest, the salt water relative permittivity is considered to be $\epsilon_1 = \epsilon_2 = 50.5 + 33.3i$.

6.5 Results and discussion

The computational procedure involves at first the calculation of the scattering properties of the volume, namely the extinction, absorption and scattering coefficients. These quantities represent the effect of the particles on the propagation of the incident wave, and do not account for the multiple scattering between the layer and the boundaries, which is solved next using the DMRT equations.

Nevertheless, these quantities provide relevant information regarding the behavior of the layer. For instance, it is possible to evaluate the relative contribution to the total extinction done by absorption and scattering, by computing the albedo

$$\tilde{\omega} = \frac{\kappa_s}{\kappa_s + \kappa_a} = \frac{\kappa_s}{\kappa_e}. \quad (6.42)$$

Fig. 6.5 shows the results for non sticky particles at 9.36 GHz. Particle diameters are in the range $d = 0.05 - 2$ cm, using the values observed by *Chanson* (2004). Volume fractions are in the range $f_v = 5\% - 45\%$ representing the upper layers of the roller. It can be seen that for small diameters extinction increases sharply until the Rayleigh limit is

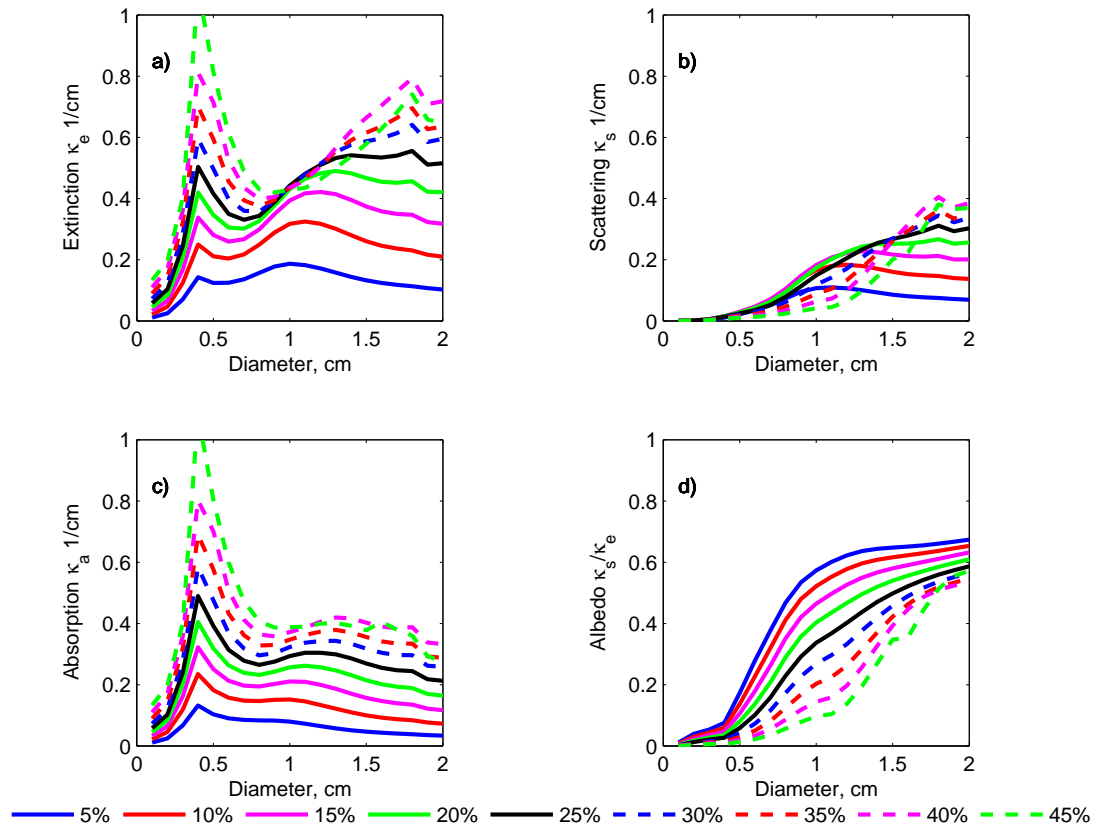


Fig. 6.5: (a) Extinction, (b) scattering, and (c) absorption coefficients for non sticky particles ($\tau = \infty$) as a function of particle diameter and volume fraction. (d) albedo. The incident frequency is 9.36 GHz

met ($d \approx 3$ mm). The position of this peak is independent of the volume fraction. Larger diameters show traces of the resonant response characteristic of the Mie regime, but the next peak occurs at larger diameters as the volume fraction increases. In addition, the extinction appears to show a direct dependency on volume fraction. Absorption tends to dominate at small diameters, where the albedo is typically less than 20% for $d \leq 0.5$ cm. As the diameter increases, the albedo increases significantly, until showing an asymptotic behavior to $\tilde{\omega} \approx 0.7$. This suggests that scattering from these aqueous particles could be significant, despite its lossy nature. The rate of increase is inversely proportional to the volume fraction due to the increase in absorption at higher volume fractions.

Fig. 6.6 shows the results for sticky particles ($\tau = 0.1$). While the absorption shows

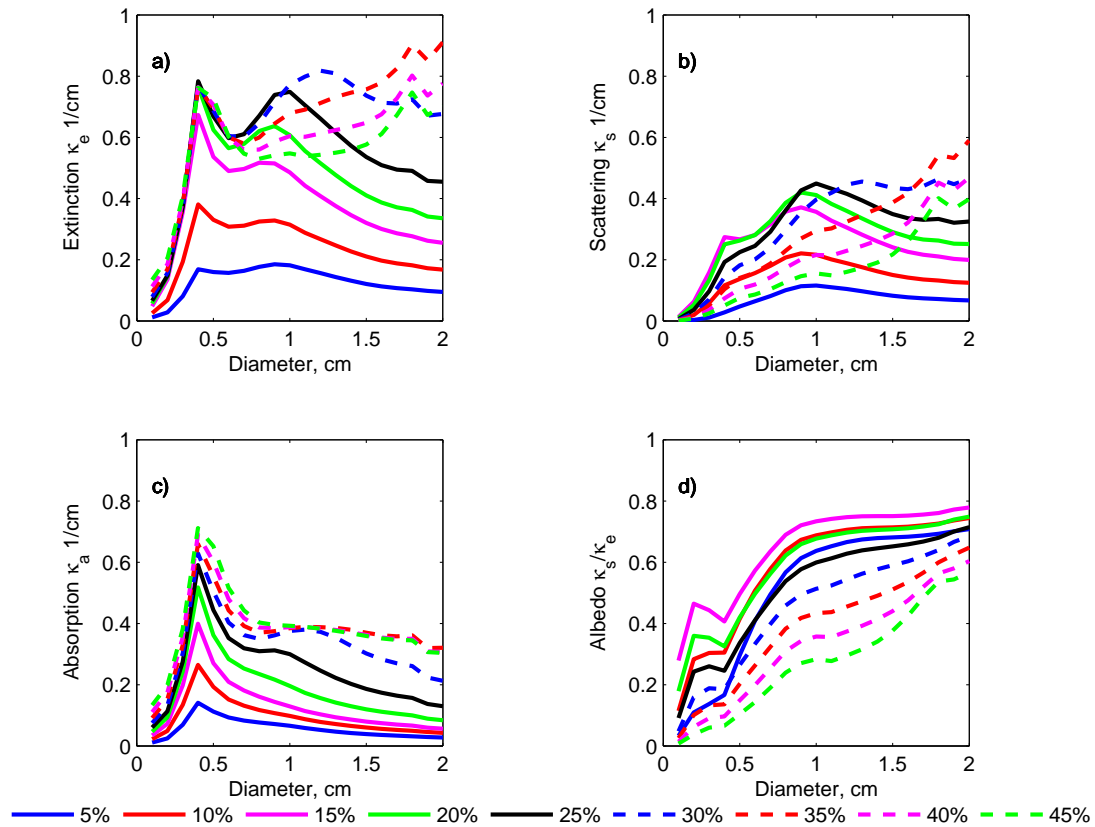


Fig. 6.6: (a) Extinction, (b) scattering, and (c) absorption coefficients for sticky particles ($\tau = 0.1$) as a function of particle diameter and volume fraction. (d) albedo. The incident frequency is 9.36 GHz

a similar pattern as that of non sticky particles, most notably in the Rayleigh regime, the scattering is greatly enhanced, especially at large volume fractions and small to medium diameters ($d \approx 1$ cm). The extinction in this diameter range is also increased, although for $d > 1.5$ cm it shows similar values as the non sticky case. The explanation for this is that at mid volume fractions and small diameters, the stickiness allows the particles to form clusters which effectively behave as particles of larger diameters. As the nominal diameter and volume fraction increase, the effect of clustering is reduced as there is less volume available to redistribute the particles and form clusters, thus the configurational averaging between sticky and non sticky is similar. However, the effect of clustering is not exactly the same as using larger particles because clustering allows the

formation of irregular shapes whose scattering properties would be different than those of a spherical particle of the same volume (*Zurk et al.*, 1995). This result is relevant for our model, because it has been mentioned that the roller shows the coexistence of multiple length scales. These structures could be treated as the result of clustering of smaller constituents, especially at relatively low volume fractions.

It can be noted as well that the extinction shows a maximum as a function of volume fraction, which is also dependent on the relative particle size kd . For sizes less than $d < 1.0$ cm, the extinction maxima are independent of f_v when $15\% \leq f_v \leq 30\%$. For $1.0 \text{ cm} \leq d \leq 1.4$ cm the maximum is reached at $f_v = 30\%$. At higher volume fractions, scattering decreases but absorption remains relatively constant. This can be explained in terms of the effect of the incoherent and coherent scattering. At small volume fractions, there are more phase fluctuations between particles due to the increased spacing between them. As the volume fraction increases, the phase fluctuations become more random until a certain level where they level off. Beyond that concentration level, the packing and clustering reduces the effect of the incoherent scattering while increasing coherent scattering in the forward direction. Absorption, on the other hand, seems to reach an asymptotic level.

The effect of the increase and decrease in scattering is notable in the albedo, which is maximum at relatively low volume fractions ($f_v = 15\%$). Beyond that fractional level, the decrease in scattering and increase in absorption significantly reduce the reflectivity. Additionally, the asymptotic behavior is reached at smaller diameters than those of the non sticky case, $d \approx O(0.7)$ cm for small volume fractions. It can also be seen that the diameters used by *Kalmykov et al.* (1976) ($d < 0.55$ cm) are typically in the Rayleigh regime, where absorption dominates. Therefore it is not surprising that they require large rainfall rates to model the observed data.

The effect of the stickiness is further illustrated in Fig. 6.7, where it can be seen that sticky particles have larger extinction mostly due to an increase in scattering. It can also be seen that the small difference between the frequency of the microwave sensors

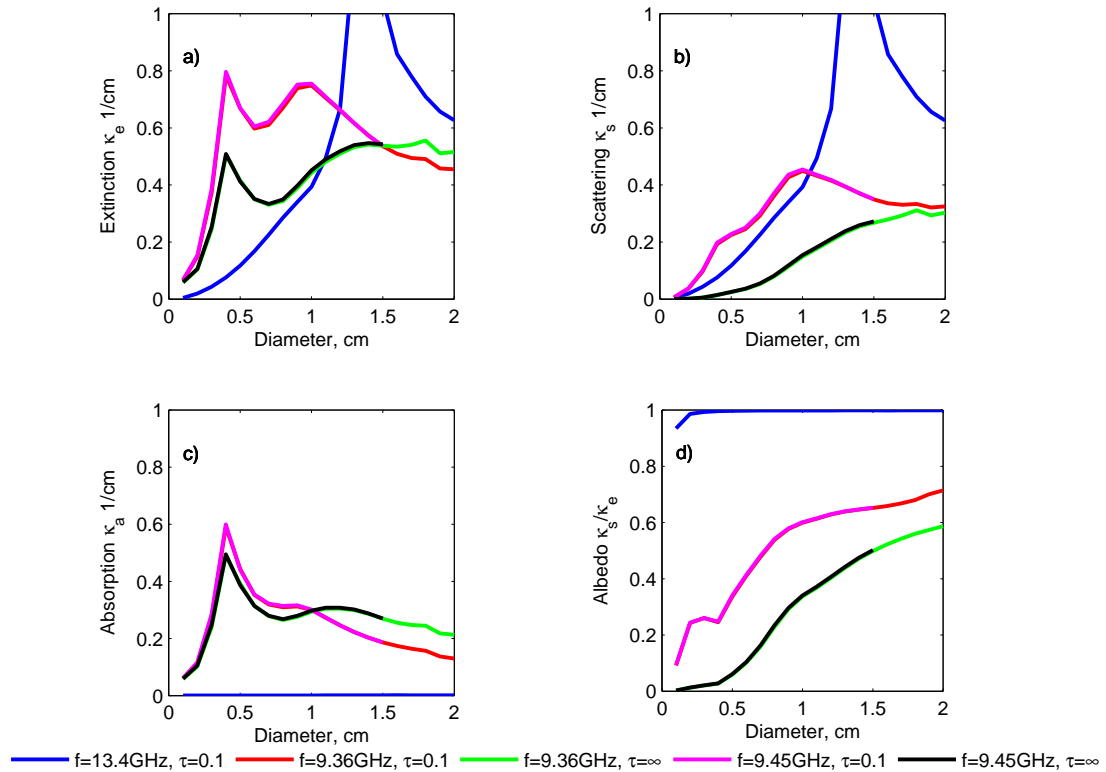


Fig. 6.7: Comparison of the (a) Extinction, (b) scattering, and (c) absorption coefficients between sticky particles ($\tau = 0.1$) and non sticky particles as a function of particle diameter and frequency. Volume fraction is 25%. (d) Albedo. $f=13.4$ GHz was used by *Tsang et al.* (2007) for the measurement of snow.

used in this work has no significant effect on the extinction parameters. That does not mean that the results are independent of frequency, as an increase in frequency is the equivalent to increasing the particle diameter. The effect of the lossy nature of water is shown by comparing the results to those of snow ($\epsilon = 3.15 + 0.001i$, *Tsang et al.*, 2007)) where absorption is almost negligible at these diameters and reflectivity is high.

The results presented are for a unit volume, thus the influence of the layer thickness has not been taken into account. However, the product of extinction and depth yields the optical depth $\kappa_e d$, which is a relevant parameter to estimate the relative importance of multiple scattering effects between the medium and the layer boundaries. If $\kappa_e d > 1$, multiple scattering becomes important (*Tsang et al.*, 2007). The present results for κ_e

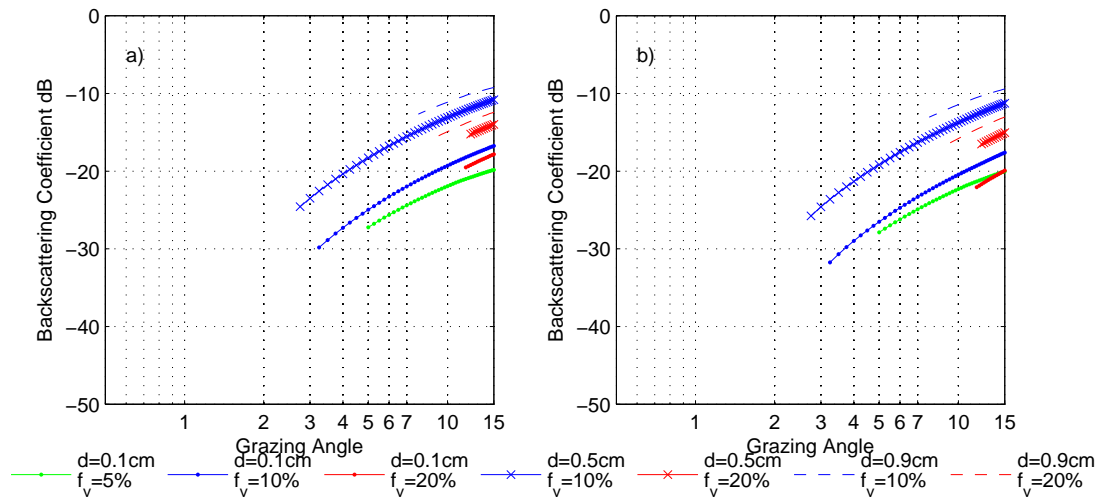


Fig. 6.8: Modeled backscattering coefficient for various diameters and volume fractions. (a) VV polarization, (b) HH. Color codes differentiate diameters and markers differentiate f_v .

mean that layers of at least 5 cm thick for the lowest volume fraction used, and thinner as the volume fraction increases are needed to induce multiple scattering. For instance, from the measurements of *Coakley et al.* (2001) it is possible to observe that the upper 15 cm of the roller had volume fractions of 10% or less. This means that thin layers of discrete scatterers above the water surface could lead to significant multiple scattering effects. However, the effect of the layer thickness on the scattering is also dependent on the incident and scattered angles, where the first order solution modes (cf. Fig. 6.4) are functions of $e^{-\kappa_e d \sec \theta_i}$. At large incidence (grazing), the argument tends to infinity and only the first mode dominates, in which case the solution becomes independent of the layer thickness and reflections with the boundaries become negligible. In other words, the bulk of the scattering is done by the particles in isolation and the characteristics of the underlying media do not play a significant role, akin to the scattering by a half space of scatterers. At the same time, it suggests that the upper layers of the roller will be most responsible for the scattering.

In consequence, when solving the DMRT equations the focus will be set on the scattering from relatively low volume fractions ($f_v < 20\%$) with diameters less than 1 cm.

The asymptotic behavior of the albedo for larger particles suggests that the results would not vary significantly beyond this limit. Model results for grazing angles in the range $0.5^\circ \leq \theta_g \leq 15^\circ$ are presented in Fig. 6.8. It must be noted that the grazing angle is measured relative to the layer. The results are truncated at different grazing angles, depending on the diameter and volume fraction. This is a result of the backscatter direction in air corresponding to a scattered direction within the layer that falls below the critical angle, thus the intensity scattered in that direction remains within the layer. The critical angle shows a stronger dependency on volume fraction than on diameter, and increases as the volume fraction increases, a result of waves propagating in a denser medium thus affecting more the effective propagation K . This situation represents a potential constraint with regard to the applicability of the model at low grazing angles.

At the same time, it can be seen that the results show a marked dependency with grazing angle, with the backscattering being greatly increased as the angle increases, regardless of the medium properties. However, there is a -10 dB variation on the backscatter results between the different (d, f_v) combinations tested. As expected, the smaller the diameter the weaker the backscattering, consistent with the behavior of the scattering coefficient κ_s . Similarly, as the volume fraction is increased, the backscattering coefficient increases, although it is expected that results at volume fractions larger than 20% would show the opposite trend based on the behavior of the scattering coefficient. Regarding polarization dependencies, both polarizations exhibit similar magnitudes and angular dependencies. In fact, as can be seen in Fig. 6.9, the polarization ratio $R = \sigma_0^{HH} - \sigma_0^{VV}$ is always less than 0 dB but values are very small. The degree of dependency on grazing angle appears to be a function of the volume fraction, becoming more dependent as the volume fraction increases.

The model is next compared with field data. The first source is the data collected during the present field experiment, with focus on the NRCS classified by source (cf. Chapter 5). Additionally, the data collected from *Coakley et al.* (2001) is included as reference, in particular the maximum NRCS measured by a pulsed-step-frequency X-band

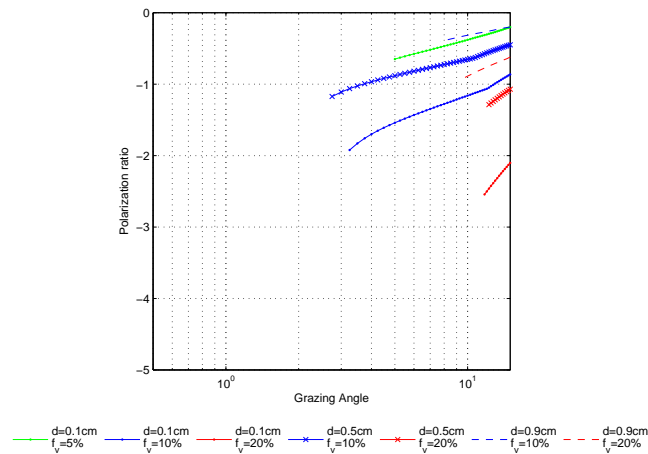


Fig. 6.9: Model results for the polarization ratio $R = \sigma_0^{HH} / \sigma_0^{VV}$, dB

sensor operating between 8 GHz and 9 GHz. Additionally, we include the mean NRCS (10.5 GHz, VV) from breaking waves measured by *Haller and Lyzenga* (2003), henceforth HL. However, these data are confined to a very narrow range of grazing angles. In order to further evaluate the model capabilities, further X-band (10 GHz, HH) measurements at smaller incidence angles are also included. These data were collected during a field campaign in September 1995 off the coast of Oregon from an airship (*Hesany et al.*, 1996). During that campaign, two isolated runs were performed where backscattered power and Doppler velocities were measured in the surf zone. The radar was mounted on an airship, therefore mid incidence angles were used and the azimuthal look was nearly up-wave. Details of the runs are given in Table 6.1. Unfortunately, unlike in the case of the present data set, it is not possible to separate the breaking from non-breaking waves without making some assumptions regarding the power of the events. We perform the discrimination based on a simple threshold in backscattered power, in this case the threshold was set at $\sigma_0 = -15$ dB. This value is somewhat higher than the values used previously, but this is necessary due to the higher backscattered power of the non-breaking waves at mid incidence in the frame of CST. The result of this discrimination is presented in Fig. 6.10, corresponding to a time-space diagram of the measured NRCS. It can be seen that this threshold allows separation of the bright signal at the front of the

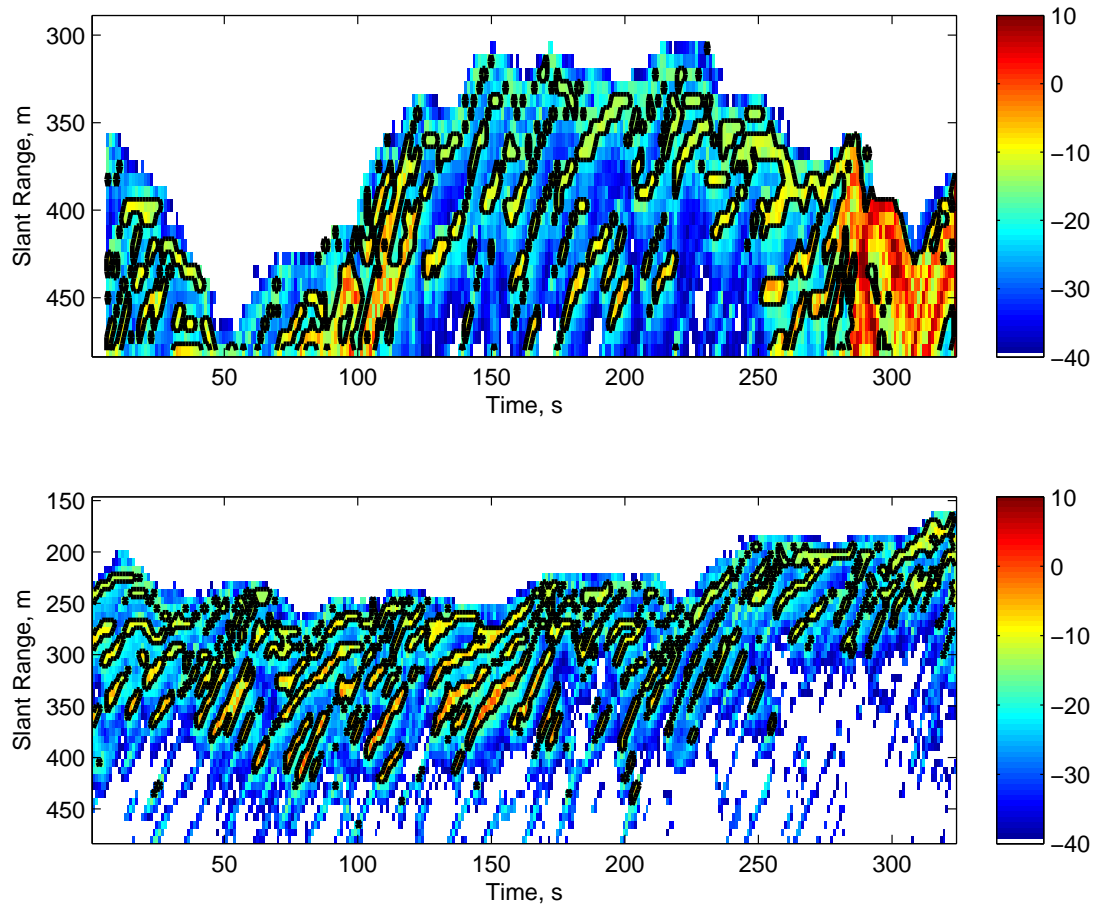


Fig. 6.10: Measured NRCS from an airship σ_0^{HH} , dB. Black contours correspond to zones identified as breaking waves. (a) Run 56; (b) Run 57.

waves from the relatively bright signal from the troughs. After separation, the median and maximum NRCS of each isolated breaker was recorded, along with the grazing angle of the centroid. Additionally, the median and maximum of the aggregate of the points was recorded and related to the nominal incidence angle.

Table 6.1: Summary of the beach measurements an airship.

Id. No.	Date	Time	θ_g °	ϕ °
56	9/19/1995	18:53 UTC	45.7	89.9
57	9/19/1995	18:59 UTC	51.9	89.9

Additionally, two other scattering mechanisms are included in the comparison. First, the traditional Bragg scattering, which is modeled using Eq. 2.1 and Eq. 2.2 for incidence angles larger than $\theta = 20^\circ$. The surface spectrum is modeled as in *Plant* (1997)

$$\psi_f = 0.0015k_B^{-4}, \quad (6.43)$$

where k_B is the Bragg wavenumber which depends on the incidence angle. Following *Coakley et al.* (2001), who found that the grazing angle dependency of the data correlated well with $\cos^2 \theta$ (θ being the incidence angle), the angular dependency of a Lambertian scattering surface is also included. It must be noted however, that both Bragg and Lambertian scattering are essentially surface scattering mechanisms.

Results of the comparison are presented in Fig. 6.11, where the model simulations have been extended to normal incidence to account for the larger grazing angles of the airship data and those from *Coakley et al.* (2001) and *Haller and Lyzenga* (2003). Regarding the present data, the focus is on the cluster of data showing NRCS about -20 dB, which was shown to be well correlated to wave breaking events in the previous chapter. Additionally, the data at $\theta_g > 3.5^\circ$ have been removed. It can be seen that the magnitude of the median from both the RiverRad and airship data, and the mean of the *Haller and Lyzenga* (2003) data can be well modeled by the present model, although there is an apparent offset with respect to the grazing angle location which will be discussed in detail below. The magnitude of the maxima from the data show a similar trend to that of the median, but usually at scattering levels about 10 dB larger. These large magnitudes were not reproduced by any of the parameter pairs (d, f_v) tested in the model. Nevertheless, the angular dependency of both the median and the maxima is well recovered by the model. The present volumetric model also gives good agreement for the angular dependency if the four data sets are considered together. It can be argued that the data would also correlate well to the angular dependency of the Lambertian model, but it must be noted that this is a surface scattering model and the actual NRCS values have not been computed here, therefore the volumetric model appears to be more complete

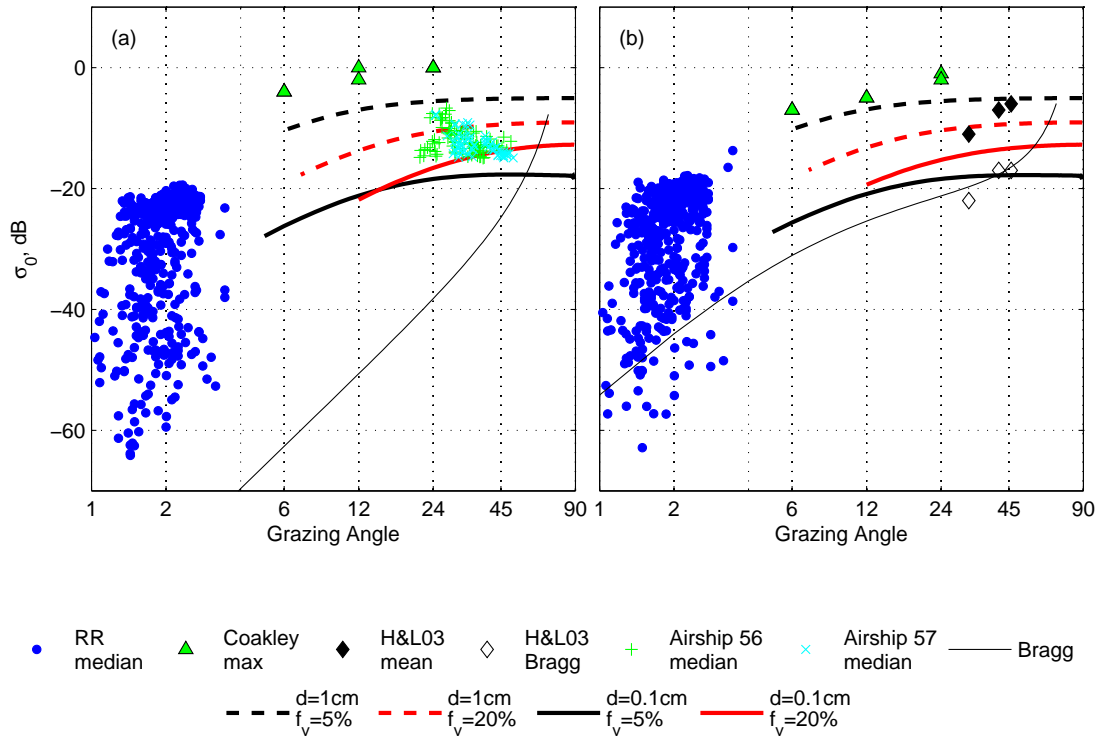


Fig. 6.11: Model data comparison. Model runs correspond to low volume fractions ($f_v=5\%$ & 10%) for two particle diameters and sticky particles ($\tau = 0.1$). Thin dashed line corresponds to the decay of a Lambertian surface and thin solid lines to Bragg scattering. (+) and (\times) correspond to the airship data, triangles to the maximum NRCS from *Coakley et al.* (2001), and diamonds to the mean from *Haller and Lyzenga* (2003). Blue dots are the median of the breaking events of the present data. (a) HH; (b) VV.

at this point. Bragg NRCS are several dB less than the observed, most notably for HH polarization and low grazing angles.

Regarding the data of *Coakley et al.* (2001) it is important to notice that it was collected at lower frequencies, whose effect on the model is the same as using particles of the smaller diameter. Based on our previous results, for those relatively small particles the model would thus predict a decrease of about -10 dB in the scattered power and increase in the absorption relative to particles of the same diameter but at a higher frequency (we have compared $d=0.5\text{ cm}$ and $f_v=10\%$ for frequencies 8.5 GHz and 9.36 GHz). The data, on the other hand, do not show this decrease and compare well with

the maximum NRCS from the airship data. The opposite effect would be expected for the HL data, which was collected at higher frequency, equivalent to larger particles.

The airship data also shows a significant amount of scatter but at magnitudes that are well predicted by the model and deviate significantly from Bragg scattering, despite being recorded at mid incidence angle where most of the scattering anomalies are less prominent. However, the median shows a decreasing trend with increasing grazing angle, which can not be accounted for by the model. A similar trend is shown by the maxima, which resembles the observations of *Farquharson et al.* (2005) who noticed a decay in the maximum NRCS of the bores as the waves progressed onshore.

Although the magnitudes and trends seem to be well recovered, it is apparent that the present data fall is at very low grazing angles that are predicted to be below the critical angle. It must be noted, however, that the model is run using the grazing angle relative to the layer, whereas the data have been presented in terms of the respective nominal grazing angles, that is, assuming a horizontal ocean surface. Therefore, there is a mismatch between the two due to the tilt of the roller surface. This effectively shifts the data on the figures toward larger grazing angles, as the effective grazing angle is $\theta_e = \theta_g + \theta_r$, where θ_r is the vertical angle of the roller. To measure this angle, *Coakley et al.* (2001) used the slope of the 50% volume fraction contour at the toe of the breaker and obtained values of $\theta_r = 20^\circ$ and 25° for the two breakers, the angle depending on the roller strength. These values are larger than the values obtained by *Duncan* (1981) for waves generated using a similar mechanism (towed hydrofoil), in which case $10.0^\circ \leq \theta_r \leq 14.7^\circ$. On the other hand, *Walstra et al.* (1996) analyzed prior laboratory data and suggested that the roller slope does not exceed $\theta_r \approx 6^\circ$. Even though the actual roller angle is not clearly defined, even slopes as small as $\theta_s = 3^\circ$ would cause the data to fall within the region where backscattering exists according to the model. However, the quality of the agreement is highly dependent on the θ_r value used. For instance in Fig. 6.12 the result of the exercise is shown for $\theta_s = 12^\circ$, the average value given by *Duncan* (1981). For this case, the different model combinations tested overpredict the median of

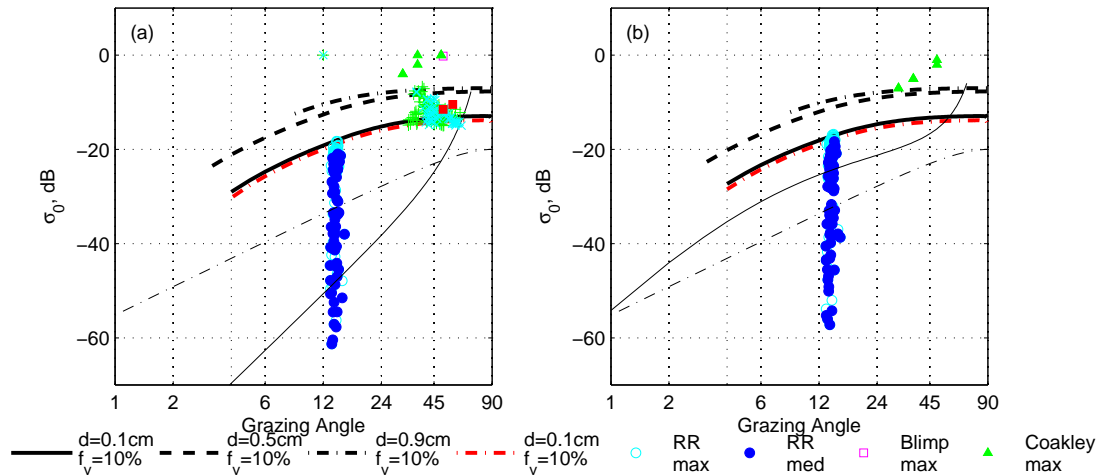


Fig. 6.12: Model data comparison including roller slope θ_s . $\theta_s = 12^\circ$ is used for the RiverRad data and $\theta_s = 25^\circ$ is used for *Coakley et al.* (2001) data. Same key as in Fig. 6.11

the data by a few dB but still agree well with the airship and HL data. This is due to the backscattering coefficient showing a stronger dependency on grazing angle at low values of θ_g .

The model predicts larger cross sections than those of the Bragg model until $\theta_g \approx 60^\circ$, where Bragg scattering predicts larger returns. However, this range is close to the limit of applicability of Bragg scattering, and at larger angles the model should be compared to specular scattering instead. Lack of experimental data in this range precludes a meaningful comparison. In addition the difference between the VV NRCS as predicted by Bragg and the present model with the smallest diameter is typically $O(10)$ dB for a wide range of grazing angles, but decreases for HH from very large at low grazing (30 dB difference at 10°) to values comparable to VV at mid incidence (6 dB difference at 50°). It is of note that the background HL data correlates well with the Bragg measurements. Although it could be argued that a surface spectrum used for the Bragg scatterers is not adequate (Eq. 6.43) to describe the very rough surface of the roller, using a more energetic spectrum would increase the backscattered power but would not affect the angular dependency significantly. Consequently, HH results would still be in

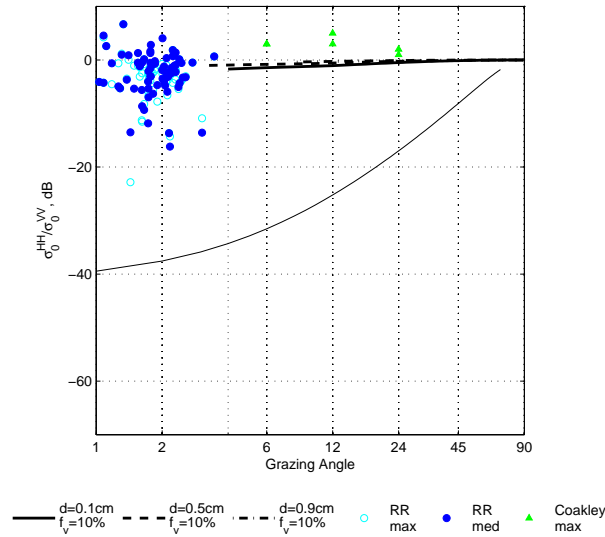


Fig. 6.13: Model data comparison of the polarization ratio. Thin line corresponds to the ratio as computed using Bragg theory.

disagreement with the data. On the other hand, it is clear that the effect of tilting could explain the difficulties in discriminating very steep waves from breaking waves, since for very steep waves (thus large θ_r) the Bragg and volumetric models could yield similar values.

Fig. 6.13 shows the model data comparison for the polarization ratio. Despite the scatter, the model predicts ratios that are in overall agreement with the results presented in the previous chapters, namely, $R \approx -5$ dB or more for breaking waves. However, the model does not reproduce the observed (weak) trend towards decaying ratios as the grazing angle increases; rather, it predicts a slightly-increasing trend. Perhaps more worrisome is the fact that model ratios do not exceed unity at any grazing angle. The latter has been considered one of the fundamental characteristics of scattering from breaking waves. However, as presented in the previous chapter, the present data suggest that most of the large polarization ratios take place near the front of the wave, where multipath interactions could be relevant as well. In fact, the present volumetric model predicts scattering in multiple directions, therefore multipath reflections can arise not only for line-of-sight (specular) reflections but also from diffuse reflections.

6.6 Summary

In the present chapter a first order volumetric model for the scattering from the wave roller was presented. The upper layers of the roller were considered as a two phase medium where water droplets immersed in air were the main scatterers. The model has a few physical parameters as input and no calibration parameters. In this study, the approach was to use a range of physically plausible values for these parameters and compare the model output with measured data.

Model results in general show a good agreement with the data, in particular with regards to the magnitude of the NRCS and its overall grazing angle dependency. It was shown that a few combinations of particle diameters and low volume fractions suffice to explain the data. Furthermore, the values of the physical parameters needed appear to be well correlated with laboratory measurements. While the resulting parameter space is considered appropriate, a proper model validation would require the use of measured parameters and distributions. For instance, it can be speculated that rather than a single diameter, multiple diameters could be present as a result of the splashing and turbulence present in the roller surface.

The model shows little differentiation between polarization states. Although the polarization ratio does not exceed unity, values are typically larger than -3 dB, consistent with the observations. The first order model presented here does not induce cross-polarized returns, a characteristic that has been observed previously from breaking waves. However, it is possible to expand the model to account to second and higher order interactions, in which case cross-polarization occurs. *Tsang et al.* (2007) showed that inclusion of higher order scattering induces larger scattering coefficients, although the difference is typically about of $O(5)$ dB or less. On the other hand, the albedo of the layer appears to be sufficiently small to suggest that the first order model is sufficiently accurate.

While the model itself cannot account for the broadness observed in the Doppler spectrum, the roller is considered to be advected by the underlying gravity wave. As

a result, the scatterers would have a net propagation speed equal to that of the phase speed of the wave. This speed would be the same for both polarization states. Therefore, the model is consistent with the observed peak at velocities near the phase speed of the carrier wave, but presently not with the broadening of the spectrum. However, the scatterers have been treated as static. Clusters traveling at different speeds relative to the roller could account for this. It is thus considered that the model is successful in reproducing most of the scattering characteristics typically associated to breaking waves.

7. SUMMARY AND CONCLUSIONS

This work has presented a study of microwave scattering from waves in the nearshore, with an emphasis on breaking waves. The rationale behind this effort is that microwave remote sensing is a relatively inexpensive tool that has shown the potential to be used in the estimation of wave related parameters over large domains synoptically. Among these parameters, wave breaking is relevant for nearshore dynamics and sediment transport. Therefore, it is of interest to evaluate if microwave remote sensing can be used for its measurement. First, a proper understanding of the mechanisms by which the ocean surface is imaged is required. A comprehensive review of the literature showed that many formulations have been proposed to explain microwave measurements at low grazing angles, a regime typical of nearshore deployments. Measurements tend to show a behavior that can not be explained by traditional scattering models such as the Composite Surface Theory. Most of these anomalous signatures have been related, although not unequivocally, to breaking waves. As a consequence of this, accurate discrimination between breaking and non-breaking waves remains elusive. Furthermore, despite the richness of the literature, most of the studies have been carried out for the analysis of deep water waves, either in the field or in the laboratory. The different dynamics and breaking characteristics between deep water and shallow water environments may prevent extrapolation of the deep water results to the nearshore. Thus it seemed that a gap in the observations was present.

With this in mind, a unique field experiment was carried out that combined three different remote sensors, namely two active microwave sensors operating at X-band and an optical sensor. One of the sensors was a marine radar (non-coherent, sector scanning and working at a single polarization) and the other a coherent, dual polarization Doppler radar operating in staring mode. The objective of the experiment was to be

able to characterize microwave backscattering in the surf zone, with a special emphasis on the differences depending on the wave stage (breaking, non-breaking and steepening waves) and to further assess the effect of remnant foam on the signals. Therefore, the first step was to develop a reliable discrimination method. In order to achieve this separation, the signals arising from the optical sensor and the marine radar were analyzed and characterized in terms of their probability density functions. It was confirmed that high microwave returns are well correlated with active wave breaking, although not uniquely. Attempts to discriminate breaking from non-breaking using each sensor separately yielded relatively good results, but required a significant amount of fine tuning. In contrast, a new hybrid methodology using the information from both sensors yielded better results specifically with regards to the overall structure and evolution of individual events. The methodology is robust in the sense that conservative values for the thresholds on each sensor suffice to provide good discrimination. However, because the remote signals from breaking waves can vary on short time and space scales, the method can be very sensitive to inaccuracies in the geo-location of individual pixels for each sensor. Finite amplitude misregistration effects and/or errors in the true heading of the microwave sensors can yield significant errors in the discrimination procedure. In addition, it is not clear how to quantitatively assess the method because no other methodology exist to date capable of identifying reliably wave breaking. Other aspects such as the difference in the size of the resolution cells could be important but have not been studied in detail here. Nevertheless, it is considered that the method is an improvement over existing methodologies such as time exposures or single sensor threshold methods, and it is capable of discriminating events on a wave-by-wave basis. This makes the method useful for estimating quantities such as the fraction of breaking waves, or to further assess the effect of foam on remotely sensed imagery. It is important to note that for the method to work, saturation of the signal needs to be avoided (which can be a problem for marine radars) to prevent false detection. This comes at the expense of decreasing the sensitivity at long ranges which in some cases is desired to expand the area coverage. The user would need

to clearly identify the monitoring needs and design the acquisition appropriately.

The discrimination results were then coupled with the data of the coherent radar to analyze several microwave parameters by source. These included the backscattered power at both polarizations, the average Doppler spectrum, and instantaneous Doppler offset (i.e., the velocity of the dominant scatterers). The analysis was carried out for different environmental conditions, with significant differences in the wind characteristics (magnitude and direction) and wave heights. In addition, foam coverage also varied significantly. It was found that breaking waves tend to show a similar response at both polarizations, whose magnitudes appear to be insensitive to the environmental conditions, usually peaking around -20 dB while exhibiting a weak grazing angle dependency. The cross-wave profile at this high scattering levels was broader for HH than that for VV, which meant that large polarization ratios, typically exceeding unity could be present. This behavior was confined to one or two resolution cells near the front of the wave, after which both polarizations showed similar magnitudes for a few resolution cells. Here VV was slightly larger, thus yielding polarization ratios slightly less than unity. Similar behavior have been observed in previous research, suggesting that the peak in HH could be due to multipath scattering from the bore front where VV could be affected by damping near the Brewster angle. Behind the front of the bore, both polarizations seem to be responding to the same population of scatterers, located on the roller surface, thus the same scattering mechanism.

Analysis of steepening waves showed that VV returns were usually larger than HH, although there were also events showing the opposite. This behavior is also consistent with prior observations, where the (long) steepening waves can be modeled in the frame of Composite Surface Theory. Local steep short waves riding on top the longer carrier waves can yield multipath effects that raise the HH returns. Most important for the purposes of discrimination, it was found that in general these steepening waves have cross sections that are a few dB less than those observed for active breaking waves, although in some cases a clear differentiation is not possible. Also it is noteworthy that the large ratios for

steepening waves mean that the polarization ratio alone is not a reliable discriminator. The analysis of foam covered surfaces presented a substantial challenge, because it was initially found that foam could be the source of large backscattered power, of similar magnitude to that of active breaking, but also of weak scattering levels that could be explained by CST as well. It was found that in many cases, the large power exhibited by foam correspond to active breaking not being identified properly for the algorithm. This situation coupled with the observed low scattering levels for other cases, confirmed that foam is typically a weak scattering source.

Analysis of the Doppler spectra showed that the presence of a few breaking events is sufficient to broaden the spectra considerably and produce a peak at high frequencies, thus large velocities. This further confirms that the power of breaking events is significantly larger than that of non-breaking waves at each polarization. The broadness of the spectrum is consistent with the notion of scatterers traveling at a range of speeds relative to the speed of the carrier wave. When breaking is absent, the Doppler spectrum was consistent with scattering from Bragg waves, with VV returns larger than HH. The time and space series of the Doppler offset from breaking waves were well correlated to the expected range of phase speeds of the gravity waves. However, near the front of the wave local speeds were significantly larger, which can be due to jet ejections, splashing and the advance of the bore front relative to the wave itself. Behind this front, speeds were smaller (but still well correlated to the phase speed of the wave) suggesting that the roller was locally expanding. Non-breaking waves showed velocities that were typically bounded by the expected value of the wave orbital velocities, although the effect of mean surface currents was not included in the analysis. This behavior is consistent with scattering in the frame of CST.

Thus, it was clear that breaking waves have backscattering characteristics that are distinguishable from other sources. These characteristics can be summarized by large backscattered power showing a weak polarization dependency; these values were sustained over relatively large distances ($O(20\text{ m})$); a weak grazing angle dependency of

the maxima; local positive peaks of the polarization ratio followed by more stable and negative values; large Doppler offsets correlated with the speed of the carrier wave and broad Doppler spectrum due to scatterers traveling at a range of speeds.

While previous scattering models can explain some of these characteristics, none can explain all of them simultaneously. In addition, all scattering models have largely neglected the multi-phase structure of the wave roller. To address this, the wave roller was modeled as a single layer of droplets above the underlying wave surface. The backscattering coefficient from this collection of scatterers was modeled using the first-order Dense Media Radiative Transfer (DMRT) theory. Under this approach, scattering and absorption of the incident electromagnetic fields are accounted for by including coherent and incoherent interactions between the fields exciting the particles and also interactions with the medium boundaries which is the water surface in this case. Collective scattering effects are included by means of the quasi-crystalline approximation (QCA) to model the extinction coefficient of the dense media. The method requires a few physical input parameters, such as individual particle size, total volume fraction, stickiness parameter (to account for clustering), the relative electric permittivity, and the operating microwave frequency. The model is state of the art and was previously applied to tenuous particles such as snow. Model results are compared against the present data set and prior data sets from field experiments at larger grazing angles. It is found that the magnitude of the backscattering and angular dependency is well reproduced, although maximum values were not well modeled. This suggests that other mechanisms could be taking place in addition to the proposed model, for example, the suggested multipath scattering from the bore front. This is considered the case because the model is capable of reproducing the observed small negative polarization ratios, but not the positive ratios observed near the wave front. By assuming the scatterers to travel with the wave speed, the observed shift toward higher frequencies in the Doppler spectrum can be explained, although the broadening of the spectrum and large velocities near the wave front are not accounted for because the scatterers are considered motionless. In addition, the model predicts values

larger than CST at very low grazing angles, but the difference becomes negligible at larger effective angles, consistent with the observed behavior as the wave steepens where the differentiation becomes less clear.

While a proper model validation would require further testing at multiple grazing angles using a more appropriate description of the particle distributions and their characteristics, the model is considered successful. In consequence, it can be said that microwave scattering from the wave roller is the result of the enhancement due to multiple particle interactions which induce incoherent interactions adding constructively. Particles of large diameter scattering in the Mie regime are the main contributors, and small volume fractions are sufficient. Furthermore, the lossy nature of sea water induces large absorption, which in addition to the large scattering causes the total extinction to be large. Therefore, the optical depth is typically large. As a result, the incoming wave energy decays quickly while propagating through the layer, reducing the contribution of multiple interactions with the underlying medium.

The implications of this modeling exercise are multifold. First, it provides partial answers to the basic science problem of microwave scattering from breaking waves. At the same time, it can provide a physical background to the scattering levels which can enhance our understanding of the signal. If a more thorough characterization in terms of frequency, grazing angle and particle sizes is achieved, it would be possible to provide definite threshold levels that would provide further guidance to breaking detection algorithms. In addition, roller length scales could be retrieved which could enhance our modeling of the roller per se, a situation desirable from the perspective of nearshore modeling. On the other hand, the model could be coupled with phase resolving models for the wave evolution to provide forward modeling of the signal, thus improving our understanding of the observed data.

BIBLIOGRAPHY

- Aarninkhof, S., and B. G. Ruessink (2004), Video observations and model predictions of depth-induced dissipation, *IEEE Transactions on Geoscience and Remote Sensing*, *42*(11), 2612–2622, doi:10.1109/TGRS.2004.835349.
- Ahmed, A. S. M., and S. Taketawa (2005), PIV analysis of filtered radar images to derive nearshore wave properties and bathymetry at Hasaki, Japan, in *Coastal Dynamics '05*.
- Andreas, E. L., J. B. Edson, E. C. Monahan, M. P. Rouault, and S. D. Smith (1995), The spray contribution to net evaporation from the sea: A review of recent progress, *Boundary-Layer Meteorology*, *72*(1), 3–52, doi:10.1007/BF00712389.
- Anguelova, M. D. (2008), Complex dielectric constant of sea foam at microwave frequencies, *Journal of Geophysical Research*, *113*(C8), C08,001, doi:10.1029/2007JC004212.
- Banner, M. L., and E. H. Fooks (1985), On the microwave reflectivity of small-scale breaking water waves, *Proc. R. Soc. London A*, *399*(1816), 93–109.
- Barrowes, B., and D. Long (2002), Evaluation of a compound probability model with tower-mounted scatterometer data, *IEEE Transactions on Antennas and Propagation*, *40*(1), 42–49, doi:10.1109/36.981348.
- Bass, F. G., I. M. Fuks, A. I. Kalmykov, I. E. Ostrovsky, and A. D. Rosenberg (1968), Very high frequency radio scattering by a disturbed sea surface: 2, Scattering from an actual sea surface, *IEEE Trans. Antennas Propag.*, *AP-16*, 560–568.
- Baxter, R. J. (1968), Percus–Yevick Equation for Hard Spheres with Surface Adhesion, *The Journal of Chemical Physics*, *49*(6), 2770–2774, doi:10.1063/1.1670482.
- Beckmann, P., and A. Spizzichino (1987), *Scattering of electromagnetic waves from rough surfaces*, 511 pp., Artech House, Norwood, MA.
- Bell, P. S. (1999), Shallow water bathymetry derived from an analysis of X-band marine radar images, *Coastal Engineering*, *37*, 513–527, doi:10.1016/S0378-3839(99)00041-1.
- Blenkinsopp, C., and J. Chaplin (2007), Void fraction measurements in breaking waves, *Proceedings of the Royal Society A: Mathematical, Physical and Engineering Sciences*, *463*(2088), 3151–3170, doi:10.1098/rspa.2007.1901.
- Braun, N., F. Ziemer, A. Bezuglov, M. Cysewski, and G. Schymura (2008), Sea-surface current features observed by Doppler radar, *IEEE Transactions on Geoscience and Remote Sensing*, *46*(4), 1125–1133, doi:10.1109/TGRS.2007.910221.

- Catalán, P., and M. Haller (2008), Remote sensing of breaking wave phase speeds with application to nonlinear depth inversion, *Coastal Engineering*, 55, 93–111, doi:10.1016/j.coastaleng.2007.09.010.
- Chanson, H. (2004), Unsteady air-water flow measurements in sudden open channel flows, *Experiments in Fluids*, 37(6), 899–909, doi:10.1007/s00348-004-0882-3.
- Chen, C.-T., L. Tsang, J. Guo, A. Chang, and K.-H. Ding (2003a), Frequency dependence of scattering and extinction of dense media based on three-dimensional simulations of Maxwell's equations with applications to snow, *IEEE Transactions on Geoscience and Remote Sensing*, 41(8), 1844–1852, doi:10.1109/TGRS.2003.811812.
- Chen, D., L. Tsang, L. Zhou, S. Reising, W. Asher, L. Rose, K.-H. Ding, and C.-T. Chen (2003b), Microwave emission and scattering of foam based on monte carlo simulations of dense media, *IEEE Transactions on Geoscience and Remote Sensing*, 41(4), 782–790, doi:10.1109/TGRS.2003.810711.
- Chen, K., A. Fung, and D. Weissman (1992), A backscattering model for ocean surface, *IEEE Transactions on Geoscience and Remote Sensing*, 30(4), 811–817, doi:10.1109/36.158877.
- Chickadel, C. C., R. A. Holman, and M. H. Freilich (2003), An optical technique for the measurement of longshore currents, *Journal of Geophysical Research*, 108(C8), 3364, doi:10.1029/2003JC001774,2003.
- Cloude, S., and D. Corr (2002), A new parameter for soil moisture estimation, in *IEEE International Geoscience and Remote Sensing Symposium, 2002. IGARSS '02.*, vol. 1, pp. 641–643vol.1, doi:10.1109/IGARSS.2002.1025131.
- Cloude, S., and E. Pottier (1996), A review of target decomposition theorems in radar polarimetry, *IEEE Transactions on Antennas and Propagation*, 34(2), 498–518, doi:10.1109/36.485127.
- Cloude, S., and E. Pottier (1997), An entropy based classification scheme for land applications of polarimetric sar, *IEEE Transactions on Antennas and Propagation*, 35(1), 68–78, doi:10.1109/36.551935.
- Coakley, D. B., P. M. Haldeman, D. G. Morgan, K. R. Nicolas, D. R. Penndorf, L. B. Wetzell, and C. S. Weller (2001), Electromagnetic scattering from large steady breaking waves, *Experiments in Fluids*, 30(5), 479–487, doi:10.1007/s003480000220.
- Cox, C., and W. Munk (1954), Statistics of the sea surface derived from sun glitter, *J. Mar. Res.*, 13(2), 198–227.
- Dankert, H., and W. Rosenthal (2004), Ocean surface determination from X-Band radar-image sequences, *Journal of Geophysical Research*, 109, C04,016, doi:10.1029/2003JC002130.
- Dano, E. B., D. R. Lyzenga, G. Meadows, L. Meadows, H. van Sumeren, and R. Onstott (2001a), Radar backscatter from mechanically generated transient breaking waves. I.

- Angle of incidence dependence and high resolution surface morphology, *IEEE Journal of Oceanic Engineering*, *26*(2), 181–200, doi:10.1109/48.922786.
- Dano, E. B., D. R. Lyzenga, G. Meadows, L. Meadows, H. van Sumeren, and R. Onstott (2001b), Radar backscatter from mechanically generated transient breaking waves. II. Azimuthal and grazing angle dependence, *IEEE Journal of Oceanic Engineering*, *26*(2), 201–215, doi:10.1109/48.922787.
- Deane, G. B. (1997), Sound generation and air entrainment by breaking waves in the surf zone, *The Journal of the Acoustical Society of America*, *102*(5), 2671–2689, doi: 10.1121/1.420321.
- Deane, G. B., and M. D. Stokes (1999), Air entrainment processes and bubble size distributions in the surf zone, *Journal of Physical Oceanography*, *29*, 1393–1403, doi: 10.1175/1520-0485(1999)029<1393:AEPABS>2.0.CO;2.
- Ding, K. H., L. Tsang, and S. E. Shih (2001), Monte carlo simulations of particle positions for densely packed multispecies sticky particles, *Microwave and Optical Technology Letters*, *30*(3), 187–192, doi:10.1002/mop.1261.
- Duncan, J. (1981), An experimental investigation of breaking waves produced by a towed hydrofoil, *Proc. R. Soc. London A*, *377*(1770), 331–348.
- Ellison, W., A. Balana, G. Delbos, K. Lamkaouchi, L. Eymard, C. Guillou, and C. Prigent (1998), New permittivity measurements of seawater, *Radio Science*, *33*(3), 639–648.
- Ericson, E. A., D. R. Lyzenga, and D. T. Walker (1999), Radar backscatter from stationary breaking waves, *Journal of Geophysical Research*, *104*(C12), 29,679–29,695, doi:10.1029/1999JC900223.
- Farquharson, G., , S. J. Frasier, B. Raubenheimer, and S. Elgar (2005), Microwave radar cross sections and doppler velocities measured in the surf zone, *Journal of Geophysical Research*, *110*(C12), C12,024, doi:10.1029/2005JC003022.
- Forget, P., M. Saillard, and P. Broche (2006), Observations of the sea surface by coherent L band radar at low grazing angles in a nearshore environment, *Journal of Geophysical Research*, *111*, C09,015, doi:10.1029/2005JC002900.
- Fowler, B. W. (1983), Expansion of Mie-theory phase functions in series of Legendre polynomials, *J. Opt. Soc. Am.*, *73*(1), 19–22.
- Frasier, S. J., Y. Liu, and R. E. McIntosh (1998), Space-time properties of radar sea spikes and their relation to wind and wave conditions, *Journal of Geophysical Research*, *103*(C9), 18,745–18,757, doi:10.1029/98JC01456.
- Frouin, R., M. Schwindling, and P.-Y. Deschamps (1996), Spectral reflectance of sea foam in the visible and near-infrared: In situ measurements and remote sensing implications, *Journal of Geophysical Research*, *101*(C6), 14,361–14,371.

- Fuchs, J., D. Regas, T. Waseda, S. Welch, and M. P. Tulin (1999), Correlation of hydrodynamic features with LGA radar backscatter from breaking waves, *IEEE Transactions on Geoscience and Remote Sensing*, 37(5), 2442–2460, doi:10.1109/36.789641.
- Gommenginger, C., N. Ward, G. Fisher, I. Robinson, and S. Boxall (2000), Quantitative microwave backscatter measurements from the ocean surface using digital marine radar images, *Journal of Atmospheric and Oceanic Technology*, 17, 665–678, doi:10.1175/1520-0426(2000)017(0665:QMBMFT)2.0.CO;2.
- Gotwols, B., and W. Keller (1990), Radar backscatter statistics from water waves, in *OCEANS '90. 'Engineering in the Ocean Environment'. Conference Proceedings*, pp. 240–242.
- Gotwols, B. L., and D. R. Thompson (1994), Ocean microwave backscatter distributions, *Journal of Geophysical Research*, 99(C5), 9741–9750, doi:10.1029/93JC02649.
- Gutnik, V., G. Kulemin, and L. Sharapov (2001), Spike statistics features of the radar sea clutter in the millimeter wave band at extremely small grazing angles, in *Physics and Engineering of Millimeter and Sub-Millimeter Waves, 2001. The Fourth International Kharkov Symposium on*, vol. 1, pp. 426–428, doi:10.1109/MSMW.2001.946876.
- Haller, M. C., and P. A. Catalán (), Remote sensing of surf zone breaking waves and roller dissipation, *submitted to Journal of Geophysical Research*.
- Haller, M. C., and D. R. Lyzenga (2003), Comparison of radar and video observations of shallow water breaking waves, *IEEE Transactions on Geoscience and Remote Sensing*, 41(4), 832–844, doi:10.1109/TGRS.2003.810695.
- Hesany, V., W. Plant, W. Keller, and K. Hayes (1996), Observed space-time structure of radar backscatter from the ocean surface, in *IEEE International Geoscience and Remote Sensing Symposium, 1996. IGARSS '96. 'Remote Sensing for a Sustainable Future.'*, vol. 3, pp. 1733–1735.
- Hessner, K., K. Reichert, J. Dannenberg, K. Hathaway, and D. Resio (2006), 2-D surface elevation measurements by means of X-band radar: An application of WAMOS II at Duck, in *9th International Workshop on Wave Hindcasting and Forecasting*.
- Holland, T. K., R. A. Holman, T. C. Lippmann, J. Stanley, and N. Plant (1997), Practical use of video imagery in nearshore oceanographic studies, *IEEE Journal of Oceanic Engineering*, 22(1), 81–92, doi:10.1109/48.557542.
- Holliday, D., L. L. DeRaad Jr, and G. J. St-Cyr (1996), Forward-backward: a new method for computing low-grazing angle scattering, *IEEE Transactions on Antennas and Propagation*, 44(5), 722, doi:10.1109/8.496263.
- Holliday, D., L. L. DeRaad, Jr, and G. J. St-Cyr (1998a), Sea-spike backscatter from a steepening wave, *IEEE Transactions on Antennas and Propagation*, 46(1), 108–113, doi:Sea-SpikeBackscatterfromaSteepeningWave.

- Holliday, D., L. L. DeRaad Jr, and G. J. St-Cyr (1998b), Forward-backward method for scattering from imperfect conductors, *IEEE Transactions on Antennas and Propagation*, *46*(1), 101–107, doi:10.1109/8.655456.
- Holman, R., and J. Stanley (2007), The history and technical capabilities of Argus, *Coastal Engineering*, *54*, 477–491, doi:10.1016/j.coastaleng.2007.01.003.
- Huang, X., and Y. Jin (1995), Scattering and emission from two-scale randomly rough sea surface with foam scatterers, *IEE Proc. Microwaves, Antennas and Propagation*, *142*(2), 109–114.
- Hwang, P. A., M. A. Sletten, and J. V. Toporkov (2008a), Analysis of radar sea return for breaking wave investigation, *Journal of Geophysical Research*, *113*, C02,003, doi:10.1029/2007JC004319.
- Hwang, P. A., M. A. Sletten, and J. V. Toporkov (2008b), Breaking wave contribution to low grazing angle radar backscatter from the ocean surface, *Journal of Geophysical Research*, *113*, C09,017, doi:10.1029/2008JC004752.
- Ishimaru, A. (1978), *Wave Propagation and Scattering in Random Media*, vol. 1 & 2, Academic Press, New York.
- Ja, S. J., J. C. West, H. B. Qiao, and J. H. Duncan (2001), Mechanisms of low-grazing-angle scattering from spilling breaker water waves, *Radio Science*, *36*(C5), 981–998, doi:10.1029/2000RS002564.
- Jähne, B., J. Klinke, and S. Waas (1994), Imaging of short ocean wind waves: a critical theoretical review, *J. Opt. Soc. Am. A*, *11*(8), 2197–2209.
- Jessup, A. T., W. C. Keller, and W. K. Melville (1990), Measurements of sea spikes in microwave backscatter at moderate incidence, *Journal of Geophysical Research*, *95*(C6), 9679–9688.
- Jessup, A. T., W. K. Melville, and W. C. Keller (1991), Breaking waves affecting microwave backscatter. 1. Detection and verification, *Journal of Geophysical Research*, *96*, 20,547–20,559.
- Kalmykov, A. I., and V. V. Pustovoytenko (1976), On polarization features of radio signals scattered from the sea at small grazing angles, *Journal of Geophysical Research*, *81*, 1960–1964.
- Kalmykov, A. I., A. S. Kurekin, Y. A. Lementa, I. E. Ostrovskii, and V. V. Pustovoitenko (1976), Characteristics of SFH scattering at breaking sea waves, *Radiophysics and Quantum Electronics*, *19*(9), 923–928, doi:10.1007/BF01044049.
- Kerr, D. E. (1951), *Propagation of Short Radio Waves*, McGraw-Hill.
- Kim, H., and J. Johnson (2002), Radar image study of simulated breaking waves, *IEEE Transactions on Geoscience and Remote Sensing*, *40*(10), 2143–2150, doi:10.1109/TGRS.2002.802475.

- Koepke, P. (1984), Effective reflectance of oceanic whitecaps, *Applied Optics*, *23*(11), 1816–1824.
- Kudryavtsev, V., D. Hauser, G. Caudal, and B. Chapron (2003a), A semiempirical model of the normalized radar cross-section of the sea surface. 1. Background model, *Journal of Geophysical Research*, *108*(C3), 8054, doi:10.1029/2001JC001003.
- Kudryavtsev, V., D. Hauser, G. Caudal, and B. Chapron (2003b), A semiempirical model of the normalized radar cross-section of the sea surface. 2. Radar modulation transfer function, *Journal of Geophysical Research*, *108*(C3), 8055, doi:10.1029/2001JC001004.
- Kwoh, D. S. W., and B. M. Lake (1984), A deterministic, coherent, and dual-polarized laboratory study of microwave backscattering from water waves, Part I: Short gravity waves without wind, *Journal of Oceanic Engineering*, *9*(5), 291–308.
- Lamont-Smith, T. (2000), Translation to the normal distribution for radar clutter, *Radar, Sonar and Navigation, IEE Proceedings -*, *147*(1), 17–22, doi:10.1049/ip-rsn:20000043.
- Lax, M. (1952), Multiple scattering of waves. II. The effective field in dense systems, *Phys. Rev.*, *85*(4), 621–629, doi:10.1103/PhysRev.85.621.
- Lee, P. H., J. D. Barter, K. L. Beach, C. L. Hindman, B. M. Lake, H. Rungaldier, J. C. Shelton, A. B. Williams, and H. C. Yuan (1995), X band microwave backscattering from ocean waves, *Journal of Geophysical Research*, *100*(C2), 2591–2611, doi:10.1029/94JC02741.
- Lee, P. H. Y., J. D. Barter, K. L. Beach, B. M. Lake, H. Rungaldier, H. R. Thompson Jr, and R. Yee (1998), Scattering from breaking gravity waves without wind, *IEEE Transactions on Antennas and Propagation*, *46*(1), 14–26, doi:10.1109/8.655447.
- Lee, P. H. Y., J. D. Barter, K. L. Beach, B. M. Lake, H. Rungaldier, H. R. Thompson Jr., L. Wang, and R. Yee (1999), What are the mechanisms for non-Bragg scattering from water wave surfaces?, *Radio Science*, *34*(1), 123–128, doi:10.1029/1998RS900024.
- Lewis, B. L., and I. D. Olin (1980), Experimental study and theoretical model of high-resolution radar backscatter from sea surfaces, *Radio Science*, *15*(4), 815–828.
- Li, Y., and J. West (2006), Low-grazing-angle scattering from 3-D breaking water wave crests, *IEEE Transactions on Geoscience and Remote Sensing*, *44*(8), 2093–2101, doi:10.1109/TGRS.2006.872129.
- Liang, D., X. Xu, L. Tsang, K. Andreadis, and E. Josberger (2007), Modeling multi-layer effects in passive microwave remote sensing of dry snow using Dense Media Radiative Transfer Theory (DMRT) based on quasicrystalline approximation, in *IEEE Geoscience and Remote Sensing Symposium, 2007. IGARSS 2007*, pp. 1215–1218, doi:10.1109/IGARSS.2007.4423024.
- Liang, D., X. Xu, L. Tsang, K. M. Andreadis, and E. G. Josberger (2008), The effects of layers in dry snow on its passive microwave emissions using dense media radiative transfer theory based on the quasicrystalline approximation (qca/dmrt), *Geoscience*

- and Remote Sensing, *IEEE Transactions on*, 46(11), 3663–3671, doi:10.1109/TGRS.2008.922143.
- Lippmann, T. C., and R. A. Holman (1989), Quantification of sandbar morphology: A video technique based on wave dissipation, *Journal of Geophysical Research*, 94(C1), 995–1011.
- Liu, Y., S. Frasier, and R. McIntosh (1998), Measurement and classification of low grazing angle radar sea spikes, *IEEE Transactions on Antennas and Propagation*, 46(1), 27–40, doi:10.1109/8.655448.
- Loewen, M. R., and W. K. Melville (1991), Microwave backscatter and acoustic radiation of breaking waves, *Journal of Fluid Mechanics*, 224, 601–623, doi:10.1017/S0022112091001891.
- Long, M. (1983), *Radar Reflectivity of Land and Sea*, Artech House, Inc.
- Longuet-Higgins, M. S. (1963), The effect of non-linearities on statistical distributions in the theory of sea waves, *Journal of Fluid Mechanics*, 17, 459–480, doi:10.1017/S0022112063001452.
- Longuet-Higgins, M. S., and N. D. Smith (1983), Measurement of breaking waves by a surface jump meter, *Journal of Geophysical Research*, 88(C14), 9823–9831.
- Lyzenga, D. R., and E. A. Ericson (1998), Numerical calculations of radar scattering from sharply peaked ocean waves, *IEEE Transactions on Geoscience and Remote Sensing*, 36(2), 636–646, doi:10.1109/36.662744.
- Lyzenga, D. R., A. L. Maffet, and R. A. Shuchman (1983), The contribution of wedge scattering to the radar cross section of the ocean surface, *IEEE Transactions on Geoscience and Remote Sensing*, 31, 502–505.
- Mandt, C., Y. Kuga, L. Tsang, and A. Ishimaru (1992), Microwave propagation and scattering in a dense distribution of non-tenuous spheres: experiment and theory, *Waves in Random Media*, 2(3), 225–234, doi:10.1088/0959-7174/2/3/004.
- McIntosh, R. E., S. J. Frasier, and J. B. Mead (1995), FOPAIR: A focused array imaging radar for ocean remote sensing, *IEEE Transactions on Geoscience and Remote Sensing*, 33(1), 115–124, doi:10.1109/36.368216.
- McNinch, J. E. (2007), Bar and Swash Imaging Radar BASIR: A mobile X-band radar designed for mapping nearshore sand bars and swash-defined shorelines over large distances, *Journal of Coastal Research*, 23(1), 59–74, doi:10.2112/05-0452.1.
- Melief, H. W., H. Greidanus, P. van Genderen, and P. Hoogeboom (2006), Analysis of sea spikes in radar sea clutter data, *IEEE Transactions on Geoscience and Remote Sensing*, 44(4), 985–993, doi:10.1109/TGRS.2005.862497.
- Melville, W. K., M. R. Loewen, F. C. Felizardo, A. T. Jessup, and M. J. Buckingham (1988), Acoustic and microwave signatures of breaking waves, *Nature*, 336, 54–56.

- Mori, N., T. Suzuki, and S. Kakuno (2007), Experimental study of air bubbles and turbulence characteristics in the surf zone, *Journal of Geophysical Research*, 112(C5), C05,014, doi:10.1029/2006JC003647.
- Morris, J., and S. Anderson (2005), Polarimetric characteristics of radar echoes from near shore wave fields at low grazing angles, in *IEEE International Geoscience and Remote Sensing Symposium, 2005. IGARSS '05.*, vol. 1, pp. 4 pp.–, doi:10.1109/IGARSS.2005.1526099.
- Morris, J., S. Anderson, and S. Cloude (2003), A study of the X-band entropy of breaking ocean waves, in *IEEE International Geoscience and Remote Sensing Symposium, 2003. IGARSS '03.*, vol. 2, pp. 711–713 vol.2, doi:10.1109/IGARSS.2003.1293892.
- Nieto-Borge, J., P. Jarabo-Amores, D. de la Mata-Moya, and F. López-Ferreras (2006), Estimation of ocean wave heights from temporal sequences of X-band marine radar images, in *XIV European Signal Processing Conference.*
- Oguchi, T. (1983), Electromagnetic wave propagation and scattering in rain and other hydrometeors, *Proceedings of the IEEE*, 71(9), 1029–1078.
- Padmanabhan, S., S. C. Reising, W. E. Asher, L. A. Rose, and P. W. Gaiser (2006), Effects of foam on ocean surface microwave emission inferred from radiometric observations of reproducible breaking waves, *IEEE Transactions on Geoscience and Remote Sensing*, 44(3), 569–583, doi:10.1109/TGRS.2006.870234.
- Phillips, O. (1988), Radar returns from the sea surface: Bragg scattering and breaking waves, *Journal of Physical Oceanography*, 18(8), 1065–1074, doi:10.1175/1520-0485(1988)018<1065:RRFTSS>2.0.CO;2.
- Phillips, O. M. (1985), Spectral and statistical properties of the equilibrium range in wind-generated gravity waves, *Journal of Fluid Mechanics*, 156, 505–531, doi:10.1017/S0022112085002221.
- Pierson, W. J. (1990), Dependence of radar backscatter on environmental parameters, in *Surface Waves and Fluxes*, vol. II, edited by G. L. Gernaert and W. J. Plant, chap. 13, pp. 173–220, Kluwer Academic Publishers.
- Plant, W., W. Keller, and K. Hayes (2005), Measurement of river surface currents with coherent microwave systems, *IEEE Transactions on Geoscience and Remote Sensing*, 43(6), 1242–1257, doi:10.1109/TGRS.2005.845641.
- Plant, W. J. (1990), Bragg sea scattering of electromagnetic waves from the air/sea interface, in *Surface Waves and Fluxes*, vol. II, edited by G. L. Gernaert and W. J. Plant, chap. 11, pp. 41–108, Kluwer Academic Publishers.
- Plant, W. J. (1997), A model for microwave Doppler sea return at high incidence angles: Bragg scattering from bound, tilted waves, *Journal of Geophysical Research*, 102(C9), 21,131–21,146, doi:10.1029/97JC01225.
- Plant, W. J. (2003a), Microwave sea return at moderate to high incidence angles, *Waves in Random Media*, 13, 339–354, doi:10.1088/0959-7174/13/4/009.

- Plant, W. J. (2003b), A new interpretation of sea-slope probability density functions, *Journal of Geophysical Research*, 108(C9), 3925, doi:10.1029/2003JC001870.
- Plant, W. J., E. A. Terray, R. A. Petitt, and W. C. Keller (1994), The dependence of microwave backscatter from the sea on illuminated area: Correlation times and lengths, *Journal of Geophysical Research*, 99(C5), 9705–9723, doi:10.1029/93JC00862.
- Pottier, E., and J. Lee (1999), Application of the H/A/Alpha polarimetric decomposition theorem for unsupervised classification of fully polarimetric SAR data based on the Wishart distribution, in *Proceedings of CEOS SAR workshop*, pp. 335–340.
- Puleo, J. A., G. Farquharson, S. J. Frasier, and K. T. Holland (2003), Comparison of optical and radar measurements of surf and swash zone velocity fields, *Journal of Geophysical Research*, 108(C3), 3100, doi:10.1029/2002JC001483.
- Raizer, V. (2007), Macroscopic foam-spray models for ocean microwave radiometry, *IEEE Transactions on Geoscience and Remote Sensing*, 45(10), 3138–3144, doi:10.1109/TGRS.2007.895981.
- Rino, C. L., and H. D. Ngo (1998), Numerical simulation of low-grazing-angle ocean microwave backscatter and its relation to sea spikes, *IEEE Transactions on Antennas and Propagation*, 46(1), 133–141, doi:10.1109/8.655460.
- Ruessink, B. G., P. S. Bell, I. M. J. van Enkevort, and S. G. J. Aarninkhof (2002), Nearshore bar crest location quantified from time-averaged X-band radar images, *Coastal Engineering*, 45, 19–32, doi:10.1016/S0378-3839(01)00042-4.
- Schuler, D. L., J. S. Lee, D. Kasilingam, and E. Pottier (2004), Measurement of ocean surface slopes and wave spectra using polarimetric sar image data, *Remote Sensing of Environment*, 91(2), 198–211, doi:10.1016/j.rse.2004.03.008.
- Seaton, N. A., and E. D. Glandt (1987), Monte Carlo simulation of adhesive spheres, *The Journal of Chemical Physics*, 87(3), 1785–1790, doi:10.1063/1.453724.
- Seemann, J., C. Senet, U. Wolff, and F. Ziemer (2000), Nautical X-band radar image processing: monitoring of morphodynamic processes in coastal waters, in *OCEANS 2000 MTS/IEEE Conference and Exhibition*, vol. 2, pp. 1329–1335vol.2, doi:10.1109/OCEANS.2000.881788.
- Sharkov, E. (2007), *Breaking Ocean Waves: Geometry, Structure and Remote Sensing*, Springer-Verlag.
- Shaw, J. A., and J. H. Churnside (1997), Scanning-laser glint measurements of sea-surface slope statistics, *Appl. Opt.*, 36(18), 4202–4213, doi:10.1364/AO.36.004202.
- Sletten, M. (1998), Multipath scattering in ultrawide-band radar sea spikes, *IEEE Transactions on Antennas and Propagation*, 46(1), 45–56, doi:10.1109/8.655450.
- Sletten, M., G. Smith, X. Liu, and J. Duncan (2004), Experimental investigation of radar backscatter from plunging breakers using an ultrawideband radar and visible/infrared cameras, in *IEEE International Geoscience and Remote Sensing Symposium, 2004. IGARSS '04.*, vol. 1, doi:10.1109/IGARSS.2004.1369045.

- Sletten, M. A., and J. Wu (1996), Ultrawideband, polarimetric radar studies of breaking waves at low grazing angles, *Radio Science*, *31*(1), 181–192, doi:10.1029/95RS01762.
- Sletten, M. A., D. B. Trizna, and J. P. Hansen (1996), Ultrawide-band radar observations of multipath propagation over the sea surface, *IEEE Transactions on Antennas and Propagation*, *44*(5), 646, doi:10.1109/8.496249.
- Sletten, M. A., J. C. West, X. Liu, and J. H. Duncan (2003), Radar investigations of breaking water waves at low grazing angle with simultaneous high-speed optical imagery, *Radio Science*, *38*(6), 1110, doi:10.1029/2002RS002716.
- Smith, J. M., E. M. Poulter, and J. McGregor (1996), Doppler radar measurements of wave groups and breaking waves, *Journal of Geophysical Research*, *101*(C6), 14,269–14,282, doi:10.1029/96JC00766.
- Stilwell, D. (1969), Directional energy spectra of the sea from photographs, *J. Geophys. Res.*, *74*(8), 1974–1986.
- Svendsen, I. A. (1984), Mass flux and undertow in the surf zone, *Coastal Engineering*, *8*, 347–365, doi:10.1016/0378-3839(84)90030-9.
- Terrill, E. J., and W. K. Melville (2000), A broadband acoustic technique for measuring bubble size distributions: Laboratory and shallow water measurements, *Journal of Atmospheric and Oceanic Technology*, *17*(2), 220–239, doi:10.1175/1520-0426(2000)017<0220:ABATFM>2.0.CO;2.
- Thompson, D. R., and B. L. Gotwols (1994), Comparisons of model predictions for radar backscatter amplitude probability density functions with measurements from SAXON, *Journal of Geophysical Research*, *99*(C5), 9725–9739, doi:10.1029/93JC02650.
- Thornton, E. B., and R. T. Guza (1982), Energy saturation and phase speeds measured on a natural beach, *Journal of Geophysical Research*, *87*(C12), 9499–9508.
- Toporkov, J., and M. Sletten (2005), Numerical study of low grazing range-resolved radar backscatter from the sea surface, in *Users Group Conference, 2005*, pp. 58–64, doi:10.1109/DODUGC.2005.47.
- Toporkov, J. V., and M. A. Sletten (2007), Statistical properties of low-grazing range-resolved sea surface backscatter generated through two-dimensional direct numerical simulations, *IEEE Transactions on Geoscience and Remote Sensing*, *45*(5), 1181–1197, doi:10.1109/TGRS.2007.894442.
- Trizna, D., J. P. Hansen, P. Hwang, and J. Wu (1991), Laboratory studies of sea spikes at low grazing angles, *Journal of Geophysical Research*, *96*(C7), 12,529–12,537.
- Trizna, D. B. (1991), Statistics of low grazing angle radar sea scatter for moderate and fully developed ocean waves, *IEEE Transactions on Antennas and Propagation*, *39*(12), 1681–1690, doi:10.1109/8.121588.

- Trizna, D. B. (1997), A model for Brewster angle damping and multipath effects on the microwave radar sea echo at low grazing angles, *IEEE Transactions on Geoscience and Remote Sensing*, *35*(5), 1232–1345, doi:10.1109/36.628790.
- Trizna, D. B. (2001), Errors in bathymetric retrievals using linear dispersion in 3-D FFT analysis of marine radar ocean wave imagery, *IEEE Transactions on Geoscience and Remote Sensing*, *39*(11), 2465–2469, doi:10.1109/36.964983.
- Trizna, D. B., and D. J. Carlson (1996), Studies of dual polarized low grazing angle radar sea scatter in nearshore regions, *IEEE Transactions on Geoscience and Remote Sensing*, *34*(3), 747–757, doi:10.1109/36.499754.
- Tsang, L., and A. Ishimaru (1985), Theory of backscattering enhancement of random discrete isotropic scatterers based on the summation of all ladder and cyclical terms, *J. Opt. Soc. Am. A*, *2*(2), 1331–1338.
- Tsang, L., and J. A. Kong (1980), Multiple scattering of electromagnetic waves by random distributions of discrete scatterers with coherent potential and quantum mechanical formalism, *Journal of Applied Physics*, *51*(7), 3465–3485, doi:10.1063/1.328200.
- Tsang, L., and J. A. Kong (1982), Effective propagation constants for coherent electromagnetic wave propagation in media embedded with dielectric scatters, *Journal of Applied Physics*, *53*(11), 7162–7173, doi:10.1063/1.331611.
- Tsang, L., and J. A. Kong (2001), *Scattering of electromagnetic waves. Advanced topics.*, *Wiley Series in Remote Sensing*, vol. III, xvi, 413 pp., Wiley, New York.
- Tsang, L., C.-T. Chen, A. T. C. Chang, J. Guo, and K.-H. Ding (2000a), Dense media radiative transfer theory based on quasicrystalline approximation with applications to passive microwave remote sensing of snow, *Radio Science*, *35*(3), 731–749.
- Tsang, L., J. A. Kong, and K.-H. Ding. (2000b), *Scattering of electromagnetic waves. Theories and applications.*, *Wiley Series in Remote Sensing*, vol. I, xiv, 426 pp., Wiley, New York.
- Tsang, L., J. A. Kong, K.-H. Ding, and C. O. Ao (2001), *Scattering of electromagnetic waves. Numerical simulations.*, *Wiley Series in Remote Sensing*, vol. II, xxiv, 705 pp., Wiley, New York.
- Tsang, L., J. Pan, D. Liang, Z. Li, D. Cline, and Y. Tan (2007), Modeling active microwave remote sensing of snow using Dense Media Radiative Transfer (DMRT) theory with multiple-scattering effects, *IEEE Transactions on Geoscience and Remote Sensing*, *45*(4), 990–1004, doi:10.1109/TGRS.2006.888854.
- Tse, K. K., L. Tsang, C. H. Chan, , K. H. Ding, and K. W. Leung (2007), Multiple scattering of waves by dense random distributions of sticky particles for applications in microwave scattering by terrestrial snow, *Radio Science*, *42*, RS5001, doi:10.1029/2006RS003476.

- Ulaby, F. T., R. K. Moore, and A. K. Fung (1986), *Microwave Remote Sensing: Active and Passive, Vol. III – Volume Scattering and Emission Theory, Advanced Systems and Applications*, Artech House, Inc., Dedham, Massachusetts.
- Vagle, S., and D. Farmer (1998), A comparison of four methods for bubble size and void fraction measurements, *IEEE Journal of Oceanic Engineering*, *23*(3), 211–222, doi:10.1109/48.701193.
- Valenzuela, G. R. (1978), Theories for the interaction of electromagnetic and oceanic waves - A review, *Boundary-Layer Meteorology*, *V13*(1), 61–85, doi:10.1007/BF00913863.
- van Dongeren, A., N. Plant, A. Cohen, D. Roelvink, M. Haller, and P. Catalán (2008), Beach Wizard: Nearshore bathymetry estimation through assimilation of model computations and remote observations, *Coastal Engineering*, *55*(12), 1016–1027, doi:10.1016/j.coastaleng.2008.04.011.
- Vandemark, D., B. Chapron, J. Sun, G. H. Crescenti, and H. C. Graber (2004), Ocean wave slope observations using radar backscatter and laser altimeters, *Journal of Physical Oceanography*, *34*, 2825–2842, doi:10.1175/JPO2663.1.
- Voronovich, A. G., and V. U. Zavorotny (2000), The effect of steep sea-waves on polarization ratio at low grazing angles, *IEEE Transactions on Geoscience and Remote Sensing*, *38*(1), 366–373, doi:10.1109/36.823932.
- Walker, D., D. Lyzenga, E. Ericson, and D. Lund (1996), Radar backscatter and surface roughness measurements for stationary breaking waves, *Proceedings of the Royal Society of London. Series A*, *452*(1952), 1953–1984, doi:10.1098/rspa.1996.0104.
- Walker, R. E. (1994), *Marine Light Field Statistics*, John Wiley & Sons.
- Walstra, D. J. R., G. P. Mocke, and F. Smit (1996), Roller contributions as inferred from inverse modelling techniques, in *Proceedings, 25th International Conference on Coastal Engr.*, pp. 1205–1218, ASCE.
- Ward, K., C. Baker, and S. Watts (1990), Maritime surveillance radar. I. Radar scattering from the ocean surface, *Radar and Signal Processing, IEE Proceedings F*, *137*(2), 51–62.
- Wen, B., L. Tsang, D. Winebrenner, and A. Ishimaru (1990), Dense medium radiative transfer theory: comparison with experiment and application to microwave remote sensing and polarimetry, *IEEE Transactions on Geoscience and Remote Sensing*, *28*(1), 46–59, doi:10.1109/36.45744.
- West, J. C. (2002), Low-grazing-angle (LGA) sea-spike backscattering from plunging breaker crests, *IEEE Transactions on Geoscience and Remote Sensing*, *40*(2), 523–526, doi:10.1109/36.992830.
- West, J. C., and S.-J. Ja (2002), Two-scale treatment of low-grazing-angle scattering from spilling breaker water waves, *Radio Science*, *37*(4), 1054, doi:10.1029/2001RS002517.

- West, J. C., J. M. Sturm, and S.-J. Ja (1998), Low-grazing scattering from breaking water waves using an impedance boundary MM/GTD approach, *IEEE Transactions on Antennas and Propagation*, *46*(1), 93–100, doi:10.1109/8.655455.
- West, R., D. Gibbs, L. Tsang, and A. K. Fung (1994), Comparison between optical scattering experiments and the quasi-crystalline approximation for dense media, *J. Opt. Soc. Am. A*, *11*(6), 1854–1858.
- Wetzel, L. (1986), On microwave scattering by breaking waves, in *Wave Dynamics and Radio Probing of the Ocean Surface*, edited by O. M. Phillips and K. Hasselmann, chap. 18, pp. 273–285, Plenum.
- Wetzel, L. B. (1990a), Electromagnetic scattering from the sea at low grazing angles, in *Surface Waves and Fluxes*, vol. II, edited by G. L. Gernaert and W. J. Plant, chap. 12, pp. 109–172, Kluwer Academic Publishers.
- Wetzel, L. B. (1990b), Sea clutter, in *Radar Handbook*, edited by M. Skolnik, chap. 13, McGraw-Hill.
- Wolf, J., and P. S. Bell (2001), Waves at Holderness from X-band radar, *Coastal Engineering*, *43*, 247–263, doi:10.1016/S0378-3839(01)00016-3.
- Wolff, U., J. Seemann, C. Senet, and F. Ziemer (1999), Analysis of morphodynamical processes with a nautical X-band radar, in *IEEE International Geoscience and Remote Sensing Symposium, 1999. IGARSS '99.*, vol. 3, pp. 1671–1673vol.3, doi:10.1109/IGARSS.1999.772056.
- Wright, J. W. (1968), A new model for sea clutter, *IEEE Transactions on Antennas and Propagation*, *AP-16*(2), 217–223.
- Wu, S. T., and A. K. Fung (1972), A noncoherent model for microwave emissions and backscattering from the sea surface, *Journal of Geophysical Research*, *77*(30), 5917–5929.
- Zuniga, M., T. Habashy, and J. A. Kong (1979), Active remote sensing of layered random media, *Geoscience Electronics, IEEE Transactions on*, *17*(4), 296–302, doi:10.1109/TGE.1979.294658.
- Zurk, L., L. Tsang, J. Shi, and R. Davis (1997), Electromagnetic scattering calculated from pair distribution functions retrieved from planar snow sections, *IEEE Transactions on Geoscience and Remote Sensing*, *35*(6), 1419–1428, doi:10.1109/36.649796.
- Zurk, L. M., L. Tsang, K. H. Ding, and D. P. Winebrenner (1995), Monte carlo simulations of the extinction rate of densely packed spheres with clustered and nonclustered geometries, *J. Opt. Soc. Am. A*, *12*(8), 1772–1781.
- Zurk, L. M., L. Tsang, and D. P. Winebrenner (1996), Scattering properties of dense media from Monte Carlo simulations with application to active remote sensing of snow, *Radio Science*, *31*(4), 803–819.

Zurk, L. M., B. Orłowski, G. Sundberg, D. P. Winebrenner, E. I. Thorsos, and A. Chen (2007), Electromagnetic scattering calculations for terahertz sensing, in *Terahertz and Gigahertz Electronics and Photonics VI, Proceedings SPIE*, vol. 6472, edited by K. J. Linden and L. P. Sadwick, p. 64720A, SPIE, doi:10.1117/12.698720.

APPENDIX

A. VIDEO AND RADAR SYNCHRONIZATION

The GATOR Experiment

Gator Acquisition of Timestacks in Optical and Radar

A.1 Motivation

The radar acquisition system has a new feature implemented, in which not only the azimuthal position of each pulse is being recorded, but also the time of this event. This procedure is based on the correct retrieval of GPS time by the acquisition card, and the update of the system clock (Windows XP). After that, the acquisition program queries the system clock and records the returned time, with a precision of 10 ms. The video system on its part, perform a similar process but on a Unix system.

In this context, it is relevant to assess the compatibility and synchronization of both systems, in order to ensure that the time stamps on both systems are accurate and synchronized enough to be used reliably to estimate possible lags associated to the imaging mechanisms of each sensor without including systemic lags.

The conceptual design of the experiment is that it is possible to track a feature in both systems, in particular changes of direction and/or acceleration phases. Since both sensors record the time of each event, it is possible to compare the temporal occurrence of an individual event to estimate the lag between the clocks. If the data record is long enough and multiple events have been recorded, it would be possible to estimate the possible drift between the clocks.

A.2 Experimental Setup

Experiments were carried at the Field Research Facility, US Army Corps of Engineers, in Duck, NC during August 5-9, 2007. Since the method relies in a tracking algorithm,

it was necessary to use a feature that would give a high contrast with its surroundings in both sensors, whilst having a record of its spatial coordinates. It was found that an all terrain vehicle (ATV) gave a good contrast signal for the video system. Regarding the radar system, the feature had to be elevated above the beach in order to overcome shadowing from the dune, and it had to have a strong scattering signature. This was achieved by mounting a pair of corner reflectors atop a mast attached to the ATV. The reflectors were positioned about 4 meters above the beach level, and rotated to face the radar antenna. This allowed it to be visible to the radar antenna at all locations along the beach. To track its position, a handheld Garmin Gecko 201 GPS unit was used on the ATV at all times, recording its spatial coordinates and time. The ATV setup can be seen in Fig. A.1.



Fig. A.1: ATV with the corner reflectors mounted. The optical contrast of the ATV with the beach is readily noticeable.

Video data was recorded using four of the ARGUS cameras permanently deployed at the FRF. The sampling rate was 2 Hz and data was collected over 2048 samples. The area of interest was a set of pixel arrays that covered a rectangular area of beach slightly north of the FRF pier. It had an extension of 580 m (alongshore) and 65 m (cross shore) with 1 m resolution. The radar remote sensing system consisted of a Sitex RADARpc-25.9 marine X-band radar sampling at 0.7 Hz at HH polarization. The radar antenna was located at $x=20.63$ m, $y=970.57$ m in the FRF coordinate system, atop a 30 ft tower. The data length was set to 650 samples. Prior to some runs, the GPS unit of the radar system was reset and the Windows system clock was updated accordingly.

Both systems were started manually within one minute.

A total of 9 runs were performed during Aug 9, 2007. During each run, the ATV routinely performed alongshore excursions in both directions (north and southbound) and it also described circular trajectories. The changes in direction and departure from rest times are the signatures we will use in the data analysis.

A.3 Data Analysis

A.3.1 Feature Tracking

A tracking algorithm was designed to track the motion of the ATV in both sensors. The centroid of the signal above a certain threshold was used as indicative of the ATV position. The algorithm was started using a known location of the ATV based on the handheld GPS data. This location was used as the center of a square window which was scanned to find a high contrast signal. The centroid of this high contrast signal was assumed to be the location of the ATV, and used as center for the next window. After that, tracking of the signal was done automatically and the GPS data from the handheld unit was used only as a predictor-corrector. If the measured (by the algorithm) location differed by more than 15 m from the GPS unit, the location window center was reset to that of the location of the handheld GPS unit and the algorithm continued. The window sides were 15 pixels for the radar, and 21 pixels for the video, owing to the different spatial resolutions.

Geolocation of the video data is performed routinely by the ARGUS system and the data is consequently retrieved in FRF coordinates. However, the design of the pixel arrays was defined at an elevation of $z=0$ m. Since the ATV ran over the beach, its elevation was not constant and therefore it induced a misregistration error (horizontal plane misplacement) of the signal. However, since our focus is related with changes of direction, it is considered that this did not affect the analysis and no correction was attempted.

Geolocation of the radar system requires knowledge of the antenna location and

orientation. Since the radar is recorded in polar coordinates, conversion to the FRF (Cartesian) coordinates involves interpolation that would degrade the inherent temporal accuracy of the system. In consequence, the tracking was performed in polar space and only the tracked positions were transformed to a Cartesian map. The time of each event is thus not affected.

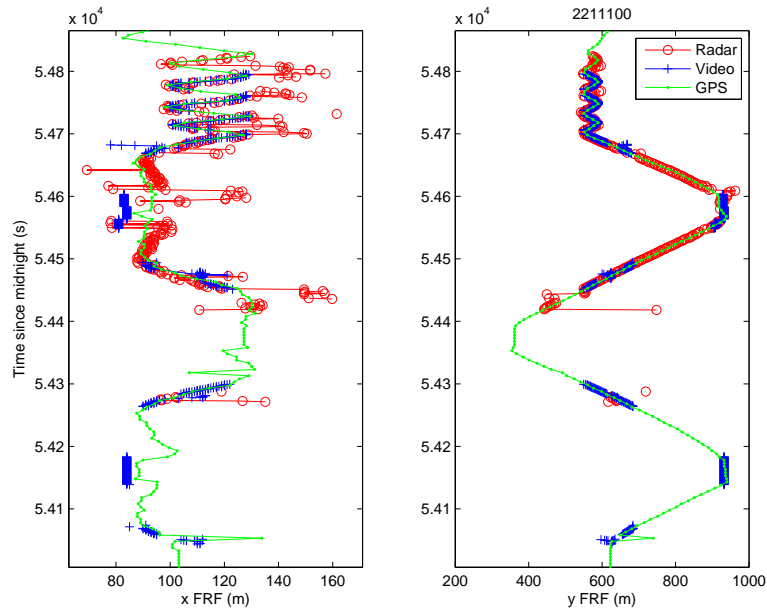


Fig. A.2: Track positions of the ATV. GPS unit (green), Radar tracked (red), Video tracked (blue). Left panel, time vs cross-shore position. Right panel, time vs alongshore position.

Fig. A.2 shows an example of the tracking results for Run 2211100 (August 9, 2007, 11:00 EST). The handheld GPS, radar and video tracks are in green, red and blue respectively. The data is presented in a two dimensional format (time versus space position) to improve readability. Several features can be seen here. First, a general good agreement between the tracks of all sensors is evident, especially at the y coordinate. The noise in the radar x coordinate is the result of small differences in the location of the centroid of the signal between consecutive rotations. It must be mentioned that the fully automated algorithm yield very noisy results for the radar dataset, hence, the selection of the window center was performed manually at each rotation. The selection of the

centroid, however, remained automated. The speed on both sensors, characterized by the slope of the linear sections is also showing good agreement. Of particular interest are the sinusoidal-like patterns near $t=5.48 \times 10^4$ s. These correspond to the circular patterns described by the ATV, which in a 3D plot would correspond to a circular spiral. Of special interest are the reversals of direction, since they provide a good opportunity to estimate the lag between the system clocks.

A.3.2 Time lag Estimation

Of the 9 runs, 6 contained data from both sensors that could be used to estimate the time lag. From these, 14 individual events were selected manually to be used in the analysis. These events typically were associated to the sinusoidal-like features shown in Fig. A.2, on which a spatial extrema associated with a change of direction can be clearly seen. Since a clean record in the x coordinate does not necessarily correspond to a clear record on the y coordinate, the events are a subset of data consisting of the time data and the spatial data associated to a single coordinate. For most of the cases, the alongshore record (y) was used. Fig. A.3 shows an example of a selected event.

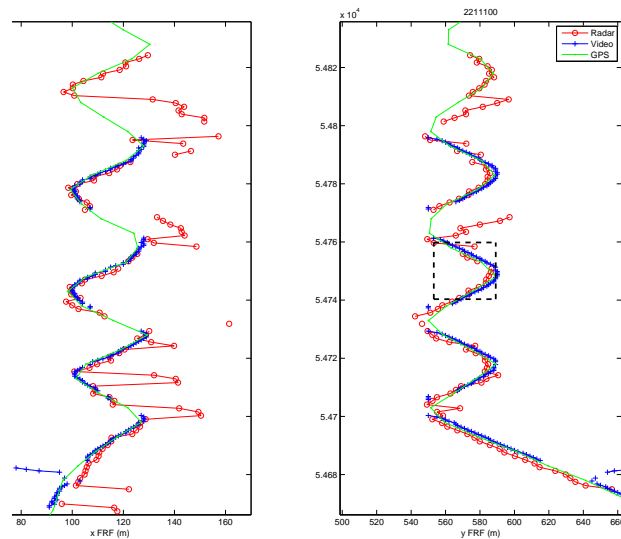


Fig. A.3: Selection of an event. In this case, the event is selected from the alongshore record (y), and is marked by the black square on the left panel.

Once the data is selected, the space-time records of each sensor are fitted with a second order polynomial. The parameters of the polynomial are then evaluated at a high resolution temporal grid ($\Delta t=0.01$ s). From this synthetic set representing the idealized trajectory, the location and time of the peak can be obtained. The difference between the time of the peaks is the lag between the records. This procedure can be seen graphically in Fig. A.4.

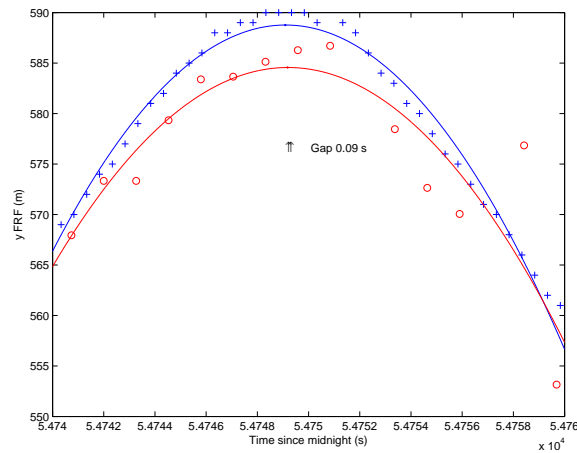


Fig. A.4: Lag estimation. Lines correspond to the synthetic second order polynomial associated to the best fit to the data. The location of the maxima is denoted by solid points. The time difference between the maxima is the lag. Blue data corresponds to video, red data corresponds to radar.

Table A.1: Results of the lag analysis.

Run #	Number of Events	Mean(lag) sec	Std Dev (lag) sec
1100	5	-0.29	0.41
1200 ¹	2	-0.46	0.23
1230	4	-0.25	0.15
1400	3	-0.20	0.29
Overall	14	-0.28	0.28

A.4 Results

The results are summarized in Table A.1. It can be seen that in general, the lag is about $1/5$ of the radar temporal resolution, suggesting that for all purposes both sensors can be considered to be synchronized.